Claire Donohoe

UNRAVELLING THE PIVOTAL ROLE OF ATROPISOMERISM FOR CELLULAR INTERNALIZATION

Tese no âmbito do doutoramento em Química, ramo de Química Médica, orientada pela Doutora Lígia C. Gomes-da-Silva e pelo Professor Doutor Mathias O. Senge e apresentada ao Departamento de Química, Faculdade de Ciências e Tecnologia da Universidade de Coimbra.

Maio de 2022

Faculdade de Ciências e Tecnologia da Universidade de Coimbra

Unravelling the Pivotal Role of Atropisomerism for Cellular Internalization

Claire Donohoe

Dissertação de Doutoramento na área científica Química, ramo de Química Médica orientada pela Doutora Lígia C. Gomes-da-Silva e pelo Professor Doutor Mathias O. Senge e apresentada ao Departamento de Química da Faculdade de Ciências e Tecnologia da Universidade de Coimbra.

Maio de 2022

1 2 9 0

UNIVERSIDADE D
COIMBRA

The work presented in this thesis was carried out at the Chemistry Department of the Faculty of Sciences and Technology of the University of Coimbra, Institute of Nuclear Sciences Applied to Health (ICNAS), Coimbra and the School of Chemistry, Trinity Biomedical Sciences Institute of Trinity College Dublin. The work received funding from the European Union's Horizon 2020 research and innovation programme under the Marie Skłodowska-Curie grant agreement number 764837 (POLYTHEA—How light can save lives), the Portuguese Foundation for Science and Technology (UID/QUI/00313/2019 and PTDC/QUI-OUT/0303/2021), the Higher Education Authority, Ireland and Science Foundation Ireland (SFI). Luzitin S.A. provided redaporfin for investigation.

“We can only see a short distance ahead, but we can see plenty there that needs to be done.”

Alan Turing

TABLE OF CONTENTS

ACKNOWLEDGEMENTS

The development of this project was the result of many people generously giving their knowledge and time. Firstly, I would like to express my sincere gratitude to both Dr. Lígia C. Gomes-da-Silva and Prof. Dr. Mathias O. Senge for their continuous supervision, patience and encouragement. I am very grateful to have had the opportunity to learn with their guidance. The interdisciplinary approach taken in this research would not have been possible without their support and expertise.

I wish to particularly thank my two host and accrediting institutions: Universidade de Coimbra and Trinity College Dublin. Many thanks to the European Union's Horizon 2020 research and innovation programme which financially supported this work under the Marie Skłodowska-Curie POLYTHEA grant agreement, the Portuguese Foundation for Science and Technology, the Higher Education Authority, Ireland, and Science Foundation Ireland (SFI). I would also like to thank Luzitin S.A. for providing redaporfin for studies.

Working as part of the POLYTHEA project afforded me the possibility to learn within two research groups. I wish to extend my sincere thanks to Prof. Dr. Luís G. Arnaut for his invaluable advice throughout the project and the opportunity to work with redaporfin's atropisomers in his group. Many thanks are also due to Prof. Dr. Mariette M. Pereira and Dr. Nuno Gonçalves for their support in this project. I wish to thank Dr. Fábio Schaberle for many helpful scientific discussions and excellent technical assistance with the photophysical experiments discussed in this work. I am very grateful to Dr. Asterios Charisiadis who provided enormous assistance with porphyrin synthesis and helpful proofreading. Special thanks also to Dr. Nitika Grover for her lab management in Trinity College Dublin, and patience in teaching me practical skills. I would also like to acknowledge the support of Prof. Dr. Carlos Serpa. Many thanks to Dr. Sophia Sarpaki and Bioemtech, Greece, who kindly hosted me for secondment training.

I would like to thank Catarina Pinto, Dr. Luísa Cortes and Dr. Ana-Clara Rodrigues who provided technical assistance with HPLC, confocal microscopy and fluorescence spectroscopy, respectively. I also wish to thank Prof. Dr. Maria João Moreno for providing liposomes. I am grateful to Dr. Christopher Kingsbury and Dr. Brendan Twamley for their assistance with X-ray crystallography studies. Special thanks to Sophie Maguire who contributed to the preparation of porphyrins. I also would like to acknowledge Dr. John O'

Brien, Dr. Manuel Ruether, Dr. Gary Hessman and Dr. Fábio Rodrigues who helped with the characterization of the compounds in this thesis.

I wish to thank all of my colleagues at the University of Coimbra including: Maria Inês, Catarina, Hélder, Amilcar, Diogo, Daniela, André, Luís, Carolina, Anita and Nidia. Special thanks to Maria Inês, Catarina and Nidia for their constant support, particularly when experiments failed! Many thanks are also due to the past and present members of the Senge research group: Alina, Keith, Grant, Elisabeth, Karolis, Jessica, Susan, Zoi, Bhavya, Harry and Piotr. Special thanks to Zoi for her support since our selection interview and to Piotr for sharing this memorable time in Portugal. I would like to recognize the work of our project manager, Aurore and the project coordinator, Prof. Dr. Stéphanie Leroy-Lhez as well as acknowledge the wider POLYTHEA network of students and supervisors who made this project so rewarding.

I would like to thank my friends who supported me through this work from afar: Aislinn, Georgia, Laura and Maddy. Finally, I would like to thank my family, my parents and my sister Róisín, for reminding me to make the most of this experience and supporting my studies in every possible way.

THESIS ABSTRACT

Atropisomerism presents an intriguing, often neglected, source of varied biological activity in drug development. For a stable atropisomeric drug mixture, assessment of individual atropisomers may reveal an individual isomer with higher efficacy. Tetrapyrrole isomerism is rarely considered during photosensitizer (PS) development for photodynamic therapy (PDT). The atropisomers of a pre-clinical bacteriochlorin PS for PDT, redaporfin, are stable and separable. They displayed vastly different photodynamic efficacy profiles, which were discovered to be a consequence of differential cellular uptake. Redaporfin atropisomer uptake was determined as a predominantly passive process *in vitro*. The α_4 atropisomer, which features sulfonamide substituents orientated on the same side of the tetrapyrrole macrocycle, appeared to enhance binding interaction with the cell membrane phospholipid bilayer and subsequent diffusion. Cells of the tumor microenvironment exhibited enhanced α_4 uptake *in vivo* which was correlated to the PDT efficacy when tumor illumination was performed 24 h after α_4 administration.

Orientation of polar groups to one side of the macrocycle plane appeared to benefit cell uptake in a manner which may be incorporated into drug design as an efficient cell-penetrating conformation. The validation of these findings was confirmed with the preparation of novel porphyrin photosensitizers with highly restrictive strap moieties to enforce the α_4 configuration of polar groups. Direct condensation methods, between pyrrole and dialdehyde, yielded multiple double strapped porphyrin isomers which were characterized by single crystal X-ray crystallography and ^{1}H NMR. Enhanced uptake of the cis-$\alpha\alpha$ isomer, analogous in structure to the redaporfin α_4 configuration, illustrated the potential of this motif to promote internalization. The success of this strategy with high molecular weight photosensitizers (> 1000 Da) demonstrates its potential for incorporation in the design of macromolecules to aid membrane passage.

Key words: Photodynamic therapy, cellular internalization, atropisomerism, anti-cancer activity, strapped porphyrins.

RESUMO DA TESE

O atropoisomerismo é uma fonte intrigante, mas muitas vezes negligenciada, de variabilidade biológica que pode ocorrer durante o desenvolvimento de fármacos. A avaliação individual de cada atropoisómero existente num fármaco pode revelar a presença de um isómero conformacional de maior eficácia. Contudo, o isomerismo conformacional é raramente tido em conta aquando o desenvolvimento de fotossensibilizadores, nomeadamente moléculas tetrapirrólicas, para terapia fotodinâmica (PDT). Os atropoisómeros do fotossensibilizador redaporfin são estáveis e possíveis de seres isolados. Estes apresentam efeitos fotodinâmicos muito diferentes, os quais resultam de níveis de internalização celular muito distintos. Os atropoisómeros da redaporfin são internalizados pelas células essencialmente por difusão passiva. No atropoisómero α_4, a presença de todos os grupos sulfonamida no mesmo lado do macrociclo tetrapirrólico aumenta a interação deste confórmore com a bicamada lipídica das membranas celulares, o que facilita a subsequente difusão. Estudos *in vivo* também confirmaram que o atropoisómero α_4 é o atropoisómero mais internalizado pelas células do ambiente micro-tumoral. Esta melhoria na internalização celular está correlacionada com uma maior eficácia da PDT em protocolos em que a iluminação dos tumores ocorre 24 h após a administração do fotossensibilizador.

A internalização celular aparenta ser beneficiada quando todos os grupos polares da redaporfin estão orientados para o mesmo lado do macrociclo. Esta informação pode ser aproveitado para o desenvolvimento de novos fármacos com conformações que permitam uma internalização celular mais eficiente. A validação desta hipótese foi confirmada pela preparação de novas porfirinas com "presilhas" altamente restritivas que forçaram a configuração do atropisomer α_4, pelo menos no que diz respeito à posição dos grupos polares. Métodos diretos de condensação entre os grupos pirrole e dialdeído permitiram a obtenção de isómeros de porfirinas, os quais foram caracterizados por cristalografia e ^{1}H NMR. O isómero cis-$\alpha\alpha$, o qual exibe uma conformação análoga ao atropisomer α_4, apresentou níveis de internalização celular mais elevados do que os outros isómeros. A validação desta estratégia com fotossensibilizadores de elevado peso molecular (>1000 Da) demonstra que as conclusões deste trabalho podem contribuir para o desenvolvimento de macromoléculas com uma internalização celular mais eficiente.

Palavras chave: Terapia fotodinâmica, internalização celular, atropoisomerismo, atividade anti-tumoral, porfirinas com pontes.

LIST OF ABBREVIATIONS

ALA - 5-Aminiolevullinic acid
ALK - Anaplastic lymphoma kinase
ANXA1 - Annexin A1
APCI - Atmospheric Pressure Chemical Ionization
ATP - Adenosine Triphosphate
B16-F10 - Mouse melanoma cells
BMS - Birstol Myers-Squibb
BSA - Bovine Serum Albumin
BTK - Bruton's Tyrosine Kinase
CALR - Calreticulin
CD - Circular Dichroism
CPP - Cell Penetrating Peptides
CT26 - Mouse colon carcinoma cells
CTLA-4 - Cytotoxic T-lymphocyte Antigen-4
DAMPs - Damage Associated Molecular Patterns
DC - Dendritic Cell
DCE - Dichloroethane
DFT - Discrete Fourier Transform
DG - 2-deoxy-D-glucose
DLI - Drug-Light Interval
ee - Enantiomeric Excess
EGFR - Epidermal Growth Factor Receptor
ER - Endoplasmic Reticulum
ESI - Electrospray Ionization
FDA - United States Federal Drug Association
GA - Golgi Apparatus
H-atom - Hydrogen atom
H_2O_2 - Hydrogen peroxide
H-bond - Hydrogen bond
HMGβ1 - High-Mobility Group Box 1
HPD - Hematoporphyrin Derivative
HPLC - High Performance Liquid Chromatography
HRMS - High Resolution Mass Spectrometry
HSP - Heat Shock Proteins
HSQC - Heteronuclear Single Quantum Coherence
i.v. - Intravenous
IFN - Type I Interferon
ISC - Intersystem Crossing
Laser - Light amplification by stimulated emission of radiation
LDL - Low Density Lipoprotein
LED - Light Emitting Diodes

LogPow - Logarithm of the n-octanol:water partition coefficient
MALDI - Matrix-Assisted Laser Desorption Ionization
MeCN - Acetonitrile
NIR - Near infrared red
O_2 - Molecular oxygen
$O_2^{\bullet-}$ - Superoxide anion
$OH^{\bullet}$ - Hydroxyl radical
OLED - Organic light emitting diodes
P11 - 5,10,15,20-tetrakis(2,6-difluoro-3-N-methylsulfamoylphenyl)porphyrin
PCI - Photochemical Internalization
PD-1 - Programmed Death-1 Associated Receptor
PD-L1 - Programmed Death-1 Associated Receptor Ligand
PDT - Photodynamic Therapy
PI3K - Phosphoinositide 3-Kinase
POPC - 1-palmitoyl-2-oleoyl-sn-glycero-3-phosphocholine
PS - Photosensitizer
PS* - Excited state PS
Q-TOF - Quadrupole Time-of-Flight
Redp. SM - Redaporfin Starting Material
ROESY - Rotating Frame Overhauser Effect SpectroscopY
ROS - Reactive Oxygen Species
RP - Reversed Phase
RT - Room Temperature
SD - Standard Deviation
SEM - Standard Error Mean
TLC - Thin-Layer Chromatography
Tol. - Toluene
$t_{1/2}$ - Half-life
U-2 OS - Human bone osteosarcoma cells
VCD - Vibrational circular dichroism
Vt-NMR - Variable temperature ^{1}H NMR
(*m,m'*) - *meta,meta'*
(*o,o'*) - *ortho,ortho'*
$^1O_2$ - Singlet Oxygen
^{3}PS* - Triplet excited state
4T1 - Mouse mammary breast cancer cells
$\Delta G^{\ddagger}$ - Activation energy barrier of interconversion
ε - Molar absorption coefficient
τ_T - Triplet lifetime
Φ_F - fluorescence quantum yield
Φ_{PD} - Photodecomposition quantum yield
Φ_Δ - Singlet oxygen quantum yield

PREFACE

Atropisomerism, is typically disregarded in the context of photosensitizers for photodynamic therapy, despite growing awareness that, similar to chiral enantiomers, the biological activity of atropisomers may vary. Redaporfin, a pre-clinical synthetic sulfonamide fluorinated bacteriochlorin, presents ideal properties for studying PDT including enhanced photostability and strong absorption at 750 nm. Hindered rotation of the meso aryl-macrocyclic bonds of the redaporfin bacteriochlorin and porphyrin structures results in different spatial orientations of the sulfonamide groups in the *meta* positions. These are defined as: α_4, $\alpha_3\beta$, $\alpha_2\beta_2$ and $\alpha\beta\alpha\beta$ depending on the position of sulfonamide group above (α) or below (β) the macrocycle plane. The company Luzitin identified dramatically varied phototoxicities of redaporfin atropisomers *in vitro* during the development of redaporfin, which prompted this investigation of the influence of atropisomerism on PDT efficacy.

Chapter 1 provides a general introduction to PDT, the factors which influence its efficacy and its current status as a clinical anti-cancer treatment. Second-generation photosensitizers are introduced, including redaporfin and its compromised purity as a mixture of four atropisomers. Atropisomerism is defined together with the analytical techniques used to elucidate atropisomer structure and stability. The impact of atropisomerism on drug biological activity, as well as methods to alter atropisomer stability, are described. Tetrapyrrole atropisomers, often referred to as 'picket-fence' porphyrins, are highlighted.

Chapter 2 describes the impact of atropisomerism on redaporfin-PDT. Atropisomers were separated by reversed-phase chromatography and characterized by ^{1}H NMR and single X-ray crystallography. The atropoisomeric purity of redaporfin and related porphyrin atropisomer samples employed for biological studies was assessed by high performance liquid chromatography (HPLC). A common indicator of lipophilicity, chromatographic elution order, was unexpectedly the same, regardless of the type stationary phase employed (normal or reversed). Enrichment of the α_4 atropisomer was observed in a non-polar solvent mixture. Photophysical and photochemical properties were determined to not vary in a manner which would suggest varied phototoxicity. In contrast to the enrichment data, determination of the $LogP_{OW}$ (logarithm of the n-octanol:water partition coefficient), revealed atropisomer lipophilicity was similar, with slightly enhanced lipophilicity for the $\alpha_3\beta$ atropisomer.

Atropisomer phototoxicity was confirmed to vary *in vitro* with four cancer cell lines of different histological origin. Altered membrane permeation of the different redaporfin atropisomers was directly correlated with their phototoxicity. The heightened uptake of α_4 was confirmed using two methods featuring fluorescence detection, by flow cytometry and following cell lysis, *in vitro*. Subcellular accumulation at the endoplasmic reticulum (ER) and Golgi apparatus (GA) was determined for all atropisomers. Atropisomer internalization was only marginally affected by adenosine triphosphate (ATP) depletion, plasma proteins and formulation in micelles. The enhanced α_4 interaction with 1-palmitoyl-2-oleoyl-sn-glycero-3-phosphocholine (POPC) liposomes indicated that a passive process was responsible for heightened uptake. Increased α_4 uptake by cells of the tumor microenvironment was observed *in vivo* following intravenous administration. The varied uptake was correlated to the PDT response when CT26 tumor illumination was performed 24 h after α_4 administration (cellular-PDT) but not when illumination was performed after 15 min (vascular-PDT).

These results showed that properly oriented tetrapyrrole polar groups may be incorporated into drug design as an efficient cell-penetrating conformation. This was explored in **Chapter 3** with the design of novel photosensitizers featuring strapped moieties to lock atropisomer rotation and impose the α_4 configuration. Double strapped porphyrins were prepared using direct condensation methods between a dialdehyde and pyrrole to yield isomers *cis*-αβ, *cis*-αα and *trans*-αβ with varied polar group orientations. Strap lengths were selected to target planarity. The number of porphyrin strap configurations formed was dependent on the condensation method. Silica chromatography separation was followed by structural elucidation with ^{1}H NMR and X-Ray crystallography. Photophysical evaluation provided insight into the relative macrocycle conformation of the porphyrin isomers. The *cis*-αα isomer, with a configuration similar to redaporfin α_4, exhibited enhanced cell internalization *in vitro*. This demonstrated the potential of our findings to be translated into molecular design to increase cell uptake.

Chapter 4 provides a reflection on future perspectives for the impact of this configuration. Conclusions regarding the α_4 configuration are discussed in the context of other strategies which enhance drug cell internalization.

1. General Introduction

1.1 PHOTODYNAMIC THERAPY

PDT relies on the interaction of three components - molecular oxygen (O_2), a PS and light - which synergistically combine to produce reactive oxygen species (ROS), mediating a therapeutic anti-cancer or anti-microbial effect. These three components, while individually non-toxic, induce localized damage to target tissue with the added potential for systemic immune stimulation.[1] A lack of toxicity in the absence of light makes selectivity an intrinsic property of PDT, imposed by the region of irradiation. Despite the clinical success of PDT for dermatological application, it has yet to gain acceptance as a first line therapy for cancer treatment, except for skin cancers.[2-3] As a multicomponent therapy, optimization of the individual features of a PDT treatment regimen is not a simple task. Appropriate administration of a PS must be selected with a suitable time interval before irradiation (drug-light interval, DLI). Light of a specific wavelength must then be delivered to the target tissue, with an adequate dose and suitable margins to effectively activate a PS for optimal therapeutic effect.[1] Multidisciplinary knowledge has been used to optimize these individual aspects of PDT, allowing its application to reach clinical use for various cancers,[4-6] age related macular degeneration,[7] dermatology,[8] and infectious diseases.[9]

1.1.1 The development of photodynamic therapy

The origins of PDT and the use of light for therapeutic effects spans thousands of years. There is evidence of Egyptian, Indian, Chinese, Roman and Greek civilizations using sunlight in therapies to treat multiple diseases, including vitiligo and psoriasis.[10] These early PDT treatments used dye extracts from seeds in combination with sunlight to induce re-pigmentation, a treatment which has evolved to become PUVA photochemotherapy. This uses psoralen and UVA light as a dermatological treatment.[11] Modern PDT emerged at the end of the nineteenth century when Oscar Raab, a student of Herman von Tappeiner, observed a toxic effect for *Paramecium* in the presence of the dye acridine, only when combined with light.[12-13] Red light exposure was observed to treat smallpox by Niels Finsen, defining it as ‘phototherapy’.[14] Von Tappeiner and Jesionek coined the term ‘photodynamic action’ to describe the treatment of basal cell carcinoma with eosin and white light.[15]

The emergence of the tetrapyrrole motif in clinical PS drugs began with hematoporphyrin, originally discovered through removal of iron from blood by Scherer.[10] The photodynamic

properties of hematoporphyrin were evaluated against *paramecia*, erythrocytes, mice, guinea pigs and humans with sunlight exposure. This work is now regarded as the first photodynamic biological experiments.[11] Early observation of skin photosensitivity was made by Friedrich Meyer-Betz who self-administered hematoporphyrin intravenously in 1912 and consequently suffered swelling and pain associated with areas exposed to sun.[5,16] Schwarz's isolation of the more tumor-localizing component of hematoporphyrin, referred to today as hematoporphyrin derivative (HPD), ushered in the modern era of PDT in the 1960s.[10] Use of this derivative's fluorescence for the purpose of tumor detection by Lipson et al.[17] was followed by its application for treatment of recurrent breast cancer.[11]

A promising breakthrough for PDT occurred with HPD in 1975, when its application by Dougherty et al. led to the eradication of mammary tumor growth in mice.[18] Successful elimination of mouse bladder carcinoma[19] was soon followed by human trials for bladder carcinoma.[20] Critically, at this time, Weishaupt et al.[21] identified the central player in photodynamic action, singlet oxygen, as the cytotoxic species. A study of 25 patients with skin cancer by Dougherty et al. featured HPD and led to complete response in 98 out of 113 tumors, partial response for 13 tumors and just 2 tumors proving resistant to therapy.[22] These findings were crucial for the clinical implementation of PDT as a number of trials followed, featuring HPD-PDT for lung cancer,[23] esophageal cancer,[24] gastric carcinoma[25] and bladder cancer.[26] Ultimately, HPD was adapted for commercial use as a partially purified form, porfimer sodium, referred to in commercial formulation as Photofrin. This was the first PS approved for clinical use, with application against bladder cancer in Canada. The PS is composed of a complex mixture of ester- and ether-linked dimers and oligomers.[4] The United States Federal Drug Association (FDA) approval for Photofrin-PDT treatment of esophageal cancer and lung cancer established the clinical use of PDT.[27] Despite more than 20 years passing since this initial approval, PDT has yet to achieve the status of other conventional treatments.[2-3]

1.1.2 Mechanisms of photodynamic action

Figure 1 illustrates the key process associated with PS activation which culminate in PDT. Upon light irradiation, absorption of a photon with the appropriate wavelength energy activates a PS to its short lived, excited state (PS*). PS deactivation may occur through several competing pathways. Relaxation of this excited state may occur by fluorescence emission, a radiative decay process or, alternatively, through intersystem crossing (ISC), a

non-radiative decay process, to the triplet excited state (^{3}PS*). For PDT, interaction with molecular oxygen can produce ROS capable of causing cytotoxicity to cells.[4,11,28]

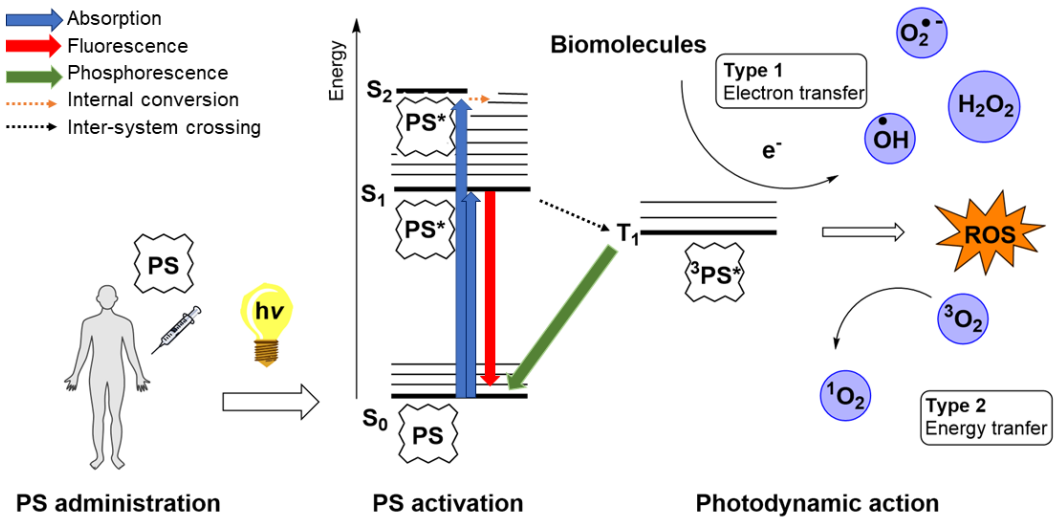

Figure 1. Modified Jablonski diagram. The main events leading to Type 1 and Type 2 photochemical reactions are illustrated. Adapted from Melissari et al.[11]

ROS generation may occur through two processes, potentially in tandem. Type 1 reactions can occur directly with a substrate, such as a biomolecule, through transfer of an electron or proton for the respective formation of a radical cation or anion. Interaction of the latter with molecular oxygen can lead to the formation of superoxide anions ($O_2^{\bullet-}$), not particularly reactive alone but capable of dismutation or electron reduction to produce cytotoxic hydrogen peroxide (H_2O_2). Superoxide anions may further react to produce hydroxyl radicals ($OH^{\bullet}$), capable of membrane passage and strong potential to oxidize cellular components.[11] Despite high reactivity, the short lifetime in biological media limits the maximal distance of hydroxyl radical action to 1 nm. Consequently, PDT activity from Type 1 processes is largely determined by PS intracellular localization.[29]

Singlet oxygen ($^1O_2$), has a slightly larger diffusion radius, but it is still lower than the diameter of most organelles, therefore also limiting the site of PDT action.[30] This major cytotoxic agent of PDT is the product of the Type 2 reaction which involves transfer of PS triplet state energy to molecular oxygen to form excited state singlet oxygen. This transfer is a fast, spin allowed process, as O_2 is also in the triplet state. Tetrapyrrole PDT is considered to be dominated by the Type 2 reaction.[11] The reaction ratio describing the contribution of each mechanism to PDT action depends on the PS structure, in addition to

the oxygen content of the irradiated tissue. Type 1 reactions may overtake the action of Type 2 as oxygen concentration is depleted.[28]

1.1.3 Photodynamic therapy for cancer treatment

PDT encounters prominent application in cancer treatment. PS biodistribution and/ or intracellular localization are critical for anti-cancer PDT efficacy. This is due to the limited lifespan of ROS (see above) which restricts oxidative damage.[31-32] Clinically, the majority of PSs for anti-cancer PDT are administered intravenously.[1] Following systemic administration, PS reaches a solid tumor with distribution through the vascular compartments and passage to the interstitial space, where it can permeate tumor cells.[33] At short dug-light intervals, PS tends to be activated within the tumor vasculature, which inhibits tumor oxygen and nutrient supply.[33] If adequate time is allowed for cells of the tumor microenvironment to internalize the PS, intracellular targets are reached and exposed to the direct cytotoxicity of ROS. Subcellular organelle preference of PS is altered, depending on lipophilicity. More hydrophobic PS accumulate in the membranes of ER, GA and/or mitochondria. Hydrophilic PS are more likely to accumulate in the endocytic pathway, specifically in lysosomes. The toxicity induced as a consequence of PDT are strongly influenced by PS subcellular localization. For example, oxidative damage at the ER/GA and mitochondria is generally considered more lethal than lysosomal destruction.[34]

When the ability of cells to achieve ROS detoxification is outweighed by the oxidative stress; cell death mechanisms are ultimately triggered (Figure 2). These pathways are complex and tend to overlap in tumor destruction. In PDT, necrosis, apoptosis and autophagy are the mechanism of cell killing most often reported. Necrosis is a non-regulated cell death mechanism which typically occurs as a result of severe stress. It rapidly culminates in organelle destruction, cytoplasmic swelling and compromises membrane integrity leading to release of intracellular contents and, ultimately, inflammation.[35] The likelihood of necrosis tends to increase with short DLI, which leads to PS membrane affinity or presence in the cytosol.[36] In contrast to necrosis, apoptosis is a regulated cell death pathway which maintains plasma membrane integrity. Cell shrinkage, fragmentation and the formation of apoptotic bodies are characteristic features of apoptosis. The mitochondria assume a central role in apoptosis pathways, which leads to effector caspase activation. Autophagy is a survival pathway, characterized by autophagosome formation

which fuses with lysosomes to clear damaged cell material. Under circumstances of permanent organelle damage, autophagy induces cell death.[34,37]

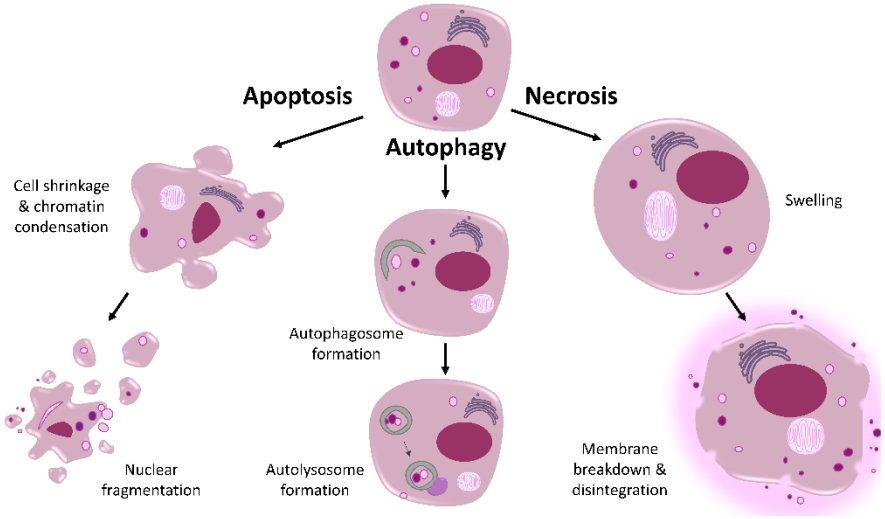

Figure 2. Prominent cell death mechanisms induced by photodynamic therapy. Representation of key morphological changes which occur upon apoptosis, autophagy and necrosis. Adapted from Donohoe et al.[34]

While these three cell death mechanisms are not the only pathways implicated with PDT, general trends associated with the impact of treatment conditions for these pathways have been identified. High dose PDT (high light dose and high PS dose) leads to necrosis as the dominant mode of cell death. With lower dose PDT, regulated cell death, for example apoptosis, is anticipated. Minor photodamage initiates autophagy which, when overwhelmed by stress or accompanied by lysosomal damage, leads to cell death.[35] Another regulated pathway significant for PDT may activate an adaptive immune response through controlled emission of a specific set of damage associated molecular patterns (DAMPs), considered the hallmarks of immunogenic cell death. Release of these DAMPs, including calreticulin (CALR) and heat shock proteins (HSP), ATP, type I interferon (IFN), high-mobility group box 1 (HMGβ1) and annexin A1 (ANXA1), are part of a major therapeutic outcome of PDT anti-tumor immunity.[38] The innate arm of the immune system responds first to PDT, which features neutrophil infiltration to the tumor. Following this, dendritic cell recruitment to tumors is initiated by ATP. CALR/HSP prompts antigen uptake while HGMβ1 stimulates DC migration to the lymph nodes where the adaptive immune response is activated, priming cytotoxic CD8+ T cells. The T cell response may not only induce local tumor destruction but also include sites of metastasis.[39] While exact mechanisms have not

been elucidated, PDT with short DLI has also been demonstrated to stimulate anti-tumor immunity (Figure 3).[40-41]

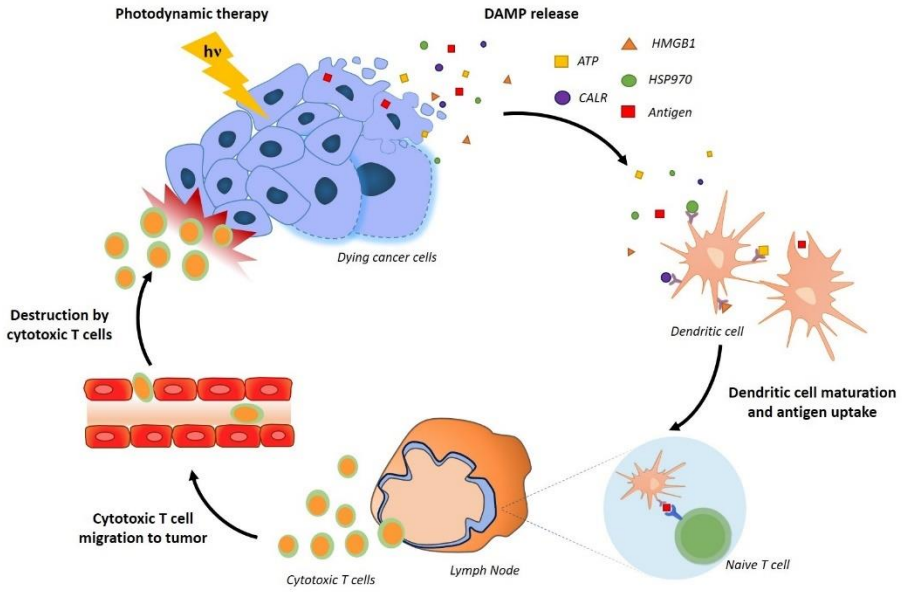

Figure 3. Anti-tumor immunity stimulated by PDT. Representation of key steps involved in DAMP release, dendritic cell maturation and migration to lymph nodes where adaptive immune response is mediated by T cells. Adapted from Donohoe et al.[34]

As a multicomponent therapy, PDT can require complex dosimetry to achieve therapeutic success. Extensive optimization is required for it to reach its full potential. However, PDT offers substantial benefit for this cost. When conventional cancer treatment modalities such as radiation, chemotherapy and molecular targeted therapies are considered, issues of treatment toxicity and drug resistance are frequent and particularly associated with late stage diseases where surgical intervention is not possible.[42] Off-target toxicity of PDT is lower than these traditional treatments. Lower risk of infection and better cosmetic results are also achieved compared to surgery.[2] A major clinical advantage of PDT is its potential to stimulate anti-tumor immunity, contributing to the long term control of disease and metastasis. Compared to the immunosuppressive effects of conventional therapies and toxicities endured by patients, due to high doses needed for optimum effect,[34,39] PDT offers significant advantage. The distinctive mode of PDT action prevents acquisition of many of the resistance mechanisms associated with frontline therapies. Additionally, preclinical evidence that PDT can overcome drug resistance pathways by reversing chemoresistance and resensitizing tumors to molecular inhibitors shows the unrealized clinical potential of PDT.[42]

While off-target toxicity is considered relatively low for PDT, indiscriminate PS tumor accumulation remains a cause of concern. Ideally, PSs should selectively target cancer lesions, preventing toxicity of healthy tissues, minimizing the dose required for therapeutic effect and consequently reducing potential side effects such as skin photosensitivity. Selectivity of PDT is to some extent intrinsic due to the defined zone of irradiation. Partial selectivity may also be induced by the passive EPR effect,[43] or due to PS low density lipoprotein (LDL) affinity which target the overexpression of LDL receptors on neoplastic cells.[44] Targeting strategies to achieve improved tumor selectivity feature as part of next generation PS preparation to enhance tumor destruction and avoid skin photosensitivity. Active targeting to cells of the tumor microenvironment can be achieved through the attachment of ligands specific to cell receptors. These include proteins, peptides, antibodies and aptamers, directly conjugated to a PS or its nanocarrier.[43] The first antibody-PS conjugate was recently approved by the Japanese government. It features the water-soluble silicon-phthalocyanine derivative IRDye700DX conjugated to cetuximab, a monoclonal antibody which targets the epidermal growth factor receptor (EGFR).[45] Exploitation of unique environmental conditions of the tumor microenvironment, such as pH, are also used in the design of novel activable photosensizers.[2]

Cancer treatment often follows a combination approach, necessary to tailor treatment for the myriad of diseases which are characterized by uncontrolled cell division.[46] A lack of overlapping toxicity with conventional treatments suggest PDT is a well suited participant for combination treatments.[42] PDT in collaboration with surgery has shown positive results, both as a fluorescence guide for tumor excision with 5-aminiolevullinic acid (ALA)-PDT[47] or as a follow up adjuvant to destroy tumor margins of head and neck cancer using temoporfin.[48] The lack of clinical exploration of PDT with more conventional treatments such as chemotherapy is unexpected, considering the preclinical evidence which supports the possibility of PDT to overcome drug resistance.[42] Increased understanding of how to exploit the immune system has supported some of the most promising developments in cancer therapy in recent years. For example, promising success with advanced stage cancer has been achieved using the transfer T-cells engineered to express chimeric antigen receptors which result in an activated T lymphocyte response. In addition to CAR-T therapy, advanced understanding of the role of immune checkpoints in suppressing the cellular response against cancer led to the development of inhibitors for cytotoxic T-lymphocyte antigen-4 (CTLA-4), anti-programmed death-1 associated receptor (PD-1) and

its ligand (PD-L1).[49] Immunotherapies, however, are highly specialized treatments which can acquire drug resistance and present side effects. PDT has proven a mutually beneficial partner for combination treatment.[50] Immune checkpoint blockade has been investigated as an adjuvant for PDT with multiple PS showing successful outcomes.[51-52] Therefore, potential exists for greater clinical use of current PSs as part of combination therapies.[53]

1.1.4 Photodynamic therapy efficacy

1.1.4.1 Light

The three individually non-toxic elements of PDT require careful consideration to ensure synergistic delivery of an optimal therapeutic effect. The properties of light used to activate the PS are dependent on the PS structure.[11] An optimal light source matches a specific wavelength of light which corresponds to the PS absorption spectra. The therapeutic effect is influenced by the interaction of the light chosen with the tissue surface. Light is required to penetrate the skin with adequate depth to ensure that the targeted tumor tissue is reached with sufficient energy to induce PS activation and subsequent ROS generation.[54] Upon interaction, light can be reflected, scattered, transmitted or absorbed depending on the optical properties of the tissue at the specific wavelength. Target tissues tend to be heterogenous regarding cell type, water content and numerous highly absorbing endogenous chromophores below 620 nm, such as hemoglobin and melanin. The heterogeneity influences the scattering and absorption of light, limiting the spectral range at which penetration is achieved to longer wavelengths. This defines the "phototherapeutic window", 620-850 nm, as the optimal range to achieve tissue penetration and PS activation.[55-56] Above this wavelength, water absorption occurs, and absorption lacks sufficient energy to promote production of excited state singlet oxygen species.[56-57]

When selecting a light source, the PS absorption and tumor characteristics such as location and size require consideration. The device cost and size are also practical considerations.[58] PDT light sources for anti-cancer treatment are most commonly lasers (light amplification by stimulated emission of radiation) or LED (light emitting diodes); however, other possibilities include daylight, filtered lamps and OLED (organic light emitting diodes).[59] Lasers are monochromatic and powerful light sources that can deliver light by optical fibers, with the potential for interstitial irradiation through diffusing tips that can access tumors which are deep below skin surface. LEDs have bandwidth around 50 nm or larger and are comparatively cheaper, but cannot be adapted for interstitial use.[58,60] Beyond the

light source and PS wavelength of activation, light dosimetry has other variables which require optimization. High light fluence, for example, can rapidly deplete tumor oxygen levels and alter efficacy.[61] Optimization of the appropriate light dose must incorporate the stability of the PS against photobleaching, where several cycles of photoactivation lead to irreversible photo-destruction of the molecule.[11] Pharmacokinetics also must be considered when deciding the DLI, the interval of time between PS administration and irradiation. In the case of intravenous administration, rapid clearance from the body implies selection of short DLI (< 1 h). PSs are likely to accumulate in the vascular compartment with short DLI, which leads to blood vessel occlusion after tumor irradiation, vascular-targeted, PDT. With slow clearance, PS activation may be targeted upon cellular internalization with long DLI (DLI 24- 72h), cellular PDT.[1]

Just as PS tumor accumulation is an important consideration for PDT efficacy, sufficient light irradiation reaching the tumor also causes concern. The pursuit of novel PSs activated by near infrared red (NIR) light is the result of a major clinical concern for PDT; the low attenuation depth in the treatment for lesions. Even with NIR activation, light can only reach up to ~ 1 cm, which is comparatively much lower than high dose X-ray radiation (> 10 cm).[42] However, dismissal of PDT on account of low penetration fails to acknowledge the promising clinical results achieved with interstitial fiber placement in tumors below the reach of frontal irradiation.[42] The success of this approach has featured as part of the clinical application of padeliporfin,[62] as well as an ongoing phase 2 trial with endoscopic ultrasound guided verteporfin-PDT for the treatment of advanced pancreatic cancer.[63] Drugs which are activated by ultrasound, sonosensitizers, produce ROS as part of sonodynamic therapy and demonstrate promising potential in terms of treatment depth in comparison to PDT.[64]

The selected area of irradiation region is critical to increase the likelihood of tumor eradication. If the margin surrounding the tumor which receives light is too small, the re-supply of nutrients required for tumor survival is high. An excessive margin can potentially induce lethal destruction of healthy tissues.[29] Optimization of the irradiation margin was revealed to be crucial with treatment of colon carcinoma CT26 tumors. The illumination surface included a 4 mm negative margin surrounding the tumor, ensuring the therapeutic threshold of ROS production in the necessary location was reached.[40]

1.1.4.2 Oxygen

A critical limiting factor of PDT is tumor oxygenation. Essential for the photochemical reactions which produce destructive ROS, low tumor oxygen concentration, significantly hinders PDT efficacy.[65] Hypoxic regions of solid tumors, therefore, limit the effectiveness of PDT.[58] The intrinsic relationship between tumor oxygenation and PDT efficacy has led to the proposed monitoring of tumor oxygenation during PDT treatments as a useful prognostic indicator.[66]

Different DLI may alter the oxygen concentration in tumors directly after irradiation. With vascular-PDT, destruction of vasculature can increase areas of hypoxia.[67] In cellular-PDT, however, limited oxygen consumption occurs with the potential for even increased tumor oxygenation due to the removal of cellular metabolic consumption.[1,29] To maintain blood vessel integrity for the duration of irradiation in vascular-PDT, fractionation of light irradiation has been utilized, allowing tissue reoxygenation. Short dark periods (150 – 200 s) may ensure PDT efficacy is maximized during the treatment which is followed by irreversible vascular damage following therapy.[1] Other strategies to improve tumor oxygenation for enhanced PDT efficacy include the use of oxygen carriers, such a liposome encapsulated hemoglobin, reactive H_2O_2 enzymes and Platinum (Pt(IV)) nanocomposities.[68]

1.1.4.3 Photosensitizers

As understanding of photodynamic mechanisms has grown, properties considered to fulfil the "ideal" PS have emerged. Desirable characteristics of PS include facile synthesis, chemical purity and stability at room temperature (rt), allowing compliance with good manufacturing standards.[2,4] Activation in the phototherapeutic window which leads to efficient ROS generation should be possible in biological media.[55] To ensure this, it is necessary that PS aggregation is minimized.[69] Photostability should also be sufficient to deliver therapeutic effect before bleaching occurs.[11] To exploit the partial selectivity associated with PDT, limited cytotoxicity in the dark is essential.[70] In terms of clearance, efficient elimination from normal tissues is required to limit skin photosensitivity.[4]

While some progress has been made to meet these requirements by second generation PSs, a PS which fulfils all these requirements for optimal PDT efficacy has eluded chemists since the introduction of PDT for clinical use. A common motif which features throughout clinically approved anti-cancer PS is the tetrapyrrole macrocycle.[4] Frequently referred to

as the 'pigments of life',[71] tetrapyrroles naturally occur in many biomolecules responsible for key processes such as oxygen transport, electron transfer and photosynthesis. The [18π]-electron heteroaromatic structure presents aromatic character with a capacity to coordinate metal ions in the inner core of nitrogen atoms. Combined with conformational flexibility and the variability of side chains, the tetrapyrrole structure leads to diverse reactivities, which account for its prevalence in nature.[72-73] These properties also account for extensive investigation of this motif for PS development. The distinct absorption spectrum of a porphyrin molecule displays strong absorption at 400 - 450 nm (Soret or B band) followed by less intense peaks between 500 - 800 nm (Q bands). These lower intensity Q bands tend to exhibit bathochromic shifts as the porphyrin macrocycle is successively reduced to chlorins and further to bacteriochlorins, leading to a favorable shift within the phototherapeutic window.[74] The development of novel tetrapyrrole PSs is benefitted by the diverse modifications available to electronically tune the macrocycle. These include pyrrole ring exchange, to produce phthalocyanines, as well as the introduction of various functional groups and the possibility of metal ion coordination.[29] Tetrapyrrole PSs feature among the natural product and synthetic molecules used for PDT (Figure 4).[4]

The efficiency of PS cell-internalization is dependent on molecular characteristics including lipophilicity, charge and charge distribution.[58] Cellular uptake can be altered if PSs associate with serum proteins. More lipophilic PSs tend to associate with LDL; this may enhance PS uptake by exploiting the LDL mechanism of internalization, receptor-mediated endocytosis.[75-76] An increase of hydrophobicity has been agreed to generally correlate with improved PS uptake.[75,77] Some PSs have disrupted this trend, indicating that characteristics beyond hydrophobicity are significant for uptake. For example, a series of asymmetric chlorophyll-a derivatives, with similar lipophilicity but varied peripheral alkyl group substitutions, exhibited different cellular uptake. A more hydrophilic compound was also observed to have higher uptake than related hydrophobic PSs. These findings pointed to the importance of substituent position for influencing PS uptake.[78] Factors outside hydrophobicity were also identified to influence uptake for a series Zn(II)N-alkylpyridylporphyrins with varying, positively charged, meso-aryl substitution patterns. Positive charge is considered to enhance electrostatic interaction with the negatively charged cell membrane. The enhanced uptake observed with *para*-substituents was justified by increased lipophilicity and a more planar charge distribution, illustrating the importance of molecular shape for uptake.[77] However, the superiority of *para* substitution

for cationic porphyrin is not absolute, as *meta*-substituents have also been observed to induce enhanced uptake despite lower lipophilicity in comparison to *para* analogues.[79-80]

Charge distribution was also acknowledged as relevant for uptake by Jensen et al.[81] with a series of *para* substituted cationic porphyrins. Nevertheless, the benefit of amphiphilicity rather than hydrophobic character was deemed more critical to improve internalization. The adjacent distribution of positive charges in *cis* (*N*-pyridyl)phenylporphyrins has also been defined as superior in membrane affinity in comparison to *trans* regioisomers as a result of amphiphilicty.[79-80,82-84] Notably, the $LogP_{OW}$ is frequently used as a quantitative indicator of lipophilicity. However; for highly hydrophobic PSs, it has been observed as a poor predictor of uptake.[85] Therefore, it is clear that internalization of PSs is not simply a matter of hydrophobicity but is multi-faceted, including other variables (e.g. charge, conformation). The properties impacting cellular internalization are not yet completely understood and require further investigation. This might provide guidelines to the rational design of new PS, as well as other molecules, with enhanced uptake.

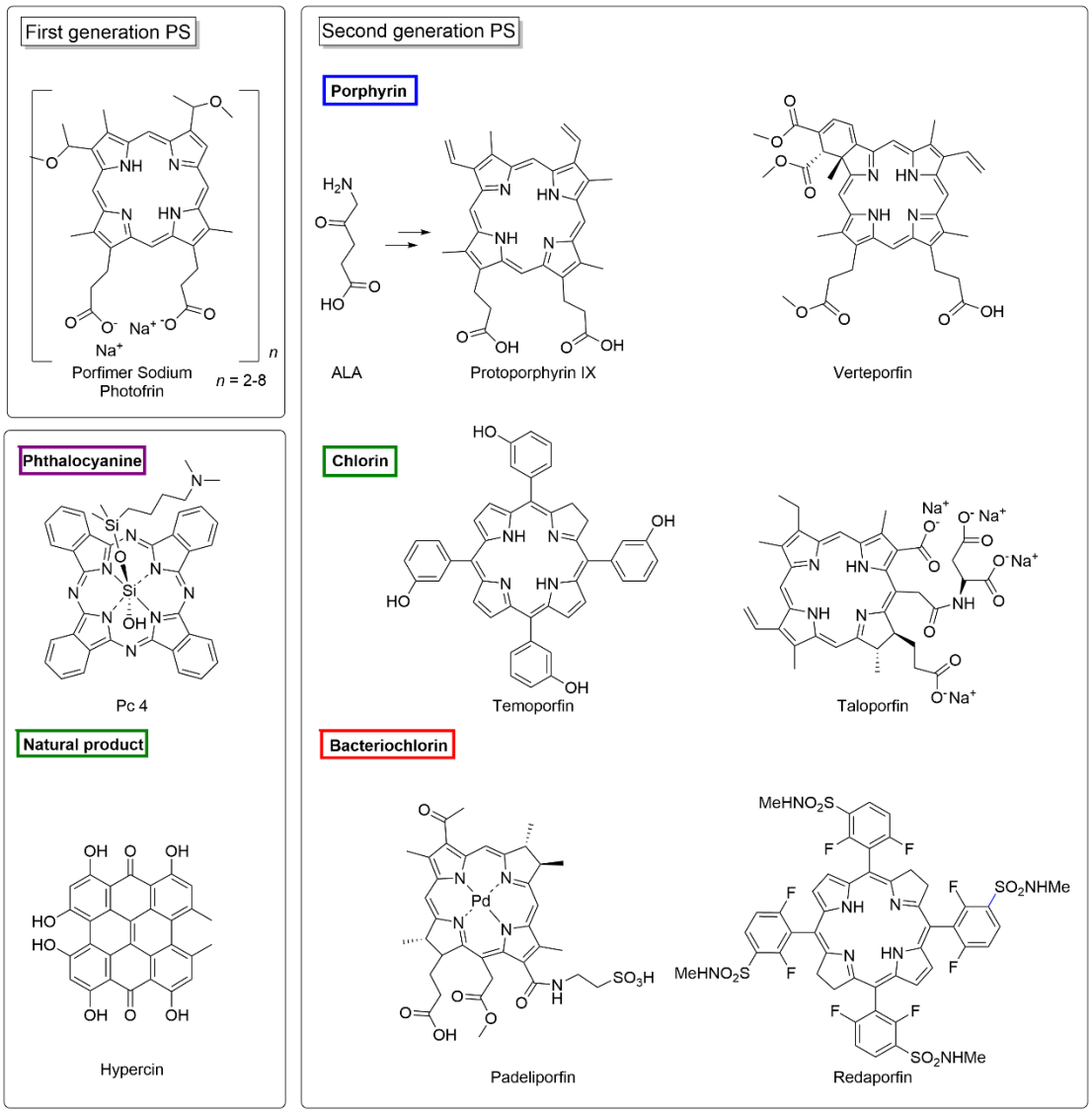

Figure 4. Molecular structures of photosensitizers. Examples of photosensitizers employed clinically against cancer or undergoing clinical trials are provided.

Photofrin advanced PDT to an anti-cancer clinical application; however, its drawbacks serve as a basis for chemists to improve PS design. High doses (2 mg/kg) combined with high light doses (120-180 J/cm^2) were required for the cellular-PDT protocols (DLI 48 h) to account for the low molar absorption coefficient at 630 nm, decreasing the likelihood of photoexcitation and limiting skin penetration. Critically for patient quality of life, a slow elimination half-life ($t_{1/2}$) leads to prolonged skin photosensitivity for several weeks.[86] Therefore, pursuit of second generation PSs which showed increased clearance was a priority. Derivatives of ALA exhibited reduced skin photosensitivity relative to Photofrin. As a biosynthetic precursor of protoporphyrin IX, ALA marked the introduction of endogenous photosensitization. Topical delivery features in application against skin

cancerous lesions including actinic keratoses and basal cell carcinoma. With low absorbance at 635 nm, penetration is limited to lesions with < 2 mm treatment depth. Additionally, pain has been observed to accompany illumination.[87] Enhanced clearance is also observed with verteporfin (Visudyne, benzoporphyrin derivative), a PS which has achieved success with the treatment of age-related macular degeneration. Notably, verteporfin exhibits some specificity for LDL receptors due to a strong affinity with LDL. Activation at 689 nm presents a bathochromic shift consistent with enhancing PDT penetration depth.[88]

Bathochromic shifts with improved molar absorption coefficients were achieved with chlorin derivatives. Taloporfin (Laserphyrin, 'mono-L-aspartyl chlorin e_6) and temoporfin (5,10,15,20-tetrakis(3-hydroxyphenyl)chlorin, (commercial formulation referred as Foscan) are both characterized by high absorptions in the phototherapeutic window at 664[89] and 652 nm,[90] respectively. The high efficacy of temoporfin cellular-PDT for the treatment of head and neck cancer is, however, associated with prolonged skin photosensitivity.[90] Taloporfin, approved for treatment of lung cancer in Japan, presents relatively lower skin photosensitivity.[91] Further improvement of PS efficacy relative to Photofrin has been presented with bacteriochlorin PSs. Padeliporfin (WST11, TOOKAD Soluble) is derived from bacteriochlorophyll α found in benthic bacteria. The high absorption at 763 nm has led to the clinical application of padeliporfin for prostate adenocarcinoma in Europe.[62,92] Rapid clearance, within minutes, limits skin photosensitivity but also requires vascular-PDT treatment regimens which combine an infusion administration with simultaneous irradiation.[93] A promising PS for PDT, redaporfin (LUZ11, 5,10,15,20-tetrakis(*N*-methyl-2,6-difluoro-3-(methylsulfamoyl)phenyl)bacteriochlorin) is a synthetic bacteriochlorin with high absorption at 749 nm currently undergoing phase 1/2 clinical trials for head and neck cancer (NCT02070432).[94-95] Notably, redaporfin presents high photostability, a critical consideration of chlorin and bacteriochlorin derivatives.[96-97]

Efficacy of redaporfin is mediated by both Type 2 and Type 1 processes with efficient formation of singlet oxygen.[98] Selective subcellular localization in the ER and GA induces immunogenic cell death upon photoactivation.[99-100] Its pharmacokinetic profile, (1st compartment (plasma) $t_{1/2}$ of 0.5 h and 2nd compartment $t_{1/2}$ of 65 h) enables the use of redaporfin for both vascular and cellular-PDT. The elimination $t_{1/2}$ is increased relative to temoporfin and consequently results in lower skin photosensitivity.[101] Preclinical studies with a redaporfin formulation of saline : EtOH : Kolliphor®EL (98.8 : 1 : 0.2 % v/v)

demonstrated that distinct therapeutic outcomes may be obtained with different DLI protocols. Vascular protocols attained the best therapeutic outcome in different mouse models of cancer when compared with cellular-PDT.[40,102] Redaporfin also exhibited a strong immune response with control of lung metastasis arising from a pseudo-metastatic model.[40,103] This enhanced efficacy can, in part, be attributed to the deep necrosis it can induce with high absorption at 749 nm.[104] A case report from the clinical trials described positive outcomes for a patient with advanced head and neck squamous cell cancer, uncontrolled by conventional treatment methods. Tumor destruction was achieved with three sessions of vascular redaporfin-PDT. Sequential treatment with an immune checkpoint blocker (Nivolumab, PD-1) prompted a two year remission, with the patient exhibiting no signs of the disease.[94]

Redaporfin presents a symmetric meso-tetrasubstituted bacteriochlorin structure. The symmetry of the molecular structure benefits the efficiency of synthesis.[97] However, it also compromises the chemical purity of redaporfin. The presence of bulky meso-aryl substituents, in conjunction with this symmetry, leads to hindered axes of rotation for the meso-aryl bonds and the generation of distinct 3D structures, named atropisomers (Figure 5). Luzitin, the company responsible for the development of redaporfin, discovered that the phototoxicity of each individual redaporfin atropisomer varied.[105] This prompted our investigation of redaporfin atropisomers, to understand the significance of tetrapyrrole atropisomerism for therapeutic efficacy.

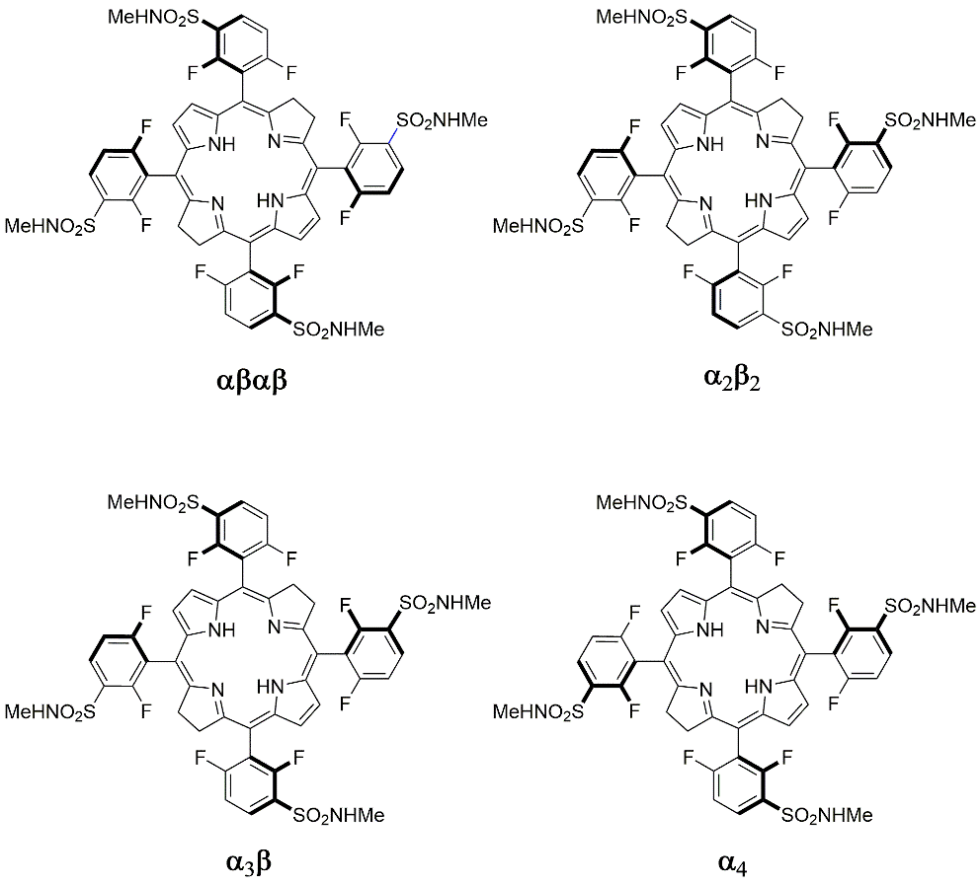

Figure 5. Redaporfin atropisomers. Restricted rotation around meso-aryl bond generates four distributions of sulfonamide groups relative to the macrocycle plane.

1.2 ATROPISOMERISM

Conformers which arise due to electronic and steric constraints, interconverting at a slow enough pace for isolation to proceed, are described as atropisomers.[106] The definition of atropisomerism has evolved from a close association with biaryl systems which may exhibit axial chirality due to hindered rotation around a single bond. Such biaryl systems were responsible for the first observation of atropisomerism made by Christie and Kenner in 1922.[107] Their attempts to characterize the molecular configuration of a diaryl scaffold, 6,6'-dinitro-2,2'-diphenic acid (Figure 6A), led to the observation that the molecules must twist, removing planar symmetry (Figure 6B). Enantiomers about a chiral axis had been discovered.[107] This delayed rotation around a single bond was originally named for biaryl compounds from the Greek 'atropos', meaning without turn.[108] The concept of axial chirality at the time of atropisomer discovery was not new. Identification by van't Hoff in 1875 was later confirmed with the synthesis of optically pure allene. Atropisomeric biaryls were distinguished from allenes due to the maintenance of axial chirality through steric interferences.[109] A later description of atropisomerism from Mislow in 1958 established a classical definition as 'isomerism arising from restricted rotation about a single bond'.[110]

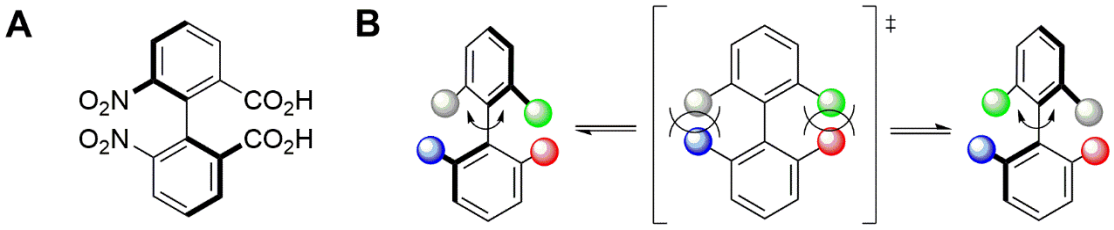

Figure 6. Biaryl atropisomerism. (A) 6,6'-dinitro-2,2'-diphenic acid atropisomerism (B) representation of biaryl atropisomerism which proceeds through a coplanar transition state.[111]

Oki later proposed an arbitrary, yet practically useful, criteria for defining atropisomerism which incorporated the temperature dependence of restricted rotation. For a conformer to be considered an atropisomer, interconversion must proceed with a $t_{1/2} > 1000$ s.[112] This definition points to a critical distinction between atropisomers and point chirality; bond rotation rather than bond breakage is responsible for interconversion.[113] The minimum $t_{1/2}$ defined corresponds to an activation energy barrier of approximately 22 kcal.mol^{-1} at rt. This would allow just ~17 minutes to analyze an atropisomer before purity starts to erode. Therefore, this definition alone is not satisfactory in biological terms for molecules which racemize during drug metabolization.[114] LaPlante et al.[115] proposed a useful classification

system for atropisomeric drugs depending on activation energy barriers. Advances in techniques employed for atropisomer separation and characterization have contributed to the recognition of primary structural motifs (Figure 7), such as hindered amides, which give rise to restricted axial rotation.[116] With motifs such as the hinder ring-flip inversion, simultaneous rotation around more than one bond is required. This has led to expansion of classified atropisomers to include other motifs including medium-sized rings and macrocycles.[114,116]

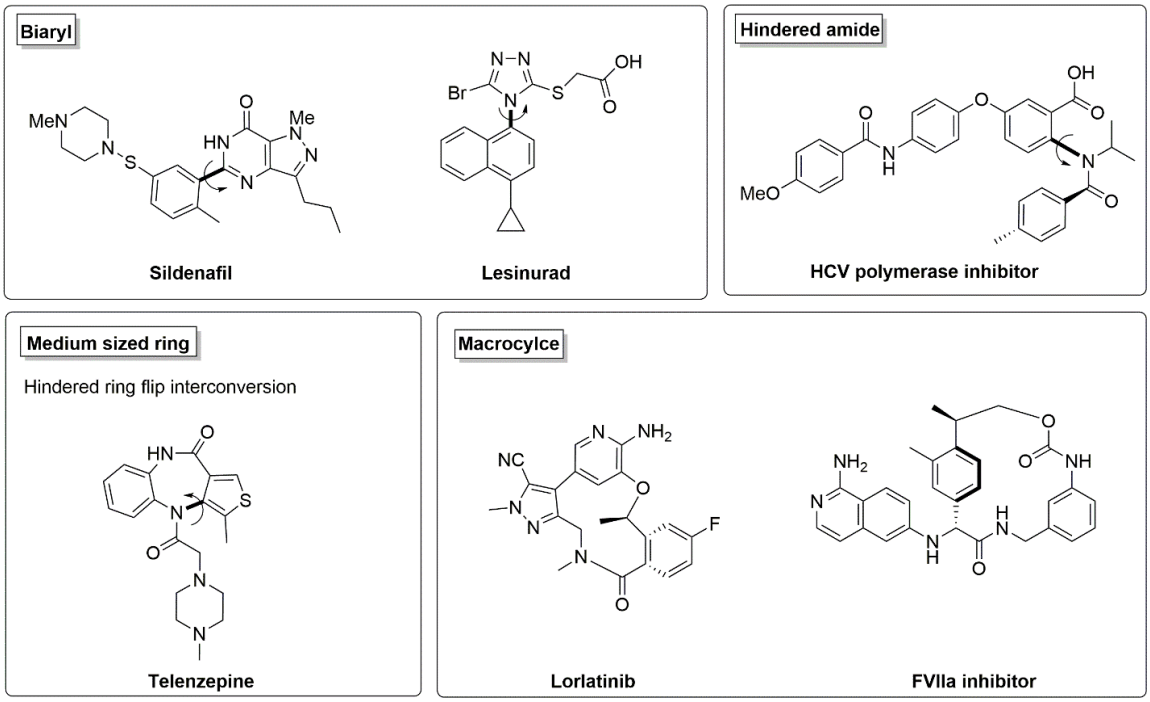

Figure 7. Characteristic atropisomer motifs. Biaryl,[117] hindered amide,[118] medium sized rings[117] and macrocycles are represented.[119-120]

Atropisomerism arises in a diverse range of motifs. This results in many common scaffolds of drug discovery featuring hindered rotation and the occurrence of atropisomerism with candidates is becoming increasing prevalent.[111,116,121] The therapeutic implications of chiral drugs are well documented with examples such as racemic thalidomide,[122] dopa[123] and bupivicaine[124] emphasizing the complications that one enantiomer of a racemic drug mixture can cause. Receptor chirality of a therapeutic target of interest may result in varied enantiomer efficacy, drug pharmacokinetics and potentially result in off-target toxicity.[115] Therefore, enantiomers are distinct substances and are treated as such in drug development, with regulatory agencies preferring development as single enantiomers in cases where safety and/or efficacy is advanced.[111] Atropisomerism is a less considered form of chirality in the context of drug development despite its prevalence. Approximately 15% US FDA

approved small molecules, such as sildenafil (Figure 7), possess at least one rapidly converting atropisomeric axis with 30% of more recently approved small molecule drugs containing an axis of chirality.[117]

There is a growing awareness that atropisomers tend to bind targets in an atroposelective manner which may favorably influence the selectivity profile of a compound or potentially lead to off-target effects. It is critical to consider how to characterize, manage and exploit atropisomerism in the parameters of a drug discovery campaign.[111,121]

1.2.1 Atropisomer characterization

To start building the biological profile of an atropisomeric drug, it is crucial to elucidate individual atropisomer structures in order to gain insight into pharmacodynamics.[111] Atropisomer configurational stability also dictates propensity to racemize (conversion of a single atropisomer to a mixture) or enantiomerize (switch configuration from one atropisomer to another)[125] and is, therefore, beneficial to quantitively characterize. Structural elucidation and interconversion kinetics inform decisions of drug development.[111,115]

Knowledge of the primary structural motifs which give rise to atropisomerism can lead to early identification in the development process.[111] In cases where less intuitive motifs generate atropisomers, occurrence is typically identified with unusual NMR spectra or the appearance of multiple peaks in HPLC chromatograms.[111,118-119] NMR is an accessible tool for structural assignment of atropisomers and a natural follow-on from initial identification of conformers through racemate spectra. Specifically, the use of NMR beyond the conventional 1D techniques including ROESY (Rotating Frame Overhauser Effect SpectroscopY) have been demonstrated as useful complimentary techniques for atropisomers.[126] Alongside variable temperature ^{1}H NMR (vt-NMR), which may highlight atropisomeric protons, relative populations of atropisomers in a mixture may be characterized.[118] In many cases of atropisomer assignment, more than one technique is used in tandem to corroborate assignment. Single X-ray crystallography,[127] while perhaps the most definitive tool for aiding structural assignment, may be assisted or replaced by techniques which rely on different principles. Circular dichroism (CD)[128] and vibrational circular dichroism (VCD)[129] have been demonstrated to differentiate absolute chirality. VCD requires a reference spectrum obtained by X-ray crystallography. In the absence of

this, quantum mechanics may be used to simulate the reference,[130] offering an alternative in cases where crystallization may not be possible.[129,131]

Characterizing individual atropisomer configuration is critical to understanding pharmacodynamics for drug candidates. However, quantitative information regarding rates of interconversion informs drug development decisions. Calculation of the activation energy barrier ($\Delta G^{\ddagger}$) and $t_{1/2}$ of interconversion benefits determination of whether a drug should be developed as a racemic mixture or as isolated single compound.[128] LaPlante et al.[115] introduced a pragmatic system for drug developers to compensate for a lack of guidelines from regulatory agencies. Atropisomeric drugs were classified in three groups depending on rotational barriers. The classes were defined to be: class 1 when rotational barriers are < 20 kcal.mol^{-1} ($t_{1/2}$ at 37 °C <10 sec), and, thereby, exist as freely rotating, inseparable mixture of stereoisomers; class 2 where the rotational barrier is between 20 - 30 kcal.mol^{-1} ($t_{1/2}$ at 37°C 10 sec - 4.5 years), therefore, racemizing on the order of hours-days-years; and class 3, which have a high rotational barrier >30 kcal.mol^{-1} ($t_{1/2}$ at 37°C >4.5 years).

The definition of a class 2 atropisomer was influenced by the work of Bristol Myers-Squibb (BMS) for development of BMS-207940 atropisomers. A 30-fold decrease in $t_{1/2}$ was observed between atropisomers in aqueous media and human plasma.[132] This factor was combined with Oki's definition of atropisomerism to reduce the 1000 sec $t_{1/2}$ to define the lower limit as 19.7 kcal.mol^{-1}. The upper limit of class 2 was defined with the practical consideration that desirable atropisomer stability would be 99.5% homogeneity over the course of 24 h *in vivo*. This, combined with the 30-fold correction factor led the threshold calculated as 29.4 kcal.mol^{-1}.[115] This guide continues to inform decisions regarding drug development ten years after publication. Class 3 atropisomers are proposed to be developed as a single stable atropisomers, while rapidly interconverting class 1 are advised to be treated as a racemic mixture if favorable pharmacokinetic and pharmacodynamic properties of both atropisomers exist. Class 2 atropisomerism has been described as a 'lurking menace' of drug discovery with advice for moderately converting atropisomers generally proposing alterations which shift the rotational barrier into class 3 or class 1 stability.[111]

Selection of an appropriate method to assess interconversion is related to atropisomer stability. A primary advantage of NMR is the possibility to evaluate enantiomerization processes from a racemic mixture and is, therefore, particularly useful for rapidly

converting class 1 atropisomers.[114] Employment of NMR relies on the presence of protons rendered diastereotopic due to the molecule's spatial configuration. Ideally, these resonances are clearly defined at low temperature and upon heating and interconversion through vt-NMR signals broaden and gradually coalesce at a specific temperature. This facilitates the application of line shape analysis and application of the Eyring equation to calculate rotational energy barriers. [114,125]

While some molecules interconvert at temperatures ideally suited for NMR evaluation,[133] the boundaries of instrument probes and solvent boiling points limits NMR temperature range.[125] Rather, vt-NMR is often employed as a predecessor to estimate interconversion barriers before the use of dynamic chromatography methods.[118] Through dynamic HPLC, enantiomeric excess (*ee*) can be monitored at various timepoints. For compounds which interconvert at higher temperature than HPLC oven capabilities, it is possible to isolate atropisomers and determine the temperature dependence of their racemization by heating samples for fixed times and submitting to analysis.[114,125] The change in relative peak area or peak height is recorded and fitted to first order reaction kinetics to calculate interconversion $t_{1/2}$.[128,130] While NMR and HPLC continue to be the most commonly used techniques to evaluate atropisomer stability, often in combination,[134-135] other techniques may also be employed. CD can be suitable in scenarios where the barrier of interconversion is too high for vt-NMR and there is some baseline overlap in peak resolution of HPLC chromatograms.[125,128] Configurational stability may also be predicted through a computational approach featuring a relaxed torsion scan[111,115] or accurately calculated by discrete Fourier transform (DFT).[136-139]

HPLC further serves this atropisomer evaluation as it can also be used to monitor atropisomer biotransformation stability. This can be achieved through monitoring of candidate interconversion kinetics in protein containing media such as human blood, plasma and serum albumin. A Pfizer development team employed this technique for a series of atropisomer drug candidates with a variety of structural motifs.[140] A similar strategy can be used for *in vivo* investigation. Chiral-liquid chromatography coupled to mass-spectrometry (Chiral-LC/MS) was applied to detect the high stability of (+)/(¬) Lesinurad atropisomers (Figure 7) in urine and plasma samples following oral administration to rats and monkeys over a 24 h period.[141] Although the interconversion barrier provides information regarding the likelihood of interconversion at physiological temperature, insurance that metabolism does not interconvert atropisomers is valuable.

1.2.2 Consequences of atropisomerism for medicinal chemistry

1.2.2.1 Varied atropisomer biological activity

Varied effects from a racemic atropisomer drug are anticipated, considering atropisomers tend to have differential target selectivity. Atropisomer specific steric, electrostatic or hydrogen bonding interactions with targets vary depending on atropisomer configuration. Evaluation of two mirror image Lamellarin atropisomers (Figure 8A), through kinase inhibition and docking studies, revealed different kinase selectivity profiles. One atropisomer displayed activity against seven out of the eight kinases evaluated while the other selectively inhibited just three.[142] A team at Bristol Myers Squibb developed a promising lead compound for Bruton's Tyrosine Kinase (BTK) inhibition, intended for treatment of autoimmune disorders including lupus and rheumatoid arthritis. However, problems were encountered in tolerability studies across multiple species.[143] Further structural activity development incorporated consideration of atropisomerism. Removal of the less relevant atropisomer species was carried out with the intent to mitigate off-target interactions. Replacement of the molecule quinazolinone with a quinazolinedione locked one axis and addition of a *meta*-chloro substituent at the other axis led to stable atropisomers. Separation by supercritical fluid chromatography yielded a single, atropisomer candidate, with substantial improvement in tolerability and blood potency (Figure 8B).[144]

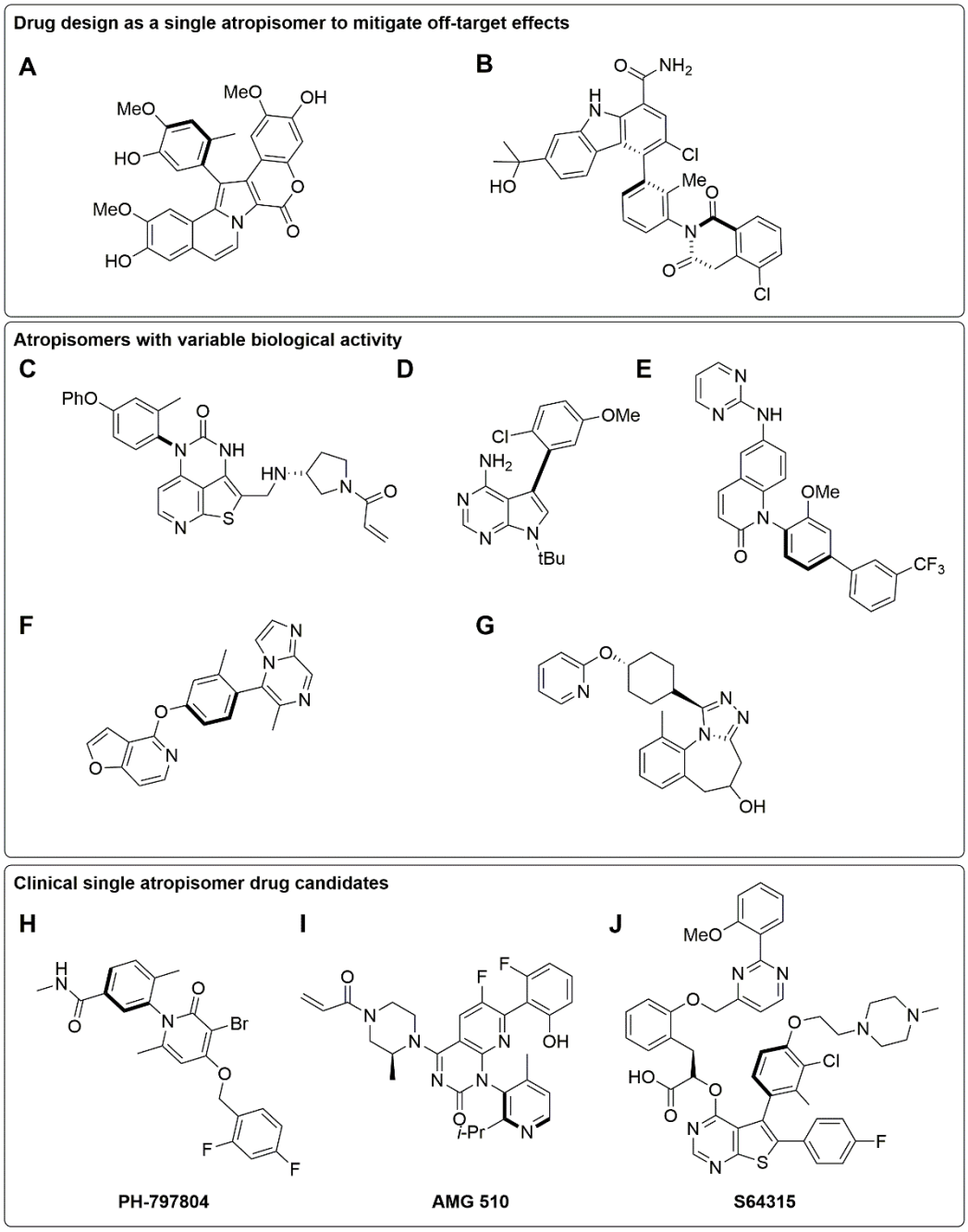

Figure 8. Consequences of atropisomerism for medicinal chemistry. Drugs design considering off target effects; (A) Lamellarin analogue[142] and (B) BMS BTK inhibitor.[144] Atropisomers with variable biological activity; (C) BTK inihibitor,[145] (D) pyrrolopyrimidine-based kinase inhibitors,[146] (E) $Na_v1.7$ inhibitor,[147] (F) D1 agonist[130] and (G) vasopressin receptor 1A antagonist.[148] Clinical single atropisomer drug candidates (H) PH-787804,[138] (G) AMG 510[149] and (H) S64315.[150]

The most extensive examination of differential atropisomer selectivity has been performed with kinase inhibitors. The attention kinase inhibiting atropisomers receive is testimony to their clinical relevance with the majority of FDA approved kinase inhibitors exhibiting at

least one rapidly interconverting atropisomeric axis.[117] During the optimization of another BTK inhibitor, the *S*-configuration of an atropisomer displayed enhanced potency in cellular activity over the *R*-form. This led to incorporation of the configuration in the inhibitor design, with the highest rotational barriers targeted through appropriate *ortho*-aryl substituents (Figure 8C).[145] Differential activities (potency and selectivity) were recently reported for atropisomers of pyrrolopyrimidine-based kinase inhibitors. While one form binds to the desired molecular target, the other causes off-target effects by interfering with other kinases (Figure 8D).[146] In another study, two heteroaromatic systems of phosphoinositide 3-kinase (PI3K) β inhibitors revealed significantly different biological profiles. One of the atropisomers demonstrated a 500-fold increase in activity accompanied by enhanced selectivity and metabolic stability (Figure 9B).[151] For a p38 mitogen-activated protein kinase inhibitor (Figure 8H) developed by Pfizer, differential activity was not only apparent *in vitro* but also *in vivo*, with different atropisomer doses required to suppress chronic inflammation in a rat model.[138]

Variable atropisomer selectivity is not restricted to kinases. Atropisomeric quinolinone inhibitors (Figure 8E) displayed selectivity for the voltage gated sodium ion channel $Na_v1.7$ targeted for pain treatment. In this case, there was a disparity in atropisomer potency. The atropisomer with higher potency also resulted in less off-target effects due to lower CYP2C9 affinity which garnered a promising candidate for Amgen pharma.[147] The lead compound in the pursuit of a dopamine receptor D1-selective agonist (Figure 8F) was separated into two atropisomers, with one of the atropisomers demonstrating 4-fold higher potency and 2-fold higher affinity towards D1 receptor in comparison to its mirror image.[130] Recently a specific atropisomer configuration of a triazolobenzazepine derivative (Figure 8G) was discovered to bind more favourably to the vasopressin receptor 1A, a target for common neurodevelopmental diseases. Molecular modelling supported the enhanced affinity of the most active atropisomer.[148] Atroposelective binding has been observed to occur across a range of receptor types.

1.2.2.2 Exploiting atropisomerism as a drug design element

The differential activity observed for atropisomers prompted the question of whether rigidifying freely interconverting atropisomers may be used as a design strategy to improve target selectivity in drug design. It has been proposed that preorganization of a rapidly interconverting atropisomer residues in a promiscuous scaffold into a target's preferred conformation could serve as a strategy to obtain more selective small molecule

inihibitors.[121,152] For macrocyclic atropisomers, successful strategies for this have involved incorporation of a methyl group, rigidifying the macrocycle for target selectivity. This was achieved with a BMS FVIIa inhibitor (Figure 7) with a 10-fold improvement in potency observed.[120] Anaplastic lymphoma kinase (ALK) inhibitor Lorlatinib (Figure 7) development also featured the introduction of a methyl group to analogs to enforce the desired conformation with high stability.[119] Smith et al.[146] leveraged atropisomerism as a design element to increase the target selectivity of a series of pyrrolopyrimidine based kinase inhibitors, with molecular modelling used to understand selectivity. A loss of potency was acknowledged. This was compared to the enhanced potency of the irreversible covalent inhibition strategies often pursued to increase kinase selectivity. These strategies, however, rely on rare events, such as binding to a specific cysteine residue. Exploitation of atropisomerism may serve as a more general approach.[146] More recently, both approaches were used in tandem to impose selectivity of a BTK inhibitor (Figure 8C).[145] In addition to improving target selectivity, the benefits of atropisomerism for drug development have generally begun to gain consideration. The potential to alter and enhance drug solubility in biorelevant media, for example, is one such recognition. Saal et al.[153] recently demonstrated this with a Merck small molecule drug which exhibited enhanced solubility in aqueous media relative to its racemic compound. This presents atropisomerism as a neglected opportunity to improve physicochemical and biopharmaceutical properties of a drug.

Beyond incorporation into drug development strategies, the relevance of atropisomerism to medicinal chemistry is apparent from the number of drugs in clinical use which exist as a mixture of stable atropisomers. Telenzepine (Figure 7), a selective muscarinic antagonist for peptic ulcer treatment, exists as a class 3 atropisomer, capable of interconversion through ring flip. The (+)-telenzepine atropisomer was found to be 500 times more active than its opposing (–) atropisomer.[154] Lesinurad (Figure 7), a selective uric acid reabsorption transport inhibitor, which is approved for the treatment of gout, was also discovered to contain two stable atropisomers.[141] Although one atropisomer showed enhanced potency due to different species specific metabolic profiles, the racemic mixture was regarded as the ideal pharmaceutical form over production as a single atropiosmer.[155]

Despite chromatographic costs, some drug discovery campaigns continue to approach single, stable class 3 atropisomers due to the potential for enhanced activity and mitigated off-target effects.[117] An Amgen development team were required to consider atropisomerism when a biaryl motif was incorporated to a KRASG12C inhibitor (Figure

8I) with the *R* atropisomer showing enhanced potency. They overcame an intermediate barrier of rotation by incorporation of a bis-*ortho* isopropyl and aryl methyl-substitution. The lead *R* atropisomer is currently in clinical trials (NCT03600883) for the treatment of solid tumors.[149,156] The biaryl motif of a Myeloid cell leukaemia 1 inhibitor (Figure 8J) also generated atropisomers, one of which benefitted binding in the target pocket. The more active atropisomer, purified by flash chromatography, is currently in phase 1/2 clinical trials with Azacitidine as a combination treatment for acute myeloid leukaemia (NCT04629443).[150,157]

1.2.2.3 Altering atropisomer stability

Atropisomerism faces the greatest challenge when interconversion barriers arise in a moderate range, existing as class 2 atropisomers. These atropisomers are problematic for drug development as atropisomeric composition may change as a function of time, leading to quality control issues.[111] LaPlante et al. proposed that class 2 atropisomers may be further defined into two subclasses depending on the rate of racemization *in vivo* relative to the elimination rates. If rapid racemization occurs, a consistent stereoisomeric mixture would be anticipated *in vivo*. For cases of moderate interconversion, however, differential elimination of the atropisomers may occur.[111] If discovered early in the drug development process, a possible method to avoid atropisomerism may be to engineer faster bond rotations so that the atropisomers interconvert rapidly through reduction of steric bulk around the bond axis. Alternatively, eliminating the atropisomeric axis through inducing symmetry may be another strategy.[115] During the development of a 1,2,4-triazole based tankyrase inhibitor, 2-chlorophenyl substituents were replaced by 2-fluorophenyl groups, mitigating atropisomerism due to less hindered rotation (Figure 9A).[158] The linker moiety of a 15-member macrocycle lead for inhibition of respiratory syncytial virus fusion proteins, also presented class 2 atropisomerism, which was eliminated during development. Transition to class 1 was achieved through ring expansion.[159]

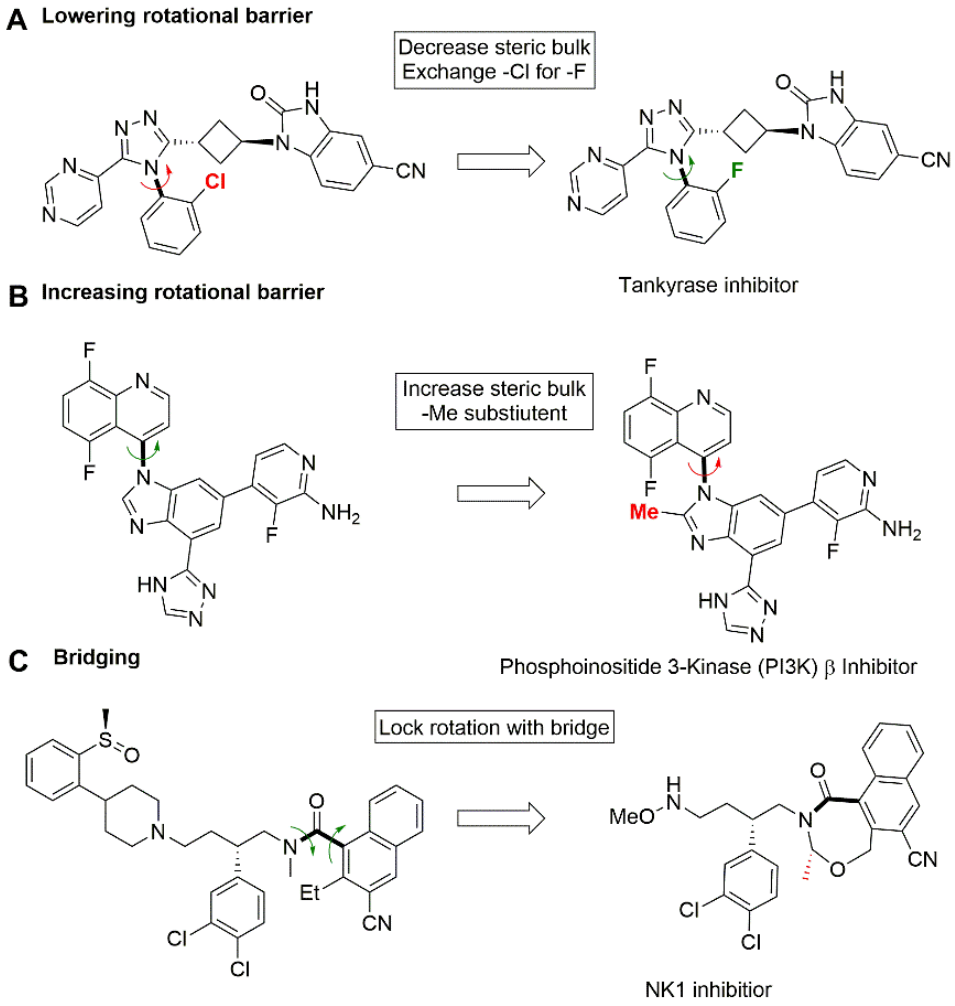

Figure 9. Mitigating class 2 atropisomerism in drug development. Strategies such as (A) reducing steric bulk,[158] (B) increasing steric bulk around the rotating axis[151] and (C) locking rotation with a bridge are illustrated.[160]

Alternatively, a single stable atropisomers may be pursued through increasing steric bulk around the atropisomeric axis to evade class 2 atropisomerism. This approach featured with the development of single atropisomer, selective and potent PI3Kβ inhibitors (Figure 9B). The Gilead Sciences teams used the strategy of LaPlante et al.[115] to implement a torsional scan of an atropisomeric C-N axis to strategically design restricted rotation around the bond of the inhibitors. Introduction of a methyl group adjacent to the axis sufficiently increased steric bulk to substantially increase the rotational barrier.[151,161] A higher rotational barrier may also be implemented through locking the axis of rotation. This was carried out with a potent NK1 antagonist, designed by AstraZeneca, which existed at physiological temperature as four atropisomeric stereoisomers. The incorporation of a seven-member bridge to the design locked the molecule into a single, stable conformer (Figure 9C).[160]

Rather than completely mitigate class 2 atropisomerism, more recently LaPlante et al.[118] provided an example of how applying a combination of techniques to profile class 2 atropisomers can inform the drug discovery process. They investigated a series of intermediate class 2 atropisomers ($t_{½}$ = 69 minutes) targeting HCV polymerase inhibitors (Figure 7). 2D NMR techniques, chiral-HPLC and X-ray crystallography were employed with the racemic mixture. An off-target effect of HIV matrix inhibition was identified for one of the atropisomers when comparing the atropisomer X-ray crystal structures bound to respective targets. While the racemic profile was deemed beneficial, further studies with the racemic mixture and caution during development was advised.[118]

1.2.3 Porphyrin atropisomers

The atropisomerism first observed with biphenyl atropisomers[107] shares similarities with the meso-aryl ring rotation of 5,10,15,20-tetraarylporphyrins, which may generate four atropisomer configurations. Just as the phenyl rings in a biaryl system pass through a coplanar transition state, hindered aryl ring rotation of porphyrins pass through the tetrapyrrole plane with significant distortion accommodating the transition (Figure 10A).[162] The steric bulk hindering this meso-aryl bond,[163] the position of the substituent[164] and surrounding temperature[165] influence porphyrin atropisomer rotational barriers, and the capacity to separate and analyze the rotamers.

Gottwald and Ullman[166] correctly identified that 5,10,15,20-tetrakis(*o*-hydroxyphenyl)porphyrin could be separated into four configurations, identifying the first porphyrin atropisomers. A moderate rotational barrier of 24 kcal.mol^{-1} was calculated with atropisomer separation following the expected statistical ratio, 1 : 4 : 2 : 1.[166] The introduction of copper was made to determine the significance of porphyrin macrocycle 'ruffling'[167] to alter the rotational barrier, but only a small increase in barrier to 25.4 kcal.mol^{-1} was determined.[166] The susceptibility of metalated porphyrins to ruffling is lowered due to less macrocycle flexibility.[164] The introduction of bulkier *meta*-aryl-substituents, such as amino groups which featured as part of 'picket fence porphyrin' synthesis, increased interconversion barriers.[168] Studies regarding the significance of metalation to atropisomer interconversion were further defined. The extent of porphyrin distortion from a planar structure, depending on metalation, lowered interconversion barriers.[169-170] Additionally barriers were also revealed to be tunable, depending on the nature of aryl-substituents and porphyrin macrocycle as a free base diacid.[163-164]

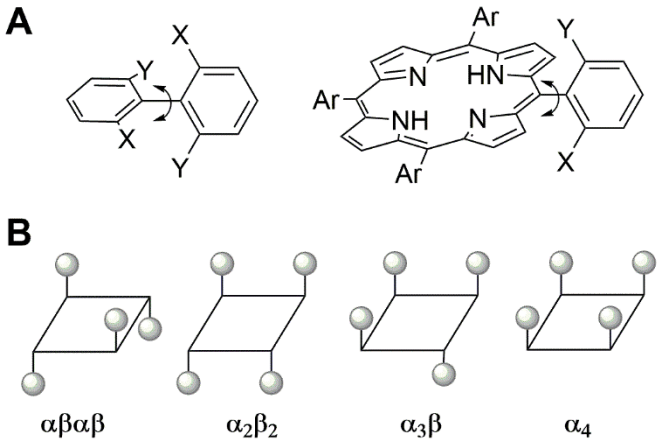

Figure 10. Porphyrin atropisomerism. (A) in comparison to biaryl derivatives and (B) possible configurations. Adapted from Norvaisa et al.[162]

Porphyrin atropisomer nomenclature distinguishes the position of the meso-aryl-substituent with respect to the macrocycle plane, α indicating above and β below. The individual configurations (Figure 10B) are designated as α_4 when the phenyl group substituents are on the same side of the macrocycle plane; $\alpha_3\beta$ when three of the substituents are in the same side of the plane and one is on the other side of the plane; $\alpha_2\beta_2$ when two substituent groups are on each side and adjacent to each other; and αβαβ when two substituents are on each side, but alternate in the positions, with respect to the macrocycle.[162,164]

NMR is perhaps the most commonly used technique to characterize porphyrin atropisomer structure and stability. As with all atropisomers, NMR can be useful to reveal atropisomerism.[171] However, the high symmetry of αβαβ and α_4 porphyrins can render even the use of 2D NMR techniques as challenging to distinguish the four conformers.[162] Some success has occurred with methods developed to alleviate this. Norvaisa et al.[162] used host-guest interactions with benzenesulfonic acid to facilitate NMR characterization of non-planar picket fence porphyrins. Single crystal X-ray crystallography, however, continues to remain a definitive method of structural elucidation.[162,172] HPLC can serve as a practical method of porphyrin atropisomer identification if characterization is required on an ongoing basis. Following clarification of the HPLC elution profile with NMR and X-ray techniques, unique atropisomer retention times can be used. This method features in Chapter 2 with redaporfin atropisomers. Vt-NMR is the most commonly used technique to determine porphyrin atropisomer interconversion barrier.[165,172] Nevertheless, in cases when the NMR timescale is not appropriate, for example due to high atropisomer stability,

HPLC[163, 171] and DFT calculations have also been used.[170,173] Such studies have benefited understanding of tuning porphyrin atropisomer interconversion.

Discovery of porphyrin atropisomer configurations have contributed significantly to the use of porphyrins in biomimetic chemistry. Collman et al.[168] exploited the α_4 atropisomer for the preparation of an Fe(II) complex (Fe(TpivPP)(*N*-RIm)$_2$(O_2)), used as a synthetic model for oxygen-binding in hemoproteins. The α_4 conformation served as a protected binding pocket for reversible O_2 binding.[168] To incorporate the proposed dome shape of deoxyhemoglobin in heme proteins to models, covalent linkages between porphyrin β-β- and meso-meso-positions were prepared, which gave rise to strapped porphyrins.[174-175] While many strapped configurations were investigated, only short straps could effectively mimic distorted shape.[175-177] 'Capped' porphyrins facilitated a suitable protective cavity for the reversible oxygenation previously exhibited by picket-fence porphyrins.[178-179] αβαβ and $\alpha_3\beta$ porphyrin atropisomers were used by Collman et al. to prepare strapped and capped tris-imidazole porphyrins to mimic Tyr^{244} key role in cytochrome c oxidase activity.[180] While straps could be considered an effective way to lock porphyrin atropisomer interconversion, long alkyl chain straps have exhibited rotation and atropisomerism by bridging picket substituents.[171] Porphyrin atropisomers also feature in the design of molecular rotors,[165] motifs for molecular recognition,[181] structures to induce chirality[182-183] and systems to study the positioning of charged groups in electrocatalysis.[184]

Minimal investigation for therapeutic study of porphyrin atropisomers as PS drugs has occurred since discovery.[185-186] While examples of tetrapyrrole regioisomers which present varied efficacy have been observed, this is typically attributed to varied lipophilicity or the distribution of positive charge.[77,79-80,187] Atropisomers have received considerably less investigation. This is due to the frequent assumption that isomers are anticipated to present similar photophysical properties[188] and, consequently, are unlikely to exhibit different PDT efficacies. Redaporfin atropisomers challenged this idea as each presented varied phototoxicities.[105] The primary objective of this work was to understand the effects of atropisomerism on tetrapyrrole PDT (Chapter 2). Following this investigation, it was possible to define a relationship between atropisomer configuration and enhanced cell uptake which could be used to design novel PS with higher internalization (Chapter 3). Fundamental understanding of the impact atropisomerism on cell internalization revealed the potential to benefit cytosolic delivery of novel drug candidates.

2. The Impact of Atropisomerism on Redaporfin Photodynamic Therapy

2.1 ABSTRACT

The intrinsic challenge of large molecules to cross the cell membrane and reach intracellular targets is a major obstacle for drug development. This chapter reports how rotation along a single C–C bond between separable atropisomers, of a drug in clinical trials, improves cell internalization and therapeutic efficacy. The atropisomers of redaporfin (a fluorinated sulfonamide bacteriochlorin PS of 1135 Da) are stable and display vastly different photodynamic efficacy profiles, which are directly related to differential cellular uptake. Redaporfin atropisomer uptake was observed to be predominantly passive and only marginally affected by ATP depletion, plasma proteins or formulation in micelles. The α_4 atropisomer, which features sulfonamide substituents orientated on the same side of the tetrapyrrole macrocycle, exhibited the highest cellular uptake and phototoxicity. The α_4 configuration appeared to enhance binding interaction with the cell membrane phospholipid bilayer and subsequent diffusion. Increased α_4 uptake by cells of the tumor microenvironment was observed *in vivo* and correlated to the PDT response when tumor illumination was performed 24 h after α_4 administration. These results show that properly oriented aryl sulfonamide groups may be incorporated into drug design as efficient cell-penetrating motifs *in vivo* and unveil unexpected biological consequences of atropisomerism.

2.1.1 Graphical abstract

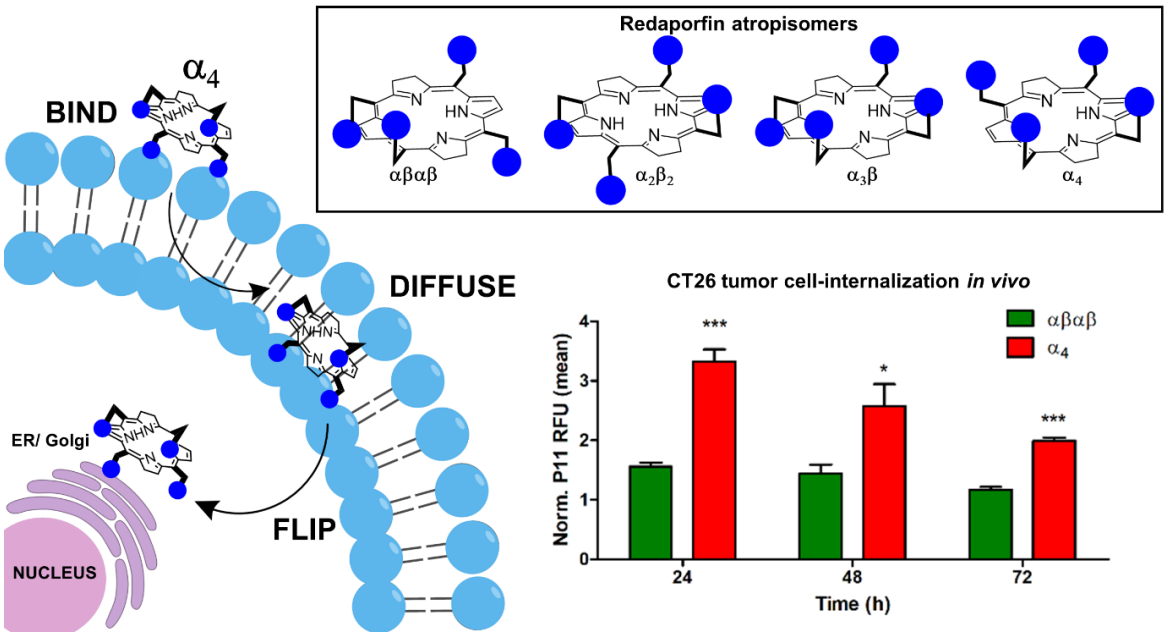

2.2 INTRODUCTION

The outer membrane of mammalian cells severely restricts the uptake of large molecules (>1000 Da) by passive diffusion. This is a major barrier in drug development and has encouraged the development of membrane-anchoring moieties to enhance membrane interaction[189] as well as cell-penetrating motifs to unlock macromolecule cytosolic delivery.[190-196] It is reasonably established that such motifs must be amphipathic in order to disrupt the interface between the bilayer membrane core and the extracellular aqueous phase.[192,197] Additionally, the motifs should reduce the energy penalty of transition from this aqueous phase to lipophilic membrane.[198-199] A good example of a cell-penetrating motif is the guanidinium group anchored to an aromatic hydrophobic scaffold. This may form bidentate bonds with sulfates and carboxylates of the cell surface and promote cell internalization.[190,197,200] Interestingly, the higher phototoxicity of PSs for PDT of cancer bearing guanidinium groups was deemed to be a result of higher cell uptake.[201] Although many advances in macromolecule cell uptake have been achieved, useful structure-function relationships are still lacking and macromolecule delivery to any and all cells in the body remains a major unmet need.

Atropisomers are separable conformers with hindered rotation along a single bond, which becomes a source of axial chirality when asymmetric substitution about the bond is present. Distinctively, conversion between stereoisomers at high temperatures occurs by bond rotation, rather than by bond-breaking-bond-forming processes. Conformers are regarded as atropisomers when their interconversion at rt occurs with a $t_{1/2}$ >1000 s, which corresponds to a barrier height for rotation > 20 kcal mol^{-1}.[106,115-117,202] Atropisomerism, although frequently disregarded, is a useful method to introduce structural diversity in drug design and increase target selectivity. Examples of atropisomers are pervasive in kinase inhibitors where ~80% of FDA-approved kinase inhibitors contains at least one rapidly interconverting axis of atropisomerism.[117] Differential activities (potency and selectivity) were recently reported for atropisomers of pyrrolopyrimidine-based kinase inhibitors, where one form binds to the desired molecular target while the other causes off-target effects by adherence to other kinases.[146] Current knowledge is conducive to limiting the scope of differential atropisomer activity to distinct interactions of the separable conformers with their targets. Passive interactions of atropisomers with cell membranes would not be expected to lead to differential activity. Nevertheless, we show here for the first time that atropisomers of a PS in phase 1/2 clinical trials for head and neck cancer

(NCT02070432),[94] redaporfin (Figure 11A), have dramatically different pharmacological performances and relate such differences to cell uptake.

PDT employs a PS molecule, light absorbed by the PS at a specific wavelength and molecular oxygen to induce a therapeutic effect. The electronically-excited PS transfers its excess energy to molecular oxygen to generate singlet oxygen, or is involved in electron transfer processes which generate additional ROS.[1-2] The local oxidative stress caused by ROS triggers cell death in the field of illumination, as well as systemic anti-tumor immune responses which contribute to long-term control of cancer.[34] The most frequently used PSs are porphyrin derivatives, including chlorins and bacteriochlorins.[203-204] The availability of robust synthetic methods to prepare large quantities of meso-arylporphyrin derivatives[205-206] promoted the synthesis of a variety of PSs with macrocycle-aryl bonds which exhibit atropisomerism. Large substituents in phenyl *ortho*-positions hinder rotation around the macrocycle-aryl bond and the asymmetry of the substitution generates atropisomers.[169] Temoporfin is clinically applied as a mixture of four atropisomers.[207] The structures of these tetrapyrrole atropisomers were originally referred to as 'picket-fence'. The biological relevance of these 'picket-fence' systems has been typically reserved as model complexes for dioxygen binding to heme.[168]

Atropisomers of meso-arylporphyrin derivatives have been isolated and characterized.[162, 185-186,208-209] Isomers with similar photophysical properties are expected to give similar ROS quantum yields because neither energy nor electron transfer reactions require close contact with oxygen.[188] For this reason, different isomers with comparable photophysical properties are typically expected to display similar behavior for PDT as PS isomer mixtures. This was observed with benzoporphyrin derivative monoacid ring A (named verteporfin), which has two regioisomers with the same phototoxicity.[210] Both isomers are present in Visudyne for PDT of age-related macular degeneration.[11] Increased photoactivity of a specific atropisomer has only been reported for a more polar atropisomer with higher propensity for differential monomeric solubilization in aqueous solutions;[186] and also for structural isomers with large differences in lipophilicity or varied distribution of positive charge which originate differences of cellular uptake.[77,79]

Redaporfin is a photostable bacteriochlorin PS with facile synthesis, intense absorption at 749 nm and high ROS yield.[97-98,211] It has exhibited high cure rates in different mouse models of cancer (e.g., CT26, B16-F10, S91, LLC cancer cells), including abscopal

inhibition of metastasis outside of the field of illumination.[40,98,102-103,212-213] A fluorine substituent in an *ortho*-position of a phenyl group is not sufficient to hinder aryl-macrocycle bond rotation to yield separable atropisomers at rt,[184] but fluorine substituents in both *ortho*-positions of redaporfin phenyl groups, together with their sulfonamide groups, lead to atropisomers with configurational stability of years at rt. Four atropisomers were separated – αβαβ, $\alpha_2\beta_2$, $\alpha_3\beta$ and α_4 – which differ by the spatial orientation of the sulfonamide groups with respect to the macrocycle (Figure 11B).[105] Although the chemical properties of the atropisomers are remarkably similar, their biological activities differ by orders of magnitude. In this work, we intended to examine the differential atropisomer activity *in vitro* and *in vivo* to establish the source of variation. Through doing this, we aimed to determine the wider potential of evaluating atropisomerism for PS design. PDT efficacies of atropisomers were revealed to be related to their ability to diffuse across the cell membrane. This unveiled unsuspected consequences of atropisomerism in cell uptake. The spatial orientation of polar substituents has profound consequences for cell internalization and opens new perspectives for cytosolic delivery of large molecules.

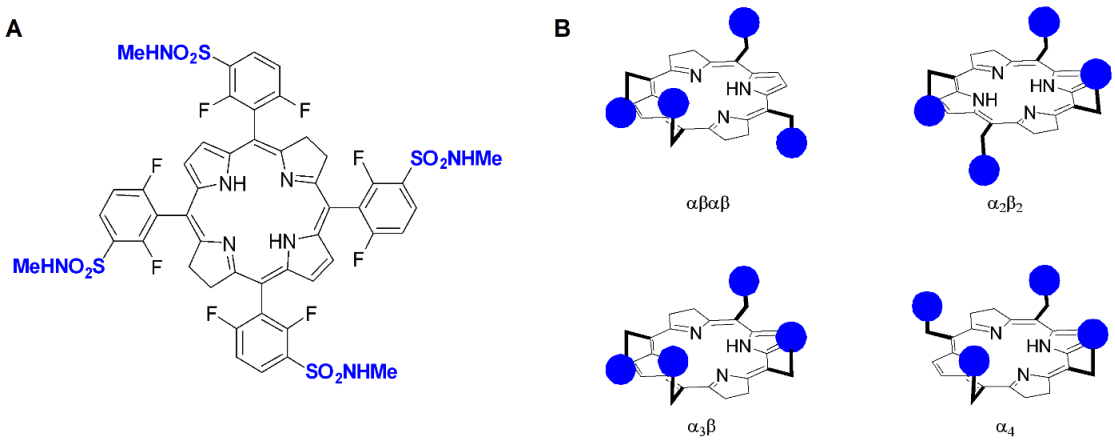

Figure 11. Redaporfin is a mixture of four atropisomers. (A) Redaporfin (i.e., 5,10,15,20-tetrakis(2,6-difluoro-3-*N*-methylsulfamoylphenyl)bacteriochlorin), molecular weight 1135 Da. (B) Atropisomers: αβαβ – two sulfonamides are on each side of the plane but in alternate positions; $\alpha_2\beta_2$ – two sulfonamides on each side of the plane and adjacent to each other; $\alpha_3\beta$ – three sulfonamides on the same side of the plane and one on the opposite side; α_4 – all sulfonamides on the same side of the macrocycle plane.

2.3 MATERIALS AND METHODS

2.3.1 Separation of redaporfin atropisomers by flash chromatography and analyses by reversed-phase high performance liquid chromatography (RP-HPLC)

Redaporfin, 5,10,15,20-tetrakis(2,6-difluoro-3-*N*-methylsulfamoylphenyl)bacteriochlorin atropisomeric mixture and the related 5,10,15,20-tetrakis(2,6-difluoro-3-*N*-methylsulfamoylphenyl)porphyrin (P11) were provided by Luzitin SA (Portugal). Redaporfin was dissolved in DMF and H_2O (4:1) (20 μg/μL) and sonicated for complete solubilization. Redaporfin atropisomers were separated by reversed-phase (RP) flash chromatography (Interchim Puriflash 420 system) using a reverse phase C18 column (Interchim PuriFlash Column, 15μ, C18 HP, 12 g). A solvent gradient of 60 to 95% acetonitrile (MeCN; Sigma) with Milli-Q H_2O was pumped at a constant flow rate of 1.5 mL/min over 70-90 minutes. The temperature of the column was kept at 23 °C and the detection of redaporfin was carried out at 743 nm. MeCN was removed from fractions *in vacuo* (water bath temperature max. = 40 °C) and removal of H_2O by lyophilization. Samples from the obtained fractions were dissolved in a solution of MeCN and ammonium acetate buffer (6:4) (100 mM, pH 8-9.0) (Merck ACS reagent grade) and further submitted to reversed-phase HPLC analysis (Varian 920-LC Integrated Analytical HPLC) using a Phenomenex® brand RP-C18 column (4.6 × 25mm, 50.1 μM) at 23 °C. A gradient of 60 to 95% MeCN with ammonium acetate buffer was used over 15 min at a constant flow rate of 1 mL/min. The four redaporfin bacteriochlorin and porphyrin P11 atropisomers were detected at 743 nm and 414 nm, respectively.

2.3.2 Mass spectrometry and ^{1}H NMR of separated atropisomers

High resolution mass spectrometry (HRMS) was performed with a Q-Tof Premier Waters MALDI quadrupole time-of-flight (Q-TOF) mass spectrometer equipped with Z-spray electrospray ionization (ESI) and matrix-assisted laser desorption ionization (MALDI) sources in negative mode with *trans*-2-[3-(4-*tert*-butylphenyl)- 2-methyl-2-propenylidene]malononitrile as the matrix. ESI mass spectra were acquired in negative modes as required, using a Micromass time-of-flight mass spectrometer (TOF) interfaced to a Waters 2960 HPLC or a Bruker microTOF-Q III spectrometer interfaced to a Dionex UltiMate 3000 LC.

Similar masses were detected for each atropisomer with high resolution mass spectrometry. HRMS (ESI): *m/z* calc. for $C_{48}H_{38}N_8O_8S_4$ $[M]^+$: 1134.1568; found **sample (αβαβ)** 1133.1460, **sample ($\alpha_2\beta_2$)** 1133.1462, **sample ($\alpha_3\beta$)** 1133.1484, **sample (α_4)** 1133.1441.

^{1}H NMR spectra were acquired for Redaporfin bacteriochlorin atropisomers[i] on a Bruker Avance 400 spectrometer (400 MHz) using $CDCl_3$ or $(CD_3)_2SO$ as solvent. Chemical shifts are reported in ppm and referenced to residual solvent peak ($CHCl_3$; δ_H = 7.26 ppm or $(CH_3)_2SO$; δ_H = 2.50 ppm). The multiplicity is indicated as follows: s = singlet, d = doublet, t = triplet, q = quartet, m = multiplet and br = broad signal.

Sample (αβαβ) ^{1}H NMR (400 MHz, $CDCl_3$): δ = 8.25-8.19 (m, 4H, Ar-H), 8.00 (s, 4H, CH_{beta}), 7.30 (t, *J* = 8.2 Hz, 4H, Ar-H), 4.69 (q, *J* = 5.1 Hz, 4H, NH), 4.03 (br, 8H, $CH_{2\ beta}$), 2.79 (d, *J* = 5.2 Hz 12H, CH_3), -1.37 ppm (s, 2H, NH_{pyr}).

Sample ($\alpha_2\beta_2$) ^{1}H NMR (400 MHz, $(CD_3)_2SO$): δ = 8.27-8.21 (m, 4H, Ar-H), 8.23 (br, 4H, NH), 7.85-7.81 (m, 4H, CH_{beta}), 7.77 (t, *J* = 8.5 Hz, 4H, Ar-H), 4.05 (br, 8H, $CH_{2\ beta}$), 2.63 (d, J = 4.4 Hz, 12H, CH_3), -1.41 ppm (s, 2H, NH_{pyr}).

Sample ($\alpha_3\beta$) ^{1}H NMR (400 MHz, $CDCl_3$): δ = 8.27-8.24 (m, 4H, Ar-H), 8.02-7.99 (m, 4H, CH_{beta}), 7.40-7.33 (m, 4H, Ar-H), 4.75-4.69 (m, 4H, NH), 4.05 (br, 8H, $CH_{2\ beta}$), 2.82-2.73 (m, 12H, CH_3), -1.39 ppm (s, 2H, NH_{pyr}).

Sample (α_4) ^{1}H NMR (400 MHz, $CDCl_3$): δ = 8.25-8.21 (m, 4H, Ar-H), 7.93 (s, 4H, CH_{beta}), 7.30 (t, 4H, *J* = 8.1 Hz, Ar-H), 4.82 (br, 4H, NH), 4.03 (br, 8H, $CH_{2\ beta}$), 2.66 (br, 12H, CH_3), -1.50 ppm (s, 2H, NH_{pyr}).

The assignments above agree with the literature.[105] The redaporfin atropisomer samples obtained and characterized as described above were employed in the studies reported in this work using their molar absorption coefficients to determine their concentrations.

2.3.3 Crystal structure analyses[ii]

Crystals of the separated atropisomers of the porphyrin P11 were grown by the following procedures: the α_4 sample was dissolved in acetonitrile and left to evaporate in a covered tube over the course of three months, whereupon crystals appeared at the base of the

[i] ^{1}H NMR spectra were recorded and analyzed with the assistance of Dr. Fábio M. S. Rodrigues
[ii] The crystallographic data was collected and analyzed by Dr. Christopher J. Kingsbury

crystallization tube. The $\alpha_2\beta_2$ sample was dissolved in DMSO layered below ethyl acetate; however, no crystallization was observed on combination of the layers. Upon standing uncovered for a further month, crystals were evident on the wall of the tube, presumably induced by the slow diffusion of atmospheric water into the hygroscopic DMSO.

A diffraction pattern was collected on each of the two crystals using CuKα radiation on a Bruker APEX-II DUO device, with extended collection times for the α_4 atropisomer to account for the poor diffraction evident at high angles across multiple crystal samples. Samples were held at 100.0(1) K with an Oxford CryoStream device. Data reductions were performed with the Bruker APEX3 package[214] and XPREP;[215] structures were solved with SHELXT[216] and refined with ShelXL[217] in the Shelxle GUI.[218] Images were generated with CrystalMaker X.[219] Critical values related to the crystal structure refinement are in Table S 1.

α_4

Reflections 4 0 0 and -13 1 6 were omitted based on disagreement with the model. Solvent was compensated for with SQUEEZE in PLATON;15 quantity was assigned at 8 molecules per unit cell (4 per formula unit) based on compromise between available solvent area (indicating 10.2 /u.c.) and the residual electron density (indicating 7.5 /u.c.). Atoms were held to SIMU commands to generate realistic thermal parameters due to the limited available data. Hydrogen bonding arrangements were identified based on distance; relevant H-atoms were constrained with DFIX commands.

$\alpha_2\beta_2$

Two reflections were omitted on scaling. Non-rotamer disorder of the SO_2NHCH_3 group on C10 (S107-C111) was modelled as a two-site model, with EADP for C111/121, O108/118, O109/119 and SIMU for other atoms. SADI commands were used for these fragments to constrict to equal bond distances. C-bound H-atoms were fixed, N-H atoms constrained except H120, which was fixed. A large residual Q-peak could be observed next to the DMSO molecule - a two site disorder model was tried but failed to reach convergence, and the one-site model gave no additional issues.

2.3.4 Selective precipitation of redaporfin more “polar” atropisomers

P11 atropisomer mixture (5 mg) was dissolved in dichloromethane (CH_2Cl_2). The solution was combined with hexane and stirred for 1 minute. The precipitate observed was separated

by centrifugation (4000 rpm, 15 minutes) to give sample X. The supernatant solvent was removed under reduced pressure to give sample Y. Both samples were analyzed by RP-HPLC in order to quantify the atropisomer relative amount in each sample. Each sample was dissolved in a solution of MeCN and ammonium acetate buffer (6:4) (100 mM, pH 9.0) (Merck ACS reagent grade) and further submitted to RP-HPLC (Elite Lachrom HPLC-DAD system with L-2455 Diode Array Detector) using a Purospher® STAR RP-C18 column (4.6 × 25mm, 0.1 μM) at 23 °C. A gradient of 60 to 95% MeCN with ammonium acetate buffer was used over 15 min at a constant flow rate of 1 mL/min. The four porphyrin atropisomers were detected at 414 nm. Table 1 presents the relative amounts of the fours revealing that the area under peaks of atropisomers αβαβ and $\alpha_2\beta_2$ increase in sample X with respect to the original sample of redaporfin, and that the peak of the atropisomer α_4 increases in sample Y with respect to the original sample.

2.3.5 Barriers for C–C single bond rotation between macrocycle and aryl substituents[iii]

The stability of redaporfin atropisomers was investigated by heating a sample of $\alpha_3\beta$ in dimethylformamide at high temperatures and for various periods of time as illustrated in Table S 2. Relative atropisomer content was determined by HPLC with UV-Vis detection. The interconversion of the atropisomers occurs rapidly at high temperatures without appreciable decomposition of the fluorinated sulfonamide bacteriochlorin.

The relaxation time for each temperature was calculated[220] as the time of exponential decay to

$$[A] - [A]_{eq} = ([A]_0 - [A]_{eq}) / e$$

where $[A]_0$ in the initial fraction of $\alpha_3\beta$ (99%), $[A]_{eq}$ is the fraction the statistical mixture in equilibrium (51%) and e = 2.718.

2.3.6 Photophysical and photochemical characterization of redaporfin atropisomers[iv]

Absorption spectra of redaporfin and P11 atropisomers were recorded on an Agilent Cary5000 UV-VIS-NIR spectrometer. Molar absorption coefficients (ε) were obtained

[iii] Calculation of barriers for C-C single bond rotation was performed by Prof. Dr. Luís G. Arnaut

[iv] Photophysical and photochemical characterization was performed with assistance of Dr. Fábio A. Schaberle.

from absorption measurements of three solutions of different concentrations, diluted from three stock 1 mM solutions with independently measured masses. The slope of the plot absorption vs concentration was used to calculate ε_{max}.

Further photophysical characterization of redaporfin atropisomers was carried out with absorption spectra recorded on a Shimadzu UV-2100 spectrophotometer. The fluorescence quantum yields were recorded in a Horiba-Jovin-Yvon Spex Fluorog 3-2.2 spectrophotometer using the near-infrared Hamamatsu R5509–42 photomultiplier, cooled to 193 K in a liquid nitrogen dewar. The fluorescence standard was 1,1′,3,3,3′,3′-hexamethylindotricarbocyanine iodide standard.[221] The wavelength of excitation, integration time and slits in one experiment were 743 nm, 0.8 s and 7 nm bandwidth (exc.) and 10 nm (em.), respectively. Samples and reference were prepared in ethanol with absorbance < 0.15 in the excitation wavelength. Triplet-triplet absorption spectra and the triplet lifetimes (τ_T) of redaporfin atropisomers were acquired with solutions with absorbances between 0.25 and 0.30, excited at 355 nm in an Applied Photophysics LKS 60 nanosecond flash photolysis kinetic spectrometer, using the third harmonic of a Spectra-Physics Quanta Ray GCR 130-01 Nd/YAG laser and a Hamamatsu 1P28 photomultiplier. The signals were recorded with a Hewlett-Packard Infinium oscilloscope (1 GS/s). Photodecomposition quantum yield (Φ_{PD}) was evaluated through photobleaching experiments involving irradiation of the bacteriochlorins in methanol:PBS (3:2) by a CW laser emitting at 745 nm (Omicron Laserage). The total output power of laser light was 640 mW. The time intervals between absorbance measurements ranged from minutes to hours of irradiation. Initial absorbances were ca 1.0. The calculation followed the method previously described in the literature.[97]

Singlet oxygen quantum yields (Φ_Δ) were recorded using a method previously described in literature.[222] Phenalenone was used as a reference (Φ_Δ = 0.95 in methanol).[223] Singlet oxygen phosphorescence was measured at 1270 nm with a Hamamastu R5509-42 photomultiplier, cooled to 193 K in a liquid nitrogen dewar (Products for Research model PC176TSCE005), following pulsed laser excitation of aerated solutions at 355 nm, using an adapted Applied Photophysics spectrometer. A Newport cutoff filter below 1000 nm was employed to avoid fluorescence light. The quantum yields were calculated using the slope obtained from the phosphorescence signal dependence with laser energy.

Aggregation studies were conducted with P11 atropisomers (2.5 μM) in pure DMSO or in water : DMSO (99.96 : 0.04). Absorption spectra in both solvents were recorded on an Agilent Cary 5000 UV-VIS-NIR spectrometer. Emission and excitation spectra were recorded on a Horiba-JY Fluoromax4 spectrofluorometer. P11 absolute values of fluorescence quantum yield were obtained for each atropisomer and were measured using the absolute method with a Hamamatsu Quantaurus QY absolute photoluminescence quantum yield spectrometer model C11347 (integration sphere).

2.3.7 Octanol/water partition coefficients ($LogP_{OW}$)

Redaporfin atropisomer $LogP_{OW}$ values were obtained using a modified shake-flask method. *N*-octanol was saturated with Milli-Q H_2O by preparing a mixture 1:1. The saturated *n*-octanol was separated after 24 h. A small sample of each compound was added to saturated *n*-octanol (4 mL) and vigorously mixed with an equal volume of Milli-Q H_2O (4 mL). Following centrifugation (3700 rpm, 3 minutes), phase partitioning was carried out. The H_2O phase was lyophilized (24 h) and re-suspended in 3 mL *n*-octanol. Emission spectra of both *n*-octanol solutions were recorded on a Horiba-JY Fluoromax4 spectrofluorometer with excitation at 505 nm. Area under curve (AUC, 720 -800 nm) was calculated and the Log(*n*-octanol AUC / *n*-octanol used to re-suspend H_2O phase AUC) was used to calculate $LogP_{OW}$ values.

2.3.8 Cell culture and preparation of stocks solutions of the atropisomers

The CT26 (mouse colon carcinoma), U-2 OS (human osteosarcoma), 4T1 (mouse breast cancer) and B16-F10 (mouse melanoma) cell lines were obtained from American Type Culture Collection Cells. Cells were maintained in Dulbecco's modified Eagle's medium (Sigma) supplemented with 10% heat inactivated fetal bovine serum (Gibco, Life Technologies) and 1% penicillin streptomycin (Sigma) in a humidified incubator with 5% CO_2 at 37 °C. Cells were detached using trypsin-EDTA solution (Sigma), counted, and seeded at the desired density in plates of the appropriate size for the different experiments.

A stock solution of each atropisomer (0.5 - 1 mM) was prepared with DMSO Hybri-MaxTM (Sigma) and stored at -20 °C. Before each experiment, the stock solutions of atropisomers were diluted in culture medium at the desired concentration and added to the cells. Due to limited amounts of redaporfin atropisomers, in some experiments, P11 atropisomers were used instead as their relative biological activities can be considered as analogous to the bacteriochlorin atropisomers.

2.3.9 Cell viability using the resazurin reduction assay

CT26 (5000 cells/ well), U-2 OS (7000 cells/ well), 4T1 (7000 cells/ well) and B16-F10 (6000 cells/well) were seeded in 96-well plates. 24 h later, cells were treated with the single atropisomers in a concentration range from 2.5 to 0.08 μM for 24 h. After a washing step with medium, cells were illuminated with a light-emitting diode (LED) at 740 nm or 410 nm, respectively for redaporfin or P11 atropisomers. The overlap between the LED and the PSs spectra was calculated in order to obtain accurate light doses.[224] A light dose of 0.2 J/cm^2 was delivered for redaporfin atropisomers whereas 0.05 J/cm^2 or 0.0125 J/cm^2 were applied in those experiments involving P11 atropisomers. Cellular viability was evaluated 24 h post-illumination using the resazurin reduction assay.[225] For this, cells were incubated with resazurin diluted in DMEM (0.01 mg/mL, Sigma-Aldrich) for approximately 2 h and the fluorescence of the metabolic product, resorufin, was recorded with a microplate reader (Biotek Synergy HT) using 528/20 nm excitation and 590/35 nm emission filters. The level of resazurin metabolization by the untreated cells (Ctrl) was assumed as 100% viability. Parallel experiments were conducted with higher concentrations of the atropisomers (1.25 to 20 μM) to assess the safety of the different atropisomers in the absence of light (dark toxicity).

2.3.10 Cellular internalization

CT26 (20,000 cells/ well), U-2 OS (30,000 cells/ well), 4T1 (40,000 cells/ well) and B16-F10 (35,000 cells/well) cells were seeded in 24-well plates. After 24 h, cells were incubated with the single atropisomers at a concentration of 2.5 μM. At different time points (2, 4, 8, 16 and 24 h), cells were washed with culture medium, detached with trypsin-EDTA and fixed in paraformaldehyde (PFA) 3.7% (w/v) for ~30 minutes. After an additional washing step with PBS, cells were resuspended in PBS and analyzed by flow cytometry using a Novocyte® TM 3000 (ACEA). Redaporfin fluorescence was measured upon excitation with the 488 nm laser and detection was performed using the 780/60 nm filter. For P11, the 405 nm laser was used with detection on the channel of 615/24 nm. An average of 10,000 events were collected and data is presented as mean fluorescence normalized to the mean fluorescence of untreated cells.

In parallel experiments, cells were incubated with the single atropisomers (2.5 μM) for 24 h, washed and submitted to cell lysis using DMSO with Triton X-100 1% (v/v). To quantify the absolute amount of internalized atropisomers, a calibration curve of the single

atropisomers was also prepared in the lysis buffer. After centrifugation to separate cellular debris, the obtained supernatant (containing the internalized atropisomers) was analyzed for detection of fluorescence. This was carried out with a microplate reader (Biotek Synergy HT) using 508/20 nm excitation and 760/34 nm emission filters for redaporfin and 420/50 nm excitation and 645/40 nm emission filters for P11. The amount of each atropisomer was extrapolated from the calibration curve and normalized to the total amount of protein. Protein quantification was carried out using the Pierce™ BCA Protein Assay Kit according to the manufacturer's instructions (Thermo Scientific).

Subcellular distribution of P11 atropisomers was evaluated in U-2 OS cells stably expressing CALR-GFP or GALT1-GFP, which were a kind gift from Prof. Guido Kroemer (Université Paris Descartes). Cells (17,000 cells/ well) were seeded in an µ-Slide 8-well treated plate (Ibidi) and let to adapt for 24 h. Following this, cells were incubated with the single atropisomers (10 µM) for 24 h, followed by a washing step and fixation with PFA 3.7% (w/v). Images were acquired with a Carl Zeiss LSM 710 Confocal Microscope. GFP was detected using a 488 nm laser and 525/50 nm emission filter while P11 was detected using a 405 nm laser and 605/70 nm emission filter.

2.3.11 Mechanism of cellular internalization

To evaluate the temperature dependence of atropisomer cellular uptake, 4T1 cells (50,000 cells/well) were seeded in 24-well plates. 24 h later, 4T1 cells were incubated with the P11 atropisomers (2.5 µM) at 37 °C or at 4 °C, for 4 h. In parallel experiments, the ATP dependence of uptake was evaluated. For this, cells were washed with glucose deficient DMEM and incubated with 2-deoxy-D-glucose (DG, 20 mM) for 1 h at 37 °C. ATP-depleted cells were then washed with glucose deficient DMEM followed by incubation with the single P11 atropisomers (2.5 µM), for 2 h. Pierce™ Recombinant GFP Protein (40 nM) was included as a positive control of endocytosis. ATP depletion was confirmed using an ATP-Assay Kit (Abcam, ab8355) according to the manufacturer´s instructions. Finally, the impact of plasma proteins on the atropisomer uptake was also evaluated. FBS deficient DMEM supplemented with bovine serum protein (4 and 8 mg/mL BSA, Sigma), human low-density lipoprotein (0.02 and 0.04 mg/mL LDL, Calbiochem) or human high-density lipoprotein (0.02 and 0.04 mg/mL HDL, Sigma) was used to prepare 2.5 µM solutions of atropisomers. These solutions were maintained at 37 °C for 30 min to favor potential interactions between the proteins and the atropisomers. Cells were then incubated with the

protein-supplemented medium containing the atropisomers for 4 h at 37 °C. In these experiments, cellular internalization was evaluated by flow cytometry, as described above.

2.3.12 Interaction of redaporfin atropisomers with 1-palmitoyl-2-oleoyl-sn-glycero-3-phosphocholine liposomes

A stock solution of each atropisomer (0.5 mM) was prepared in DMSO which was further diluted in PBS to a final concentration of 5 µM (1% DMSO). To this solution, POPC liposomes were added at a final concentration of 0.125 mM. After 20 min of incubation, fluorescence was measured with a microplate reader (Biotek Synergy HT) using 528/20 nm excitation and 590/35 nm emission filters. This was followed by 6 cycles of POPC liposome additions until the stabilization of redaporfin fluorescence (final POPC concentration of 3.25 mM).

2.3.13 Atropisomer internalization by cells of the tumor microenvironment

All the animal experiments were approved by the Portuguese Animal and Food Authority (DGAV authorization 0421/000/000/2020). Tumors were established by subcutaneous (sc) injection of 350,000 CT26 cells in the right flank of female BALB/c mice ca. 10-12 weeks old (20 g).

When tumor diameter reached ca. 5 mm, P11 atropisomers (2.5 mg/kg) were delivered intravenously (via the tail vein) as a formulation of saline : DMSO : Kolliphor®EL (97 : 1: 2% v/v). Relative micelle size was determined by acquisition of hydrodynamic radius (z-average) by dynamic-light scatter (Zetasizer Nano Series). Tumors were collected 24, 48 and 72 h after the atropisomers administration and incubated with 1 mL of Liberase (Sigma, 16 µg/ mL) and Deoxyribonuclease I from bovine pancreas (Sigma, 8300 U/mL) for 1 h at 37 °C. The obtained tumor cell suspension was resuspended in DMEM, passed through a 70 µm cell strainer and washed with PBS. Cells were then incubated with the Zombie-violetTM live dead stain (1:500) (Biolegend) for 15 minutes at 4 °C in the dark. After washing with cold PBS, cells were immediately analyzed by flow cytometry (Novocyte 3000, ACEA). The Zombie-violet^{TM} signal was detected upon excitation with the 405 nm laser and detection at the channel 445/45 nm. P11 fluorescence was acquired using the 405 nm laser (excitation) with detection at the channel of 615/24 nm. An average of 5000 events negative to Zombie-violet^{TM} (live cells) were collected and data is presented as mean fluorescence normalized to the signal of tumors suspensions from untreated mice.

2.3.14 Treatment of BALB/c mice bearing CT26 tumors with PDT using redaporfin atropisomers

Tumors were established by subcutaneous injection of 350,000 CT26 cells in the right flank of female BALB/c mice ca. 10-12 weeks old (20 g) or male BALB/c ca. 10 – 12 weeks (25 g). Treatments were performed when tumors reached ca. 5 mm. Redaporfin atropisomers were delivered intravenously (via the tail vein) as a formulation of saline : EtOH : Kolliphor®EL (98.5 : 1 : 0.5% v/v). Relative micelle size was determined by acquisition of hydrodynamic radius (z-average) by dynamic-light scatter (Zetasizer Nano Series). The illumination was performed with a laser at 749 nm (Omicron Laserage). Vascular-PDT (0.45 mg/kg, DLI = 15 min, 40 J/cm^2 @ 137 mW/cm^2, 1.33 cm^2 area of illumination) and cellular-PDT (0.35 mg/kg, DLI = 24 h, 60 J/cm^2 @ 137 mW/cm^2, 1.33 cm2 area of illumination) protocols were optimized in order to obtain the best therapeutic outcomes without significant toxicity. Tumors were measured twice a week with a caliper and the volume was calculated using the formula $V = (a \times b^2)/2$, where a corresponds to the major diameter and b to the minor diameter. The humane endpoint of tumor size followed was major diameter > 12 mm. Cured mice were subjected to re-challenge with subcutaneous injection of 350,000 CT26 cells ca. 6 weeks after PDT treatment.

2.3.15 Assessment of α_4 skin photosensitivity in BALB/c mice

Hair from the dorsum of male BALB/c mice ca. 10 - 12 weeks old was removed using depilatory cream followed by intravenous administration of redaporfin mixture (0.45 mg/kg) or the α_4 atropisomer (0.45 mg/kg). After three or seven days, skin areas of 0.5 cm^2 were illuminated for 90 J/cm^2 or 180 J/cm^2 using a solar simulator (Oriel with global filter AM 1.5, 100 mW/cm^2). Mice without administration of any compound were included as control. Skin effect, specifically erythema, were measured by means of a Mexameter (Courage-Khazaka).

2.3.16 Enrichment of redaporfin mixture with the α_4 atropisomer

Redaporfin, (10 mg) and silica gel (1.5 g, Sigma) were added to a dried 100 mL Schlenk tube under argon and dried under vacuum. The reaction flask was purged with argon three times. Anhydrous-toluene (6 mL, Sigma) was added and argon was used to degas the solution for 15 minutes. The solution was heated to 111 °C and stirred under argon for 24 hrs. Cooling to rt was followed by filtration. Extraction of enriched mixture from silica was carried out with washing using EtOAc (200 mL, Sigma) followed by solvent evaporation

under reduced pressure. Atropisomer separation via flash chromatography with HPLC analysis proceeded as described in section 2.3.1.

2.3.17 Statistical analysis

Data from cellular studies are presented as the mean ± standard error mean (SEM) of 2-3 independent experiments, each one in triplicates. Unpaired student's t test, one- or two-way ANOVA were used when indicated to determine statistically significant differences between the atropisomer α_4 mean and the other atropisomers. Survival analysis of PDT-treated mice was performed by means of a Kaplan–Meier estimator with long-rank (Mantel-Cox) test to evaluate the significance of the differences between different PDT treated groups.[226]

2.4 Results and Discussion

2.4.1 Redaporfin atropisomers are stable and separable at room temperature

Redaporfin (and related chlorin and porphyrin derivatives)[97] atropisomers were initially separated by semi-preparative HPLC at rt.[105] This time-consuming process was advantageously replaced by reversed-phase (RP) flash chromatography. Rapid and efficient separation of the redaporfin atropisomers was possible using a RP silica gel C18 column with an increasing gradient of acetonitrile in water (60% to 90% MeCN) at T = 23 °C for 90 min. This was followed by acetonitrile evaporation under vacuum (maintaining pressure at 220 mbar and T < 40 °C) and water removal by lyophilization. Each fraction molecular mass was deemed similar by ESI mass spectrometry (calculated 1135 Da, Figure S 1) and was evaluated for atropisomeric purity by ^{1}H NMR (Figure S 2) and RP-HPLC (Figure S 3). The retention times of the atropisomers of redaporfin and the corresponding precursor porphyrins (named P11) are similar (Figure 12A and Figure S 3). Fractions of atropisomeric purity (> ~90%) confirmed by RP-HPLC were used for photochemical, photophysical and biological evaluations. The RP-HPLC of redaporfin (Figure 12A) indicates that the α_4 atropisomer accounts for the lowest proportion of the mixture (~13%) followed by $\alpha\beta\alpha\beta$ (~14%), $\alpha_2\beta_2$ (~24%) and $\alpha_3\beta$ (~49%), which is consistent with their expected statistical abundance, 1:1:2:4.[168] Redaporfin is formed as a statistical mixture of atropisomers following synthesis.

It is important to emphasize that the order of RP-HPLC retention times in Figure 12A is the same as the order of R_f (Retention factor) values of atropisomers separated by silica-

gel thin-layer chromatography (TLC) and in silica gel columns using ethyl acetate: dichloromethane (20:1, v/v followed by 3:2, v/v) as eluent.[105] The assignment in Figure 12A does not follow the conventional expectation that α_4, with all dipole moments of polar groups pointing to the same side of the macrocycle, should be the most polar atropisomer. Typically, the more polar atropisomer should have the highest retention time in silica gel chromatography and the lowest retention time in RP-HPLC. It was, therefore, unexpected that α_4 was observed to have the highest chromatographic retention time regardless of the choice of stationary phase. Order of atropisomer elution was the same with normal phase silica gel (ethyl acetate: dichloromethane as eluent) or a RP silica gel, hydrophobic octadecylsilane (C18) column (acetonitrile: water as eluent). This was also observed with saddle-shaped picket fence porphyrins with acetyl *ortho*-substituents, separated with the same order of elution in silica gel chromatography and RP-HPLC.[227] The retention factors of drugs in a C18 column with acetonitrile:water as a mobile phase are generally anticipated to correlate with lipophilicity and $LogP_{OW}$.[228] α_4 shows a greater affinity for hydrophobic C18 in the stationary phase than for the polar eluent. Thus, the higher retention factor of α_4 in RP-HPLC suggests that it is the most lipophilic atropisomer, whereas its higher retention in normal phase silica gel column chromatography can be assigned to stronger hydrogen bonding of its four sulfonamide groups with silanol (SiOH) groups on the surface of silica (Figure S 4). Together, these results demonstrate the strong amphipathic character of α_4.

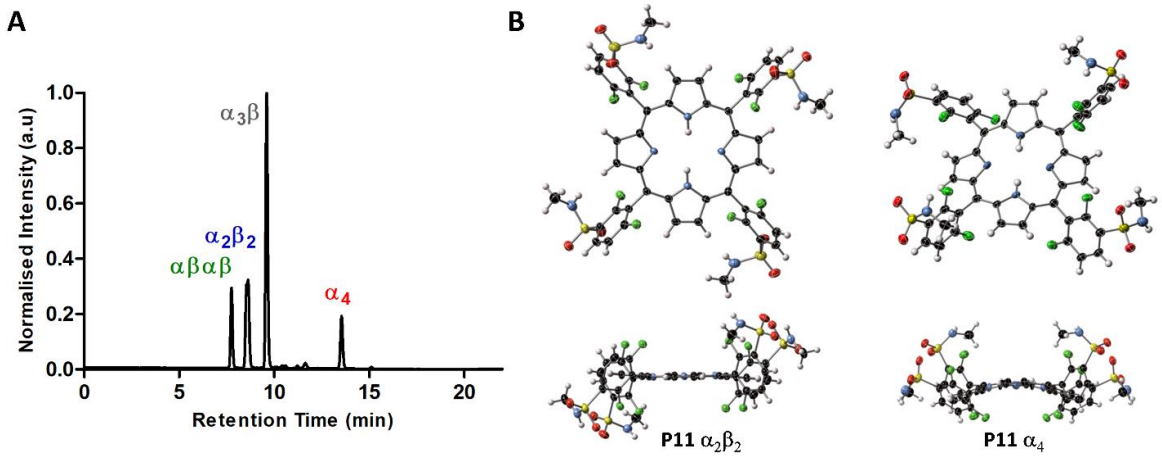

Figure 12. Separation and X-ray crystal structures of redaporfin atropisomers. (A) Representative RP-HPLC chromatogram of redaporfin where the individual atropisomers were detected by absorption at 743 nm (B) View of the molecular structure in the crystal of $\alpha_2\beta_2$ and α_4 atropisomers of P11, where the $\alpha_2\beta_2$ and the α_4 atropisomers were obtained from $\alpha_2\beta_2$.2Me_2SO and α_4.4MeCN respectively (ellipsoids are shown at the 50% probability level and H atoms are represented as spheres of fixed radius).

Crystals were grown from the fractions assigned to $\alpha_2\beta_2$ and α_4 P11 atropisomers and their molecular structures determined with X-ray diffraction studies. Modelling of diffraction data unambiguously confirmed structure assignment, with the identified atropisomer as the sole component of each structure (Figure 12B, Table S 1 and Figure S 5-Figure S 6). Hydrogen bonding of the sulfonamide moiety was the most prominent of intermolecular interactions in each case. The $\alpha_2\beta_2$ P11 atropisomer interacted with DMSO solvate through the N-H protons on the sulfonamide group (2.825(7) Å N···O) and with sulfonamide groups of adjacent molecules (3.036(16) Å N···O). One of these sulfonamide groups exhibited minor conformational disorder (Figure S 5C). In the $\alpha_2\beta_2$ atropisomer, the porphyrin core adopted a primarily planar modality with localized H-atoms. Consistent with the $\alpha_2\beta_2$ atropisomerism, inversion symmetry existed at the center of the molecule; aryl rings were inclined at 76° and 64° to the mean plane of the porphyrin (Figure 12B and Figure S 5A-D), as expected for *ortho*-substituted 5,10,15,20-tetraarylporphyrins. In contrast, the α_4 P11 atropisomer (α_4-1·4MeCN) did not interact strongly with the included solvate; hydrogen bonding (H-bonding) networks of porphyrins defined channels of 17% of the crystal volume which were filled with disordered MeCN (Figure 12B and Figure S 6).[229] Individual α_4 P11 atropisomers were linked together by N-H···O bonding (2.984(13) and 3.020(12) Å N···O) between proximal sulfonamide groups, thus forming a three-dimensional hydrogen-bonded lattice (Figure S 5E-G). The α_4 structure showed out-of-plane deformation primarily of the saddle type, similar in magnitude to the most distorted Heme B subunits in protein structures.[230]

In view of the non-intuitive retention factors of silica gel and RP-HPLC, we evaluated the relative "polarity" of the atropisomers dissolving the P11 atropisomer mixture in dichloromethane, combined with an equal volume of hexane. The solvent mixture was less polar than the initial solvent and a fraction of P11 precipitates (fraction X). The fraction remaining in the solvent mixture was recovered by solvent evaporation (fraction Y). RP-HPLC of P11, fraction X and fraction Y revealed that the content of α_4 is higher in fraction Y than in fraction X. This means that α_4 is more soluble in a less polar solvent mixture and suggests it as the most lipophilic atropisomer (Table 1), although, it was also the atropisomer that bound more strongly to silica gel, further indicating amphipathic character.

Table 1. Relative atropisomer contents of P11 sample (initially present in dichloromethane), samples X (which precipitated upon addition of hexane) and Y (which remained in the dichloromethane:hexane (1:1) solvent mixture.) calculated with chromatogram peak areas. Mean of value of two independent experiments.

	Relative Atropisomer Proportion (%)		
P11 Atropisomer	**P11**	**Sample X**	**Sample Y**
αβαβ	16.1	17.2	11.5
$\alpha_2\beta_2$	24.8	27.6	20.5
$\alpha_3\beta$	48.4	47.9	51.4
α_4	10.7	7.4	16.8

The rates of interconversion of the atropisomers were studied at 140 °C in dimethylformamide starting with 99% of the $\alpha_3\beta$ atropisomer (Table S 2).[105] The content of $\alpha_3\beta$ was reduced from 99% at t = 0, to 60% in 5 min, 58 % in 10 min and 52% in 20 min. At t = 20 min all atropisomers nearly recovered their proportions in the statistical mixture. Applying relaxation kinetics, this corresponded to a relaxation time ~4 min at 140 °C. A similar experiment at 85 °C gave a relaxation time ~1000 min, which led to a barrier-height for bond rotation ~29 kcal.mol^{-1}. The high stability of atropisomers at rt is marked by slow conversion.

2.4.2 Redaporfin and P11 atropisomers have similar photophysical and photochemical properties

Atropisomers of redaporfin and P11 exhibited similar photophysical and photochemical properties. Absorption spectra were comparable (Figure 13A) between the four redaporfin atropisomers. Absorption maxima (λ_{max}) and corresponding molar absorption coefficients (ε_{max}) are presented in Table 2. The triplet decays were mono-exponential with atropisomer triplet lifetimes (τ_T) in the 250-300 ns range. Photodecomposition studies, evaluated through photobleaching experiments involving irradiation of the bacteriochlorins in methanol:PBS (3:2), indicate that α_4 (photodecomposition quantum yield $\Phi_{PD} = 9 \times 10^{-6}$) was slightly more photostable than the other atropisomers. Singlet oxygen emissions followed mono-exponential decays and their intensities relative to a reference allowed for the determination of singlet oxygen quantum yields (Φ_Δ). The Φ_Δ values obtained for the

$\alpha_3\beta$ and α_4 atropisomers were higher than for the other atropisomers. The fluorescence quantum yields (Φ_F) of all atropisomers were reasonably similar.

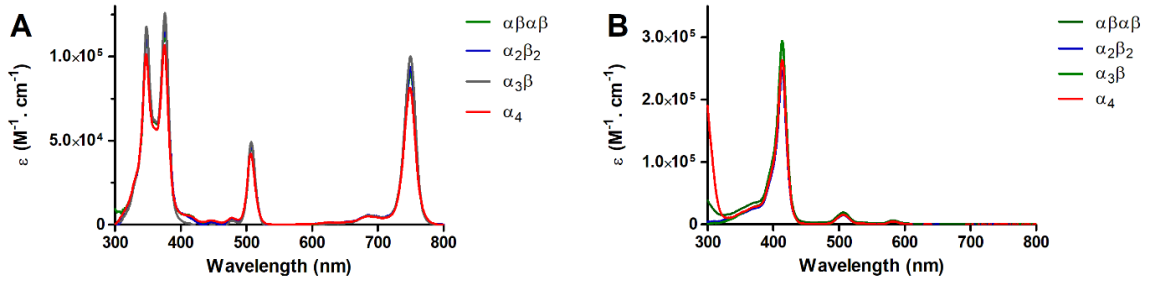

Figure 13. Absorption spectra of (A) redaporfin and (B) P11 atropisomers recorded in DMSO.

Some deviations between porphyrin atropisomer photophysical/photochemical properties can occur.[208,231] The differences in the case of redaporfin atropisomers were small and tended to compensate each other. For example, whilst α_4 was slightly more photostable and its Φ_Δ was high, it also had the lowest ε_{max}. On the basis of these properties, all atropisomers should have very similar PDT efficacies. Table 2 also presents $LogP_{OW}$ values obtained with a modification of the shake-flask method. Interestingly, the higher lipophilicity of α_4, revealed with the addition of hexane to dichloromethane, was not reflected in its $LogP_{OW}$ value. Together with the chromatographic elution profiles, this suggests amphipathic character is associated with α_4 which defies typical classifications of polarity or lipophilicity.

Table 2. Photophysical and photochemical properties of redaporfin atropisomers.[105]

Sample	λ_{max}[a] nm	ε_{max}[a] $mM^{-1}\ cm^{-1}$	τ_T[a] ns	Φ_{PD}[b] $/10^{-6}$	Φ_Δ[a]	Φ_F[a]	LogP$_{OW}$
Redp. mix[97]	743	140	216	10	0.43	0.138	1.9
αβαβ	743	126	257	15	0.39	0.182	2.6
$\alpha_2\beta_2$	743	137	296	15	0.35	0.201	2.6
$\alpha_3\beta$	743	137	268	12	0.50	0.206	3.3
α_4	743	122	266	9	0.49	0.171	2.9

[a] In ethanol. [b] In methanol:PBS, 3:2.

Similar to Redaporfin atropisomers, P11 atropisomer respective absorption spectra (Figure 13B), Soret wavelength (λ_{Soret}) and associated molar absorption coefficients (ε) (Table 3), did not significantly vary. Φ_F were also similar between the four atropisomers.

Table 3. Molar absorption coefficients (ε) and fluorescence quantum yield (Φ_F) of P11 porphyrin atropisomers in DMSO.

P11 Atropisomer	λ_{Soret} (nm)	ε ($mM^{-1}\ cm^{-1}$)	Φ_F DMSO
αβαβ	414	360	0.064
$\alpha_2\beta_2$	414	281	0.064
$\alpha_3\beta$	414	312	0.054
α_4	414	318	0.055

2.4.3 Redaporfin atropisomer phototoxicity varied significantly *in vitro*

As previously observed with the redaporfin mixture,[102] individual atropisomers were confirmed to not cause cytotoxicity in the absence of light, up to at least 20 μM (Figure 14A). The same applied to P11 atropisomers (Figure 14B).

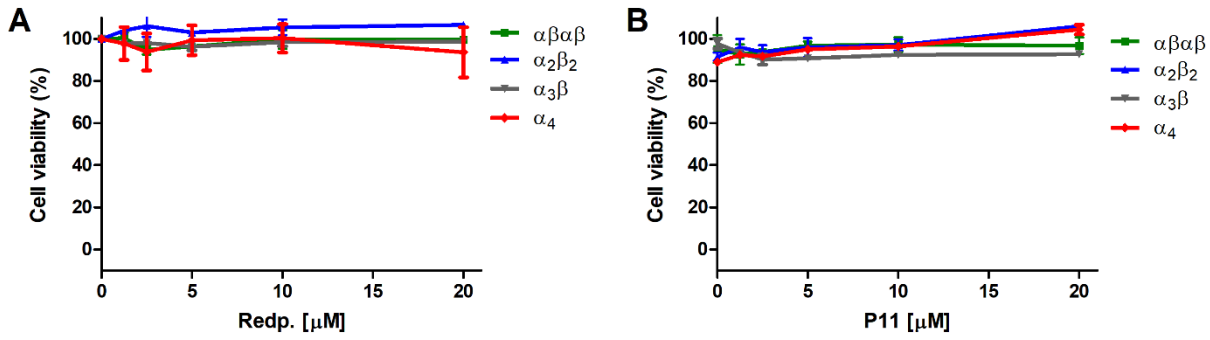

Figure 14. Lack of dark toxicity of redaporfin and P11 porphyrin atropisomers in 4T1 cells (A) Redaporfin and (B) P11 atropisomers cellular viability in 4T1 cells following 24 h incubation. Result indicates the mean ± SEM of 2 independent experiments. Statistical significance was evaluated using two-way ANOVA versus the α_4 atropisomer, no symbol $p > 0.05$.

Remarkably, the phototoxicities of isolated atropisomers differed by orders of magnitude following exposure to the same light dose (Figure 15). The highest phototoxicity was attained with the α_4 atropisomer, which reduced cell viability to less than 10% when concentration exceeded 1 μM. The $\alpha_3\beta$ configuration induced moderate phototoxicity and the $\alpha_2\beta_2$ and αβαβ atropisomers generated considerably less toxicity. 0.2 μM of α_4 killed 50% of U-2 OS cells with a light dose of 0.2 J/cm^2 at 740 nm, whereas the phototoxicity of αβαβ with the same light dose remained negligible at 2.5 μM. The same order of phototoxicity, α_4 (high phototoxicity) > α3β > $\alpha_2\beta_2$ > αβαβ (low phototoxicity), was observed in all cancer cell lines investigated in this work (Figure 15A-C), human bone osteosarcoma (U-2 OS), mouse mammary gland breast cancer (4T1) and mouse colon carcinoma (CT26). Similar results were obtained with the P11 porphyrin atropisomers (Figure 15D-F). This indicated that the different relative atropisomer phototoxicities was not specific to the oxidation state of the tetrapyrrole ring.

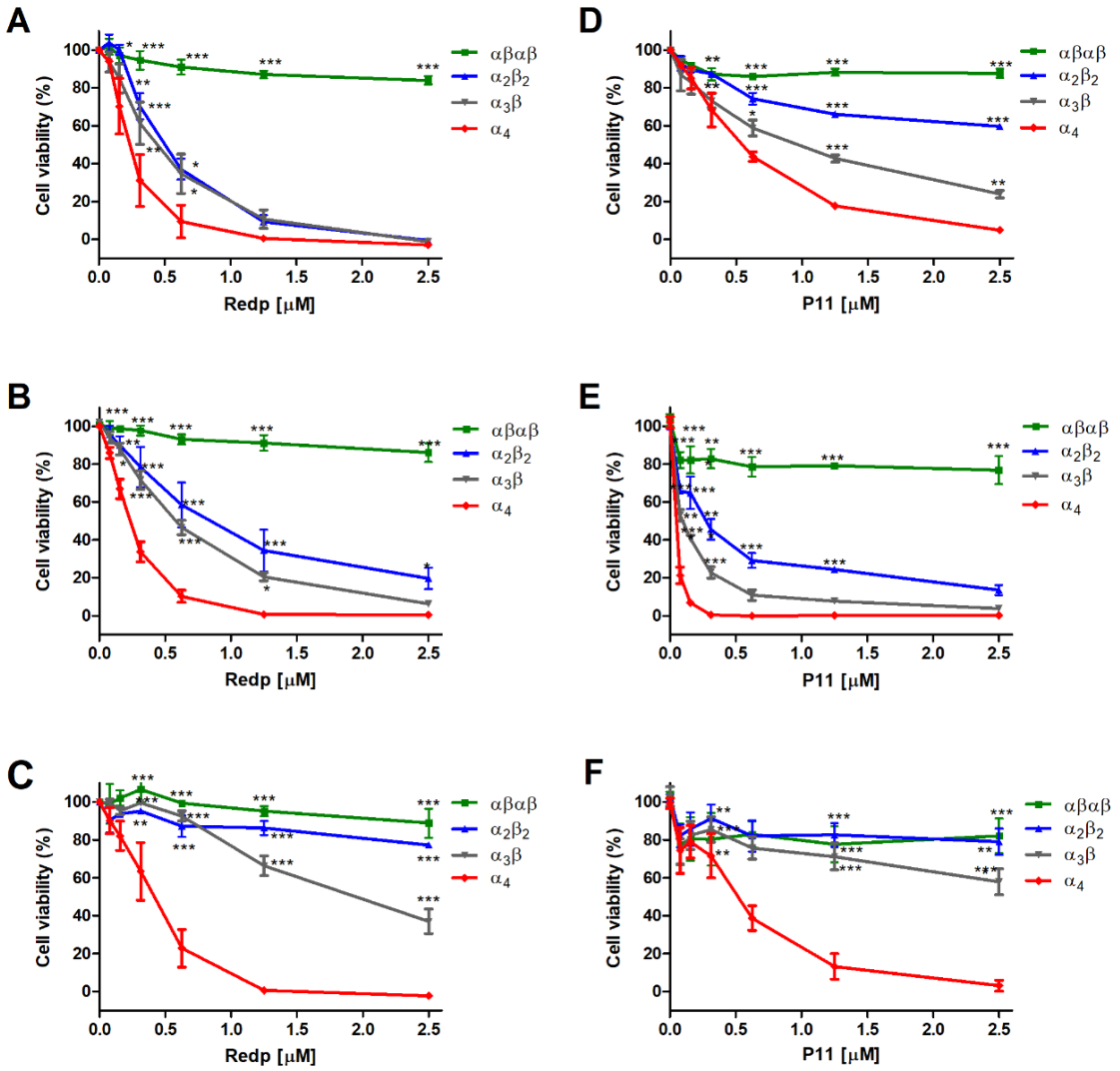

Figure 15. Phototoxicities of redaporfin atropisomers and of P11 atropisomers upon illumination at 740 nm (0.2 J/cm^2) or 410 nm (0.0125 or 0.05 J/cm^2), respectively, after 24 h of incubation. (A-C) U-2 OS, 4T1 and CT26 cells treated with redaporfin atropisomers. (D) U-2 OS cells treated with P11 atropisomers and 0.0125 J/cm^2. (E,F) 4T1 and CT26 cells treated with P11 atropisomers and 0.05 J/cm^2. Dose-response curves indicate the mean ± SEM of 2 - 3 independent experiments. Statistical significance was evaluated using two-way ANOVA *versus* the α_4 atropisomer, * $p < 0.05$, ** $p < 0.01$ and *** $p < 0.001$.

U-2 OS cells demonstrated the highest sensitivity to treatments (Figure 16). A dose light (0.0125 J/cm^2), lower than that applied to the CT26 and 4T1 cells (0.05 J/cm^2), was required to highlight the different phototoxicities of the P11 atropisomers. Of note, the viability of U-2 OS cells incubated with 1 μM of the αβαβ P11 atropisomer decreased by >90% after treatment with 0.05 J/cm^2. This demonstrated that all the atropisomeric forms can efficiently destroy the target cancer. However, different concentrations and light doses

may be required. The photophysical and photochemical properties of redaporfin atropisomers were not sufficient to explain the differential phototoxicity, but it was noted that their order of phototoxicity was the same as atropisomer RP-HPLC retention times.

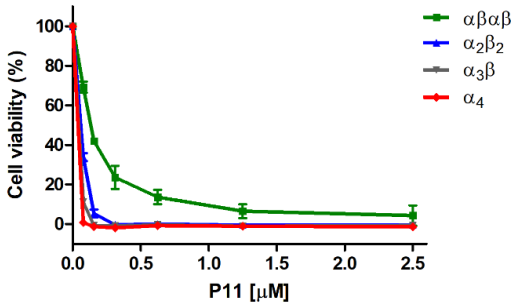

Figure 16. P11 atropisomer phototoxicity in U-2 OS cells. DL = 0.05 J/cm^2. Results indicate mean ± Standard Deviation (SD) of a single representative experiment. Statistical significance was evaluated using two-way ANOVA *versus* the α_4 atropisomer, no symbol $p > 0.05$.

2.4.4 Redaporfin atropisomers differ in their ability to passively diffuse across cell membranes

The contrast between similar photochemical behavior and differential phototoxicity of redaporfin atropisomers prompted us to investigate *in vitro* atropisomer activity in detail. Fluorescence microscopy showed that α_4 had a higher fluorescence intensity in U-2 OS cells after 24 h of incubation, followed by $\alpha_3\beta$, $\alpha_2\beta_2$ and finally by $\alpha\beta\alpha\beta$ (Figure 17A). The kinetics of cell uptake were followed by flow cytometry at fixed incubation periods (2, 4, 8, 16, and 24 h) with the atropisomers (Figure 17B-G). Uptake of all atropisomers increased over time but their relative intracellular concentrations maintained the same trend: $\alpha_4 > \alpha_3\beta > \alpha_2\beta_2 > \alpha\beta\alpha\beta$.

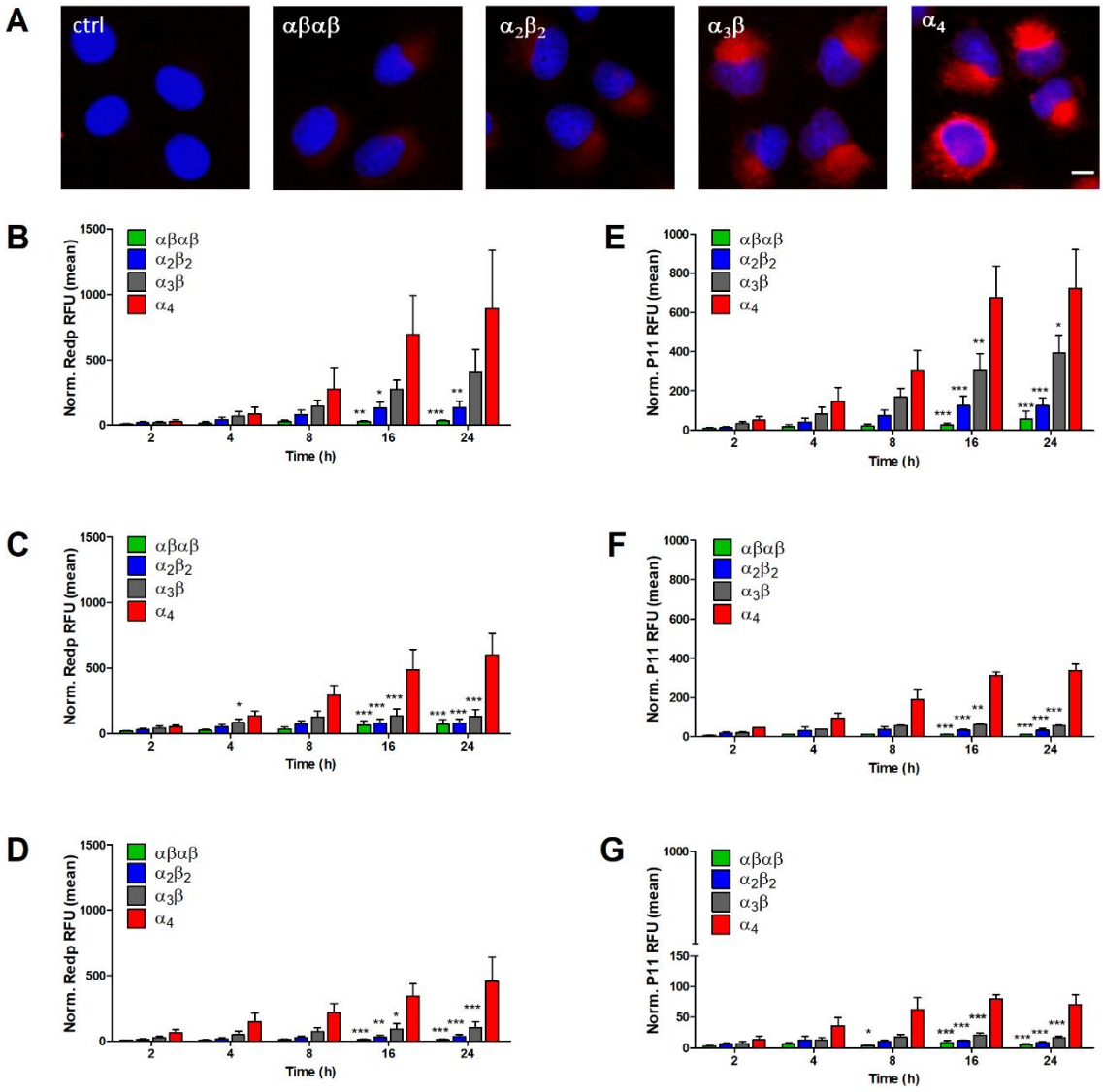

Figure 17. Cell uptake of redaporfin and P11 atropisomers at different incubation times. (A) Fluorescence from U-2 OS cells incubated with redaporfin atropisomers (red) for 24 h followed by nucleus staining with DAPI (blue); scale bar = 10 µm. (B-D) Cellular internalization of redaporfin atropisomers evaluated by flow cytometry at the indicated time points in U-2 OS, 4T1 and CT26 cells. (E-G) Cellular internalization of P11 atropisomers evaluated by flow cytometry at the indicated time points in U-2 OS, 4T1 and CT26 cells; bars indicate the mean ± SEM of 2 - 3 independent experiments; the fluorescence signal from treated cells was normalized to the untreated cells. Statistical significance was evaluated using two-way ANOVA *versus* the α_4 atropisomer, * $p < 0.05$, ** $p < 0.01$ and *** $p < 0.001$.

The order of increasing cell uptake in Figure 17 was the same as the order of phototoxicity in Figure 15. Moreover, U-2 OS cells exhibited the highest levels of atropisomer internalization (Figure 17B, E) and were the cells that also experienced greatest response to PDT (Figure 15A, D). Conversely, CT26 cells showed the lowest internalization of the

atropisomers (Figure 17D, G) and were more difficult to treat with PDT (Figure 15C,F). The pattern of varied uptake was validated using an alternative method based on the lysis of cells, pre-incubated with the atropisomers for 24 h. Measurement of redaporfin or P11 fluorescence from the supernatant of cells confirmed the order of atropisomer internalization (Figure 18).

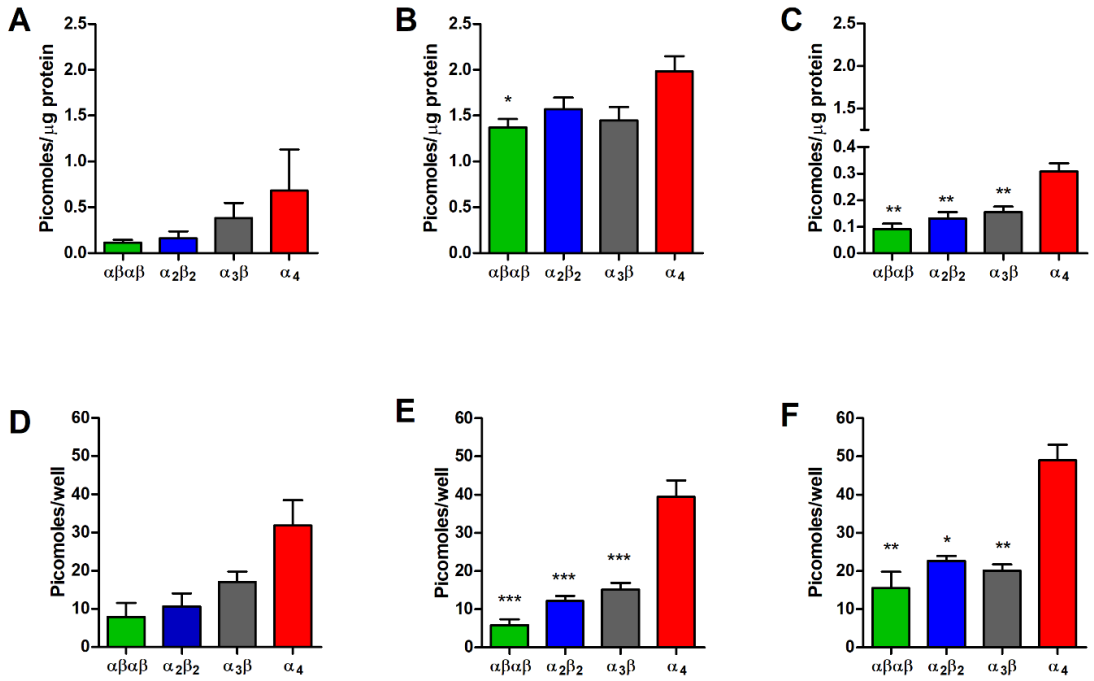

Figure 18. Quantification of redaporfin and P11 atropisomers in the supernatant of cancer cells. Cancer cells were incubated with redaporfin or P11 atropisomers for 24 h followed by cell lysis. Quantification of redaporfin atropisomers was inferred by redaporfin fluorescence on the supernatant of (A) U-2 OS, (B) 4T1 and (C) CT26 cells. Similarly, P11 atropisomers were also quantified on the supernatant of (D) U-2 OS, (E) 4T1 and (F) CT26 cells. Bars indicate the mean ± SEM of 2 - 3 independent experiments. Statistical significance was evaluated using one-way ANOVA *versus* the α_4 atropisomer, * $p < 0.05$ ** $p < 0.01$ and *** $p < 0.001$.

Assessment of the uptake of the atropisomers by fluorescence microscopy (Figure 17A) indicated that the pattern of atropisomer intracellular distribution was very similar to that reported for redaporfin, suggesting tropism for the ER and GA compartments.[99-100] This was further confirmed with P11 as all atropisomers demonstrated fluorescence overlap with GFP-CALR expressed in the ER and GFP-GALT1 expressed in the Golgi (Figure 19). Atropisomer cell uptake clearly varied but upon cytosolic delivery, the intracellular targets reached did not.

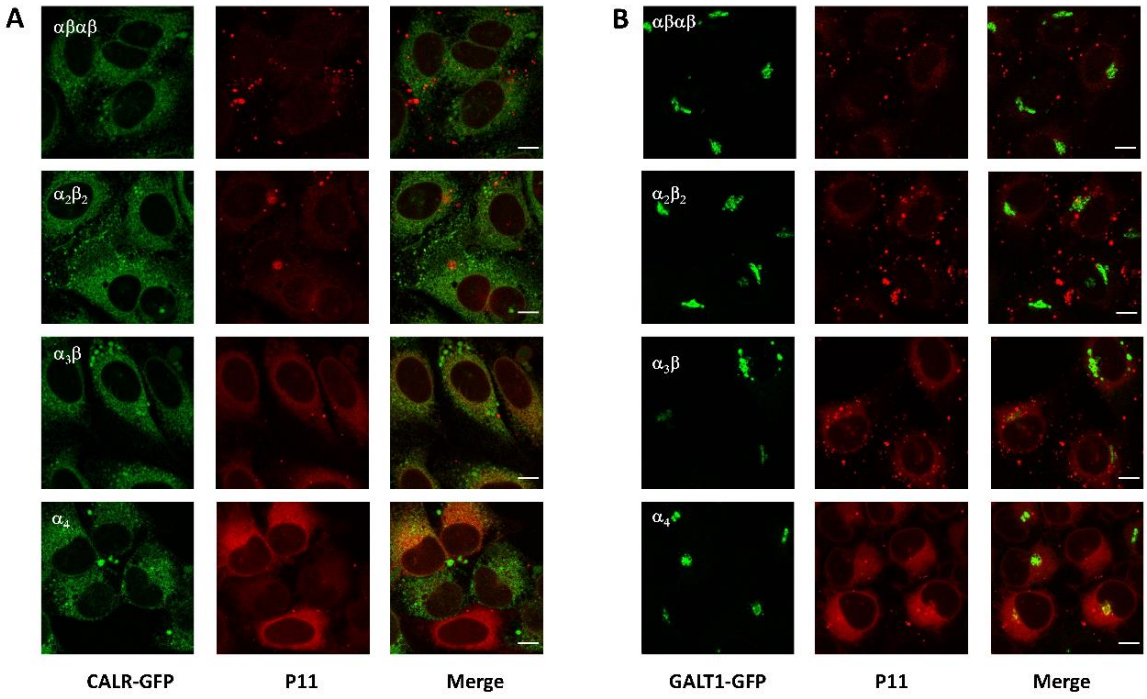

Figure 19. P11 atropisomers preferentially accumulated at the endoplasmic reticulum and Golgi compartments. Representative images of the co-localization of P11 atropisomers (red) with markers of (A) the endoplasmic reticulum (CALR-GFP) and (B) Golgi apparatus (GALT1-GFP) in U-2 OS cells. For each experiment, 10 µM of each atropisomers were used and images were acquired using the same settings. Brightness and contrast were adjusted using Image-J varying degrees for each atropisomer to visualize subcellular targeting. Scale bar represents 10 µm.

These results show that the phototoxicities of redaporfin and P11 atropisomers are directly related with the efficiency of cell uptake. Thus, differential phototoxicity of atropisomers can be explained through understanding the differential uptake of the atropisomers; specifically, why α_4 has enhanced internalization by the cells relative to αβαβ. Notably, the order of retention in RP-HPLC is the same as the order of atropisomer cell uptake. For example, α_4 demonstrated highest affinity to the column as well as enhanced internalization. The photophysical properties of redaporfin atropisomers did not vary to an extent which would suggest different phototoxicities *in vitro*. Varied biological activity of atropisomers is typically associated with differential target selectivity. Isomerism is generally overlooked in PDT as the action of a PS is primarily dependent on its interaction with molecular oxygen and light.[1] This was observed with verteporfin, a PS mixture of regioisomers.[210] It is only more recently that structural isomers of new PS candidates are being investigated with changes in photosensitizing potential observed between

isomers.[77,79,187,232] However, atropisomers, which arise only due to varied rotation of PS substituents, continue to lack extensive study.

The first report on the photosensitizing ability of 5,10,15,20-tetrakis(*o*-acetamidophenyl)porphyrin atropisomers did not identify differences between atropisomers,[185] but such differences later became evident with more lipophilic 5,10,15,20-tetrakis(*o*-propionamidophenyl)porphyrin atropisomers with varied chain lengths.[186] Despite the similar photophysical and photochemical behavior of the porphyrin atropisomers, they were shown to inhibit the activity of the mitochondrial enzymes, succinate dehydrogenase and cytochrome c oxidase differently. The *in vitro* potency of enzyme inhibition decreased in order $\alpha_4 > \alpha_3\beta > \alpha_2\beta_2 > \alpha\beta\alpha\beta$ and the porphyrins with smaller alkyl chain (C_2 and C_3) were more potent PSs. Additionally, smaller differences between the atropisomer activities were observed for the porphyrins with the longest alkyl chain (C_6). The photosensitizing abilities of the atropisomers of these "picket fence" porphyrins were correlated with their retention in silica gel, $\alpha_4 > \alpha_3\beta > \alpha_2\beta_2 > \alpha\beta\alpha\beta$, which aligns with our findings. However, the data was interpreted in terms of propensity for monomeric solubility in aqueous solution rather than on the basis of molecular shape.[186]

With cellular internalization identified as the likely cause of varied atropisomer efficacy *in vitro*, the manner in which atropisomers were internalized was investigated. The lipophilicity of PSs is widely accepted to correlate with PS ability to diffuse across cell membranes and, consequently, to affect PDT efficacy.[85,233-235] The higher $LogP_{OW}$ of $\alpha_3\beta$ and α_4 (Table 2) may have facilitated the interactions of these atropisomers with cell membranes but does not explain the superiority of α_4 compared to $\alpha_3\beta$. Additionally, $\alpha_2\beta_2$ exhibited higher uptake than $\alpha\beta\alpha\beta$ although they have similar $LogP_{OW}$. In contrast, P11 and its $\alpha_3\beta$ atropisomer had similar uptakes, despite their different $LogP_{OW}$ (Figure 20).[97] However, this can be attributed to the fact that more than 50% of redaporfin is the $\alpha_3\beta$ atropisomer.

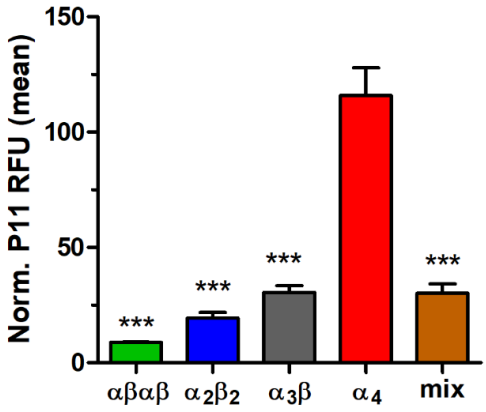

Figure 20. Cellular internalization of P11 atropisomers and P11 drug mixture. 4T1 cells were incubated with the indicated atropisomers for 24 h and cellular internalization was evaluated by flow cytometry. Bars indicate the mean ± SEM of 3 independent experiments. Fluorescence signal from treated cells was normalized to the untreated cells. Statistical significance was evaluated using two-way ANOVA *versus* the α_4 atropisomer, * $p < 0.05$ ** $p < 0.01$ and *** $p < 0.001$.

Another factor that may interfere with PDT efficacy of weakly soluble tetrapyrrole PSs is a tendency to self-aggregate.[69] Planar macrocycles aggregate via strong interactions between adjacent π systems. Aggregated porphyrin derivatives have lower absorbance, lower fluorescence, shorter triplet lifetime and lower singlet oxygen quantum yield. The interaction with the cell membranes and the mechanisms of cellular internalization are also different between aggregates and monomers.[236] Therefore, self-aggregation of atropisomers may impact their performance.[235] P11 atropisomers were investigated in water with 0.4% DMSO. The absorbance (Figure 21A) and emission (Figure 21B-D) spectra of all atropisomers were similarly quenched and broadened when compared to the molecules in pure DMSO. The fluorescence in DMSO/water was shifted in the same proportion for all atropisomers. In particular, the emission spectra of αβαβ and α_4 had similar bathochromic shifts (Figure 21C,D). This data indicated that atropisomer self-aggregation cannot explain the differences observed in atropisomer cell uptake.

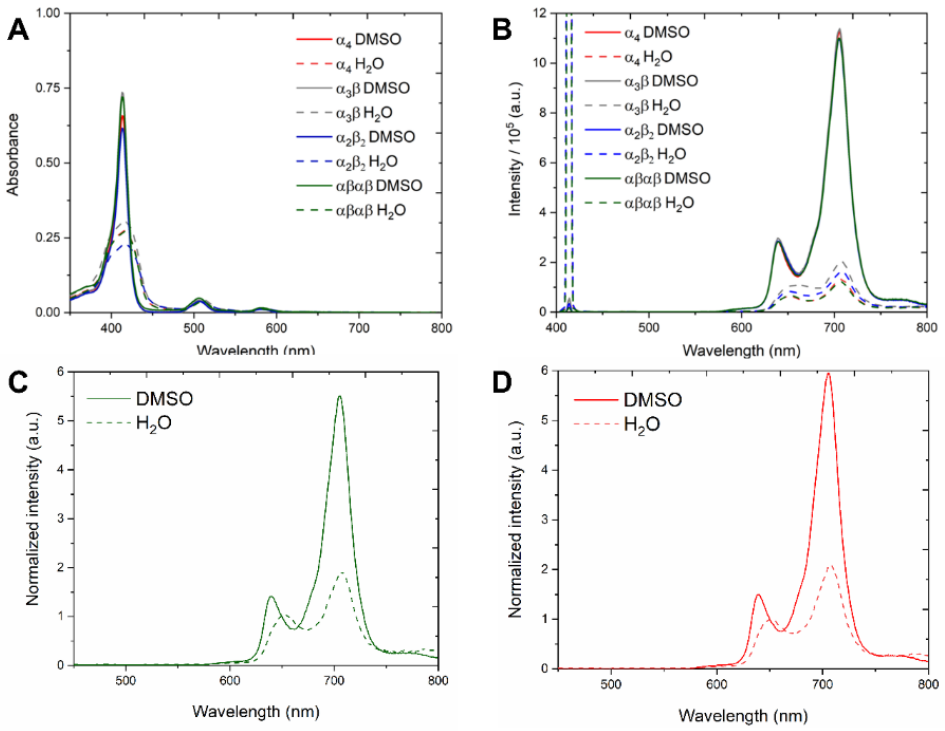

Figure 21. P11 atropisomers aggregated similarly in aqueous solution. Steady state characterization or P11 atropisomers in H_2O (with < 1% DMSO). (A) Absorption spectra and (B) emission spectra of P11 atropisomers. Atropisomers (C) αβαβ and (D) α_4 emission spectra normalized to peak maxima at 605 nm.

Next, we investigated the mechanism of atropisomer cell internalization to obtain a better insight into α_4 enhanced uptake and PDT efficacy. Cell uptake rates, which increase dramatically with temperature above 20 °C, are commonly associated with an active mechanism of transport requiring energy such as endocytosis.[237] Endocytosis tends to be inhibited at 4 °C,[238] and Figure 22A shows that atropisomer cell uptake was significantly reduced, but not entirely suppressed, at 4 °C in comparison to 37 °C after 4 h of incubation. Passive permeation of the membrane is also dependent on the temperature, as octanol-water partition coefficients are influenced by temperature.[233] Therefore, to clarify whether atropisomer uptake was an active or passive process, we conducted uptake studies with depletion of ATP by means of 2-deoxy-D-glucose.[233,239] Our results showed that partial depletion of ATP (Figure S 7A) had no significant impact on the uptake of all P11 atropisomers (Figure 22B); whereas, in the same conditions, inhibition of the recombinant GFP cell uptake (known to be energy dependent)[240] was observed (Figure S 7B). Thus, passive diffusion of the atropisomers, and in particular of α_4, along a concentration gradient is the main mechanism responsible for the enhanced cell internalization.

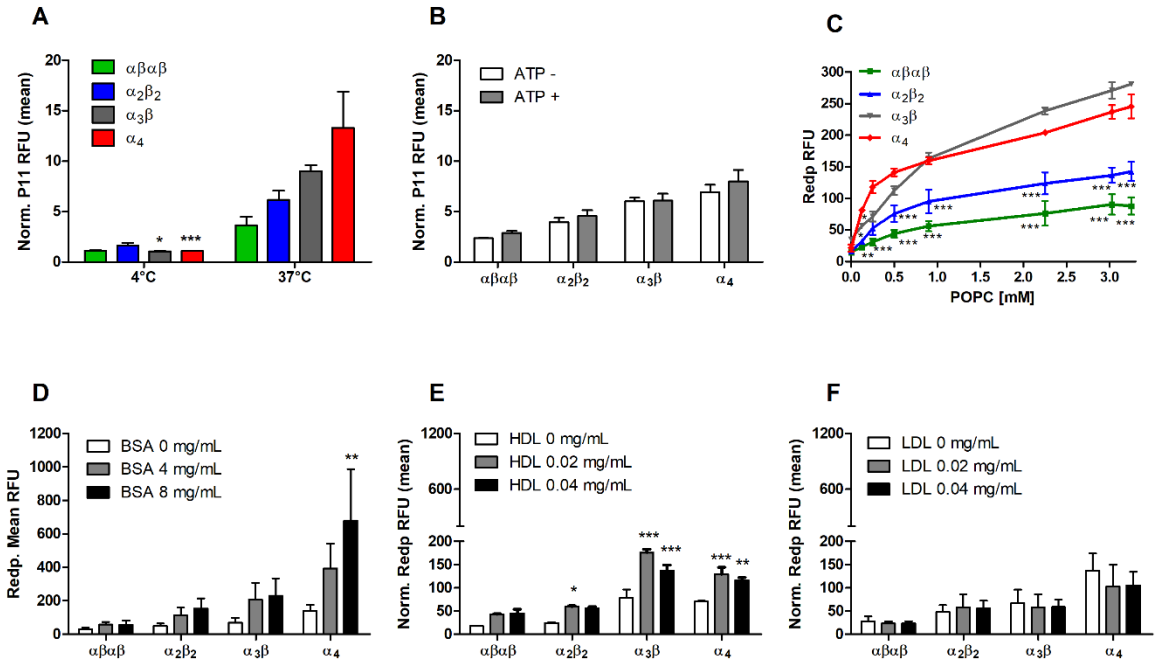

Figure 22. Mechanism of atropisomer internalization in 4T1 cells. (A) P11 atropisomers (2.5 µM) incubated for 4 h at 4 °C or 37 °C, or (B) incubated for 2 h upon ATP depletion; bars indicate the mean ± SEM of 2 or 3 independent experiments. (C) Fluorescence of redaporfin atropisomers (5 µM) after 20 min incubation with various concentration of POPC liposomes; each point is mean ± SEM of 2 independent experiments; statistical significance was evaluated using two-way ANOVA *versus* the α_4 atropisomer, * $p < 0.05$ ** $p < 0.01$ and *** $p < 0.001$. (D-F) Internalization of redaporfin atropisomers evaluated following co-incubation for 4 h with serum proteins (D) BSA, (E) HDL or (F) LDL; bars indicate the mean ± SEM of 3 independent experiments. Statistical significance was evaluated *versus* the absence of serum using two-way ANOVA * $p < 0.05$ ** $p < 0.01$ and *** $p < 0.001$.

Liposomes are useful models to predict the interactions of molecules with the cell membranes.[235,241] We incubated redaporfin atropisomers with increasing concentrations of POPC liposomes in PBS and measured atropisomer fluorescence intensities (Figure 22C) as an indicator of their interactions with phospholipid bilayer membranes. A stronger interaction will lead to more atropisomer present in the membrane where the molecules can disaggregate and yield monomers, which emit stronger fluorescence. The strong fluorescence of the α_4 atropisomer with small quantities of liposomes demonstrated that it interacted strongly with the membrane and disaggregates. It is very improbable that the atropisomers moved from the bilayer membrane of the liposome to its aqueous compartment. This was not the case in cell uptake where the atropisomer may have bound to lipophilic domains inside the cell and accumulated there. The increased cell uptake of α_4

can be understood on the basis of a strong affinity to phospholipid bilayer membranes, followed by fast crossing of the membrane and accumulation in the interior of the cell. The low uptake of αβαβ is clearly related to its weak interaction with lipidic membranes, at least to form fluorescent monomers. The results with low POPC concentrations were entirely consistent with the observed cell uptake. At high POPC concentrations, the $\alpha_3\beta$ atropisomer eventually becomes the most fluorescent atropisomer and the order of atropisomer incorporation in liposomes follows their $LogP_{OW}$ values. This is consistent with an approach to bulk properties when large POPC concentrations are present.

The interaction of PSs with plasma proteins may alter cellular internalization; for example, by inhibiting passive diffusion and facilitating endocytic uptake. We investigated the impact of BSA, HDL and LDL on atropisomer cellular uptake to identify challenges in the transfer from *in vitro* to *in vivo* studies. BSA and HDL (but not LDL) indistinctly enhanced the level of uptake for all atropisomers (Figure 22C-D). Similar results have been described for other PSs. For instance, LDL impaired porfimer sodium uptake, whereas BSA and HDL enhanced the cellular internalization of padeliporfin and temoporfin.[92,242-243] Our results show that the presence of these plasma proteins introduces very minor changes in the pattern of membrane interaction identified for redaporfin atropisomers.

Evaluated together, RP-HPLC retention times, differential phototoxicity, interaction with small quantities of liposomes and cell uptake with the depletion of ATP, indicate that differential redaporfin atropisomer internalization by cells is essentially a passive process. It is strongly dependent on individual interactions between the atropisomer configuration and the phospholipid bilayer. Although redaporfin is a large molecule, cell uptake of its α_4 atropisomer is fast and efficient *in vitro*. In view of the lack of specificity of plasma proteins in cell uptake, varying atropisomer tumor uptake should also be observed *in vivo*.

2.4.5 *In vivo* tumor accumulation of redaporfin atropisomers

Following evaluation of how redaporfin (and its related porphyrin) atropisomers interact differently with cell membranes *in vitro*, our studies turned to understand whether the same occurs at the *in vivo* level. The poor water solubility of redaporfin and P11 atropisomers required the use of Kolliphor®EL-based formulations for intravenous administration. A formulation similar to that in clinical use for redaporfin (atropisomer mixture) was prepared, although a slightly higher Kolliphor®EL content (0.5%, v/v) was required for individual atropisomers relative to the 0.2%, (v/v) used for redaporfin mixture.[101] The

isolated atropisomers were more difficult to solubilize than their mixture, likely due to stronger crystal packing forces. A further increase of Kolliphor®EL to 2 % (v/v) was required to formulate P11 atropisomers, as the porphyrins showed lower solubility. Although Kolliphor®EL contents are different in these formulations, dynamic light scattering revealed that the micelles have similar relative sizes, ranging from 13 nm to 25 nm (Table 4). Studies of cellular internalization and phototoxicity conducted with redaporfin atropisomers formulated in Kolliphor®EL maintained the differential uptake and phototoxicity profile, previously described for the unformulated atropisomeric forms (Figure 23A,B).

Table 4. Dynamic light scattering results for the Kolliphor®EL formulations employed for redaporfin and P11 atropisomers. The relative average size (z-average) of the redaporfin (saline : EtOH : Kolliphor®EL, 98.5 : 1 : 0.5% v/v) and P11 (saline : DMSO : Kolliphor®EL, 97 : 1: 2% v/v) micelle size in formulations indicated. Prepared on day of injection.

Atropisomer	Redp. Z average (nm)	P11 Z average (nm)
αβαβ	13.2 ± 0.2	14.3 ± 0.1
$\alpha_2\beta_2$	19.9 ± 6.3	13.2 ± 0.2
$\alpha_3\beta$	19.0 ± 7.9	23.8 ± 1.8
α_4	23.03 ± 3.2	18.1 ± 5.9

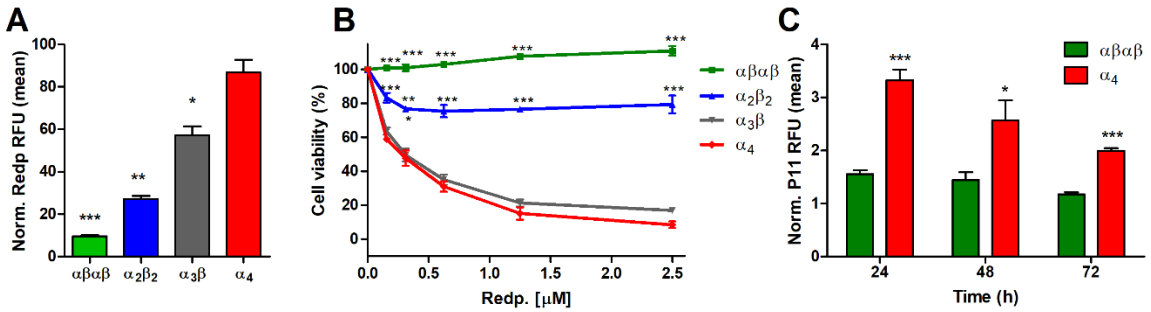

Figure 23. Atropisomer micelle formulation cell-internalization. (A) Cellular internalization of redaporfin atropisomers *in vitro* formulated in Kolliphor®EL assessed by flow cytometry after 24 h of incubation with 4T1 cells. Bars indicate mean ± SEM of 2 independent experiments, the statistical significance was evaluated using two-way ANOVA *versus* the α_4 atropisomer. (B) Phototoxicities of redaporfin atropisomers (formulated in Kolliphor®EL) *in vitro* upon illumination at 740 nm (0.2 J/cm^2) after 24 h of incubation with 4T1 cells; statistical significance was evaluated using two-way ANOVA

versus the α_4 atropisomer (C) Level of internalization of α_4 and $\alpha\beta\alpha\beta$ P11 atropisomers in single cell suspensions obtained from CT26 tumors on female BALB/c at the indicated timepoints after i.v. administration, measured by flow cytometry; bars indicate in the mean ± SEM of 4-5 mice, the fluorescence signal from treated cells was normalized to the untreated cells. Significance level of the difference between the two atropisomers was evaluated via unpaired t-test, * $p < 0.05$ ** $p < 0.01$ and *** $p < 0.001$.

To establish whether this was also the case *in vivo*, the differential accumulation of P11 atropisomers was studied following intravenous (i.v.) administration of the 2% (v/v) Kolliphor®EL formulation in mice bearing CT26 subcutaneous tumors. Intravenous injection was followed, after appropriate times, by tumor excision and preparation of single cell suspensions which were submitted to P11 fluorescence detection by flow cytometry. We selected α_4 and $\alpha\beta\alpha\beta$ atropisomers for this comparison in view of their differences *in vitro*. The highest signal for both atropisomers was observed 24 h post administration, although significant internalization was still detected at 72 h (Figure 23C). Of note, significantly higher α_4 internalization into the tumor cells, relative to $\alpha\beta\alpha\beta$, was revealed at all time points. These observations aligned with the results previously obtained *in vitro*, thus, confirming the superiority of α_4 to penetrate across cell membranes. The orientation of the aryl sulfonamide groups present in these conformers has profound implications in tumor cell uptake *in vitro* and *in vivo*.

2.4.6 Optimization of redaporfin α_4-PDT for CT26 subcutaneous tumor model *in vivo*

PDT is ideally suited to evaluate the impact of differential atropisomer uptake by tumor cells. The drug-to-light interval (DLI) between the administration of the PS and the illumination of the target tissue determines whether the therapeutic effect results from ROS outside the cells (short DLI) or inside the cells (long DLI). At DLI = 0.25 h, the PS circulates in the vasculature and is, therefore, described as vascular-PDT. Using DLI ≥ 24 h, the PS has adequate time to accumulate at the tumor and be internalized by tumor cells, an approach which is termed cellular-PDT.[234] In view of the data presented in this chapter, an effect of differential atropisomer uptake in vascular-PDT would not be anticipated. In cellular-PDT, however, α_4 should prove superior, and $\alpha\beta\alpha\beta$ inferior, to the other atropisomers.

Preliminary optimization of cellular-PDT protocols to compare atropisomer therapeutic outcome *in vivo* was necessary. Screening of drug and light doses was carried out with the

redaporfin α_4 atropisomer due to the enhanced phototoxicity indicated by *in vitro* data. Selection of conditions was informed by previous work of Rocha et al.[40] which led to the pre-clinical optimization of the redaporfin mixture. The best PDT outcome was reported with a shorter DLI, specifically 0.25 h, which led vascular-PDT (0.75 mg, 50 J/cm^2) selection as providing preferable conditions. Some success was observed with DLI = 72 h, where one protocol with high redaporfin dose (1.5 mg/kg) led to 17% efficacy.[40] A DLI of 72 h was included in cellular-PDT screening alongside 24 h. DLI = 24 h was also selected as it was observed to be the timepoint of highest redaporfin cellular internalization (Figure 23C). BALB/c mice bearing CT26 tumors with a targeted minimum diameter of 5 mm were treated. The protocol screening conditions are presented in Table 5. PDT impact was determined from a visual assessment of tumor edema and necrosis and scored as: no effect = 0, low = 1, moderate = 2, high = 3.

Table 5. PDT parameters tested for CT26 model with redaporfin α4. Drug and light doses were tested to obtain the best outcome in terms of impact on treatment. n refers to number of mice per group. Survival to PDT refers to first 72 h of treatment. F-female, M-male. Laser fluence (137 mW/cm^2) and irradiation area (1.33 cm^2) were kept constant between all the tested protocols.

Prot.	DLI	PS dose (mg/kg)	Light dose (J/cm^2)	BALB/c Sex	n	Survival to PDT	PDT impact factor	
							Edema	Necrosis
1	24	0.30	50	F/M	4	100	2	1
2	24	0.30	60	F	2	100	2	1
3	24	0.30	70	F	1	100	2	1
4	24	0.30	80	F	2	100	1	1
5	24	0.35	50	F/M	12	100	2	1
6	24	0.35	60	F	1	100	2	1
7	24	0.35	70	F	3	100	2	1
8	24	0.40	50	F	3	100	2	1
9	24	0.40	60	F	2	0	-	-
10	24	0.45	50	M	2	50	2	1
11	24	0.50	40	M	1	100	0	0
12	24	0.50	60	F	1	100	2	2
13	24	0.60	60	F	2	0	-	-
14	24	0.75	70	F	2	0	-	-
15	48	0.80	70	F	1	100	2	1
16	72	0.50	85	F	2	100	2	1
17	72	0.60	85	M	2	100	2	1
18	72	0.65	85	F	2	0	-	-
19	72	0.70	75	F	2	100	2	1
20	72	0.70	85	F	1	0	-	-
21	72	0.75	80	F	2	0	-	-
22	72	0.80	75	F	4	75	1	1
23	72	0.80	85	F	1	100	1	2
24	72	0.80	90	F	1	0	-	-
25	72	0.90	75	F	3	33	1	2
26	72	1.00	75	F	2	50	2	2

Whilst significant regression of tumor growth was observed with α_4 cellular-PDT, it was not possible to completely eradicate tumor growth in any mice following the protocols presented in Table 5. An early indication that the α_4 atropisomer displayed higher toxicity *in vivo,* in comparison to the redaporfin mixture, was the onset of PDT induced lethality using lower doses than those employed by Rocha et al.[40] For protocols where all animals survived PDT treatment, a mild tumor response was observed in the immediate aftermath of treatment, with the full effect only visible at 48 - 72 h post treatment. Similar to what was previously observed with redaporfin cellular-PDT, moderate edema was apparent with regions of necrosis restricted to the tumor only.[97]

Dosimetry for cellular-PDT was limited by a low therapeutic index. This was particularly the case with a DLI = 24 h as 0.35 mg/kg and 70 J/cm^2 were the maximum conditions tolerated by a group (protocol 7, Table 5) prior to the onset of lethality. Higher doses were safe at a longer DLI (72 h) with up to 0.60 mg and 85 J/cm^2 tolerated (protocol 17, Table 5). While some promising eschar formation led to moderate survival times, higher than for control animals, mild irritation/erythema were observed which at times caused the effect to be unclear. This was common issue which led to the high number of protocols investigated as there was a lack of consistency in the effect observed. The timing of i.v. injections to ensure irradiation of tumors which did not exceed 5 mm maximum diameter in size was challenging and likely contributed to variability This favored the choice of DLI = 24 h to compare atropisomers. It was also beneficial due to the lower amount of PS required. Screening led to the combination of 0.35 mg/kg PS dose with a light dose of 60 J/cm^2 (protocol 6, Table 5) to compare atropisomer cellular-PDT efficacy. Insignificant difference in efficacy was observed between protocol 6 and protocol 7 which employed 70 J/cm^2. This indicated that photobleaching might start to occur for a PS dose of 0.35 mg/kg beyond 60 J/cm^2, when a DLI = 24 h is employed.

Optimization of conditions to evaluate atropisomer vascular-PDT of CT26 tumors required less screening than for cellular-PDT. Redaporfin vascular-PDT has been previously shown to demonstrate much higher efficacy than cellular-PDT,[40,212] and the clinical translation of redaporfin to the treatment of advanced head and neck cancer employs vascular-PDT.[94] However, related lipophilic PSs demonstrate enhanced efficiency in cellular-PDT protocols.[234] Vascular-PDT produces a strong and selective destruction of the tumor blood vessels and is associated with extensive edema and necrosis.[40] In comparison, cellular-PDT facilitates optimal distribution of the compound in cellular compartments, with therapeutic

outcome dependent on PS cellular localization.[34] Screening of vascular-PDT in female BALB/c mice bearing implanted CT26 tumors with the α_4 atropisomer, using DLI = 15 min, led to the combination of 0.45 mg/kg with 40 J/cm^2 to obtain ~100% cures without lethality. One protocol with a marginally higher PS dose, 0.50 mg/kg and 40 J/cm^2, resulted in lethality. When the PS dose was reduced to 0.35 mg/kg, only 50% cures were obtained. Therefore, PS dose 0.45 mg/kg and light dose 40 J/cm^2, were selected as the most promising conditions for vascular-PDT and also deemed suitable to compare the atropisomers.

The comparatively lower efficacy of α_4 cellular-PDT relative to vascular-PDT may be partly attributed to the limited tumor specificity of redaporfin. Cellular-PDT protocols for redaporfin present an unfavorable biodistribution which means that if a higher PS dose is used, results may be lethal due to irradiation of neighboring organs. The redaporfin concentration at the tumor with cellular-PDT is comparatively lower than for vascular-PDT and insufficient to achieve tumor elimination.[212] Tumor cures were not necessary to investigate the differential atropisomer effect for cellular-PDT. However, to fully exploit benefit of enhanced α_4 internalization for cellular-PDT, *in vivo*, optimization in a larger animal model will be required. Cell lines U2-OS (Figure 17B) and B16-F10 (Figure S 8C) displayed higher internalization of α_4. A 3- and 2-fold increase in α_4 internalization was observed in comparison to CT26, resulting in greater sensitivity to PDT (Figure 15A,D and Figure S 8A,B). Potentially, these may be more suitable candidates to observe efficacious redaporfin α_4 cellular-PDT.

2.4.7 Impact of differential atropisomer tumor uptake on PDT efficacy *in vivo*

With conditions optimized to evaluate atropisomer cellular-PDT *in vivo*, the combination of 0.35 mg/kg of redaporfin atropisomer with a light dose of 60 J/cm^2 was applied with all atropisomers to treat BALB/c female mice with subcutaneous CT26 tumors with a minimum diameter of 5 mm at the day of treatment (Figure 24).

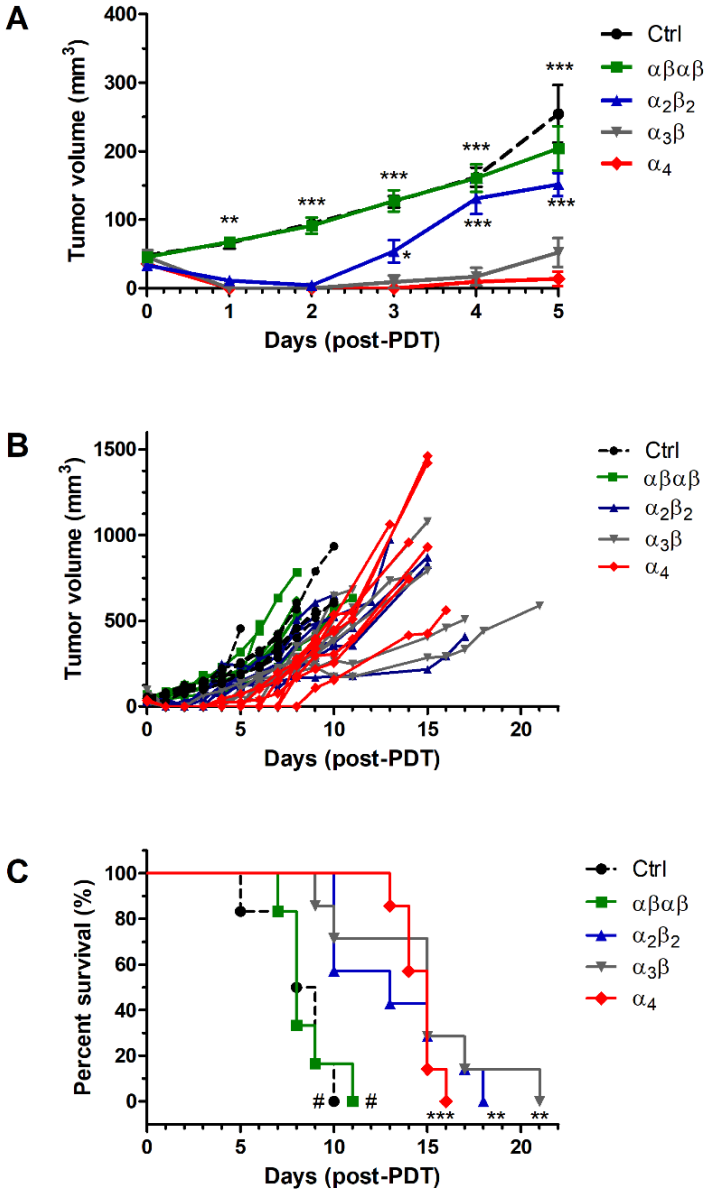

Figure 24. Cellular-PDT (DLI = 24 h) of female BALB/c mice bearing CT26 tumors with 0.35 mg/kg redaporfin atropisomers and 60 J/cm^2 at 750 nm. (A) Tumor volume represented as mean ± SEM five days post-PDT, which corresponds to the time interval where no mouse reached the humane endpoint; significance level *versus* the α_4 atropisomer was evaluated by two-way ANOVA. (B) Tumor volume for each individual mouse until the humane endpoint was reached. (C) Survival curves for treatment groups with 6-7 mice. The significance level between the different treated groups was evaluated by Log-rank (Mantel-Cox) test *versus* Ctrl (* $p < 0.05$ ** $p < 0.01$ and *** $p < 0.001$) or *versus* α_4 (# $p <. 0.001$).

Mice treated with the α_4 atropisomer showed the highest edema with undefined tumor boarders. 24 h post-treatment tumor necrosis was visible. No changes relative to the control (Ctrl) group were observed with the αβαβ atropisomer, whilst $\alpha_2\beta_2$ and $\alpha_3\beta$ induced moderate edema and necrosis within the boundaries of the tumor 24 to 48 h post-PDT (Figure 25). The largest differences in the ability of atropisomers to control tumor growth were observed in the first 5 days post-treatment (Figure 24A,B). Although CT26 tumors regrew after cellular-PDT, overall survival times exhibited statistically significant differences. PDT with α_4 and $\alpha_3\beta$ atropisomers increased median survival to 15 days in comparison to the slightly lower improvement mediated by $\alpha_2\beta_2$ (13.5 days). In contrast, no improvement of the overall median survival was attained with the αβαβ (8 days) compared to the Ctrl group (8.5 days). Comparison of PDT efficacy for each individual atropisomer with the Ctrl group revealed the largest statistical significance for α_4 ($p = 0.0002$), which was in contrast to the αβαβ atropisomer ($p = 0.8549$). The p values of 0.0028 and 0.0017 were obtained for $\alpha_3\beta$ and $\alpha_2\beta_2$, respectively (Figure 24C). Representative images of the tumors are presented in Figure 25. These results verify that the orientation of aryl sulfonamide substituents in redaporfin atropisomers changes their internalization by cells of the tumor microenvironment and, consequently, alters cellular-PDT efficacy.

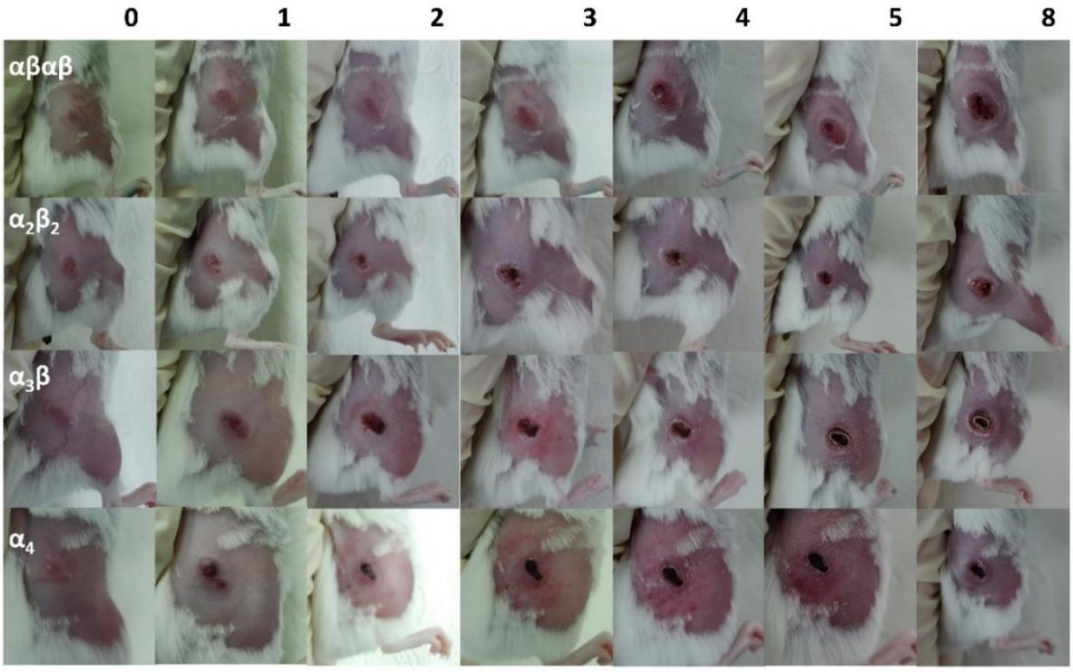

Figure 25. Representative images of CT26 tumors on female BALB/c mice 0-8 days after cellular-PDT with redaporfin atropisomers.

The enhanced cellular-PDT efficacy observed with the α_4 atropisomer prompted assessment of the α_4 sun photosensitivity *in vivo*. Male BALB/c mice were irradiated with a solar simulator, using two light doses following α_4 and redaporfin mixture i.v. administration (Figure 26). Skin erythema observed post α_4 treatment (0.45 mg/kg, DLI = 3 days, 30 min, 300 mW/cm^2) was significantly higher than for the control group (irradiation only). This was not the case for the redaporfin mixture (Figure 26B). Despite this, when the redaporfin mixture was compared to α_4, the visual difference observed between the two treatments (Figure 26E) was not detected as significant by the mexameter used to record the erythema level. Critically, 7 days after α_4 i.v. administration and 30 min exposure to a solar simulator did not elicit any measurable skin reaction. Therefore, similar to the redaporfin mixture,[101] potential clinical application of the α_4 atropisomer for cellular-PDT is unlikely to be inhibited by skin photosensitivity.

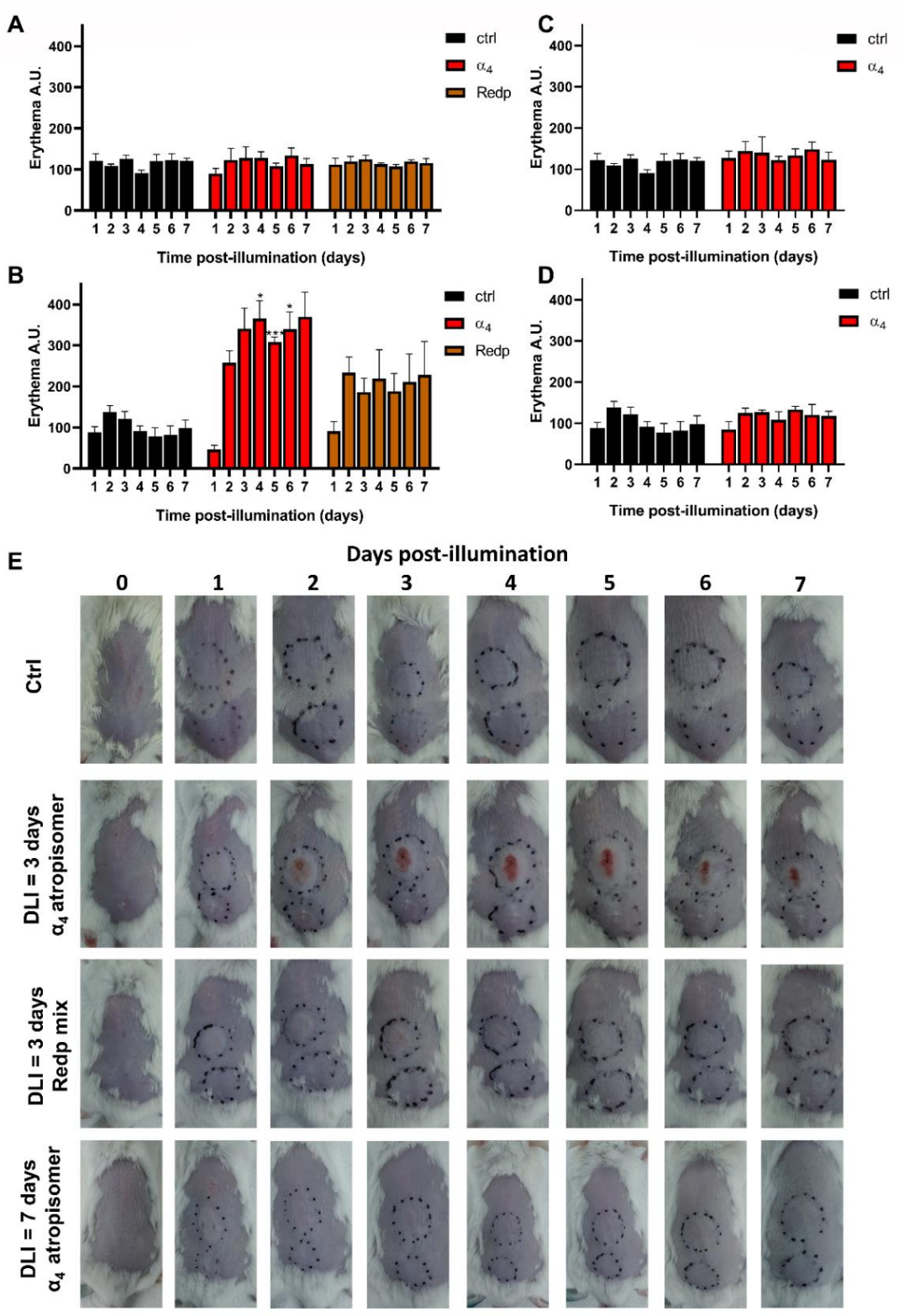

Figure 26. Skin photosensitivity of depilated BALB/c mice after exposition to light from a solar simulator. Skin areas of 0.5 cm^2 were illuminated with (A, C) 90 J/cm^2 or (B, D) 180 J/cm^2 using a solar simulator (A, B) 3 or (C, D) 7 days post-i.v. administration of α_4 or redaporfin mixture (0.45 mg/kg). Erythema was scored using a mexameter. Bars indicate the mean ± SEM of at least 3 mice, the statistical significance was evaluated using

two-way ANOVA. * $p < 0.05$ and *** $p < 0.001$ *versus* Ctrl. (E) Representative images of skin effects on male BALB/c mice after exposition to light from a solar simulator.

Screening of vascular-PDT in female BALB/c mice bearing implanted CT26 tumors with the α_4 atropisomer, using DLI = 15 min, led to the combination of 0.45 mg/kg with 40 J/cm^2 chosen for application with all atropisomers. Although conditions appeared safe when tested with a small number of mice (n = 3), vascular-PDT with α_4 and $\alpha_3\beta$ displayed toxicity within the first 72 h of treatment, with the death of one animal from each group (included in the Kaplan-Meier analysis, Figure 27A). Cures (between 60% to 100 %) were observed in all treatment groups. Tumors regrew in two animals of the αβαβ and α_4 groups. As anticipated, the overall impact of atropisomeric configuration on vascular-PDT efficacy was not statistically significant (Figure 27A,B). In order to confirm this result in the absence of PDT induced lethality, male BALB/c mice bearing CT26 tumors were treated under the same conditions using αβαβ and α_4 atropisomers (Figure 27C,D). The higher weight of male BALB/c improved the tolerance to PDT when the same size tumors and drug and light doses were employed. 100% cures were obtained with male mice treated with α_4, whilst one mouse from the αβαβ group experienced tumor regrowth. This difference between α_4 and αβαβ groups was not statistically significant. Vascular-PDT data confirmed that the similarity of the photophysical and photochemical properties of the different atropisomers leads to similar therapeutic outcomes when cellular uptake is not relevant.

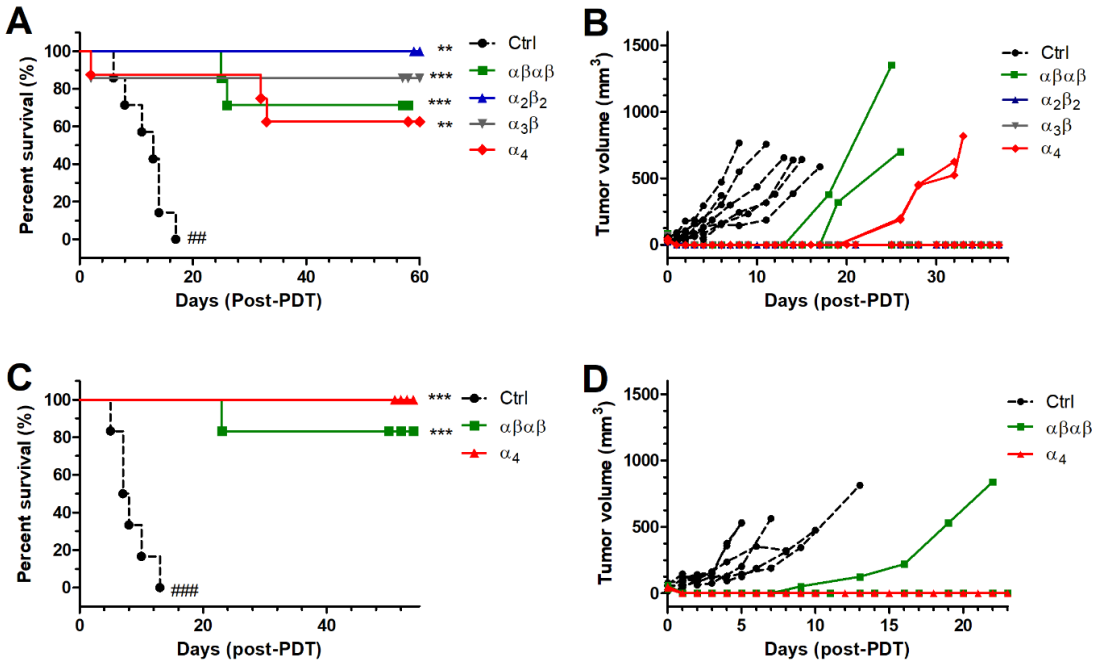

Figure 27. Vascular-PDT (DLI = 15 min) of BALB/c mice bearing CT26 tumors with 0.45 mg/kg redaporfin atropisomers and 40 J/cm^2 at 750 nm. (A) Survival curves for treatment groups with 6-8 female mice. (B) Tumor volume for each individual female mouse until the endpoint was reached. (C) Survival curves for treatment groups with 6-8 male mice. (D) Tumor volume for each individual male mouse until the endpoint was reached. The significance level between the different treated groups was evaluated by Log-rank (Mantel-Cox) test *versus* Ctrl (* $p < 0.05$, ** $p < 0.01$ and *** $p < 0.001$) or *versus* α_4 (## $p < 0.01$, and ### $p < 0.001$).

One important property of photoactivated redaporfin drug mixture in the vascular compartment is its ability to trigger anti-tumor immunity with immunological memory.[40] To evaluate if the atropisomers were contributing differently to the immunological properties of redaporfin, the cured mice (both female and male) mentioned above were subjected to re-challenge with CT26 cells 6 weeks post-PDT. Significant tumor rejection was observed for all atropisomers without major differences between them (Figure 28). This indicated that the immune response after vascular-PDT was not atropisomer specific.

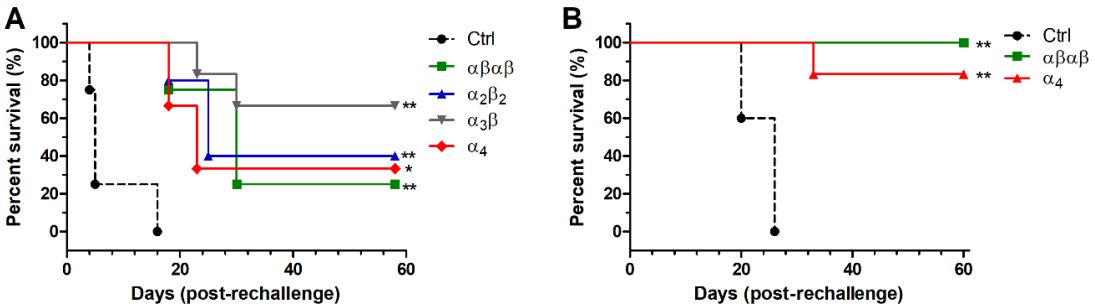

Figure 28. Immunological memory was identical for redaporfin atropisomers following vascular-PDT treatment. Tumor protection was observed following tumor re-challenge of (A) female BALB/c mice (at least n = 3) and (B) male BALB/c mice (at least n = 5) that remain tumor-free for 60 days after vascular-PDT. Significance level was evaluated by Log-rank (Mantel-Cox) test, *versus* Ctrl mice, * $p < 0.05$ and ** $p < 0.01$.

2.4.8 The consequences of enhanced α_4 internalization for PDT efficacy

The enhanced α_4 tumor cell-internalization for PDT efficacy supports a new motif suitable for the rational design of large molecules to experience higher cellular uptake. This work demonstrated that redaporfin atropisomers: (i) have the same order of retention times in normal phase silica gel and in reverse phase-HPLC, $\alpha_4 > \alpha_3\beta > \alpha_2\beta_2 > \alpha\beta\alpha\beta$; (ii) the order of atropisomer $LogP_{OW}$ values, $\alpha_3\beta > \alpha_4 > \alpha_2\beta_2 \approx \alpha\beta\alpha\beta$, correlates with the order of monomeric solubilization at high POPC concentrations and is a measure of lipophilicity; (iii) the addition of hexane to a dichloromethane solution of atropisomers increases the fraction of α_4 in the less polar solvent mixture, which is a different measure of lipophilicity; (iv) atropisomer monomeric fluorescence at low POPC concentrations follows the order of cellular uptake, $\alpha_4 > \alpha_3\beta > \alpha_2\beta_2 > \alpha\beta\alpha\beta$. While the enrichment of α_4 in a less polar dichloromethane/hexane solution suggested enhanced α_4 lipophilicity, the LogPow measurement presented $\alpha_3\beta$ as the most lipophilic atropisomer. This data, combined with the shared atropisomer chromatographic elution order, regardless of stationary phase, presented α_4 as the most amphipathic atropisomer, prone to locate at the interface between polar and lipophilic domains.

The enhanced amphipathic character proposed for α_4 is likely to result in differential solvation on the two sides of the macrocycle, which benefits α_4 cell uptake *in vivo* and *in vitro*. In agreement, (i) the order of cellular uptake, $\alpha_4 > \alpha_3\beta > \alpha_2\beta_2 > \alpha\beta\alpha\beta$, is the same as the order of *in vitro* phototoxicity; (ii) depletion of ATP or the presence of plasma proteins has little effect on the pattern of cellular uptake; (iii) tumor uptake *in vivo* is larger for α_4

than for αβαβ; (iv) atropisomers with higher cell uptake have enhanced photodynamic effect in cellular-PDT but not in vascular-PDT. These results are consistent with cell uptake predominantly by passive diffusion through the cell membrane, which is much more efficient for the α_4 atropisomer and explains its higher phototoxicity *in vitro* and in cellular-PDT.

The varied atropisomer uptake observed with the Kolliphor®EL formulation *in vitro* and *in vivo* suggested that the amphipathic α_4 atropisomers orientate within micelles in a manner that favors their interaction with the cell membranes. The topological orientation of "picket fence" porphyrins atropisomers in micelles has been previously shown by Barber et al.[244] to be a result of "picket" polarity. In an aqueous environment, a "face-in" orientation was anticipated for hydrophobic pickets (long alkyl chains), orientated towards the hydrophobic center (Figure 29). Shorter chain "pickets" with increased hydrophilicity (such as carboxamide groups) favor a "face-out" orientation, directed towards the surroundings aqueous environment. Metalation (Cu^{2+} and Zn^{2+}) of these porphyrins was affected by their interfacial orientation within the micelles. Enhanced reaction rates were obtained with the α_4 configuration followed by $\alpha_3\beta > \alpha_2\beta_2 > \alpha\beta\alpha\beta$.[244-245]

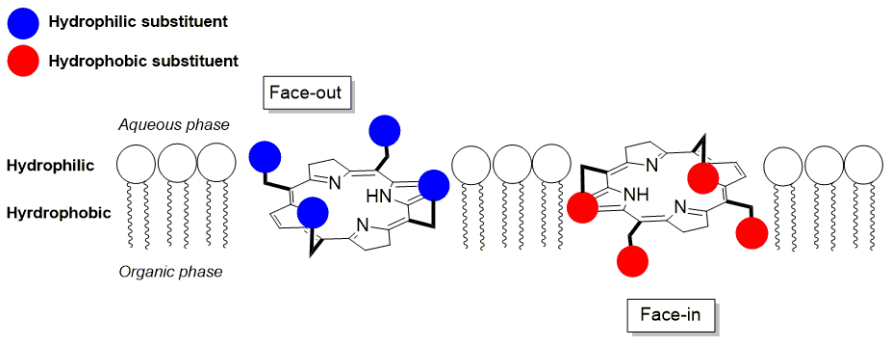

Figure 29. α_4 picket-fence porphyrin interfacial orientation in micelles adapted from Barber et al.[244]

Considering that for the redaporfin α_4 atropisomer, sulfonamide substituents of the phenyl groups are hydrophilic, it is likely that a "face-out" orientation is adapted. The sulfonamide group orientation may control access to the cellular membrane. The hydrophilic points of interaction between the sulfonamide groups and polar head groups of cellular membranes are least hindered in the cases of α_4 and $\alpha_3\beta$, thereby enabling diffusion across cell membranes. Two hydrophilic points are available on $\alpha_2\beta_2$. Consistent with redaporfin atropisomer cell internalization studies *in vitro* (Figure 17) and *in vivo* (Figure 23C), αβαβ is the most hindered ring in terms of hydrophilic interaction,[246] which likely inhibits

membrane permeation. For the α_4 atropisomer, it is suggested that the polar sulfonamide groups are most likely orientated towards the micelle exterior, facilitating the interaction of the polar sulfonamide groups with the outer polar heads of the cell membrane phospholipids. Additionally, the X-ray crystal structure of α_4 P11 reveals a slight saddle deformation of its macrocycle (Figure 12B), potentially driven by steric interactions between the polar groups, and a preference for a three-dimensional hydrogen-bonded network with disordered acetonitrile (solvate) molecules (Figure S 6). This suggests that the energy penalty for the transition between aqueous media to membranes is lower for α_4 than for the other atropisomers.

The topology of α_4 and cyclosporin can be compared. Cyclosporin is a rare example of a large molecule (molecular weight = 1203 Da, Figure 30) that efficiently crosses cell membranes by passive diffusion.[247] Nα-methylation of the cyclosporine backbone amides reduces the number of H-bond donors to 5 and intramolecular H-bonding lowers its desolvation energy. Cyclosporine is in an "open" *trans* conformation in aqueous solutions, which allows amides to interact with cell membranes via hydrogen bonds. However, it changes to a "closed", *cis* conformation in the lipid bilayer, making use of intramolecular hydrogen bonding to decrease its polarity.[247-248] For the redaporfin α_4 atropisomer, hydrogen-bonding with the cell surface is also expected to be favored. Its amphipathicity potentially aids the macromolecule diffusion into the cell membrane at a lower desolvation energy cost. This hypothesis is supported through examination of the varied atropisomer uptake *in vitro* and *in vivo*, which uncovers the importance of spatial orientation of aryl methylsufonamide groups for the cellular uptake of large molecules. α_4 feature 8 H-bond acceptors and 4 H-bond donors, which point to the same side of the macrocycle and may facilitate hydrogen bonding with the silanol groups on silica surface or with the phosphate groups of membrane phospholipids. However, the lipophilicity of α_4 also causes higher retentions in RP-HPLC and facilitates monomeric solubilization within the hydrophobic interior of membranes. This suggests a cell uptake mechanism where hydrogen-bonding promotes the transfer of α_4 from water : DMSO (99.96 : 0.04, v/v or 2% v/v Kolliphor®EL micelles, or plasma proteins) to the surface of membranes; α_4 then flips to accommodate its lipophilic moiety inside the lipid bilayer, diffuses through the membrane and eventually orientates to pass into the interior of the cell.

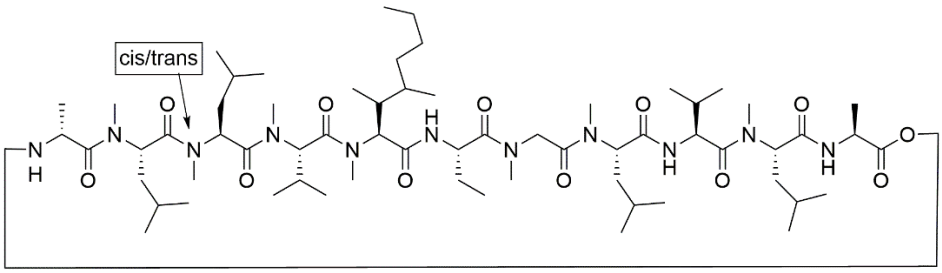

Figure 30. Molecular structure of cyclosporin adapted from Wang et al.[248]

PDT is ideally suited to investigate atropisomer pharmacodynamics as the activation of a PS by light is intrinsic to the biological activity and allows study with spatiotemporal control. The pharmacodynamics of atropisomers, before they had time to be internalized by cells (vascular-PDT) and after cellular uptake (cellular-PDT), were studied. Redaporfin atropisomers exhibited differential pharmacodynamics in cellular-PDT, providing evidence that a specific orientation of aryl methylsufonamide substituents can benefit cell uptake *in vivo*.

2.4.9 Enrichment of redaporfin with the α_4 atropisomer

The superiority of the α_4 atropisomer as a PS with enhanced membrane permeation is limited by its small proportion (~12.5%) of the drug mixture. The low abundance of the desired atropisomer is a common problem with drug discovery campaigns that aim to isolate atropisomerically stable compounds which are heavily reliant on chromatography. This is highly inefficient from a material-throughput perspective, when only one atropisomer is needed; for example, with redaporfin α_4, approximately 86.5% of the drug is not used. Additionally, repetitive chromatography with repeated cycles of separation and heating are typically required.[117] It was possible to precipitate the redaporfin atropisomers in a mixture of dichloromethane and hexane (1:1), which resulted in a sample enriched with α_4 following partition (Table 1). However, this procedure would require repetitive re-equilibration and precipitation, similar to the repetitive chromatography method, to convert a high proportion of the mixture to the α_4 atropisomer.

A promising solution to limit chromatography separations is a method developed by Lindsey,[249] which exploited the equilibrium nature of atropisomer interconversion as well as the higher relative affinity of α_4 for silica gel. Induction of picket-fence atropisomer conversion in the presence of silica gel and benzene by heating for 20 h resulted in an enriched mixture with α_4. Preferentially silica-bound α_4 was subsequently extracted using

polar solvents.[249] This protocol was successfully incorporated by Collman et al. into preparative method development for selectively modified picket-fence porphyrins[250] and corrole-based hemoprotein analogs.[251] More recently, Ishizuka et al.[252] proposed the selective convergence of a picket-fence porphyrin atropisomer mixture to enrich α_4 in the absence of silica gel through heating in chloroform. This protocol, however, was specifically designed for meso-tetraarylporphyrins with bulky mesityl *ortho*-substituents, which formed a hydrophobic cavity capable of accommodating solvent molecules and stabilizing the configuration for enrichment. In the case of redaporfin, relatively smaller *ortho*-fluorine substituents led to selection of Lindsey's method[249] for enrichment of redaporfin with the α_4 atropisomer.

Optimization of conditions for enrichment was required to avoid oxidation of redaporfin. Despite high photostability of redaporfin due to electron withdrawing groups which stabilize the macrocycle against oxidation,[97] there is a possibility of conversion to chlorin upon heating in solution. Initial attempts to optimize the protocol were carried out by refluxing the drug mixture with silica and dichloroethane under inert conditions. Moderate success was observed via HPLC chromatograms with 18% (Figure 31A,B), 27% and 39% α_4 peak areas relative to the starting material (11%) following 24 h, 48 h and 60 h respectively. Enrichment success achieved beyond 24 h of heating was accompanied by substantial oxidation to chlorin (Figure 31D), even in the presence of strictly inert conditions. This was monitored through comparison of the characteristic chlorin peak height, at 414 nm, in the starting material and enriched samples.

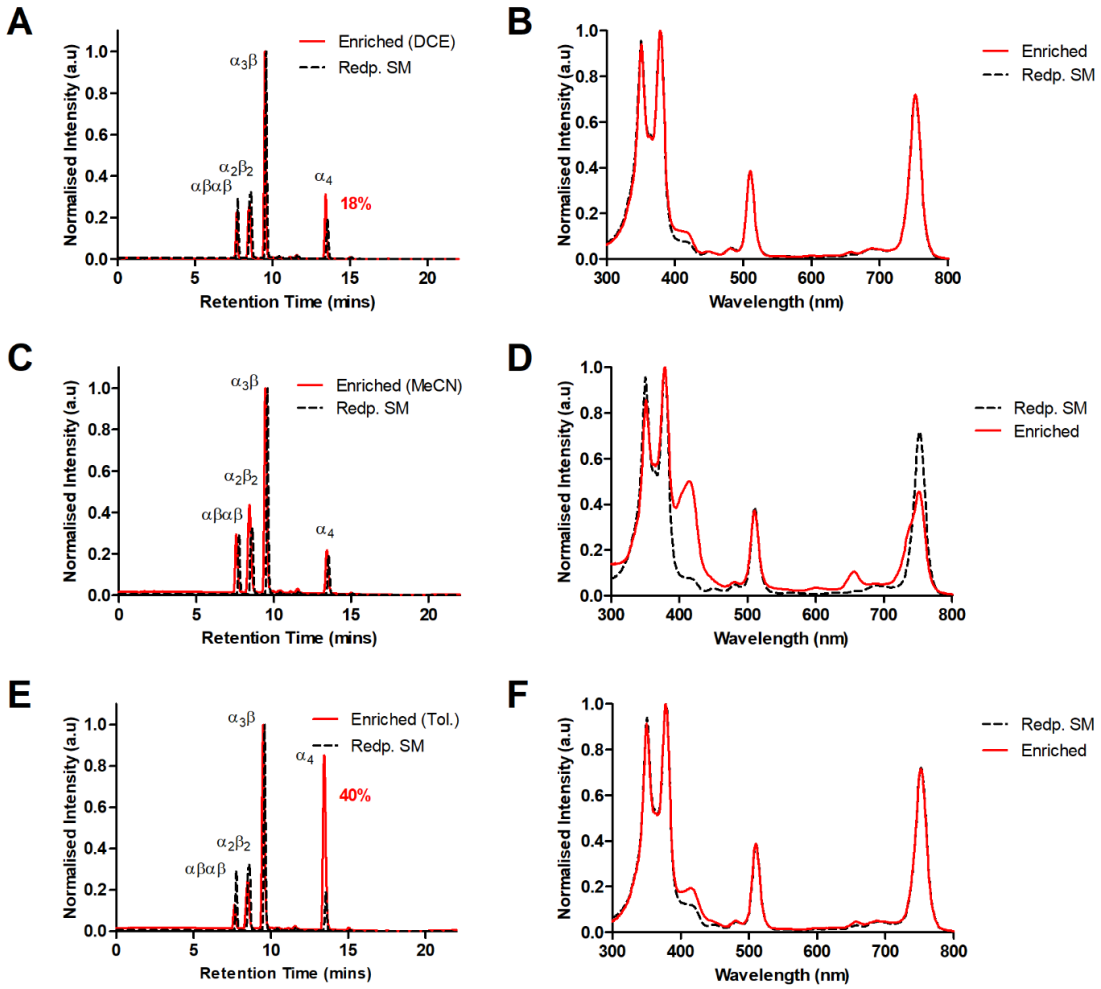

Figure 31. Optimization of redaporfin enrichment with α_4. HPLC chromatograms of redaporfin samples which followed 24 h of heating in the presence of silica with (A) dichloroethane (DCE), (C) acetonitrile (MeCN) and (E) toluene (Tol.) in comparison to redaporfin starting material (Redp. SM). Detection at 743 nm. Absorption spectra of redaporfin samples enriched with α_4 atropisomer following heating in DCE for (B) 24 h, (D) 60 h and (F) Tol. for 24 h with comparison to redaporfin starting material (Redp. SM).

The importance of suitable solvent selection and the necessity of adherence to silica gel was observed when a solvent with a similar boiling point to dichloroethane, acetonitrile, resulted in no enrichment (Figure 31C). Selection of a less polar solvent, which ensured adherence to silica and a higher boiling point, toluene, resulted in more efficient enrichment success (40% α_4 peak area) in the absence of significant chlorin production following 24 h heating (Figure 31E,F). This procedure required an appropriate silica:solvent ratio (0.25 g:1 mL) for enrichment success. Further heating in toluene for 48 h to improve enrichment led to excessive chlorin production. For this reason, it was not possible to reach the enrichment success of 66% yielded by Lindsey. Nevertheless, this enrichment protocol

allows adequate quantities to be obtained for further clinical translation, without the need for tedious repetitive chromatography or solvent precipitation techniques.

2.5 CONCLUSION

In summary, atropisomers of meso-tetraarylporphyrin derivatives with fluorine atoms in the *ortho*-positions of the aryl rings and a sulfonamide group in a *meta*-position were separable by flash chromatography and highly stable at rt. The atropisomer with four sulfonamide groups on the same side of the macrocycle, i.e., the α_4 atropisomer, exhibited enhanced ability to access the cellular membrane and diffuse into the cell. It was possible to improve the yield of this atropisomer through an enrichment method based on heating in the presence of toluene and silica gel. Efficient cytosolic delivery by passive diffusion of molecules as large as redaporfin is rare and a substantially increased delivery by rotation of C–C single bonds was unexpected. The α_4 atropisomer was proposed to exhibit surfactant properties, in which the macrocycle was orientated towards lipophilic domains and the arylsulfonamides to polar environments This is expected to favor hydrogen-bonding of the four sulfonamide groups with sulfates and carboxylates of the cell membrane, increasing passive diffusion. Most significantly, the seamless α_4 cell internalization observed *in vitro* could be transferred to an animal model relevant in oncology. The differential pharmacodynamics of redaporfin atropisomers are a new example of the far-reaching consequences of atropisomerism in biological activity and drug action.

2.6 SUPPLEMENTARY MATERIAL

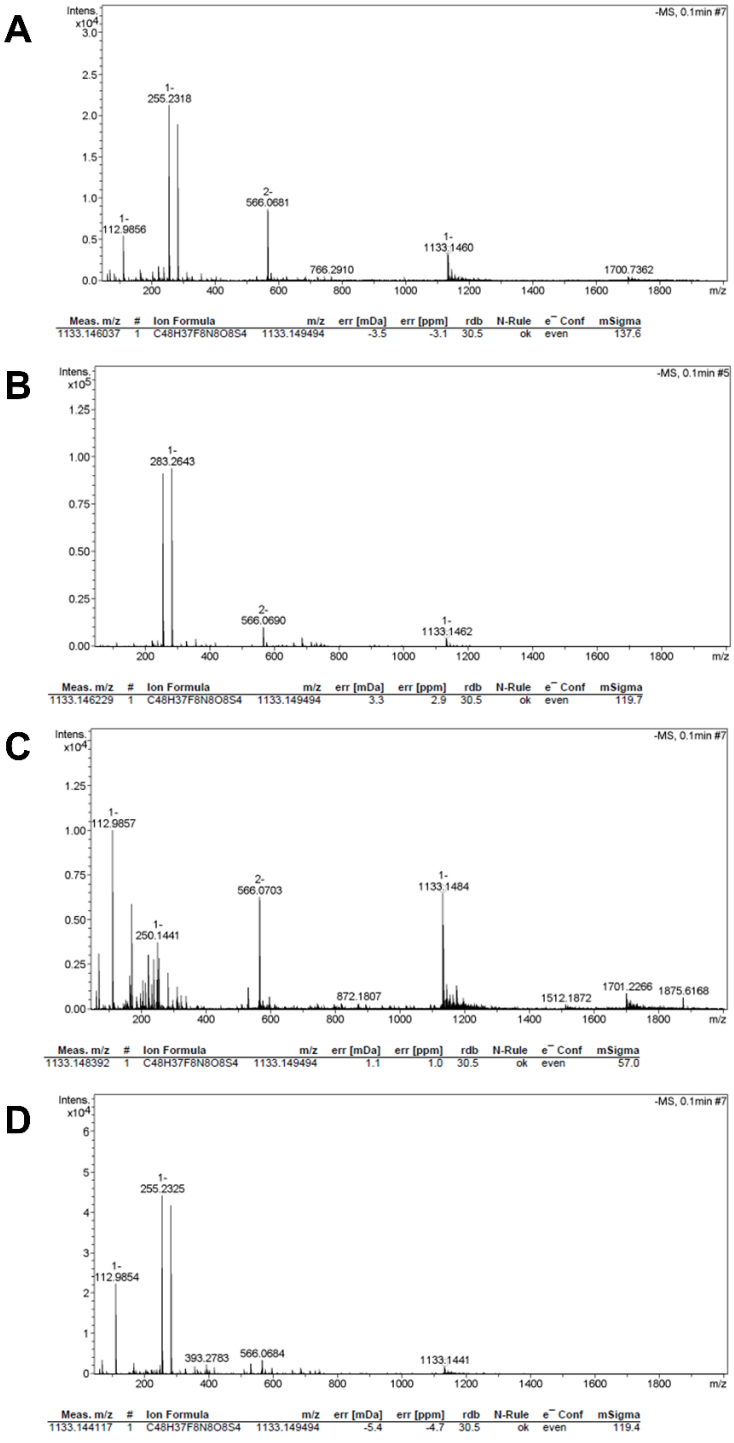

Figure S 1. HRMS (ESI) of redaporfin atropisomers (A) Sample αβαβ, (B) sample $\alpha_2\beta_2$, (C) sample $\alpha_3\beta$ and (D) sample α_4.

A

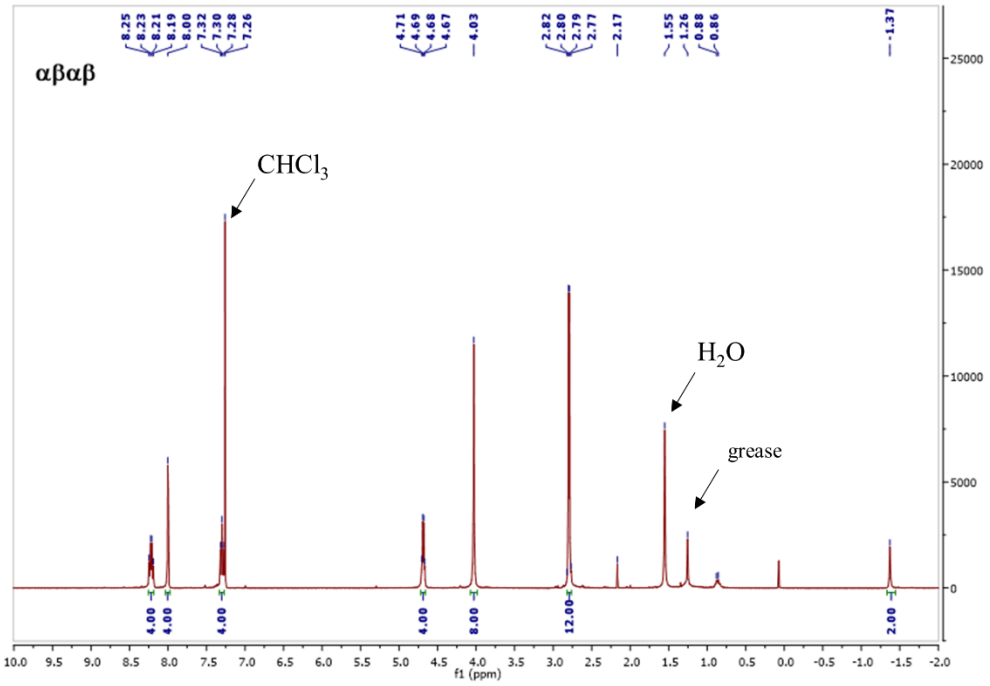

B

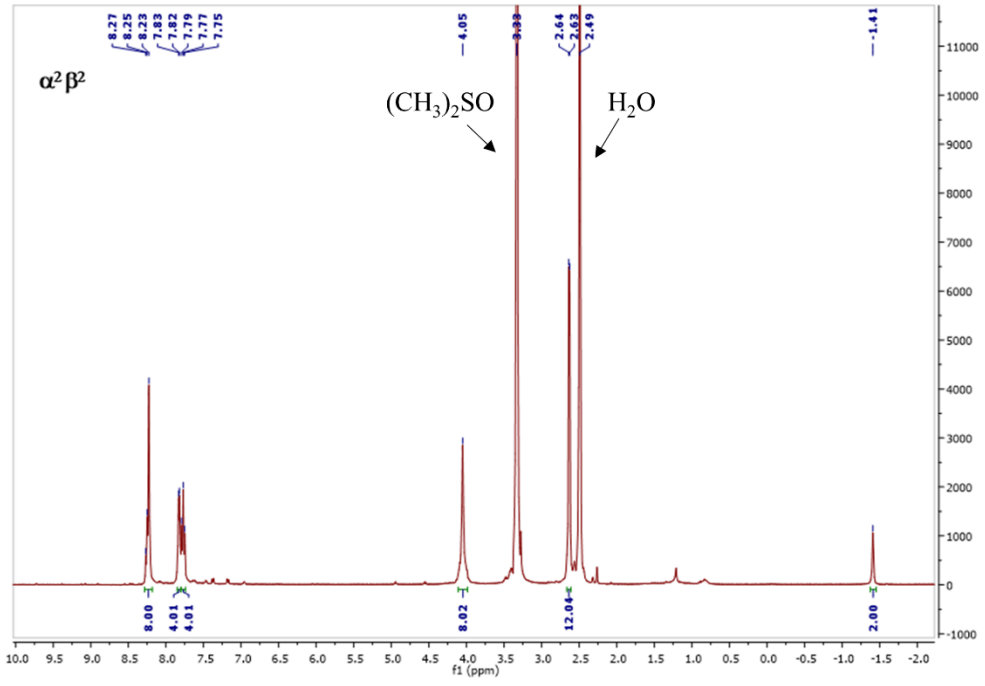

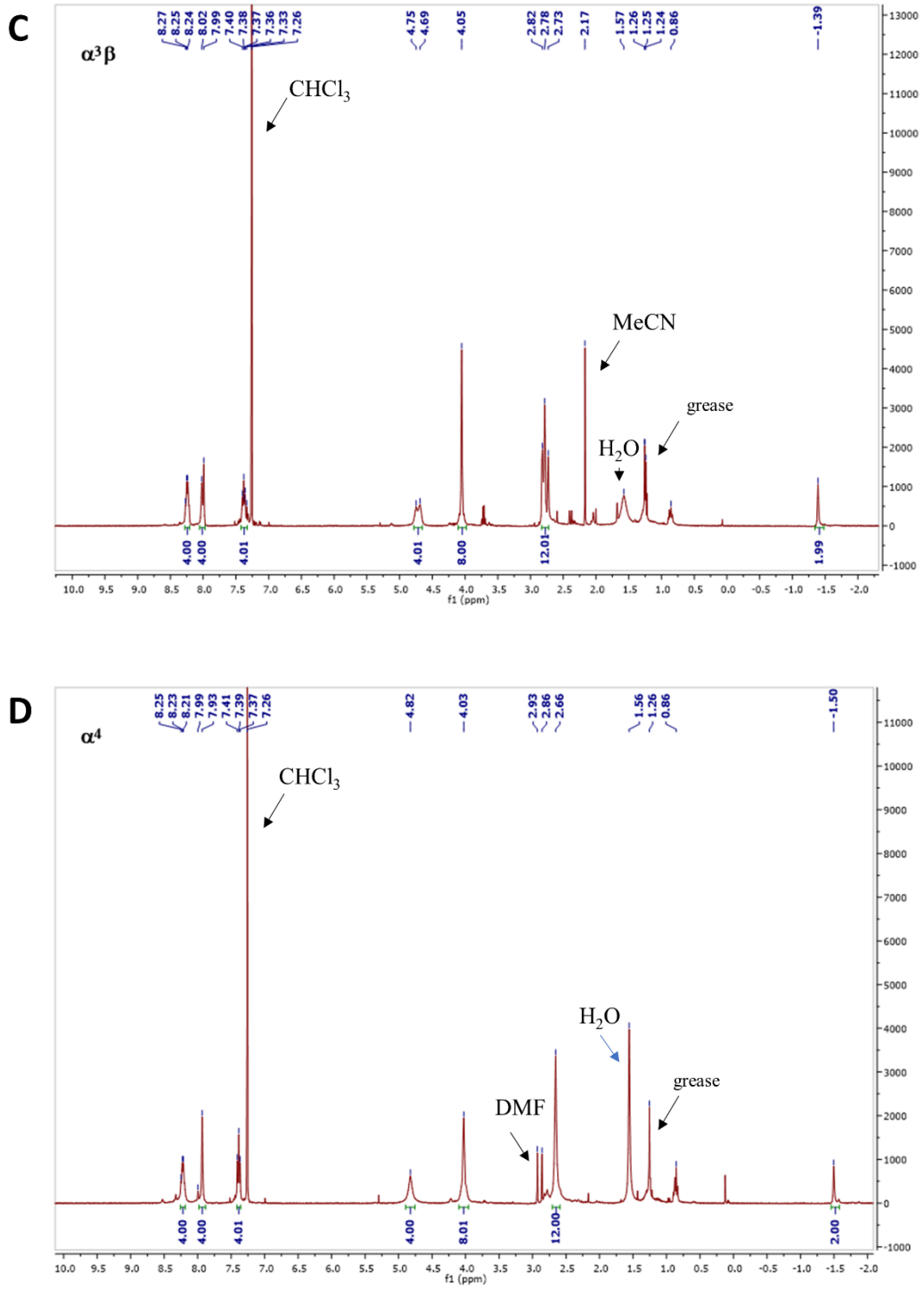

Figure S 2. ^{1}H NMR spectra of redaporfin atropisomers. (A) Sample αβαβ, (B) sample $\alpha_2\beta_2$, (C) sample $\alpha_3\beta$ and (D) sample α_4.

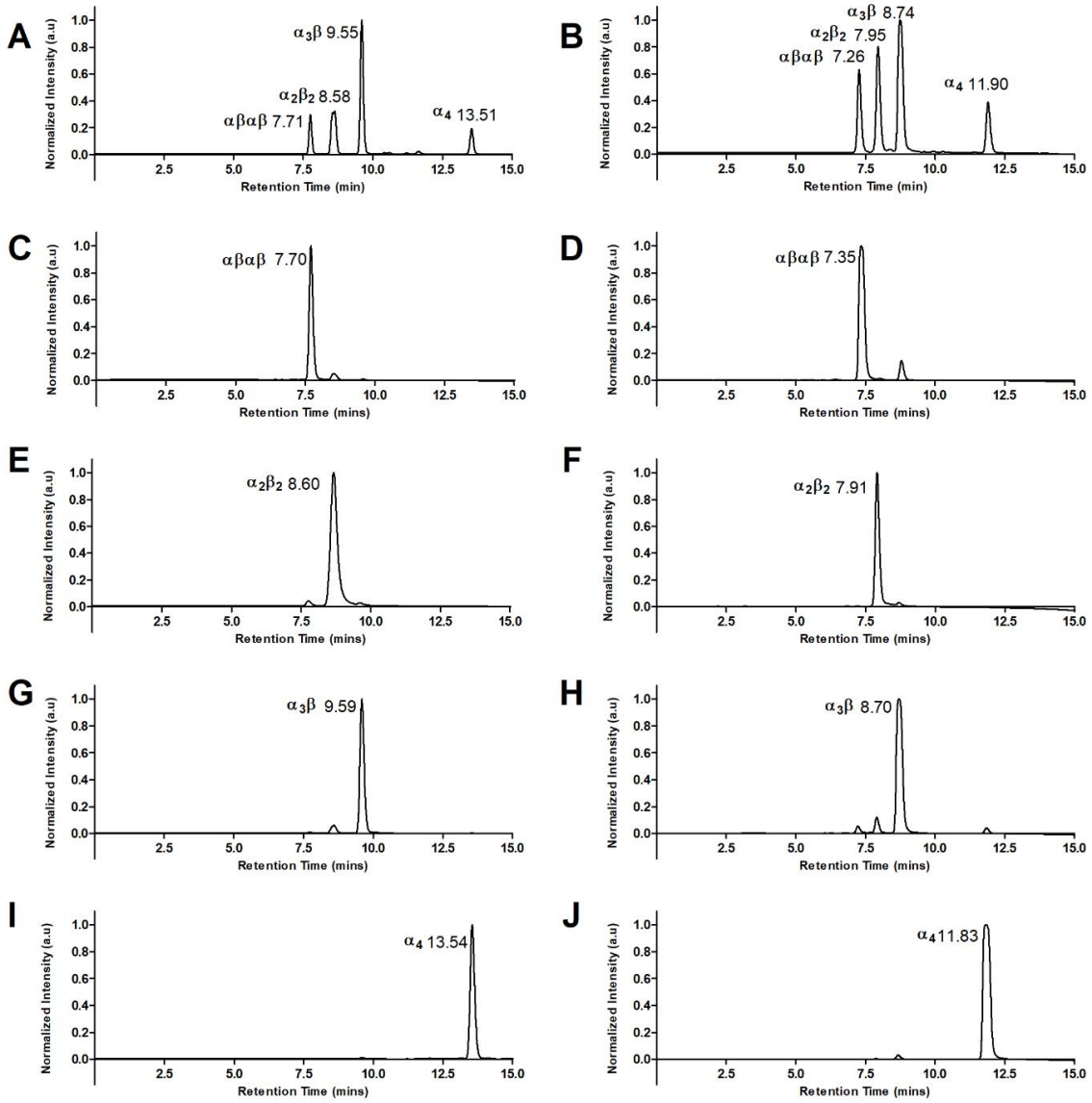

Figure S 3. HPLC chromatograms of redaporfin and P11 porphyrin atropisomers. (A) redaporfin mixture, (C) sample αβαβ, (E) sample $\alpha_2\beta_2$, (G) sample $\alpha_3\beta$ and (I) sample α_4. (B) P11 mixture, (D) sample P11 αβαβ, (F) sample P11 $\alpha_2\beta_2$, (H) sample P11 $\alpha_3\beta$ and (J) sample P11 α_4

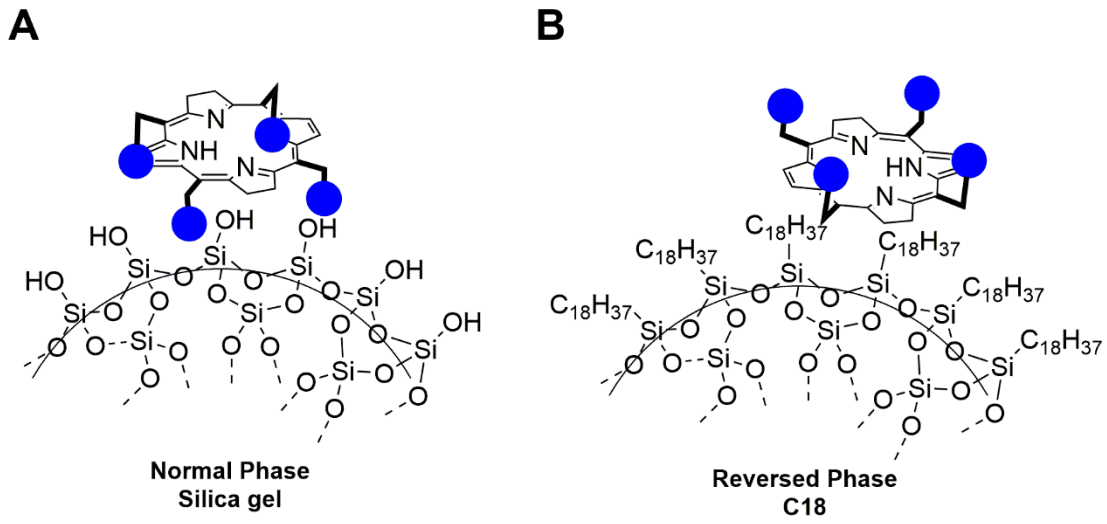

Figure S 4. Representation of enhanced α_4 retention in different chromatographic stationary phases. Potential (A) hydrogen bonding with normal phase silica gel and (B) hydrophobic interaction with reversed phased C18 columns.[253]

Table S 1. Crystallographic data associated with P11 atropisomers.

	P11 $\alpha_2\beta_2$	**P11 α_4**
Identification code	CJK_013	CJK_059
CCDC deposition number	2124975	2124976_2
Chemical formula	$C_{52}H_{46}F_8N_8O_{10}S_6$	$C_{52}H_{40}F_8N_{10}O_8S_4$
Formula weight	1287.33 g/mol	1213.18 g/mol
Temperature	100(2) K	100(2) K
Wavelength	1.54178 Å	1.54178 Å
Crystal size	0.039 x 0.047 x 0.074 mm	0.032 x 0.064 x 0.103 mm
Crystal system	Monoclinic	Monoclinic
Space group	P 1 21/c 1	C 1 2/c 1
Unit cell dimensions	a = 12.0820(7) Å, α= 90° b = 17.5200(9) Å, β=	a = 32.616(3) Å, α= 90°. b = 12.4059(12)) Å, β=
Volume	2677.5(3) $Å^3$	5342.0(9) $Å^3$
Z	**2**	4
Density (calculated)	1.597 g/cm^3	1.508 g/cm^3
Absorption coefficient	3.207 mm^{-1}	2.451 mm^{-1}
F(000)	1324	2488
Theta range for data collection	3.73 to 68.39°	2.87 to 69.35°
Index ranges	-14<=h<=13, -21<=k<=21, -15<=l<=15	-38<=h<=39, -14<=k<=10, -16<=l<=16
Reflections collected	23203	10652

Independent reflections	4898 [R(int) = 0.0990]	4125 [R(int) = 0.0994]
Completeness to theta= 67.679°	99.5%	82.6%
Absorption correction	Multi-Scan	Multi-Scan
Max. and min. transmission	0.7531 and 0.5629	0.7531 and 0.5721
Refinement method	Full-matrix least-squares on F^2	Full-matrix least-squares on F^2
Function minimized	$\Sigma\, w(F_o^2 - F_c^2)^2$	$\Sigma\, w(F_o^2 - F_c^2)^2$
Data/ restraints/ parameters	4898 / 148 / 410	4125 / 706 / 349
Goodness-of-fit on F^2	1.065	1.071
Final R indices [I>2σ(I)]	R1 = 0.0683, wR2 = 0.1931 3092 data; I>2σ(I)	R1 = 0.1253, wR2 = 0.3011 1892 data; I>2σ(I)
R indices (all data)	R1 = 0.1060, wR2 = 0.2157	R1 = 0.2188, wR2 = 0.3540
Largest diff. peak and hole	0.983 and -0.811 e.Å^{-3}	1.466 and -0.549 e.Å^{-3}

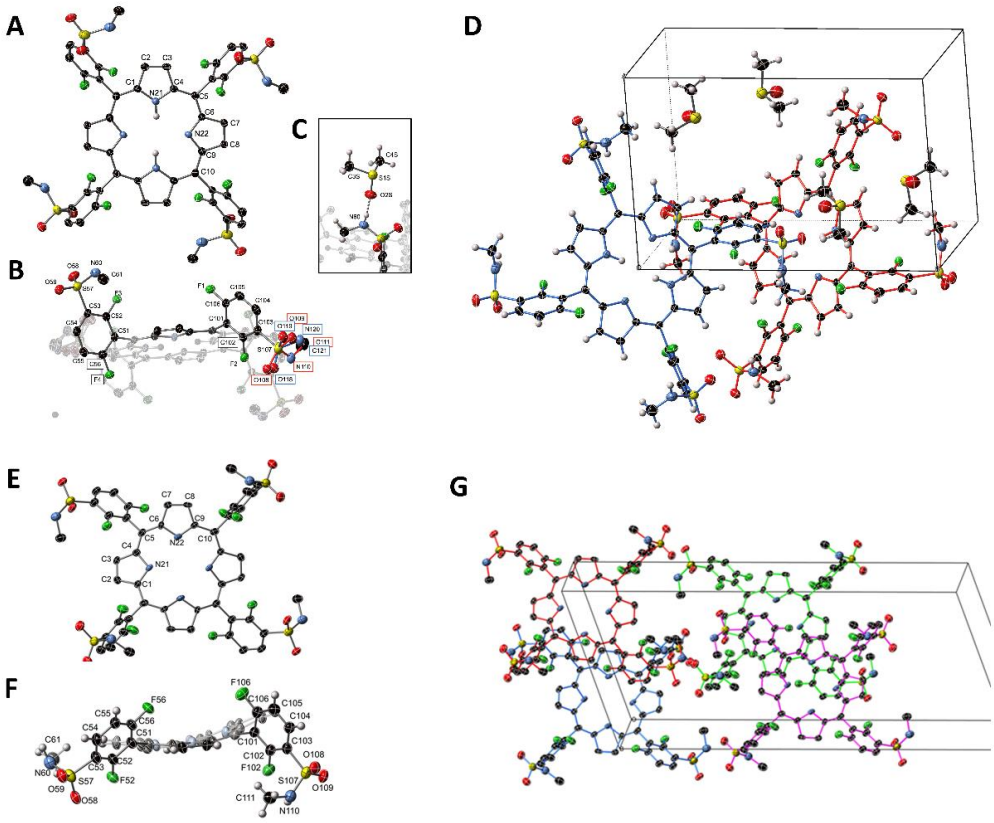

Figure S 5. Crystal structures of P11 $\alpha_2\beta_2$·2Me2SO and P11α_4·4MeCN. (A-C) Labelled atom positions from the crystal structure of $\alpha_2\beta_2$·2Me$_2$SO: (A) porphyrin ring, (B) side-chains and, (C) DMSO solvate. Thermal ellipsoids are shown at the 50% occupancy level, H-atoms are represented as spheres or omitted. The disordered O108-C111 (red, 62.4(5) %) and O118-C121 (blue, 37.6(5)%) are shown in (B) and omitted elsewhere. (D) P11 molecules (Z = 2) within the unit cell of $\alpha_2\beta_2$-1·2Me$_2$SO. Two equivalent P11 porphyrin molecules are shown in red and blue bonds, with solvate molecules in black. The minor disorder fraction has been omitted and ellipsoids are shown at the 50% probability level. (E-F) Labelled atom positions from the crystal structure of α_4·4MeCN: (E) the porphyrin ring and (F) the side-chains. Thermal ellipsoids are shown at the 50% occupancy level, H-atoms are represented as spheres or omitted. (G) P11 molecules (Z = 4) within the unit cell of α_4·4MeCN. The four equivalent P11 porphyrin molecules are shown in red, blue, green and magenta bonds, with solvate compensated by the SQUEEZE technique.

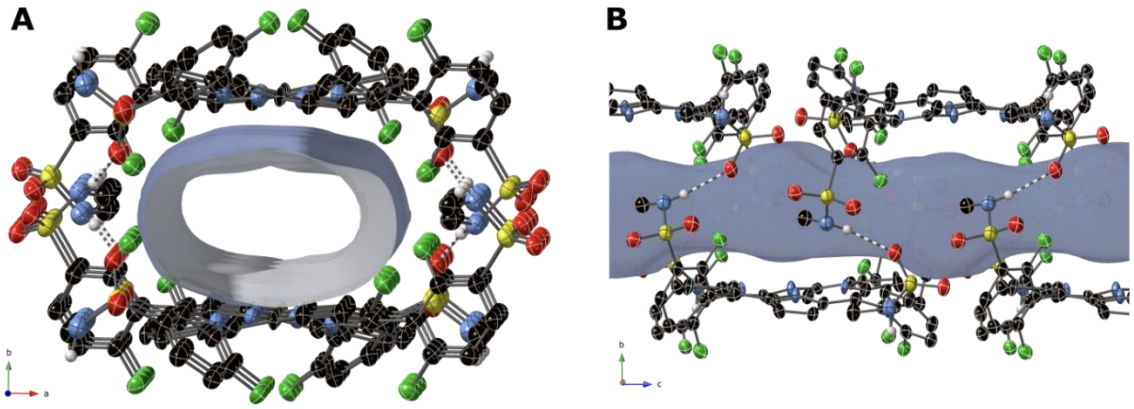

Figure S 6. An indication of the solvent-filled channel (blue/grey) in the crystal structure of P11 α_4·4MeCN with a 1.4 Å probe radius, viewed perpendicular to the (A) ab- plane and (B) bc- plane. Hydrogen bonding interactions are indicated with striped bonds.

Table S 2. Relative atropisomer contents after heating a $\alpha_3\beta$ sample in dimethylformamide. The indicated periods of time and temperatures, open to the atmosphere, were tested.[105]

		Relative Atropisomer Proportion (%)			
	Initial	Temperature Time	Temperature Time	Temperature Time	Temperature Time
		85 °C 12 h	140 °C 5 min	140 °C 10 min	140 °C 20 min
Assay		(%w/w)	(%w/w)	(%w/w)	(%w/w)
αβαβ	-	5	14	9	12
$\alpha_2\beta_2$	1	14	19	20	23
$\alpha_3\beta$	99	74	60	58	52
α_4	-	7	5	11	11

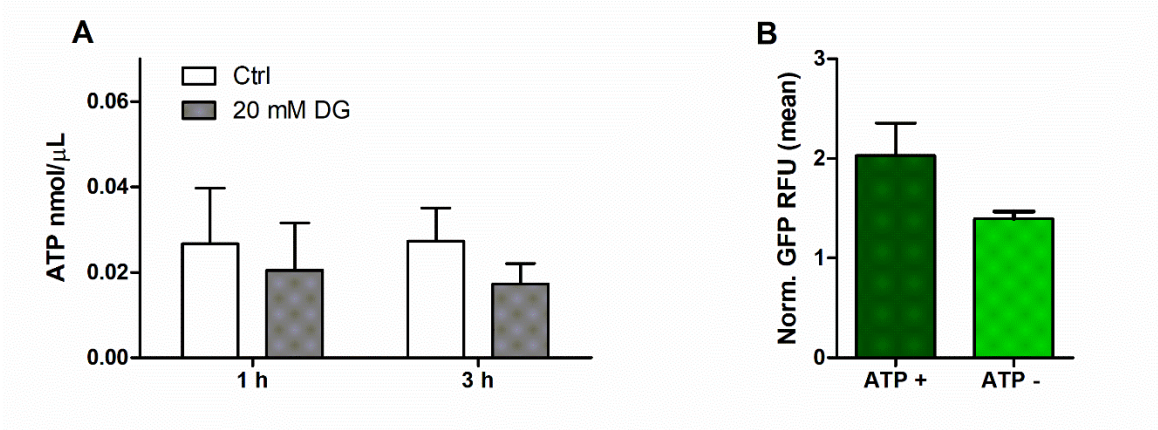

Figure S 7. ATP depletion on 4T1 cells using 2-deoxy-D-glucose (DG). (A) Quantification of ATP in untreated (Ctrl) cells and following treatment with 20 mM of DG, for 1 h. (B) Reduced GFP uptake under conditions of ATP depletion. Bars indicate the mean ± SEM of at least 3 independent experiments.

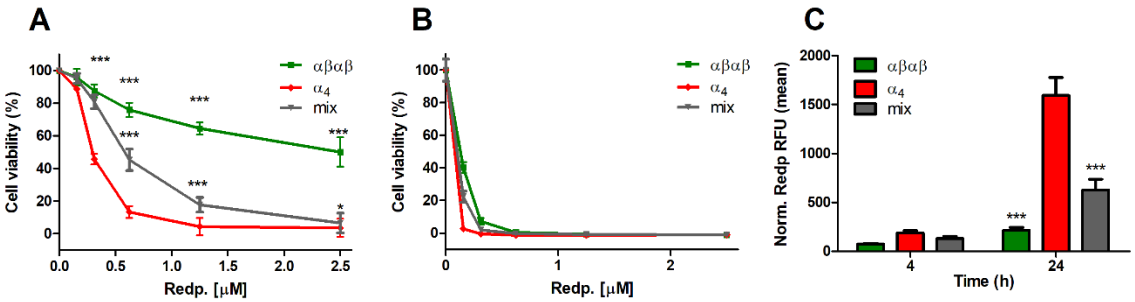

Figure S 8. Evaluation of redaporfin atropisomers and redaporfin mixture in B16-F10 melanoma cells. Phototoxicities of redaporfin atropisomers and mix *in vitro* upon illumination at 740 nm with light doses (A) 0.05 J/cm^2 (n = 2) and (B) 0.2 J/cm^2 (n = 1) after 24 h of incubation with B16-F10 cells; statistical significance was evaluated using two-way ANOVA *versus* the α_4 atropisomer. (C) Cellular internalization of redaporfin atropisomers and mix evaluated by flow cytometry at the indicated time points in B16-F10 cells (n = 2). Bars indicate the mean ± SEM of n independent experiments; the fluorescence signal from treated cells was normalized to the untreated cells; the statistical significance was evaluated using two-way ANOVA *versus* the α_4 atropisomer, * $p < 0.05$, ** $p < 0.01$ and *** $p < 0.001$.

3. Strapped porphyrins as model systems for atropisomeric porphyrins

3.1 ABSTRACT

The time dependence of atropisomer interconversion has limited the pursuit of single atropisomer drug candidates, even in circumstances where one atropisomer presents favorable biological activity over another. Moderate interconversion energy barriers risk compromising drug stability. As a result, examples of atropisomerically pure drugs in current clinical use are rare. However, in recent years, there has been a shift towards the development of single, stable atropisomer drug candidates.[149-150] Assessment of whether the enhanced biological activity offered by an individual isomer can outweigh the potential for interconversion features as part of hit-to-lead optimization. Consequently, development of methods which effectively restrict rotation in a configuration which favors activity are highly beneficial. For PDT, the meso-tetrasubstituted porphyrin atropisomer, α_4, has been demonstrated to improve cell-internalization and subsequently potentiate phototoxicity relative to the drug mixture. In this work, the α_4 configuration was modeled with novel porphyrin PSs through strapped moieties which effectively fixed the atropisomeric configuration. Structural elucidation to confirm strapped-porphyrin configurations was provided by NMR spectroscopy and single crystal X-ray crystallography. Photophysical evaluation gave insight to the relative macrocycle conformation of the porphyrin isomers. The stable *cis*-αα configuration demonstrated enhanced cell membrane permeation, effectively predicting the behavior of the α_4 configuration.

3.1.1 Graphical abstract

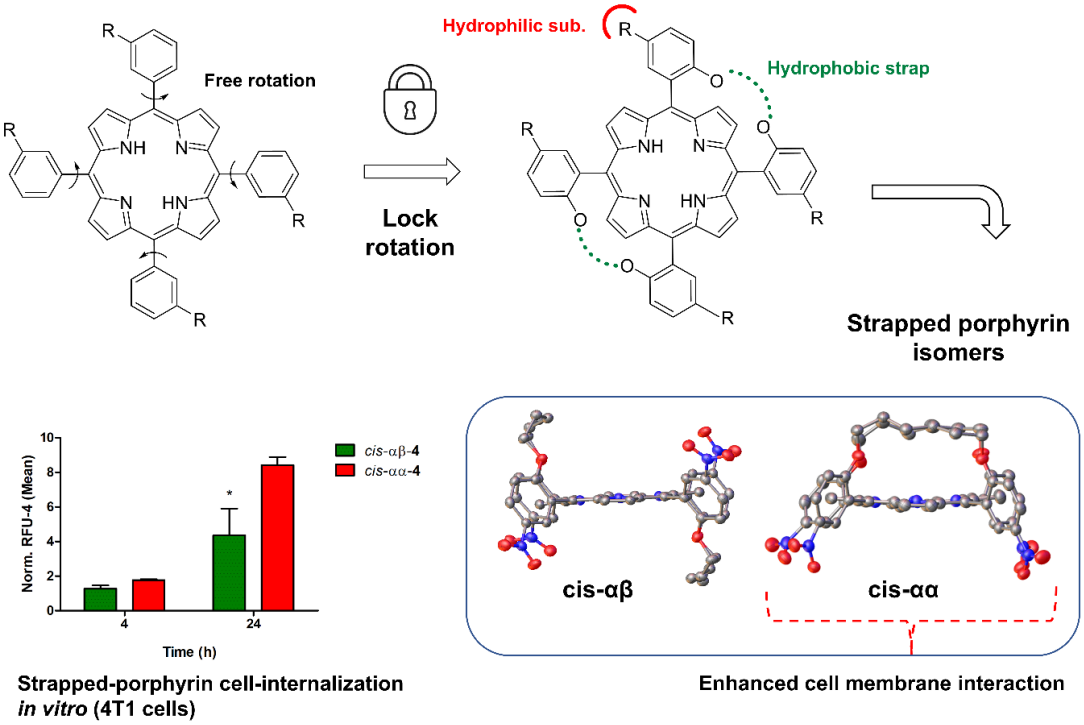

3.2 INTRODUCTION

An intrinsic issue for atropisomer drugs is the time dependence of interconversion with dramatically different racemization half-lives ranging from minutes to years. With the potential to undermine the efficacy and production of stable drug substances, it is perhaps unsurprising that atropisomerism has been dubbed a 'lurking menace' for drug development.[111] Even atropisomers with large interconversion barriers ($\geq$ 30 kcal.mol^{-1}), considered class 3 atropisomers, require careful evaluation.[115] As with chiral stereoisomers, pre-clinical assessment of atropisomer drug candidates generally involves consideration of atropisomer pharmacokinetic profiles due to the potential racemization of pure isomers upon metabolism.[111] A Pfizer team demonstrated the use of chromatographic methods to evaluate atropisomer biotransformation for a variety of drug candidates *in vitro* and *in vivo*.[140] Similar evaluation was retroactively carried out with the individual atropisomers of a hURAT1 inhibitor, Lesinured, employed as a racemate for the treatment of gout. Atropisomeric species specific metabolic stability was uncovered.[141] In cases where an individual atropisomer presents a favorable biological activity, alterations to molecular structure which increases rotational barriers in a manner that preserves metabolic stability is highly desirable.

A prevalent strategy to improve stability involves an increase of steric bulk around the atropisomer axis.[115] Additionally, there are cases where a rotating axis interconversion energy barrier can be increased through creation of a bridge. This featured in a development campaign by AstreZeneca during the preparation of Nuerokinin-1 receptor antagonists.[160] The high stability associated with these bridging motifs can also be observed with the racemate atropisomer drug Telenzepine (Figure 7) which features a 7-membered ring.[154] Strategies such as these can be particularly useful when the rigidification of an axis also results in enhanced biological activity. The relevance of this approach for kinase inhibitors, in terms of altering target selectivity is well established.[121] For PDT, a specific tetrapyrrole atropisomer configuration, the α_4 atropisomer, was identified in Chapter 2 to increase cellular internalization and consequently enhanced phototoxicity *in vitro* and *in vivo*. The source for this varied efficacy was rationalized in terms of the atropisomer molecular structure with the distribution of polar substituents oriented on one side of the macrocycle plane, enhancing interaction with the cell-membrane and improving passive permeation. In this work, restrictive straps moieties (Figure 32) were used in novel porphyrin PSs to

enforce an α_4 configuration while effectively locking the axis of rotation for enhanced stability.

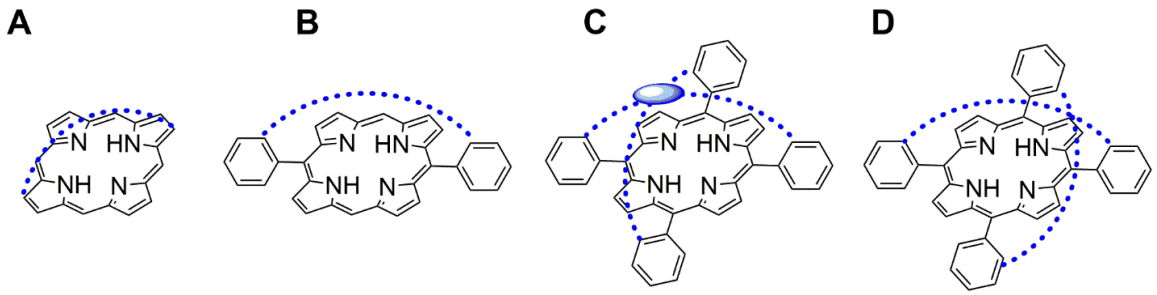

Figure 32. Schematic representation of strapped porphyrin configurations. (A) β-β- Strapped porphyrin (B) meso-meso- strapped porphyrin (C) capped-porphyrin (D) double strapped porphyrin.

Strapped porphyrins feature covalent connections between either β- β-[254-255] (Figure 32A) or meso-meso-[256] positions of the porphyrin macrocycle.[174] These systems were originally developed in order to gain understanding of the structure and activity of biologically active sites. The domed shape of deoxyhemoglobin, known to feature as part of the heme protein, was pursued.[175] Linkage at phenyl substituents of 5,10,15,20-teraphenylporphyrins (Figure 32B) gave rise to a variety of strapped porphyrin shapes with names derived from macroscopic objects including 'capped porphyrins' (Figure 32C) and double strapped 'basket handle' porphyrins (Figure 32D and Figure 33).[257] Investigation of biomimetic models was dominated by the pursuit to induce porphyrin distortion. This was successfully achieved by Dolphin's group, with the preparation of a β-β- single strapped porphyrin by acidic cyclisation of a bis-dipyrromethane.[176] Single strapped meso-linked porphyrins were also prepared to target a cytochrome c oxidase model by Wytko et al. through condensation between a dipyrromethane and dialdehyde.[258] However, a more accurate model was later obtained with a double strapped porphyrin through post-functionalization of porphyrin atropisomers with linkers.[180] Single strapped porphyrins have featured in areas beyond biomimetic models as chiral catalysts[259] and scaffolds in molecular engineering[260] as well as potential oxygen storage devices with anthracene straps.[261]

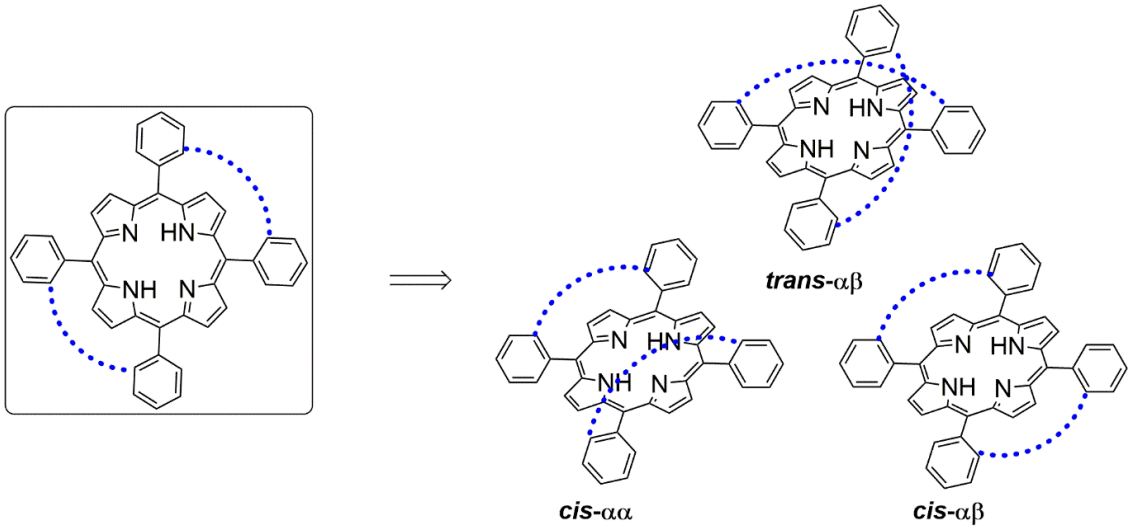

Figure 33. Schematic representation of three double strapped porphyrin configurations. '*cis*' refers to linkages at the 5,10- and 15,20-meso-positions, '*trans*' to linkages at the 5,15- and 10,20-meso-positions, and α and β to the faces of the porphyrin.[257]

Double strapped porphyrins have also been reported which direct meso-aryl substituents relative to the macrocycle plane, above or below, in a manner analogous to porphyrin atropisomers (Figure 33). Two major strategies have been developed to prepare these systems (Scheme 1). Direct condensation of a dialdehyde and pyrrole in propionic acid was adapted from the Adler-Longo condensation.[262] This was used as part of method development to target *trans*-αβ isomers by Momenteau et al.[263] as well as the double strapped systems of Weiser et al.[264] and Simonis et al.[175] The Lindsey group optimized their original Lindsey condensation[265] as a more efficient method to produce *cis*-isomers using a BF_3 catalyzed direct condensation with subsequent DDQ oxidation (Scheme 1A).[257] 18 dialdehydes were investigated with linkages at both the meso-aryl *ortho,ortho*'- (*o,o*'-) and *meta,meta*'- (*m,m*'-) positions. This demonstrated the variety of strap-types such as alkyl or phenyl linkers which could be employed in studies of strapped-porphyrin stability[171] and distortion.[177] An alternative method of double strapped porphyrin synthesis employs the later introduction of a strap to porphyrin atropisomers (Scheme 1B). This was originally employed by Bisagni and coworkers to increase *trans*-αβ isomer yield[263] and later used in the synthesis of straps featuring pyridine, also termed 'hanging base' porphyrins.[266] Regardless of the above synthetic route selected, isolation and preparation of stereoisomerically pure strapped porphyrins in reasonable yield remains a challenge.[171] Despite this, interest in strapped porphyrin synthesis continues[267-268] alongside their role as heme models.[269-270]

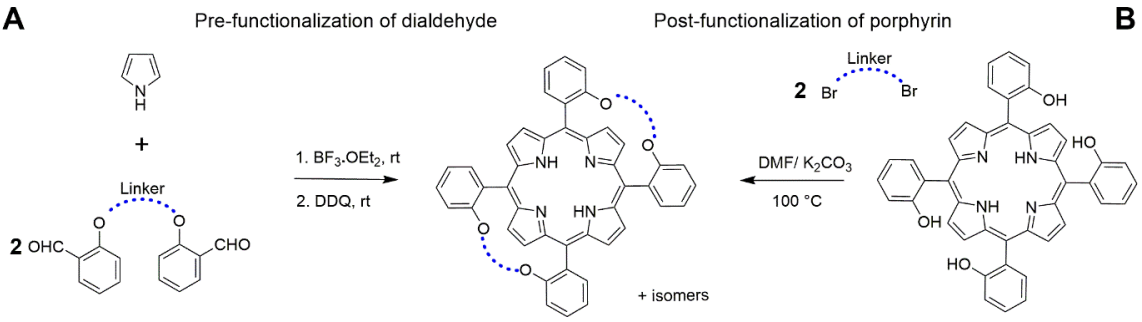

Scheme 1. Major synthetic routes for preparation of double-strapped porphyrins. Adapted from Wagner et al.[257]

Examples of strapped porphyrins as PSs are limited. In addition to low synthetic yields, the lack of investigation may be partly due to the primary focus of these systems generally involving macrocycle distortion. With short strap lengths, a non-planar conformational change may occur which quenches fluorescence quantum yields[271] and consequently reduces singlet oxygen quantum yield generation,[272] a property detrimental to PDT efficacy. Therefore, strap length for integration in PSs must be tuned to ensure planarity. Glycosyl containing single strapped porphyrins were studied as PSs and compared to hematoporphyrin derivative. The porphyrins were prepared by a BF_3 catalyzed direct condensation of a dipyrromethane and dialdehyde. A mixture of 5,10- and 5,15-single strapped porphyrins were derived with the latter showing enhanced phototoxicity *in vitro*.[273] Double strapped systems, specifically calix[4]pyrroles have been demonstrated to act as synthetic transmembrane carriers with the *cis*-αα configuration providing a suitable aromatic cavity for proline transport.[274] The potential for these systems to enhance cellular uptake is high.

In this work, we aimed to introduce strapped linkages to porphyrins intended to alter membrane passage. Alkyl and phenyl straps were used to lock rotation of three meso-tetraarylporphyrins. Polar phenyl substituents were incorporated to achieve enhanced membrane permeation for the *cis*-αα isomer. Direct condensation methods were employed to pursue both *cis*-isomers which could be compared *in vitro*. Structural elucidation was assisted through a combination of NMR spectroscopy and single crystal X-ray crystallography. Photophysical studies provided insight into the relative planarity between isomers. The isomers *cis*-αα, *cis*-αβ and *trans*-αβ are analogous in configuration to porphyrin atropisomers, α_4, $\alpha_2\beta_2$ and αβαβ respectively. Membrane passage was determined in two cell lines with the *cis*-αα isomer exhibiting preferential uptake, illustrating the advantage of the α_4 motif to enhance internalization.

3.3 MATERIALS AND METHODS

3.3.1 General synthetic and analytical methods

All chemicals were commercially sourced and used without further purification. Analytical TLC was performed using silica gel 60 (fluorescence indicator F_{254}, pre-coated sheets, 0.2 mm thick, 20 cm × 20 cm; Merck) plates and visualized by UV irradiation (λ =254 nm). Column chromatography was carried out using Fluka Silica Gel 60 (230–400 mesh; Merck). NMR spectra were recorded on a Bruker AV 600, Bruker Advance III 400 MH or a Bruker DPX400 400 MHz or an Agilent 400 spectrometer. Accurate mass measurements (HRMS) were carried out using a Bruker microTOF-Q™ ESI-TOF mass spectrometer. Mass spectrometry was performed with a Q-Tof Premier Waters MALDI quadrupole time-of-flight (Q-TOF) mass spectrometer equipped with Z-spray electrospray ionization (ESI) and matrix-assisted laser desorption ionization (MALDI) sources in positive mode with *trans*-2-[3-(4-*tert*-butylphenyl)-2-methyl-2-propenylidene]malononitrile as the matrix. ESI mass spectra were acquired in positive modes as required, using a Micromass time-of-flight mass spectrometer (TOF) interfaced to a Waters 2960 HPLC or a Bruker microTOF-Q III spectrometer interfaced to a Dionex UltiMate 3000 LC. Atmospheric pressure chemical ionization (APCI) experiments were performed on a Bruker microTOF-Q III spectrometer interfaced to a Dionex UltiMate 3000 LC. Melting points were measured using an automated melting point meter, SMP50 (Stuart), and are uncorrected.

3.3.2 Dialdehyde synthesis

Dialdehyde 1: 1,6-Bis(2-formyl-4-nitro-phenoxy)hexane

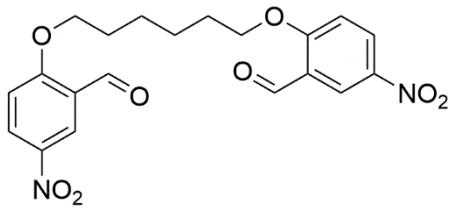

5-Nitrosalicylaldehyde (1.0856 g, 6.5 mmol) and K_2CO_3 (716.2 mg. 5.18 mmol) were dried under high vacuum. Anhydrous DMF (8 mL) was added and the solution was stirred at 60 °C for 1 h prior to the addition of 1,5-dibromohexane (417.2 mg, 1.71 mmol). The reaction mixture was stirred at 80 °C under Ar overnight. DMF was evaporated by high vacuum distillation. The residue was washed with CH_2Cl_2 and EtOH (250 mL). Solvent was removed under reduced pressure. The resulting residue was recrystallized three times from EtOH (75 °C) to yield a pale white solid (663.3 mg, 1.59 mmol, 95%). M.p. = 205 °C; R_f = 0.80 (EtOAc:n-hexane, 9:1); ^{1}H NMR (600 MHz, DMSO-d_6): δ = 10.32 (s, 2H, CHO), 8.48 (dd, J = 9.2, 3.0 Hz, 2H, Ar-H), 8.40 (d, J = 3.0 Hz, 2H, Ar-H), 7.47 (d, J = 9.3 Hz, 2H, Ar-H), 4.32 (s, 4H, CH_2), 1.89 – 1.85 (m, 4H, CH_2), 1.56 ppm (s, 4H, CH_2); ^{13}C NMR (151 MHz, DMSO-d_6): δ = 188.02, 187.98, 165.06, 140.66, 130.98, 123.92, 123.55, 114.70, 69.65, 28.09, 24.85 ppm; HRMS (APCI): *m/z* calc. for $C_{20}H_{20}N_2O_8$ $[M]^+$: 416.1220; found $[M + Na^+]$ 417.1292.

Dialdehyde 2: 1,3-Bis(2-formyl-4-nitro-phenoxy)xylene

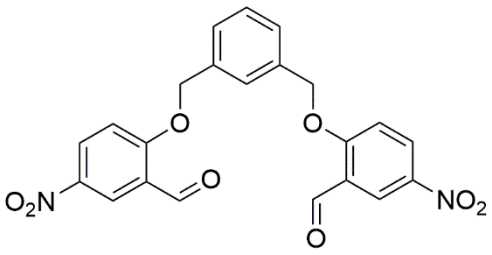

5-Nitrosalicylaldehyde (503.2 mg, 3.01 mmol) and K_2CO_3 (278.8 mg. 2.02 mmol) were dried under high vac. Anhydrous DMF (3.5 mL) was added and the solution was stirred at 60 °C for 1 h prior to the addition of α,α‘–dibromo-*m*-xylene (263.9 mg, 0.0.997mmol). The reaction mixture was stirred at 80 °C under Ar overnight. DMF was evaporated by high vacuum distillation. The residue was washed with CH_2Cl_2 and EtOH (100 mL).

Solvent was removed under reduced pressure. The resulting residue recrystallized three times from EtOH (75 °C) to yield a pale white solid (181 mg, 0.41 mmol, 42%). M.p. = 191 - 193 °C; R_f = 0.17 (CH_2Cl_2); ^{1}H NMR (600 MHz, $CDCl_3$): δ = 10.49 (s, 2H, CHO), 8.73 (d, J = 2.9 Hz, 2H, Ar-H), 8.43 (dd, J = 9.2, 2.9 Hz, 2H, Ar-H), 7.57 – 7.45 (m, 4H, Ar-H), 7.19 (d, J = 9.2 Hz, 2H, Ar-H), 5.36 ppm (s, 4H, CH_2); ^{13}C NMR (151 MHz, $CDCl_3$): δ = 187.41, 187.37, 164.46, 142.10, 135.73, 130.77, 129.92, 128.04, 126.38, 125.14, 113.48, 71.24 ppm; HRMS (ESI): *m/z* calc. for $C_{22}H_{16}N_2O_8$ $[M]^+$: 436.0907; found [M + Na^+] 459.0803.

Dialdehyde 3: Dimethyl 4,4'-((1,4-phenylenebis(methylene))bis(oxy))bis(3-formylbenzoate)

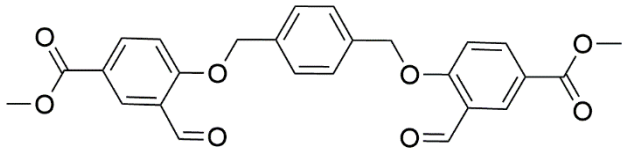

Methyl 3-formyl-4-hydroxybenzoate (1 g, 5.55 mmol) and K_2CO_3 (920.44 mg. 6.66 mmol) were dried under high vacuum. Anhydrous DMF (15 mL) was added and the solution was stirred at 60 °C for 1 h prior to the addition of α-α'-dibromo-*p*-xylene (585.99 mg, 2.22 mmol). The reaction mixture was stirred at 80 °C under Ar overnight. DMF was evaporated by high vacuum distillation. The residue was washed with CH_2Cl_2 followed by acetone (100 mL). Solvent was removed under reduced pressure to yield a pale-yellow solid (1.9565 g, 4,.231 mmol, 96%). M.p. = 219 - 221 °C; R_f = 0.17 (CH_2Cl_2); ^{1}H NMR (400 MHz, $CDCl_3$): δ = 10.53 (s, 2H, CHO), 8.53 (d, J = 2.3 Hz, 2H, Ar-H), 8.23 (dd, J = 8.8, 2.3 Hz, 2H, Ar-H), 7.50 (s, 4H, Ar-H), 7.11 (d, J = 8.8 Hz, 2H, Ar-H), 5.29 (d, J = 3.2 Hz, 4H, CH_2), 3.91 ppm (s, 6H, CH_3); ^{13}C NMR (101 MHz, $CDCl_3$): δ = 188.70, 165.93, 163.71, 137.10, 135.77, 135.53, 130.79, 127.84, 112.77, 70.41, 52.22, 30.93 ppm; HRMS (ESI): *m/z* calc. for $C_{26}H_{22}O_8$ $[M]^+$: 462.1315; found [M + Na^+] 485.1233.

3.3.3 Synthesis of strapped porphyrins

Strapped porphyrins 4 via Lindsey condensation

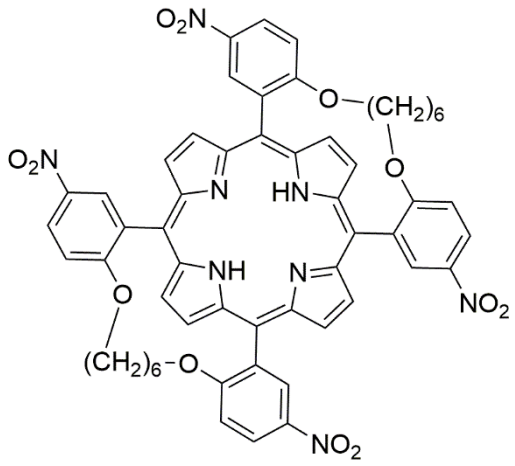

1,6-Bis(2-formyl-4-nitro-phenoxy)hexane (1.09 g, 2.62 mmol) was dissolved in CH_2Cl_2 (750 mL) and pyrrole (351.26 mg, 5.24 mmol) was added to the solution. The mixture was purged with Ar for 15 minutes prior to the addition of BF_3•OEt_2 (520.15 mg, 3.66 mmol). The reaction mixture was shielded from light and stirred overnight at rt. DDQ (2.082 g, 9.17 mmol) was added to the solution and stirred for an additional 2 h. A color change of orange/red to black/purple was observed. The mixture was quenched by the addition of TEA (318.14 mg, 3.14 mmol). The solution volume was reduced to half by removal of solvent under reduced pressure. The resulting crude residue was filtered through a short silica column (CH_2Cl_2:EtOAc, 98:2, v/v). The mixture of two strapped porphyrins which was separated by a second column (CH_2Cl_2:n-hexane, 98:2, v/v).

***cis*-αβ-4**

Removal of solvent under reduced pressure, from the first fraction, ***cis*-αβ-4**, yielded a red solid (6 mg, 0.586 mmol, 0.22%). M.p. > 300 °C; R_f = 0.45 (CH_2Cl_2:EtOAc, 98:2, v/v); ^{1}H NMR (600 MHz, $CDCl_3$/TFA-d_1 excess): δ = 9.18 (s, 8H, CH_{beta}), 8.84 (d, J = 9.2 Hz, 4H, Ar-H), 8.80 (s, 4H, Ar-H), 7.49 (d, J = 9.3 Hz, 4H, Ar-H), 4.13 (s, 1H, CH_2), 3.91 (s, 4H, CH_2), 1.11 (d, J = 35.7 Hz, 4H, CH_2), 0.66 (s, 4H, CH_2), 0.43 – 0.26 ppm (m, 8H, CH_2); ^{13}C NMR (151 MHz, $CDCl_3$/ TFA-d_1 excess): δ = 185.59, 164.04, 159.60, 159.32, 159.05, 158.77, 146.01, 144.57, 141.30, 130.84, 130.34, 128.69, 128.33, 117.26, 116.70, 115.36, 113.47, 112.49, 111.58, 70.26, 29.85, 28.81, 26.34, 14.25 ppm; UV-vis (DMSO) λ_{max} ($M^{-1}.cm^{-1}$) = 424 (210,300), 516 (11,330), 590 (3513), 647 nm (1237); HRMS (MALDI LD$^+$): *m/z* calc. for $C_{56}H_{46}N_8O_{12}$ $[M]^+$: 1022.3235; found 1022.3198.

***cis*-αα-4**

The crude second fraction (58.7 mg, 0.0574 mmol) was dissolved in CH_2Cl_2 (20 mL) and stirred at rt. $Zn(OAc)_2$•$2H_2O$ (126.2 mg, 0.575 mmol) dissolved in MeOH (3 mL), was added to the solution and stirred overnight at rt. Removal of solvent occurred under reduced pressure. The resulting residue was dissolved in CH_2Cl_2 and washed sequentially with H_2O (× 3). The organic layer was dried over $MgSO_4$ and the solvent removed under reduced pressure to yield a red solid. Recrystallization from EtOAc (75 °C) was set-up to remove 1,6-bis(2-formyl-4-nitro-phenoxy)hexane **1** impurity. Cooling of the solution to rt resulted in dialdehyde **1** precipitation which was separated by filtration. EtOAc of the filtrate was removed under reduced pressure. Column chromatography with CH_2Cl_2:EtOAc (99:1, v/v) yielded pure Zn strapped porphyrin **4**. M.p. > 300 °C; R_f = 0.16 (CH_2Cl_2); HRMS (ESI): *m/z* calc. for $C_{56}H_{46}N_8O_{12}Zn$ $[M]^+$: 1084.2370, found $[M+H^+]$ 1085.2443. Removal of Zn was achieved by stirring in CH_2Cl_2 (20 mL) and TFA (1.5 mL) at rt for 1 h. The solvent was removed under reduced pressure and the resulting residue dissolved in CH_2Cl_2, washed sequentially with sat. aq. $NaHCO_3$ twice and deionized H_2O. The organic layer was dried over $MgSO_4$ and the solvent removed under reduced pressure. Column chromatography (CH_2Cl_2) purification was used to yield a red solid, ***cis*-αα-4** (14 mg, 0.137 mmol, 0.52%). M.p. > 300 °C; R_f = 0.29 (CH_2Cl_2:EtOAc, 98:2, v/v); ^{1}H NMR (400 MHz, $CDCl_3$/ TFA excess): δ = 9.06 (s, 4H, Ar-H), 8.95 (s, 1H, CH_{beta}), 8.92 – 8.85 (m, 4H, Ar-H), 8.78 (s, 4H, CH_{beta}), 7.62 (d, J = 9.4 Hz, 4H, CH_2), 4.30 (t, J = 9.4 Hz, 4H, CH_2), 4.23 – 4.14 (m, 4H, CH_2), 1.48 (d, J = 13.2 Hz, 4H, CH_2), 1.02 (s, 4H, CH_2), 0.88 – 0.64 (m, 8H, CH_2), -1.69 ppm (d, J = 38.8 Hz, 2H, NH); ^{13}C NMR (101 MHz, $CDCl_3$/ TFA excess): δ = 164.27, 146.18, 145.62, 140.68, 139.80, 132.65, 130.11, 129.14, 128.32, 125.70, 116.60, 116.03, 115.00, 113.38, 113.21, 112.17, 70.66, 29.62, 28.61, 26.03 ppm; UV-vis (DMSO) λ_{max} ($M^{-1}.cm^{-1}$) = 424 (227,600), 516 (12,090), 590 (3469), 647 nm (1100); HRMS (MALDI LD^+): *m/z* calc. for $C_{56}H_{46}N_8O_{12}$ $[M]^+$: 1022.3235; found 1022.3193.

Strapped porphyrins 5 via Adler- Longo condensation

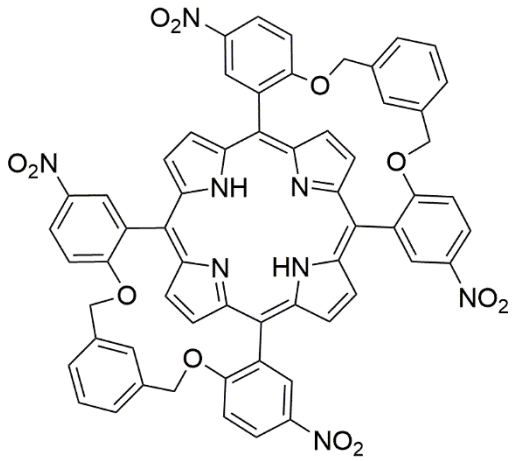

1,3-Bis(2-formyl-4-nitro-phenoxy)xylene (904.1 mg, 2.07 mmol) was dissolved in propionic acid (40 mL) at 100 °C. An addition of pyrrole (277.75 mg, 4.14 mmol) was made to the solution. The mixture was shielded from light and refluxed at 150 °C for 4 h. A color change of yellow to black/purple was observed. $CH_3CH_2CO_2H$ was evaporated by distillation under high vacuum. The resulting crude residue was filtered through a short silica column (CH_2Cl_2). The complete purification was performed through a repetitive silica gel column chromatography. An initial column with CH_2Cl_2:EtOAc (98:2, v/v) separated the ***trans*-αβ-5** as the first fraction and a mixture of the *cis* strapped porphyrins which was followed by a second column ($CHCl_3$:EtOAc 96:4, v/v) to separate the mixture.

***trans*-αβ-5**

The first fraction which eluted from the column was dried under reduced pressure to yield a red solid, ***trans*-αβ-5**, (2.0 mg, 0.018 mmol, 0.1%). M.p. > 300 °C; R_f = 0.29 (CH_2Cl_2:EtOAc, 98:2, v/v); ^{1}H NMR (400 MHz, CD_3CN/TFA excess): δ = 9.76 (d, J = 2.8 Hz, 4H, Ar-H), 8.97 (s, 8H, CH_{beta}), 8.59 (dd, J = 9.0, 2.8 Hz, 4H, Ar-H), 7.00 (d, J = 9.0 Hz, 4H, Ar-H), 6.47 (t, J = 7.6 Hz, 2H, Ar-H), 5.89 (dd, J = 7.6, 1.6 Hz, 4H, Ar-H), 5.10 (d, J = 3.7 Hz, 2H, Ar-H), 3.85 ppm (s, 8H CH_2); ^{13}C NMR (101 MHz, CD_3CN/TFA excess): δ = 162.90, 142.08, 141.68, 140.45, 133.68, 132.56, 128.09, 127.95, 127.07, 126.56, 123.31, 118.96, 116.22, 116.20, 116.19, 116.13, 116.09, 116.07, 116.05, 116.03, 113.43, 113.38, 113.36, 113.34, 113.30, 110.51, 71.31, 29.71, 29.39, 29.27, 22.78, 13.10, 12.94 ppm; HRMS (MALDI LD$^+$): *m/z* calc. for $C_{60}H_{38}N_8O_{12}$ $[M]^+$: 1062.2609; found 1062.2638.

***cis*-αβ-5**

The first fraction which eluted from the second column was dried under reduced pressure to yield a red solid, ***cis*-αβ-5**, (5.6 mg, 0.053 mmol, 0.25%). M.p. > 300 °C; R_f = 0.44 ($CHCl_3$:EtOAC, 98:2, v/v); ^{1}H NMR (400 MHz, CD_3CN/TFA excess): δ = 9.47 (s, 4H, CH_{beta}), 9.29 (d, *J* = 2.0 Hz, 4H, Ar-H), 9.21 (s, 4H, CH_{beta}), 8.89 (dd, *J* = 9.2, 2.7 Hz, 4H, Ar-H), 7.72 (d, *J* = 9.3 Hz, 4H, Ar-H), 7.22 (s, 2H, Ar-H), 6.60 (d, *J* = 7.3 Hz, 4H, Ar-H), 6.48 (t, *J* = 7.4 Hz, 2H, Ar-H), 5.28 (d, *J* = 9.7 Hz, 4H, CH_2), 4.78 ppm (d, *J* = 9.7 Hz, 4H, CH_2)[v]; UV-vis (DMSO) λ_{max} ($M^{-1}.cm^{-1}$) = 427 (21,325), 519 (925), 594 (668), 647 nm (79); HRMS (MALDI LD$^+$): *m/z* calc. for $C_{60}H_{38}N_8O_{12}$ $[M]^+$: 1062.2609; found 1062.2614.

***cis*-αα-5**

Removal of solvent under reduced pressure, from the third fraction, yielded a red solid, **cis-αα-5**, (22.6 mg, 0.212 mmol, 1%). M.p. > 300 °C; R_f = 0.67 ($CHCl_3$:EtOAc, 98:2, v/v), ^{1}H NMR (400 MHz, CD_3CN/TFA excess): δ = 9.18 (d, J = 2.7 Hz, 4H, Ar-H), 9.14 (s, 4H, CH_{beta}), 8.94 (dd, J = 9.2, 2.7 Hz, 4H, Ar-H), 8.87 (s, 4H, CH_{beta}), 7.90 (d, *J* = 9.3 Hz, 4H, Ar-H), 7.77 (s, 2H, Ar-H), 6.95 (d, *J* = 7.6 Hz, 4H, Ar-H), 6.89 – 6.82 (m, 2H, Ar-H), 5.67 (d, *J* = 10.0 Hz, 4H, CH_2), 5.00 ppm (d, *J* = 10.0 Hz, 4H, CH_2); ^{13}C NMR (101 MHz, CD_3CN/TFA excess): δ = 162.84, 146.12, 145.77, 141.63, 135.31, 134.10, 129.84, 128.82, 128.24, 127.41, 118.90, 116.07, 112.81, 110.41, 71.79 ppm; UV-vis (DMSO) λ_{max} ($M^{-1}.cm^{-1}$) = 428 (81,510), 519 (5199), 594 (2105), 648 nm (1981); HRMS (MALDI LD$^+$): *m/z* calc. for $C_{60}H_{38}N_8O_{12}$ $[M]^+$: 1062.2609; found 1062.2558.

[v] ^{13}C NMR was not possible to obtain due to low solubility

Strapped porphyrins 6[vi]

COOMe-*cis*-*αα*-6 via Lindsey condensation

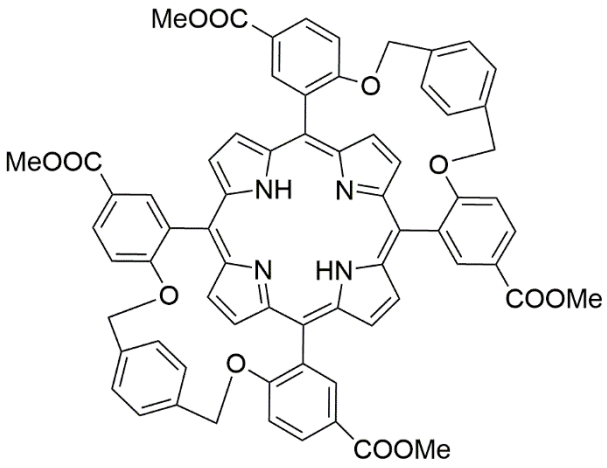

Dimethyl 4,4'-[(1,4-phenylenebis(methylene)bis(oxy)]bis(3-formylbenzoate)] (2 g, 4.23 mmol) and pyrrole (0.6 mL, 8.46 mmol) were dissolved in chloroform (1.4 L) and the solution was shielded from light and purged with an Ar stream for 20 min, followed by the addition of BF_3•OEt_2 (730 µL, cat.). The reaction mixture was stirred at r.t. for 24 h under an Ar atmosphere. DDQ (3g, 13.12 mmol) was added and the reaction mixture was stirred for an additional 2h. The reaction was quenched by the addition of TEA (3 mL), and the crude product was filtered through a short silica column. The complete purification was performed through a silica gel column chromatography using CH_2Cl_2:EtOAc (50:1, v/v) as eluent. The first fraction was collected. Solvents were removed under reduced pressure and recrystallization from CH_2Cl_2 and ethanol was carried out to obtain the product as a purple crystalline solid (61 mg, 55.41 µmol, 1.3%). M.p. > 300 °C; R_f = 0.33 (CH_2Cl_2: EtOAc, 50:1, v/v); ^{1}H NMR (600 MHz, $CDCl_3$): δ = 8.78 (s, 4H, CH_{beta}), 8.67 (d, J = 2.2 Hz, 4H, Ar-H), 8.52 (dd, J = 8.8, 2.2 Hz, 4H, Ar-H), 7.87 (s, 4H, CH_{beta}), 7.61 (d, J = 8.9 Hz, 4H, Ar-H), 5.13 (d, J = 1.1 Hz, 8H, CH_2), 3.90 (s, 12H, CH_3), -2.90 ppm (s, 2H, NH); ^{13}C NMR (151 MHz, $CDCl_3$): δ = 167.32, 163.84, 136.89, 136.74, 133.80, 132.32, 123.12, 116.89, 115.07, 52.47 ppm; UV-vis (CH_2Cl_2) λ_{max} ($M^{-1}.cm^{-1}$) = 426 (288,403), 519 (10,233), 588 nm (10,233); HRMS (ESI): *m/z* calc. for $C_{68}H_{51}N_4O_{12}$ $[M]^+$: 1115.34980; found 1115.352107.

[vi] Strapped porphyrins 6 were prepared by undergraduate student, Sophie Maguire

COOH-*cis*-*αα*-6 via basic hydrolysis

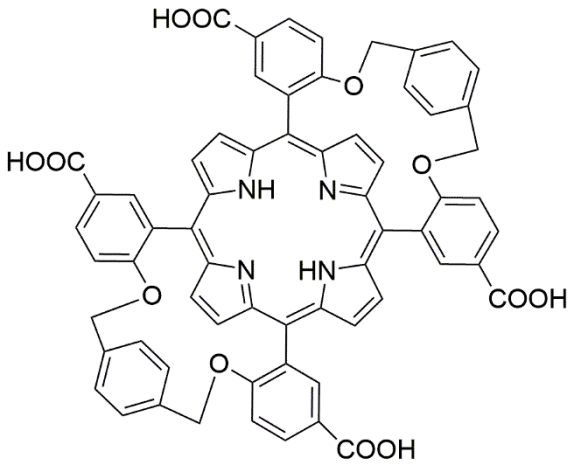

Strapped porphyrin **COOMe-*cis*-*αα*-6** (38 mg, 0.03384 mmol) was added to a 100 mL round bottom flask containing MeOH (30 mL) and THF (45 mL). KOH (0.4756 g, 8.476 mmol) dissolved in water (10 mL) was added. The reaction mixture was refluxed at 100 °C for 60 h and cooled to rt. Solvents were removed under reduced pressure and the solution was acidified to pH 5 with hydrochloric acid (1 M) to precipitate the product. Solid was isolated by filtration and washed with water (3×15 mL). The purple solid was oven dried for 3 days (37.5 mg, 99%, 0.0335 mmol). M.p. > 300 °C; R_f = 0.54 (DCM: EtOH, 100:1, v/v); ^{1}H NMR (400 MHz, DMSO-d_6): δ = 12.94 (s, 4H, COOH), 8.72 (s, 4H, CH_{beta}), 8.53-8.50 (m, 8H, Ar-H), 8.14 (s, 4H, CH_{beta}), 7.95 (d, J = 8.8 Hz, 4H, Ar-H), 5.44 (d, J = 11.6 Hz, 4H, CH_2), 5.06 (d, J = 11.4 Hz, 4H, CH_2), -3.24 ppm (s, 2H, NH);^{13}C NMR (151 MHz, DMSO-d_6): δ = 167.65, 163.22, 136.89, 136.25, 132.53, 132.15, 128.57, 123.29, 116.93, 115.19, 74.14.ppm; UV-vis (THF) λ_{max} ($M^{-1}.cm^{-1}$) =424 (51,287), 519 (2818), 555 nm (1096); HRMS (ESI): *m/z* calc. for $C_{64}H_{43}N_4O_{12}$ $[M+H]^+$: 1059.287199; found 1059.284924.

COOMe-*trans*-αβ-6 via Adler- Longo condensation

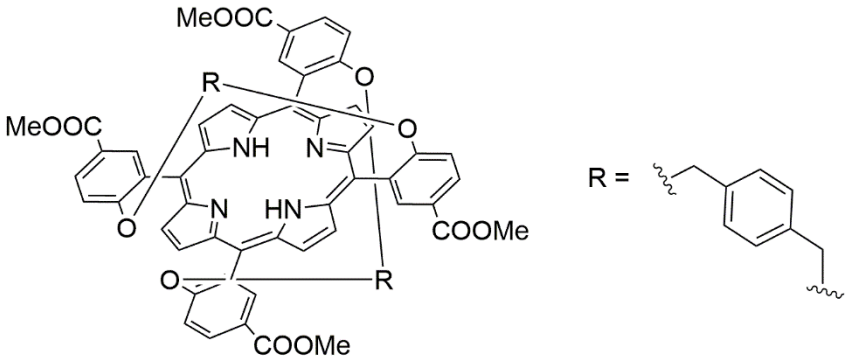

Dimethyl 4,4'-[(1,4-phenylenebis(methylene)bis(oxy)]bis(3-formylbenzoate)) (700 mg, 1.51 mmol) was added to a 100 mL flask and dissolved in propionic acid (50 mL). The mixture was heated to 100 °C, and pyrrole (209 µL, 3.03 mmol) was added dropwise. The reaction mixture was shielded from light and left stirring under reflux at 150 °C for 3 h. After reaction completion, propionic acid was removed through vacuum distillation and the crude product was filtered through a short silica column using CH_2Cl_2:MeOH (99:1). Complete purification was performed via column chromatography using CH_2Cl_2/EtOH (gradient 99.9:0.1 to 98:2). After removing the solvents under reduced pressure, the desired product was obtained as a purple crystalline solid (8 mg, 7.17 µmol, 0.5%). M.p > 300 °C; R_f = 0.27 (CH_2Cl_2: EtOH, 100:1, v/v); ^{1}H NMR (600 MHz, $CDCl_3$): δ = 9.48 (d, J = 2.2 Hz, 4H, Ar-H), 8.69 (s, 8H, CH_{beta}), 8.32 (dd, J = 8.4, 2.2 Hz, 4H, Ar-H), 6.78 (d, J = 8.5 Hz, 4H, Ar-H), 4.19 (s, 8H, Ar-H), 4.10 (s, 12H, CH_3), 3.94 (s, 8H, CH_2), -0.26 ppm (s, 2H, NH); ^{13}C NMR (151 MHz, $CDCl_3$) δ = 167.75, 162.69, 134.37, 132.73, 130.53, 130.40, 125.19, 122.53, 113.15, 112.40, 69.71, 52.63.ppm; UV-vis ($CHCl_3$) λ_{max} ($M^{-1}.cm^{-1}$) = 426 (58,884), 521 (4467), 598 nm (1950); HRMS (APCI): *m/z* calc. for $C_{68}H_{51}N_4O_{12}$ $[M]^+$: 1115.34980; found 1115.347064.

COOH-*trans*-αβ-6 via basic hydrolysis

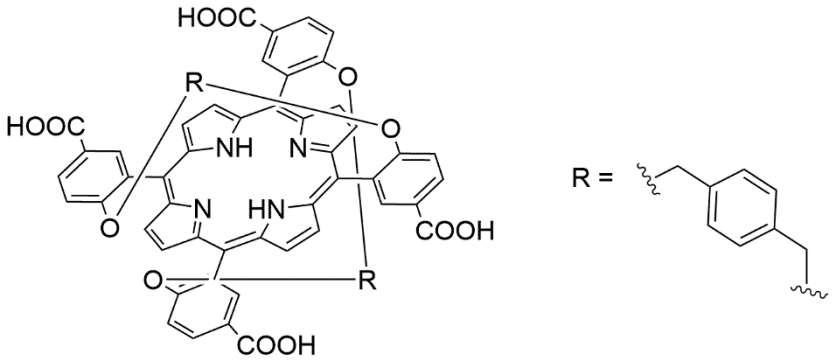

Strapped porphyrin **COOMe-*trans*-αβ-6** (11 mg, 9.8 μmol) was added to a 100 mL round bottom flask containing MeOH (20 mL) and THF (30 mL). KOH (120 mg, 2.15 mmol) dissolved in water (10.0 mL) was added. The reaction mixture was refluxed at 100 °C for 60 h and cooled to rt. Solvents were removed under reduced pressure and the solution was acidified to pH 5 with hydrochloric acid (1 M) to precipitate the product. Solid was isolated by filtration as a purple solid (10 mg, 96%, 9.4 μmol). M.p. > 300 °C; R_f = 0.54 (CH_2Cl_2: EtOH, 100:1, v/v); ^{1}H NMR (400 MHz, THF-d_8) δ = 10.86 (s, 4H, COOH), 9.48 (d, J = 2.0 Hz, 4H, Ar-H), 8.71 (s, 8H, CH_{beta}), 8.31 (dd, J = 8.4, 1.9 Hz, 4H, Ar-H), 6.91 (d, J = 8.5 Hz, 4H, Ar-H), 4.23 (s, 8H, Ar-H), 4.00 (s, 8H, CH_2), -0.15 (s, 2H, NH) ppm; ^{13}C NMR (101 MHz, THF-d_8) δ = 168.04, 163.41, 145.23, 135.54, 133.40, 131.49, 131.24, 131.15, 125.65, 123.96, 114.36, 112.99, 108.57, 108.48, 107.12, 104.65, 70.12 ppm; UV-vis (THF) λ_{max} ($M^{-1}.cm^{-1}$) = 434 (5623), 527 (417), 607 nm (151).

3.3.4 Synthesis of protected dialdehyde

Dialdehyde 9: 1,3-Bis(2-(1,3-dioxolan-2-yl)-4-nitrophenoxy)xylene

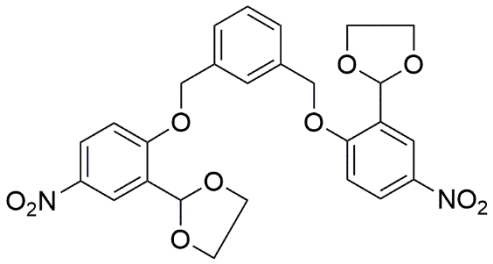

1,3-Bis(2-formyl-4-nitro-phenoxy)xylene, dialdehyde **2** (20.3 mg, 0.46 mmol) was dissolved in dry benzene (20 mL). Additions of *p*TsOH (3 mg, 0.017 mmol) and ethylene glycol, (30 uL, 0.53 mmol) were made and the reaction mixture was purged with Ar. The mixture was heated under Ar in a Dean-Stark apparatus for 24 h. The cooled reaction

mixture was dried under reduced pressure, redissolved in EtOAc and washed with brine (20 mL) three times prior to drying over $MgSO_4$. Solvent was removed under reduced pressure to yield a yellow oil (30.1 mg) which was used immediately to for reduction attempt. M.p. = 139-140 °C; R_f = 0.24 (CH_2Cl_2); ^{1}H NMR (600 MHz, $CDCl_3$): δ = 8.45 (d, J = 2.8 Hz, 2H, Ar-H), 8.21 (dd, J = 9.0, 2.9 Hz, 2H, Ar-H), 7.53 – 7.39 (m, 4H, Ar-H), 6.98 (d, J = 9.1 Hz, 2H, Ar-H), 6.20 (s, 2H, CH), 5.27 (s, 4H, CH_2), 4.20 – 4.11 ppm (m, 4H,CH_2), 4.09 – 4.01 (m, 4H, CH_2); ^{13}C NMR (151 MHz, $CDCl_3$): δ = 161.38, 136.21, 127.97, 127.17, 126.36, 125.78, 123.49, 111.95, 98.35, 70.59, 65.49 ppm; HRMS (APCI): *m/z* calc. for $C_{26}H_{24}N_2O_{10}$ $[M]^+$: *m/z* calcd. 524.1431; found $[M + Na^+]$ 547.1323.

3.3.5 X-Ray Crystallographic analyses of strapped-porphyrins **4**[vii]

Crystals of the separated strapped porphyrins **4** were grown by the following procedures: the *cis*-αβ-**4** and *cis*-αα-**4** samples were dissolved in dichloromethane and layered with hexane. Samples were left to diffuse over the course of one week and crystals appeared at the side of the crystallization tube.

A diffraction pattern was collected for each of the two crystals on a Bruker APEX-II DUO device, with an Oxford Cobra Cryosystem low temperature device using a MiTeGen micromount. Using the OLEX2 Software Package,[275] the structure was solved with the SHELXT structure solution program[217] using Intrinsic Phasing and refined with the SHELXL refinement package[218] with Least Squares minimization. Data reductions were performed with the Bruker APEX3 package[276] and SAINT;[277] structures were solved with SHELXT11 and refined with ShelXL[217] in the Shelxle GUI.[218] Data were corrected for absorption effects using the Multi-Scan method (SADABS).[278] Images were generated with OLEX2 software package.[275] Critical values related to the crystal structure refinement are in Table S 3.

[vii] The crystallographic data was collected and analyzed by Dr. Brendan Twamley

Refinement details:

***cis*-αβ-4**

For the half molecules in the asymmetric unit, pyrrole hydrogens were located and refined with restraints (DFIX). One of these has disorder in one nitro group position, modelled in two positions, 63:37% occupancy, with restraints (SADI, SIMU). There was also disorder in the hexyl chain linker (O56-C60) and this was modelled in two positions, 52:48% occupancy, with restraints (SAID, ISOR).

***cis*-αα-4**

Disorder was seen in both 1,6-bis(4-nitrophenoxy)hexane substituents with complete disorder seen in C25-C44 (87:13% occupancy) and disorder in the remaining nitrophenlhexyl moiety C45-C57 (78:22% occupancy). Disorder was modelled with restraints (SADI, DFIX, SIMU and DANG). Pyrrole hydrogens were located on the difference map and refined with restraints (DFIX).

3.3.6 Photophysical and photochemical evaluation of strapped porphyrins

Absorption spectra of strapped porphyrins were recorded on an Agilent Cary5000 UV-VIS-NIR spectrometer. ε were obtained from absorption measurements of three solutions of different concentrations, diluted from two stock solutions with independently measured masses. The slope of the plot absorption vs. concentration was used to calculate ε.

Further photophysical characterization of strapped porphyrins were carried out with emission and excitation spectra recorded on a Horiba-JY Fluoromax4 spectrofluorometer. Strapped-porphyrin absolute values of Φ_F, obtained for each strapped porphyrin, were measured using the absolute method with a Hamamatsu Quantaurus QY absolute photoluminescence quantum yield spectrometer model C11347 (integration sphere). Solutions with absorbance < 0.1 were used.

The Φ_Δ were recorded once in a Horiba-Jovin-Yvon Spex Fluorog 3-2.2 spectrophotometer using the near-infrared Hamamatsu R5509–42 photomultiplier, cooled to 193 K in a liquid nitrogen chamber. The singlet oxygen yield reference was phenalenone (Φ_Δ = 0.95).[223] A band-pass filter (Newport, 10LWF-1000-B, AE23) facilitated collection of phosphorescence intensity between 1240 and 1340 nm. The wavelength of excitation, integration time and slits was 424 nm, 1 s, and 14 nm bandwidth (exc.) and 14 nm (em.),

respectively. Samples and reference were prepared in DMSO with absorbance ~0.3 at the excitation wavelength.

3.3.7 Cellular internalization

Cellular internalization of the strapped porphyrins was evaluated according to the methods described in Chapter 2, section 2.3.10 in 4T1 and CT26 cell lines.

For strapped porphyrins **4**, cells were incubated with single isomers, diluted from DMSO stock solutions, at concentration of 0.25 μM for 4 and 24 h. Cells were fixed and fluorescence detection by flow cytometry was carried out using the 405 nm laser with detection on the channel of 615/24 nm.

For strapped porphyrins **6**, cells were incubated with single isomers, diluted from DMSO stock solutions, at concentration of 0.5 uM for 4 and 24 h. Cells were lysed and fluorescence detection of the supernatant was performed with a microplate reader (Biotek Synergy HT) using 420/50 nm excitation and 645/40 nm emission filters. Protein quantification was carried out using the Pierce™ BCA Protein Assay Kit according to the manufacturer's instructions (Thermo Scientific).

3.4 Results and Discussion

3.4.1 Strapped porphyrin synthesis

Double strapped porphyrins were prepared using a direct condensation reaction between a dialdehyde and pyrrole. This approach was favored to ensure *cis*-isomers were the major product, as we aimed to investigate whether the locked *cis*-αα configuration, an analogue of redaporfin α_4, conferred an advantage in membrane passage over other isomers. Linker straps were selected with two requirements. Firstly, the length of the strap needed to be long enough to ensure an absence of macrocycle distortion. Such distortion is inversely proportional to linker length.[175,279] Porphyrin planarity was pursued due to the decrease in singlet oxygen generation which tends to occur with distorted porphyrin macrocycles,[272] inhibiting PS potential.[2] Secondly, it was necessary to ensure that strap length was short enough to prevent flexible s-shaped straps and free rotation.[257] Additionally, the strap chosen was hydrophobic in order to induce amphipathic behavior in the case of *cis*-αα, with hydrophobic straps on one side of the macrocycle and polar hydrogen bonding groups on the other. The simplicity and stability of an alkyl chain strap was first targeted with a hexyl chain. This strap was used for double strapped porphyrin preparation in the absence of

distortion by the Lindsey group with *o,o*'-linked straps. Increase of an alkyl strap length to eight carbons or more was proposed to lead to undesirable, flexible s-shaped conformations.[257]

A series of dialdehydes were prepared by alkylation of the appropriate commercially available salicylaldehyde derivative; 5-nitrosalicylaldehye or 5-(methoxycarbonyl)salicylaldehyde, according to the procedure of Scheme 2A. The alkylation method was adapted, Charisiadis et al.,[280] featured activation of the salicylaldehyde derivative precursor by stirring for 1 h in the presence of K_2CO_3 in DMF prior to the addition of the brominated linker. Dialdehydes **1** – **3** were obtained in adequate yields, suitable for multigram condensation. Similar linker types have been prepared by Wagner et al.[257] and Reddy et al.[177] with comparable yields.

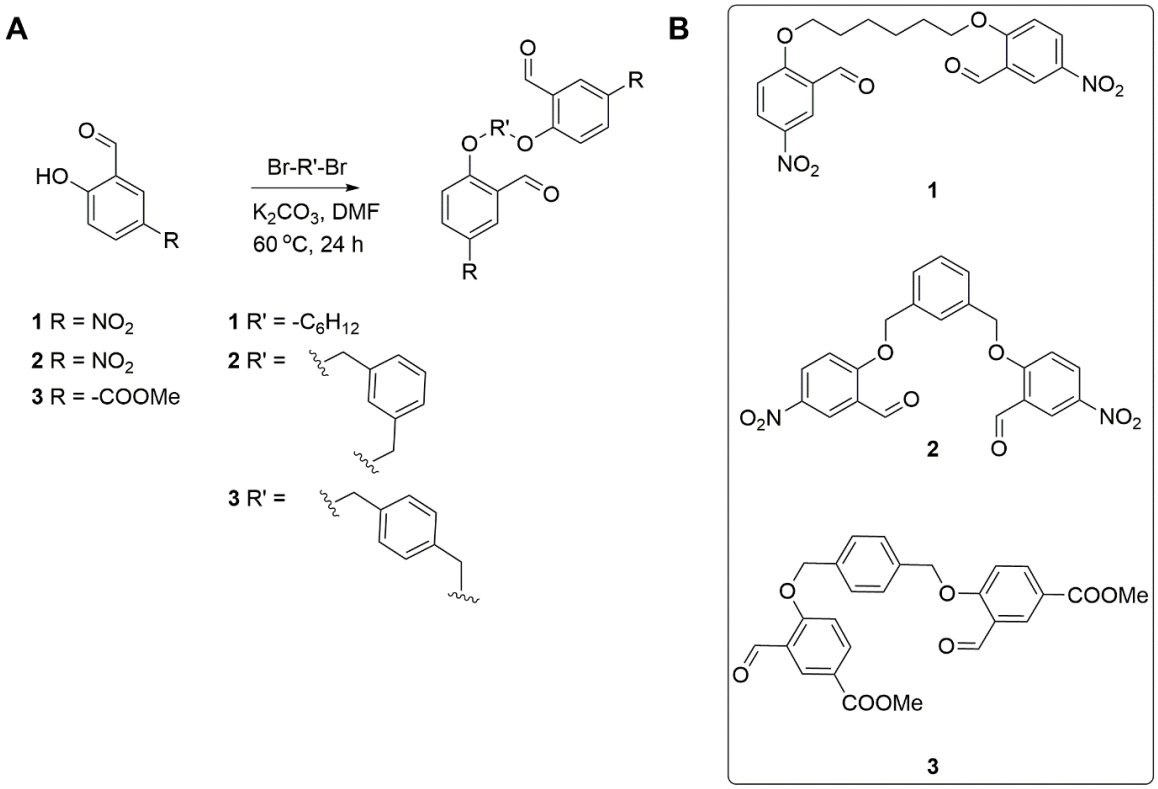

Scheme 2. (A) Synthesis of dialdehydes. (B) Target dialdehydes for strapped porphyrin preparation.

A common obstacle for the preparation of double strapped porphyrin *cis*-isomers is low yields. This was somewhat met by the one-flask synthesis developed by the group of Lindsey.[205] However, the alkyl linker dialdehyde **1** demonstrated limited solubility in solvents acceptable for this strategy including CH_2Cl_2 or $CHCl_3$. As a result, condensation was first attempted using adapted Adler-Longo conditions[262] of refluxing dialdehyde and

pyrrole in propionic acid, originally optimized for direct condensation of pyrrole and dialdehyde by Momenteau et al.[263] Conditions are shown in Scheme 3A. After 3 h of heating at 150 °C, purification by chromatography to remove pyrrole impurities proceeded. Three spots were visible on TLC. The combined porphyrin yield was inadequate (<0.5%) to allow complete characterization following separation. Mass spectrometry analysis (MALDI) indicated that each fraction corresponded to the mass of the targeted strapped porphyrin **4** (Scheme 3B).

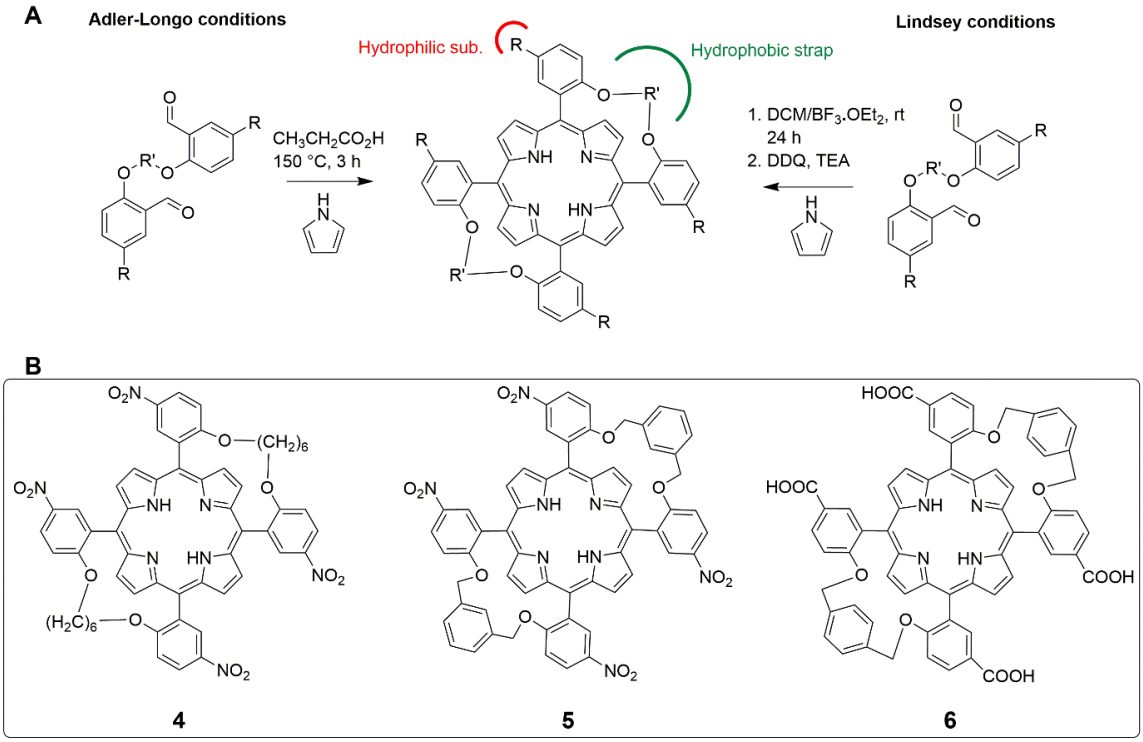

Scheme 3. (A) Condensations of dialdehyde and pyrrole to prepare double strapped porphyrins. (B) Target strapped porphyrins.

As an attempt to improve yield, Lindsey conditions[257] were used under conditions of high dilution. Marginally greater solubility of dialdehyde **1** was observed in CH_2Cl_2 over $CHCl_3$ and was, thus, selected for condensation with BF_3•OEt_2 as a catalyst. After 24 h stirring at rt under argon, DDQ was added as an oxidation step and neutralized with TEA. Two spots with color indicating porphyrin were visible by TLC.

Characterization confirmed that two strapped porphyrins were successfully obtained with Lindsey conditions. A low isolated yield (< 1%) in comparison to similar *o,o*'-linked strapped porphyrins (15%) was attained.[257] This was likely caused by the low solubility of the dialdehyde **1** in CH_2Cl_2 which led to incomplete condensation of starting material. This

was apparent from a dialdehyde peak visible at 10.3 ppm in ^{1}H NMR following porphyrin separation, contaminating the *cis*-αα-**4** porphyrin. The low solubility of the dialdehyde **1** across a variety of organic and aqueous solvents prevented column chromatographic purification of the porphyrin. Metalation with zinc using $Zn(OAc)_2$ in CH_2Cl_2 altered the porphyrin polarity relative to the dialdehyde **1** sufficiently to allow recrystallization from ethyl acetate. The pure Zn-porphyrin **4** subsequently underwent demetallation with TFA to yield the *cis*-αα-**4**. Dialdehyde solubility limited condensation and ultimately led to extensive purification steps which likely contributed to a reduced yield.

Elucidation of the strapped porphyrins **4** configuration was possible due to ^{1}H NMR and single crystal X-ray crystallography. Mass spectrometry (MALDI) analysis and absorption spectra were identical for both strapped porphyrins fractions following separation. The order of elution of similar double strapped porphyrins on silica gel has previously been reported as *trans*-αβ followed by *cis*-αβ and *cis*-αα.[171,263] For the two porphyrin fractions, prepared using Lindsey conditions, retention factors aligned with the latter fraction of the Adler-Longo condensation on TLC. This suggested that the two porphyrins were the *cis*-isomers, which conforms with the almost exclusive formation observed by the Lindsey group during method development for the condensation.[257] While the ^{1}H NMR of the alkyl strap porphyrins (Figure S 12 and Figure S 13) were similar, they displayed distinctive resonances for β-pyrrolic protons. The first fraction displayed eight magnetically equivalent β protons as a singlet. This is generally a feature more consistent with the *trans*-αβ symmetry.[177,263] However, the methylene protons of the hexyl strap did not exhibit the characteristic upfield shift associated with the diamagnetic anisotropy typical of *trans* configurations.[179] The second fraction β-pyrrolic protons split into two singlet resonances in agreement with anticipated C_{2v} symmetry of the *cis*-αα configuration.[263] However, ^{1}H NMR could not unambiguously distinguish the two isomers' configuration alone.

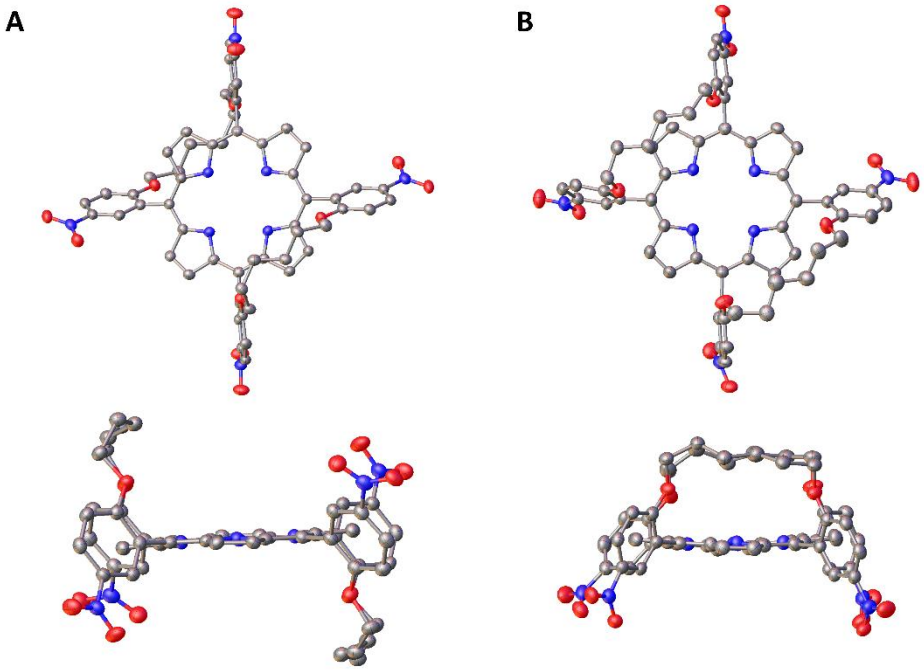

Figure 34. View of the molecular structure in the crystal of (A) *cis*-αβ-**4** and (B) *cis*-αα-**4** isomers. (A) Schematic symmetry generated complete molecules of *cis*-αβ-**4** from the unique half molecules of the asymmetric unit. (B) *cis*-αα-**4** molecular structure with hexane solvent omitted. Major occupied moiety of each isomer represented only. Atomic displacements are at the 50% probability level and hydrogen atoms are omitted for clarity.

Alkyl-strapped porphyrin configurations were both confirmed as *cis*-isomers by single crystal X-ray crystallography. Crystals were grown from the chromatographic fractions and structures could be conclusively assigned as *cis*-αβ for the first fraction to elute and *cis*-αα for the second (Figure 34, Figure S 21 and Table S 3). The order of elution was in agreement with literature sources.[171,177,263] The *cis*-αβ-**4** isomer porphyrin core adopted a primarily planar conformation (Figure 34A). The asymmetric unit was identified as two unique half molecules. The *cis*-αα-**4** isomer (Figure 34B) showed slight saddle deformation. Crystallization occurred as one complete molecule which was highly disordered at both 1,6-bis(4-nitrophenoxy)hexane substituents. Crystals were partially occupied by hexane solvent molecules. The intramolecular hydrogen bonding distances between the pyrrole macrocycle subunits were identical for the *cis*-αβ-**4** isomer as 2.31 Å. The *cis*-αα-**4** isomer demonstrated small deviation between the two bonding distances, 2.33 and 2.31 Å, respectively, consistent with the observed minor deformation. Crystal packing is presented in Figure S 21. Interconversion of the straps at rt was not observed in solution by ^{1}H NMR over approximately one week and the isomer configuration assigned to each fraction were the sole components of each.

To improve double strapped porphyrin yield, dialdehydes with greater solubility under condensation conditions were pursued with phenyl-linked dialdehydes **2** and **3**. A more rigid strap linker may lead to improved strapped porphyrin yields.[257] Both dialdehydes were acquired with similar success to dialdehyde **1** but enhanced chloroform solubility was observed. This facilitated the Lindsey condensation method with dialdehyde **2**. A single spot by TLC was observed after condensation and an initial column chromatography to remove pyrrole impurities. This suggested selective formation of a single, double-strapped porphyrin. Following purification, mass spectrometry analysis (MALDI) revealed that the fraction corresponded to mass of the target double strapped porphyrin **5**. ^{1}H NMR analysis indicated a single double strapped porphyrin with a *cis* configuration due to two characteristics (Figure S 14). β-Pyrrolic protons were observed as two singlet signals. Additionally, the splitting observed for methylene proton peaks at 5.67 and 5.00 ppm, correlated to an equivalent ^{13}C peak at 71.79 ppm by HSQC (Heteronuclear Single Quantum Coherence) analysis. Thus, these methylene carbons were indicated to be potentially orientated in the same environment relative to the macrocycle plane as a *cis*-αα isomer.

Selective formation of a single double strapped porphyrin is unlikely. The Lindsey group[257] was confronted by the same issue during the preparation of a series of *m,m*'-linked strapped porphyrins. They discovered through ^{1}H NMR analysis that the porphyrins were rapidly interconverting. This was unlikely to be the case with strapped-porphyrin **5,** as the Lindsey group had only observed interconversion with longer alkyl strap units.[257] Therefore, it may be possible that the other isomer formed but to such a lower extent that it was not possible to isolate during purification. The preferred formation of *cis*-αα over *cis*-αβ has been previously established, initially by Momenteau et al.[171] for the Adler-Longo condensation and later confirmed for the Lindsey condensation method by the Lindsey group.[257]

The use of the rigid linker in dialdehyde **2** proved beneficial for the Lindsey condensation with an isolated yield of 8.1%. In order to prepare the other isomer, the Adler-Longo condensation method was employed. Three strapped porphyrins were indicated by TLC (Table 6). Repetitive chromatography purification was required to isolate the three fractions. A substantially lower combined yield, 1.25%, was observed for this procedure. The elution order, previously established for porphyrins with similar straps[177] and comparison of ^{1}H NMR, confirmed the dominant Lindsey condensation product as *cis*-αα. The ^{1}H NMR of *trans*-αβ-**5** (Figure S 16) indicated the characteristic features of D_{2d}

symmetry associated with *trans* double strapped porphyrins, such as eight magnetically equivalent β-pyrrolic protons and shielding of the strap's methylene protons due to its position stretching the porphyrin plane.[179] Both *cis*-isomers were formed in a higher proportion with respect to the *trans*-αβ, a common outcome of these reaction conditions.[263]

Table 6. Synthesis of strapped porphyrins

Dialdehyde	Strapped porphyrin	Condensation conditions	Number of porphyrins by TLC	Isolated comb. yield (%)
1	**4**	Adler-Longo	3	< 0.5
1	**4**	Lindsey	2	< 1.0
2	**5**	Lindsey	1	8.14
2	**5**	Adler-Longo	3	1.25
3	**6**	Lindsey	1	1.30
3	**6**	Adler-Longo	2	0.5

The stability of the strapped-porphyrin *cis*-αα-**5** isomer was probed. The *cis*-αα isomer was selected due to the lower thermal stability observed by Urbani et al.[171] An initial attempt was made to induce strap rotation through heating a sample of the strapped porphyrin for 24 h in toluene at 111 °C. However, no conversion was observed. Subsequent attempts in DMF (153 °C) and DMSO (189 °C) lead to no observable conversion by TLC. The strapped porphyrin was deemed stable against conversion at elevated temperatures.

The number of double strapped porphyrins formed varied depending on the condensation protocol employed (Table 6). Lindsey condensation conditions resulted in formation of only *cis* configurations. The Adler-Longo reaction yielded the *cis* configuration with preference over *trans* isomer formation.[263] This trend, which conforms with similar strapped systems in literature, has prompted alternative preparative strategies specific to the *trans* isomer including post-functionalization of the porphyrin with the strap[263] or condensation between a bis-dipyrromethene and dialdehyde.[261] In both the Lindsey and Adler-Longo condensations, the *cis*-αα isomer dominated, consistent in the preparation of double strapped porphyrins with both respective strategies in this work.[257,263]

A consistent issue encountered with the isolation of each strapped porphyrin was low solubility across a variety of solvents, which hindered characterization during preparation.

TFA was employed to solubilize all porphyrins for ^{1}H NMR analysis via dication salt formation. Poor solubility also raises a problem for biological evaluation and limits PS potential. To improve solubility, reduction of strapped porphyrins **4** and **5** nitro groups to yield porphyrins **7** and **8** (Scheme 4) was targeted, but unsuccessful. This was an unexpected result considering the typically high yielding reduction of 5,10,15,20-tetrakis(*o*-nitrophenyl)porphyrins.[168,184]

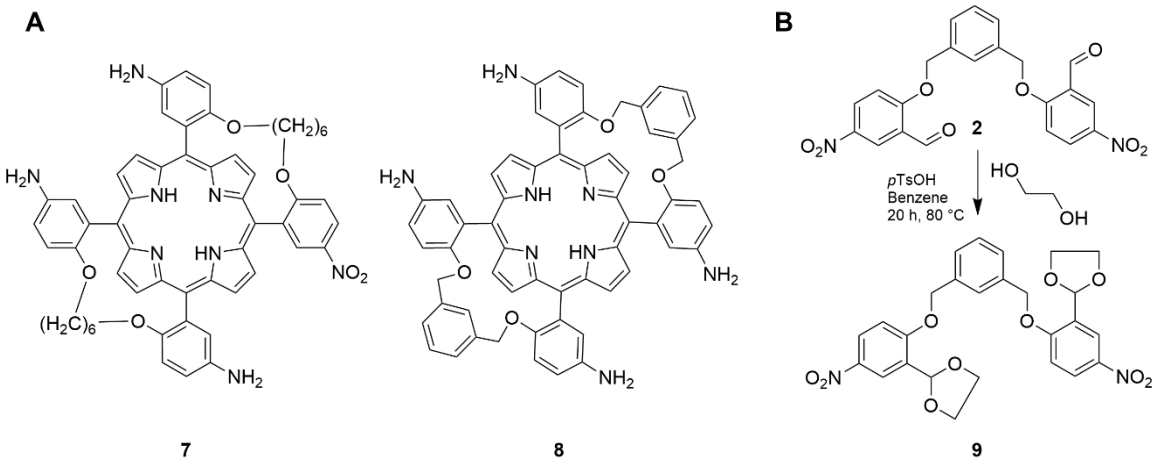

Scheme 4. (A) Target strapped porphyrins to improve solubility. (B) Synthesis of protected dialdehyde.

Initially a standard reduction approach featuring stannous chloride and hydrochloric acid was employed. This method was previously used during the original preparation of 'picket fence' porphyrins to target 5,10,15,20-tetrakis(*o*-aminophenyl)porphyrin atropisomers.[168] This procedure (Table 7, procedure 1), recently adapted by Martin et al.[184] to feature a mixture of CH_2Cl_2/HCl for porphyrin dissolution, was a starting point for optimization. Partial reduction likely occurred for the strapped-porphyrin *cis*-αα-**4** with the mono- and difunctionalized products observed by MALDI mass spectrometry (Figure S 22). Reaction screening which featured an increase to the excess of stannous chloride used as well as hydrochloric acid did not improve the conversion. When the method was attempted with strapped porphyrin **5**, a complete absence of nitro reduction was observed. All reaction screenings were carried out with the *cis*-αα configuration due to the greater availability from condensation reactions. Alterations to the reduction conditions (Table 7, procedure 2), previously successful with peripherally crowded non-planar porphyrins through use of a 1 : 2 ratio of EtOH : HCl with excess stannous chloride, were made.[181] However, no conversion for the strapped porphyrin was observed.

Table 7. Strapped porphyrin nitro group reduction attempts

Procedure	Starting material	Reduction reaction conditions
1	*cis*-αα-**4,** *cis*-αα-**5**	$SnCl_2$ (23 eq.), DCM/HCl (2 : 1), 60 °C, 24 h
2	*cis*-αα-**4,** *cis*-αα-**5**	$SnCl_2$ (23 eq.), EtOH/HCl (1 : 2), 70 °C, 24 h
3	*cis*-αα-**5**	H_2, Pd/C (cat.), TEA (50 eq.), THF, rt, 24 h
4	*cis*-αα-**5**	Zn (cat.), HCl/EtOH (2 : 1), 70 °C, 2 h
5	**9**	H_2, Pd/C, EtOH/EtOAc (1 : 1), rt, 24 h

Two alternative post-functionalization methods were attempted to induce nitro reduction. First, hydrogenation with palladium/carbon was attempted in the presence of TEA and THF (Table 7, procedure 3). No conversion was observed by mass spectrometry. Stronger reduction conditions featuring HCl and Zn powder as a catalyst were also attempted (Table 7, procedure 4).[281] The risk of conversion to chlorin was deemed low due to the established lower potential of macrocycle reduction for a double strapped porphyrin relative to the unstrapped counterpart.[177] However, no nitro reduction was observed. Baldwin et al.[179] encountered inefficient nitro reduction for the phenyl groups of a *trans* single strapped porphyrin. Reduction earlier in the reaction sequence by pre-functionalization of the dialdehyde led to better yields. Thus, this strategy was employed with dialdehyde **5**. Acetal protection of the aldehyde (Scheme 4B) was carried out successfully to yield **9** and taken directly for reduction by hydrogenation (Table 7, procedure 5), but reduction did not occur. A new double strapped porphyrin **6** was instead targeted in an attempt to improve solubility. The strap length of dialdehyde **2** was increased to attempt to alter the number of porphyrins accessible from the Lindsey condensation. However, Adler-Longo conditions were necessary to form multiple porphyrins: *cis*-αα-**6** and *trans*-αβ-**6**. The strapped porphyrin *cis*-αβ-**6** was not observed to form. Carboxylic acid functionality was introduced by base catalyzed hydrolysis of methyl-ester groups following condensation.[viii] The solubility of strapped porphyrins **6** was significantly higher than that of strapped porphyrins **5**.

[viii] Strapped porphyrins **6** were prepared by undergraduate student, Sophie Maguire.

3.4.2 Strapped porphyrin photophysical and photochemical properties

Evaluation of double strapped porphyrin photophysical properties provided valuable insight into the relative porphyrin conformation. Results are presented in Table 8 and Figure 35.

Table 8. Photophysical and photochemical properties of strapped porphyrins.

Strapped porphyrin	λ_{Soret} nm	ε M^{-1} cm^{-1}	Φ_F	Φ_Δ[b]
***cis*-αβ-4**	424	210300	0.084	1.19
***cis*-αα-4**	424	227600	0.095	1.02
***cis*-αβ-5**	428	21325	0.067	-
***cis*-αα-5**	428	81510	0.089	-
***trans*-αβ-6**[a]	424	5623	0.064	0.85
***cis*-αα-6**[a]	434	51286	0.111	0.94

[a] λ_{Soret} and ε recorded in THF. All other measurements recorded in DMSO. [b] One independent experiment performed.

Strapped porphyrins **4** with moderate length hexyl straps were indicated by X-ray crystallography to share a lack of significant distortion. Overlapping absorption spectra (Figure 35A) confirmed that there were no major changes in the porphyrin macrocycle conformation between the isomers which would alter photophysical properties. If macrocycle distortion was present, a bathochromic shift would be anticipated.[174-175] The *cis*-isomers of strapped porphyrin **5** also exhibited overlapping absorption spectra with the Soret wavelength (λ_{Soret}) at 428 nm, however, the *trans* isomer demonstrated a bathochromic of 10 nm to 434 nm. This would indicate that when the phenyl straps of porphyrin **5** are linked between positions 5,15 and 10,20, some distortion is introduced to the porphyrin macrocycle. A similar shift was observed for the *trans*-αβ-**6** isomer, also alluding to distortion. The propensity of these rigid linkers to induce slight distortion has previously been observed by Reddy et al.[177]

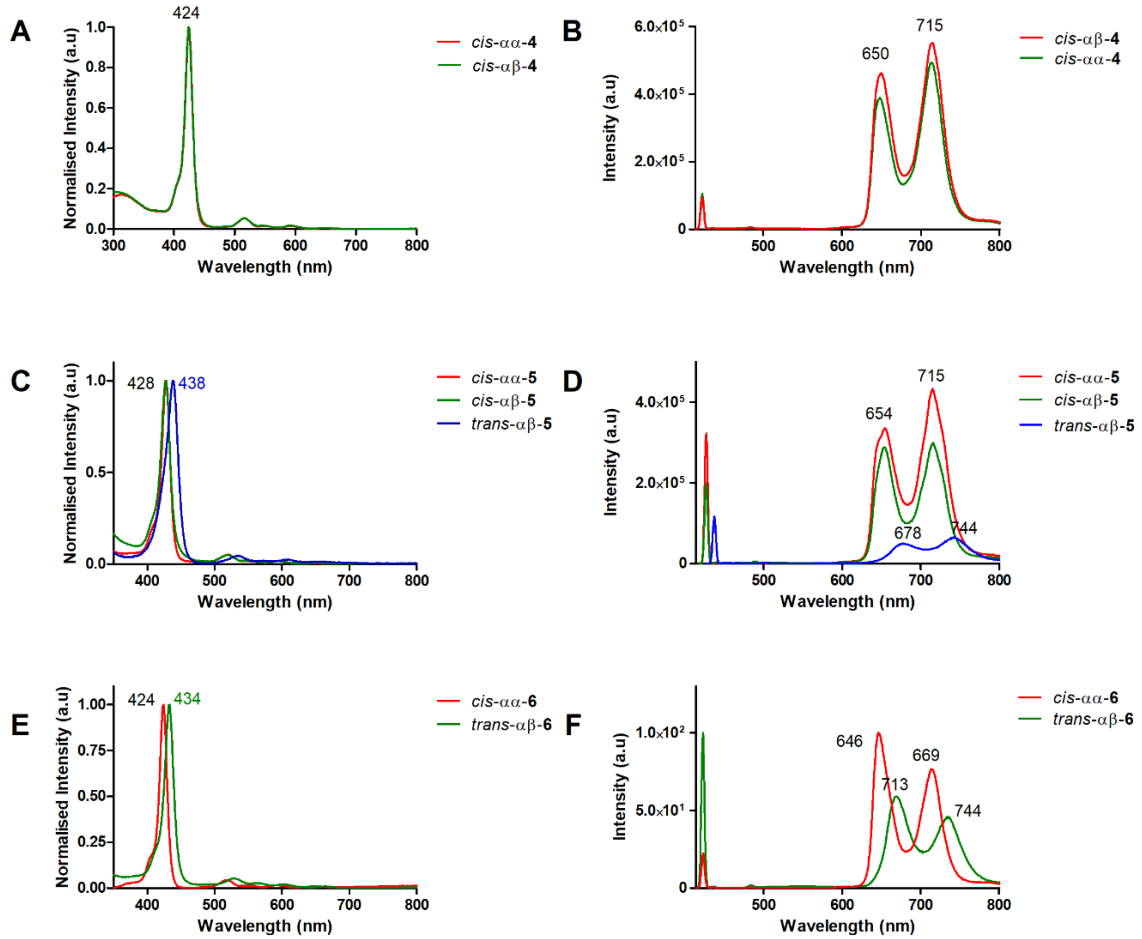

Figure 35. Absorption and emission spectra of strapped porphyrins recorded in DMSO. (A,B) Strapped porphyrins **4**, (C,D) strapped porphyrins **5**, (E,F) strapped porphyrins **6**. Excitation at λ_{Soret}.

An accompanying indication of distortion was not only a bathochromic shift but significant reduction in molar absorptivity, particularly for *trans*-αβ-**5** and *trans*-αβ-**6** isomers. Reddy et al.[177] rationalized the changes in intensity of Soret and Q bands, specifically with a *trans*-αβ isomer, due to changes in degeneracy of the π-molecular orbitals of the porphyrin ring, resulting in red shifts and a significant decrease in intensity. Fluorescence quenching tends to accompany these signs of distortion for absorption spectra.[271] Indeed, the absolute values of fluorescence quantum yield (Φ_F) of the double strapped porphyrins *cis*-αβ-**5** and *trans*-αβ-**6**, recorded using an integrating sphere, were both lower relative to the respective *cis*-αα isomers.

The consequences of distortion for the *trans*-αβ-**6** were apparent with a slightly lower singlet oxygen quantum yield (Φ_Δ) value. These values were recorded by relative

assessment of phosphorescence intensity for a reference phenalenone[223] and the strapped porphyrins.[282] It should be noted that results presented for singlet oxygen are from a single representative experiment and, thus, should only be viewed as a relative assessment between isomers prior to calculation of absolute values following repetition. This is particularly critical for these porphyrins given that they demonstrate an absence of solubility in solvents which favor longer lifetimes of singlet oxygen such as toluene or ethanol.[222] Instead, it was required to use DMSO. A decrease in singlet oxygen quantum yields has been established as relevant to the planarity of the porphyrin macrocycle.[272] As indicated in Chapter 2, distribution of polar substituents relative to the porphyrin macrocycle influences cellular internalization, thus, insight into porphyrin shape is critical.

3.4.3 Strapped porphyrins exhibited conformation dependent uptake

Strapped porphyrin cell-internalization varied in two cell lines depending on configuration. The cell lines selected for evaluation, CT26 and 4T1, were also used to evaluate redaporfin atropisomers, facilitating comparison of the isomer specific uptake. As described in Chapter 2, redaporfin atropisomer cell internalization varied according to $\alpha_4 > \alpha_3\beta > \alpha_2\beta_2 > \alpha\beta\alpha\beta$. Fluorescence signal of cells incubated with strapped porphyrins **4** was acquired by flow cytometry following fixed incubation periods (Figure 36A,B). At both 4 and 24 h, uptake of *cis*-αα-**4** was increased relative to the *cis*-αβ-**4** atropisomer with a 1.9 and 1.8-fold difference for 4T1 and CT26 cells, respectively. Of the phenyl-strapped porphyrins prepared, the strapped porphyrins **6** were selected for evaluation due to higher DMSO solubility. It was necessary to use an alternative method to evaluate uptake for strapped porphyrins **6** due to significant variation of fluorescence quantum yield values (Table 8).

Measurement of strapped porphyrin fluorescence from the supernatant of cells confirmed the enhanced uptake of strapped-porphyrin internalization *cis*-αα-**6** at 24 h relative to *trans*-αβ-**6 (**Figure 36C,D**)**. Internalization at 4 h was not detected, likely due to the necessity to employ low porphyrin concentration to limit DMSO exposure for the cells (< 1 %). As with strapped porphyrins **4**, a slightly greater difference in internalization was observed for the 4T1 cells (3.4-fold) in comparison to the CT26 (2.7-fold).

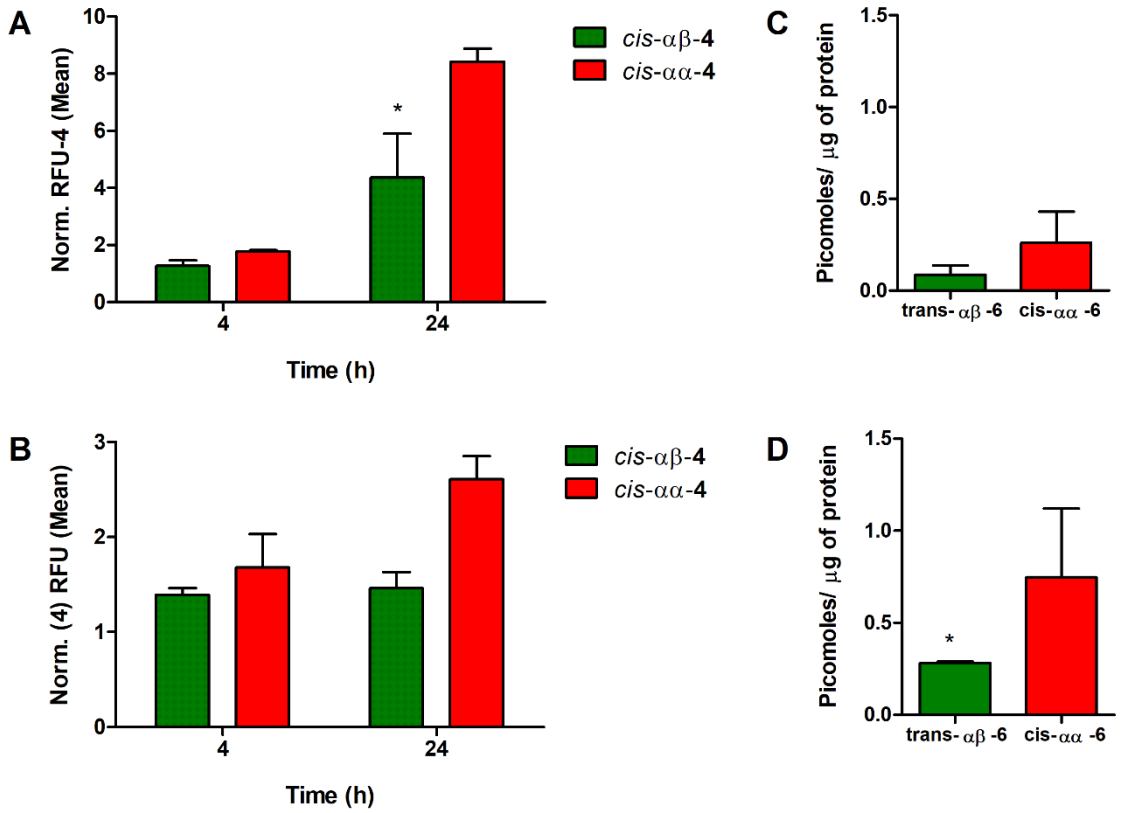

Figure 36. Cellular internalization of strapped-porphyrins. (A,B) Strapped porphyrins **4** uptake evaluated by flow cytometry at the indicated time points in (A) 4T1 and (B) CT26 cells. (C,D) Quantification of strapped porphyrins **6** in the supernatant of cancer cells. Cancer cells were incubated with strapped porphyrins **6** for 24 h followed by cell lysis of (C) 4T1 and (D) CT26 cells. Bars indicate the mean ± SEM of at least two independent experiments with statistical significance evaluated using two-way ANOVA and one-way ANOVA respectively in comparison to the *cis*-αα porphyrin, * $p < 0.05$ ** $p < 0.01$ and *** $p < 0.001$.

In terms of distribution of polar substituents relative to the porphyrin macrocycle, the *cis*-αα, *cis*-αβ and *trans*-αβ isomers of double strapped porphyrins are analogues to porphyrin atropisomers α_4, $\alpha_2\beta_2$, and αβαβ respectively. The increased cell-internalization of *cis*-αα relative to *cis*-αβ and *trans*-αβ follows the pattern of uptake observed with redaporfin atropisomers in Chapter 2; enhanced internalization for the α_4 atropisomer relative to the other atropisomers of the drug mixture. As with the α_4 atropisomer, the *cis*-αα polar substituents are oriented to one side of the porphyrin macrocycle hydrophobic core. This induces amphipathicity which is expected to confer an advantage for passive membrane permeation. The presence of straps effectively locks this favorable configuration to ensure stability against interconversion. Incorporation of the α_4 molecular configuration proved successful as a transferable motif for the design of molecules with enhanced cell-

internalization. This is particularly critical for strapped-systems where molecular weight tends to exceed that of unstrapped counterparts.

3.5 CONCLUSION

Restrictive strap moieties effectively stabilized a favorable atropisomer configuration to enhance cell-internalization. A series of double strapped porphyrins were prepared using direct condensations which favor the formation of *cis*-isomers. Characterization was assisted with NMR spectroscopy and X-ray crystallography methods. Photophysical evaluation indicated relative planarity between strapped porphyrin isomers and the appropriate method to evaluate cellular uptake. Internalization was assessed across two cell lines and revealed enhanced membrane passage of the *cis*-αα isomer. This isomer was formed in greatest yield following the Lindsey condensation method. Lack of interconversion at elevated temperatures confirmed *cis*-αα stability. The structure of *cis*-αα was analogous to the α_4 atropisomer of redaporfin in terms of distribution of polar substituents. Straps concomitantly stabilized atropisomer interconversion and enforced a structure which would potentiate cellular uptake. Development of strategies which can impose high interconversion barriers while exploiting the benefit of a single atropisomer configuration endorse the potential of atropisomer drugs candidates.

3.6 SUPPLEMENTARY MATERIAL

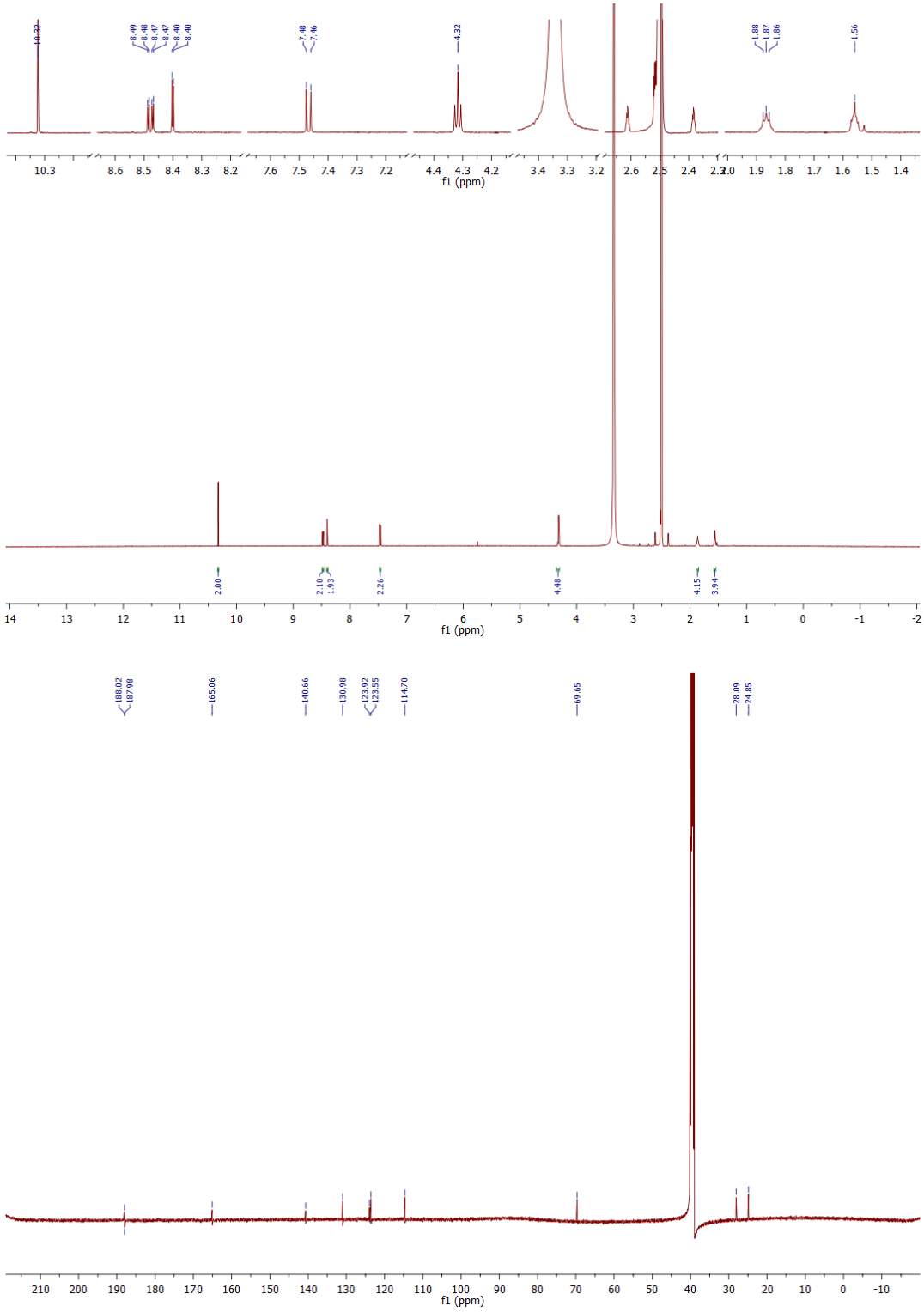

Figure S 9. ^{1}H NMR (600 MHz) and ^{13}C (151 MHz) spectra of dialdehyde **1** in DMSO-d_6.

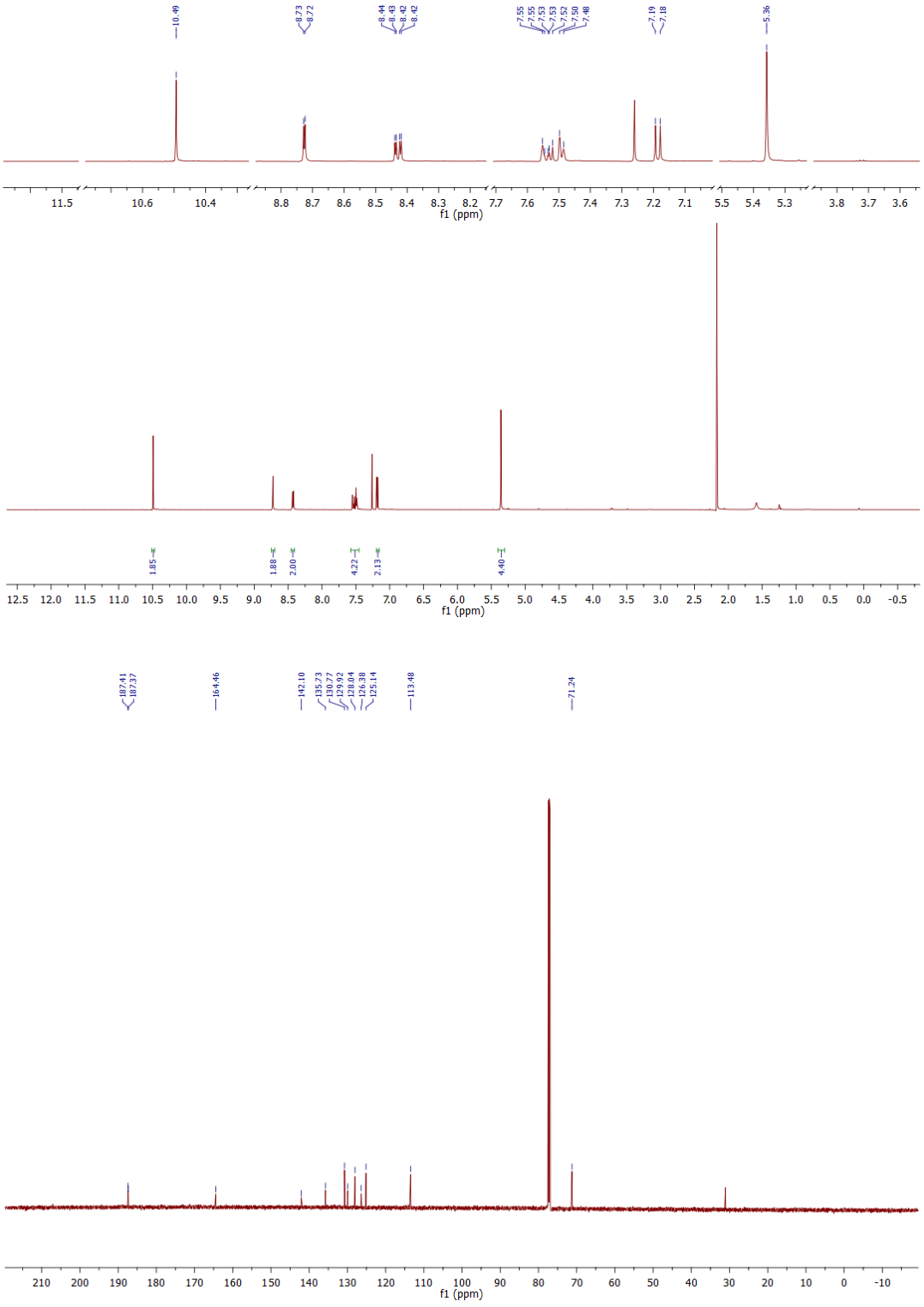

Figure S 10. ^{1}H NMR (600 MHz) and ^{13}C (151 MHz) spectra of dialdehyde **2** in $CDCl_3$.

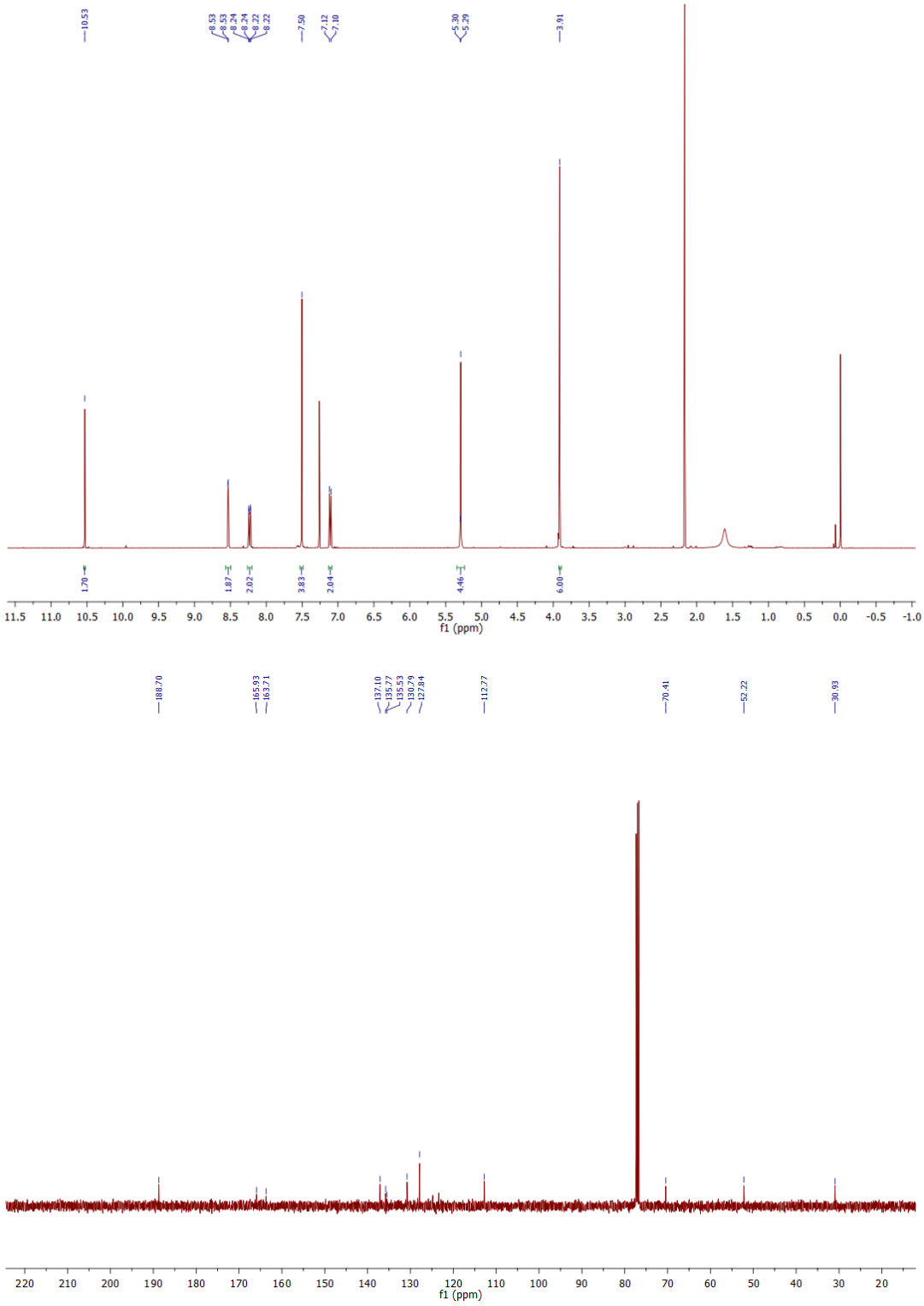

Figure S 11. ^{1}H NMR (400 MHz) and ^{13}C (151 MHz) spectra of dialdehyde **3** in $CDCl_3$.

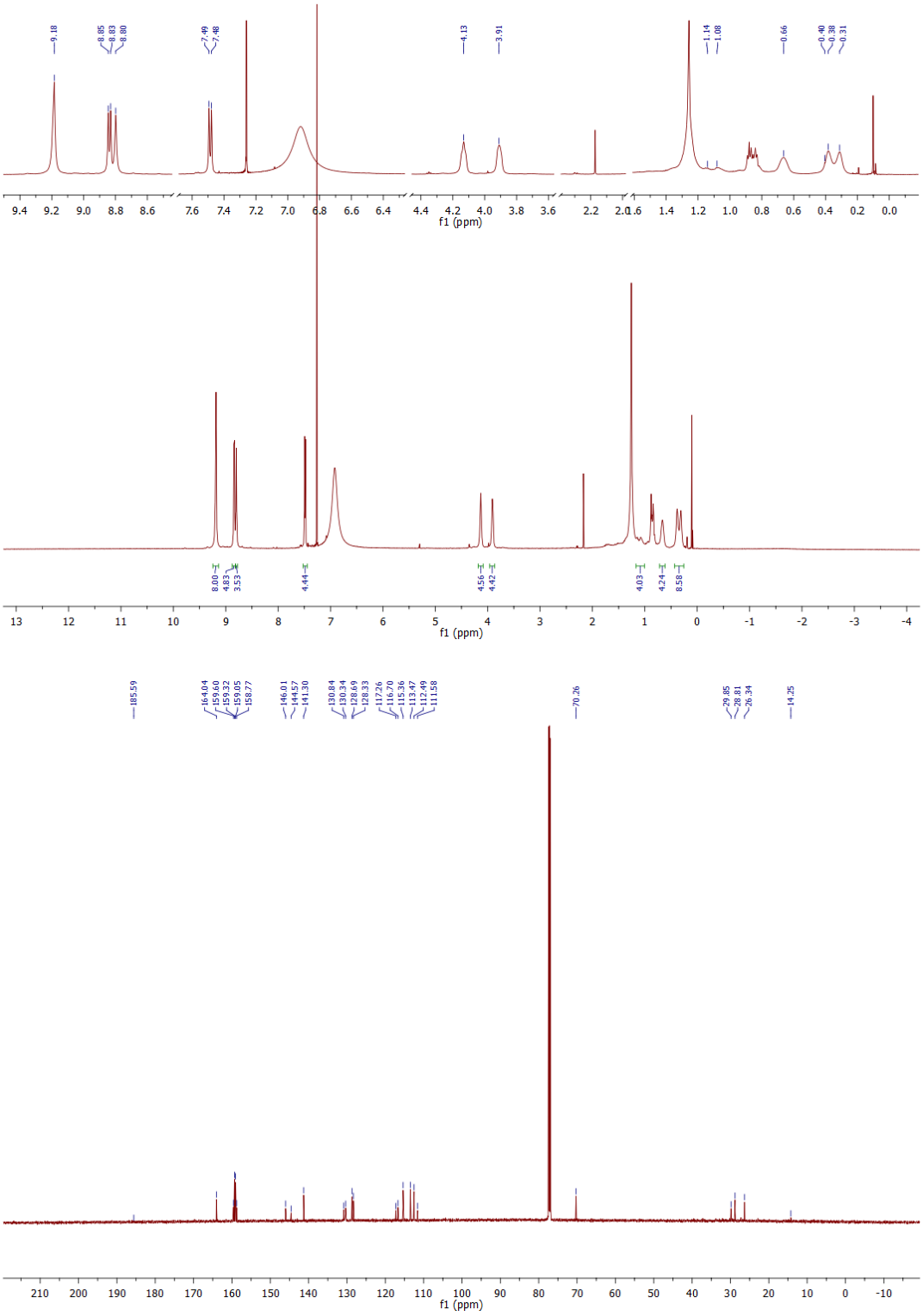

Figure S 12. ^{1}H NMR(600 MHz) and ^{13}C (151 MHz) spectra of strapped porphyrin *cis*-αβ-**4** in $CDCl_3$ with excess TFA-d_1.

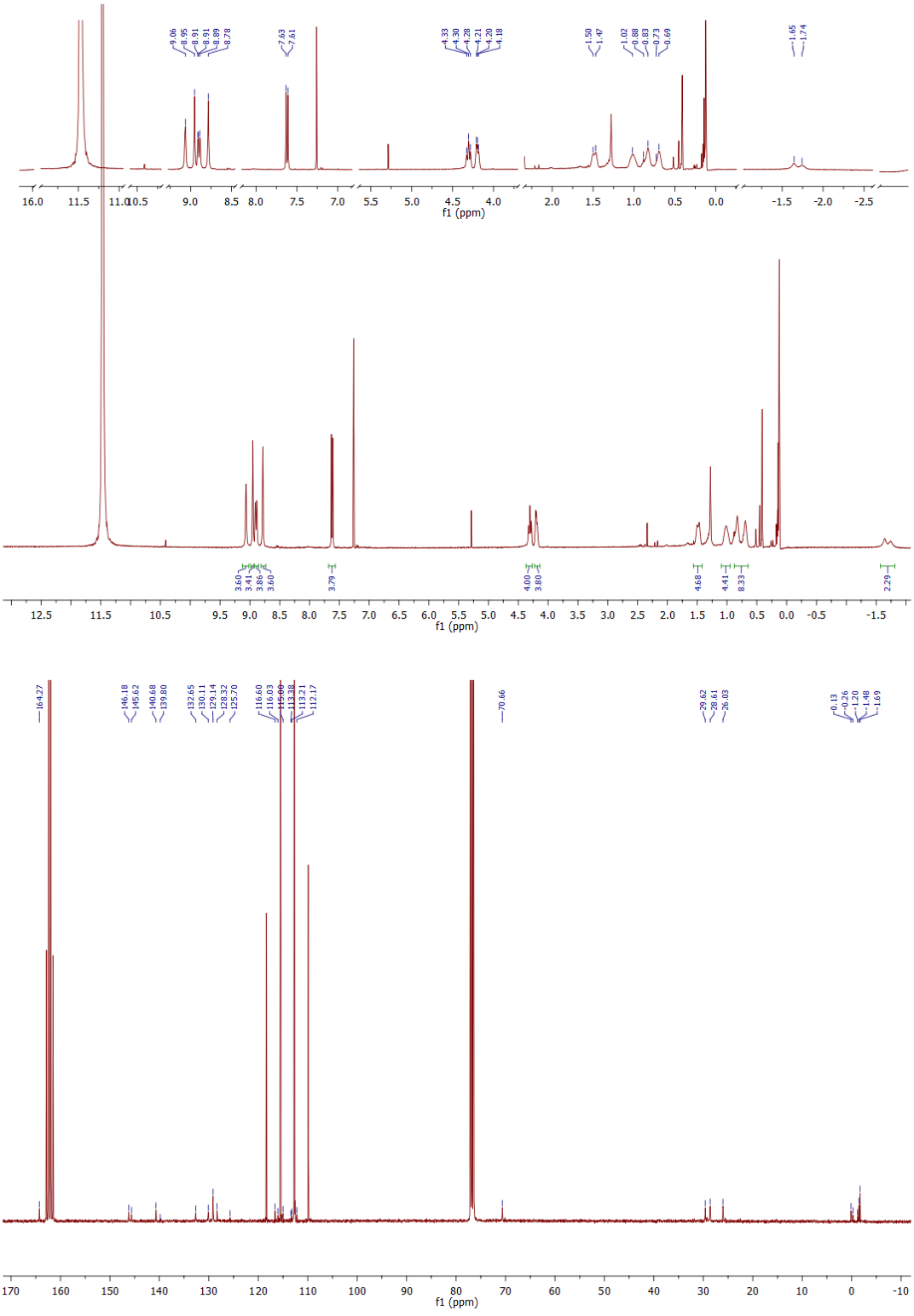

Figure S 13. ^{1}H NMR (400 MHz) and ^{13}C (101 MHz) spectra of strapped porphyrin *cis*-αα-**4** in $CDCl_3$ with excess TFA.

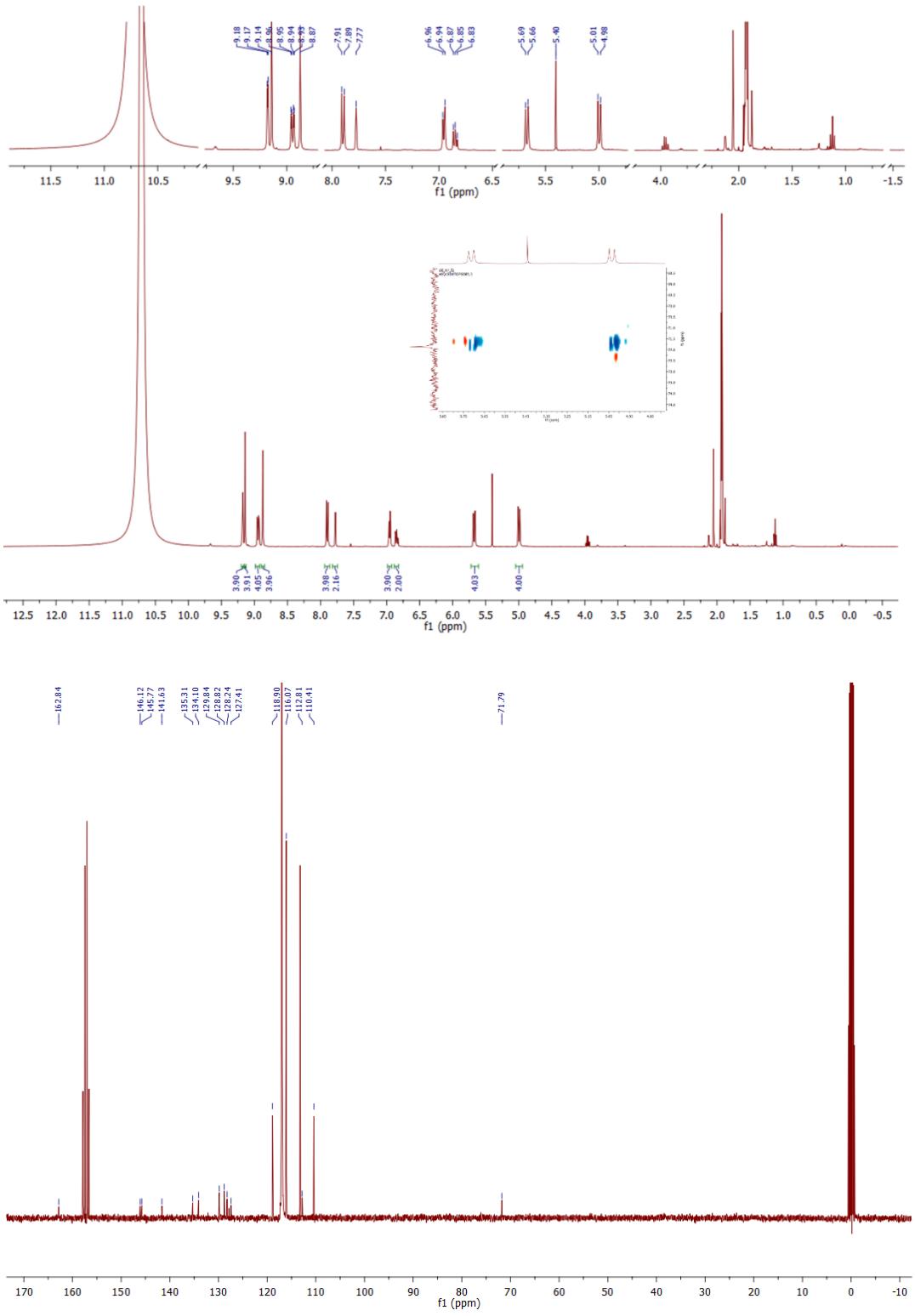

Figure S 14. ^{1}H NMR (400 MHz) and ^{13}C (101 MHz) spectra of strapped porphyrin *cis*-αα-**5** in CD_3CN with excess TFA.

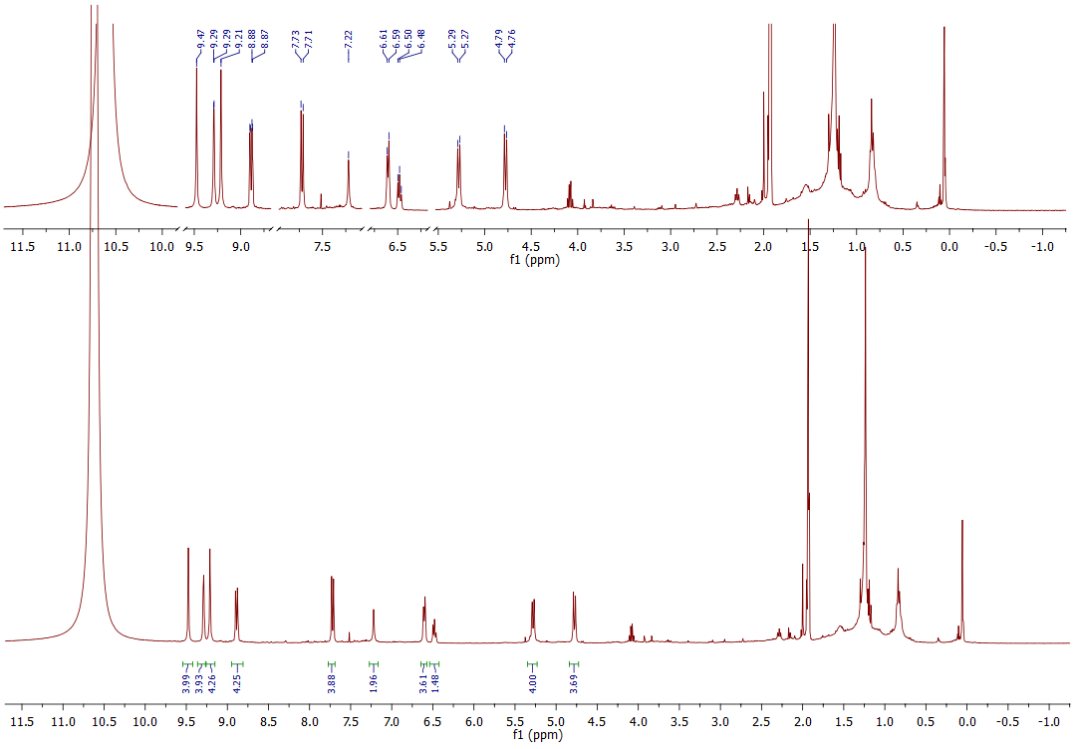

Figure S 15. ^{1}H NMR (400 MHz) spectra of strapped porphyrin *cis*-αβ-**5** in CD_3CN with excess TFA.

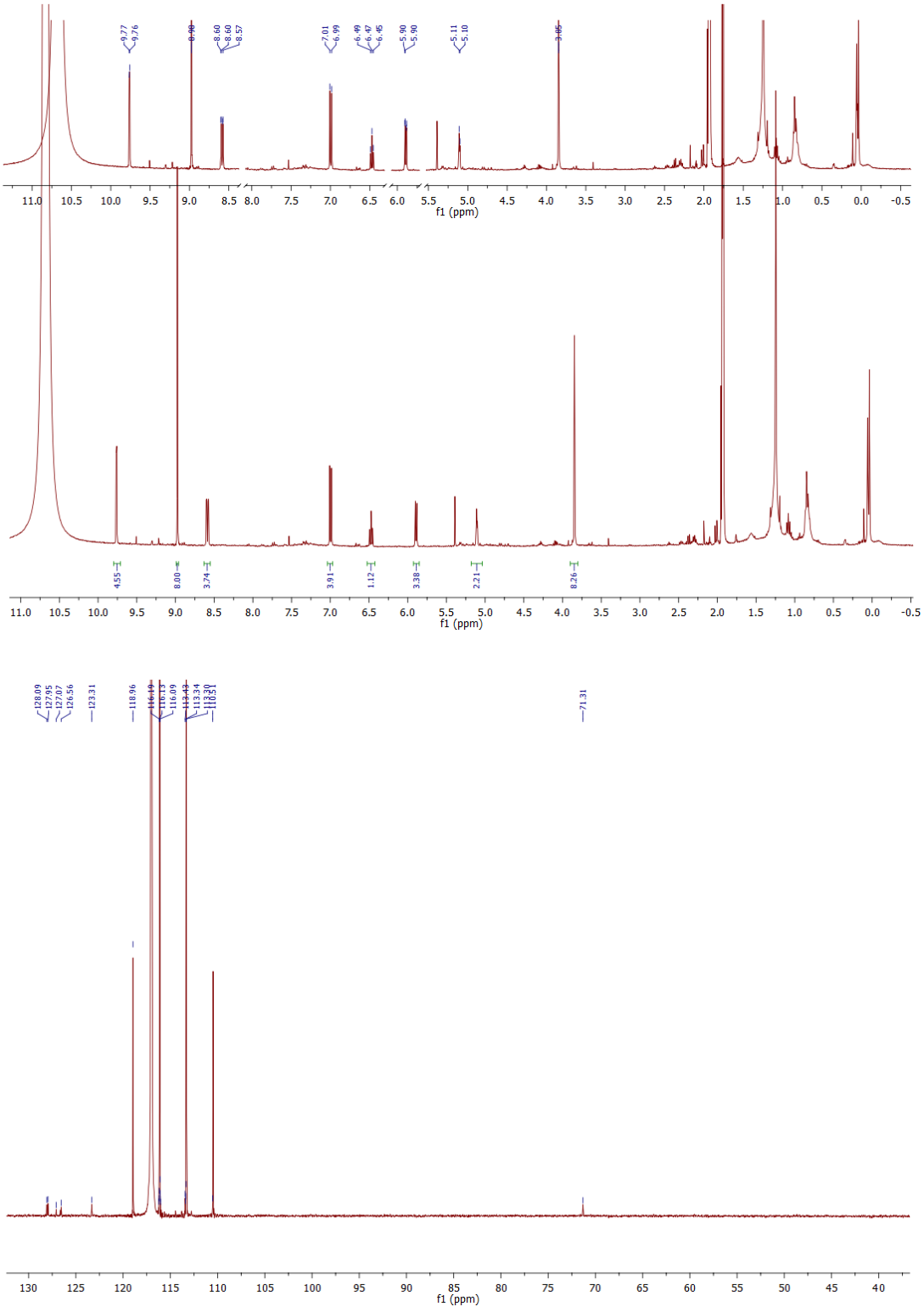

Figure S 16. ^{1}H NMR (400 MHz) and ^{13}C (101 MHz) spectra of strapped porphyrin *trans*-αβ-**5** in CD_3CN with excess TFA.

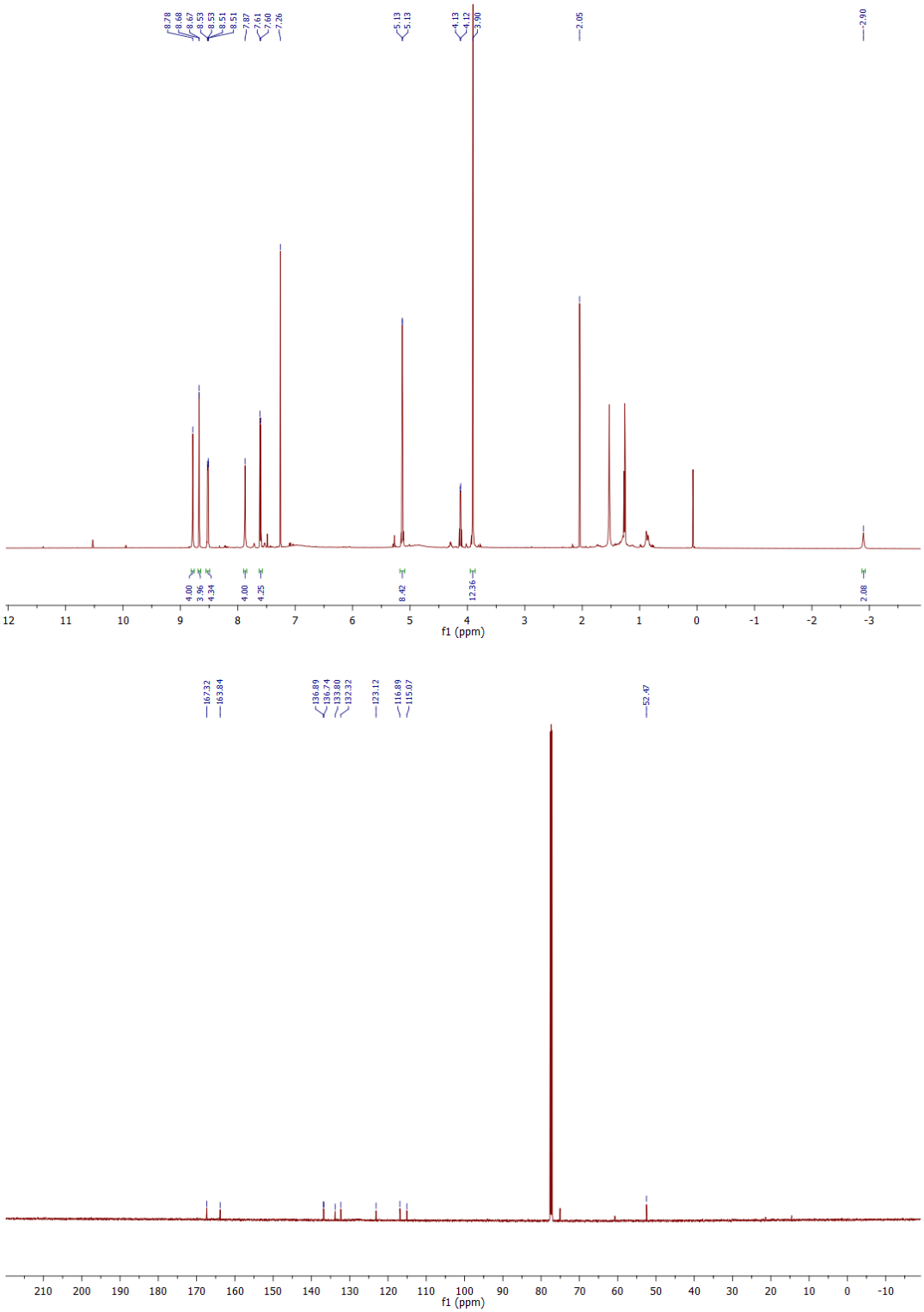

Figure S 17. ^{1}H NMR (600 MHz) and ^{13}C (151 MHz) spectra of strapped porphyrin COOMe-*cis*-αα-**6** in $CDCl_3$.

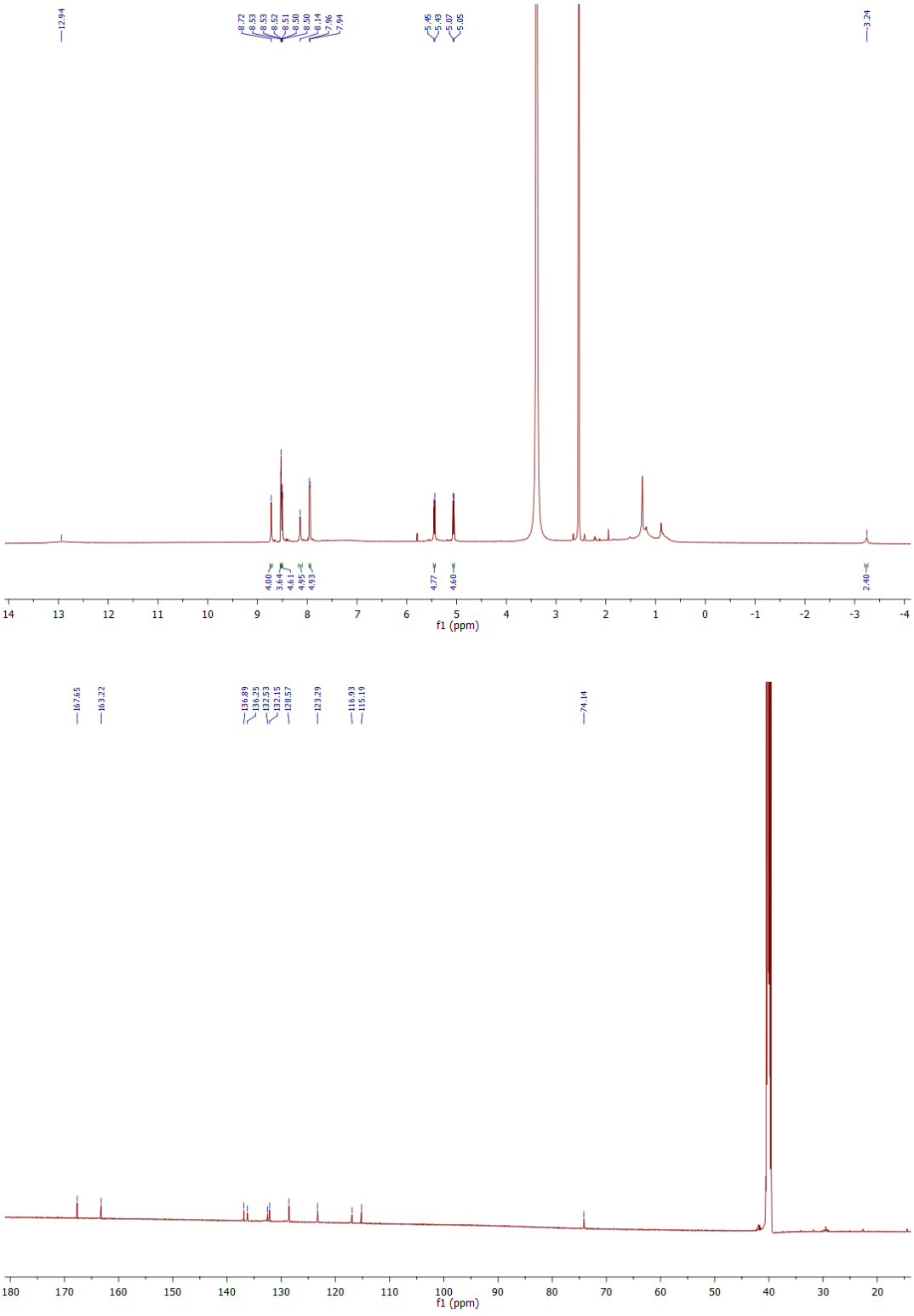

Figure S 18. ^{1}H NMR (600 MHz) and ^{13}C (151 MHz) spectra of strapped porphyrin COOH-*cis*-αα-**6** in DMSO-d_6.

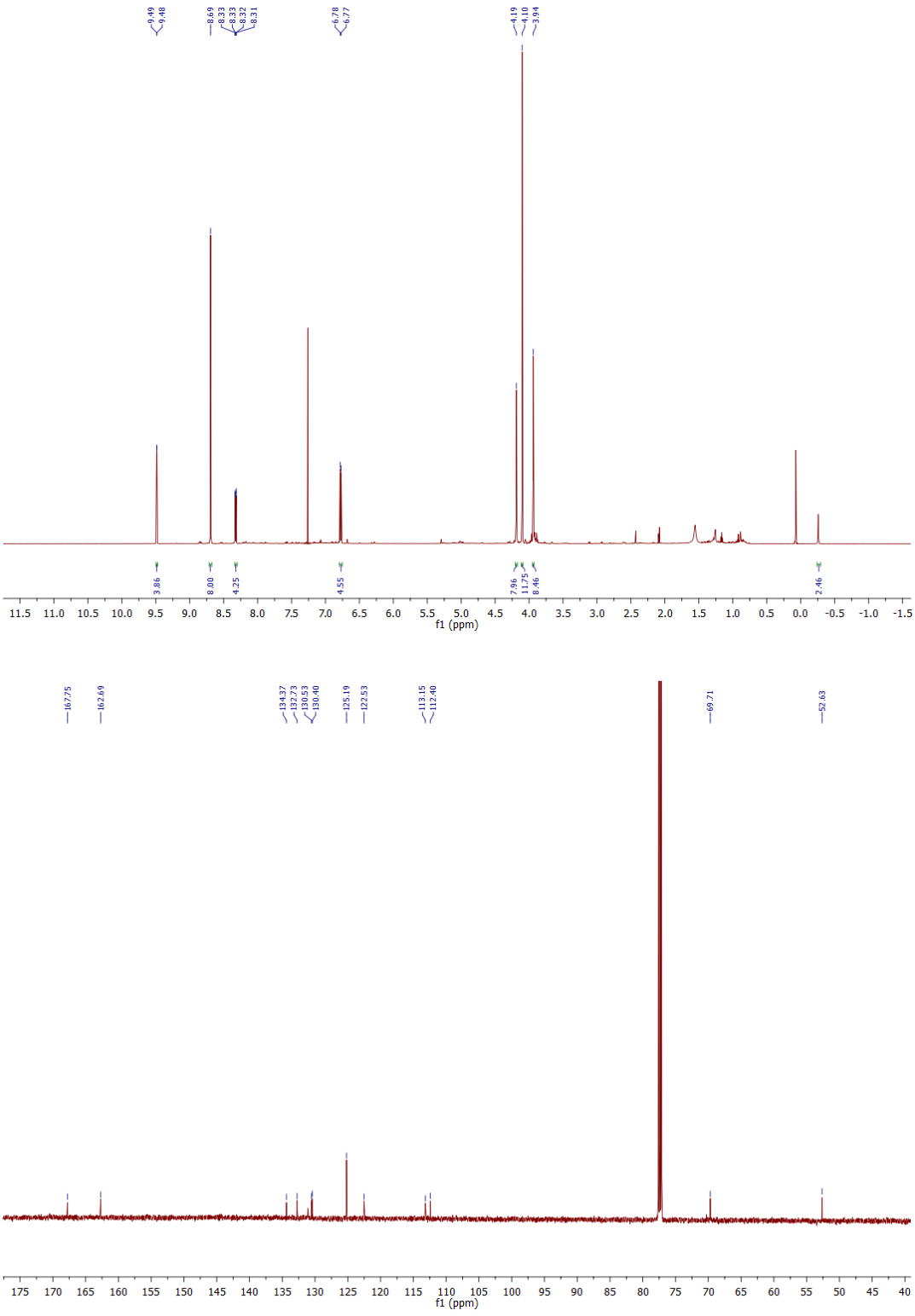

Figure S 19. ^{1}H NMR (600 MHz) and ^{13}C (151 MHz) spectra of strapped porphyrin COOMe-*trans*-αβ-**6** in $CDCl_3$.

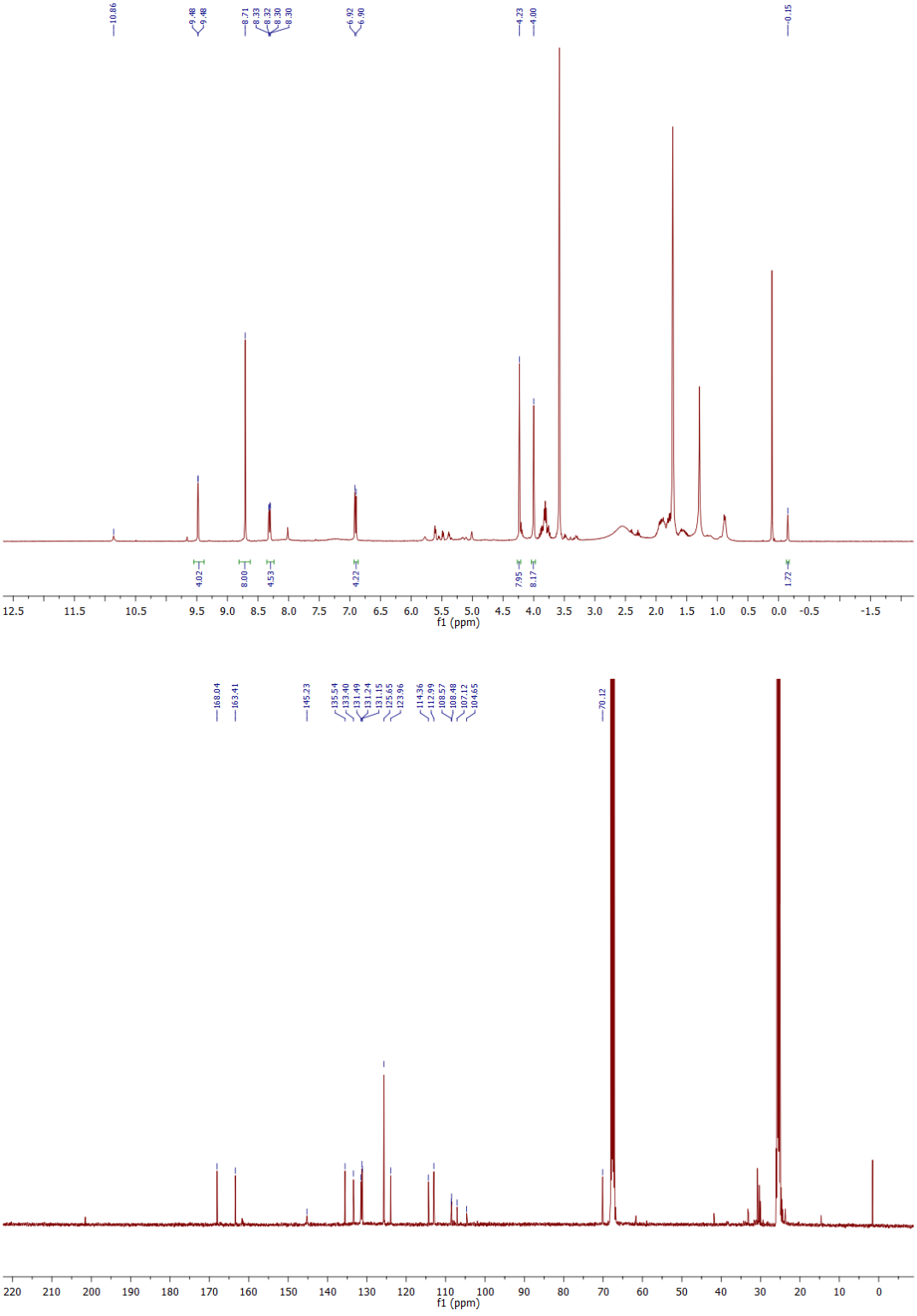

Figure S 20. ^{1}H NMR (600 MHz) and ^{13}C (151 MHz) spectra of strapped porphyrin COOH-*trans*-αβ-**6** in DMSO-d_6.

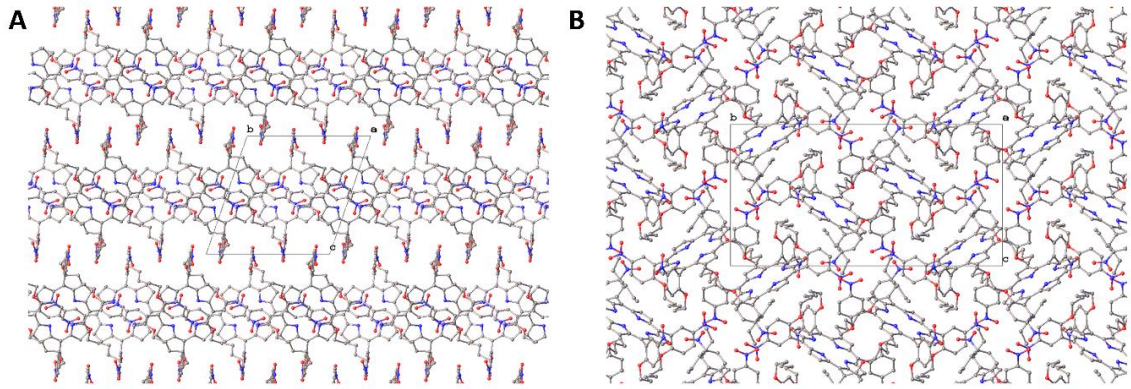

Figure S 21. View of the molecular packing in the crystal of (A) *cis*-αβ-**4** and (B) *cis*-αβ-**4** viewed along the *a*-axis showing the majority occupied moiety only. Hydrogen atoms omitted for clarity.

Table S 3. Crystal data and structure refinement for strapped porphyrins 4

	***cis*-αβ-4**	***cis*-αα-4**
Identification code	tcd1808	tcd1824
Empirical formula	$C_{56}H_{46}N_8O_{12}$	$C_{62}H_{60}N_8O_{12}$
Formula weight	1023.01 g/mol	1109.18 g/mol
Temperature	100(2) K	100(2) K
Wavelength	1.54178 Å	1.54178 Å
Crystal system	Triclinic	Monoclinic
Space group	$P\bar{1}$	$P2_1/c$
Unit cell dimensions	a = 11.8958(3) Å, α= 71.5336(16)°. b = 14.4969(4) Å, β= 71.5101(15)°. c = 15.4551(4) Å, γ = 88.9149(16)°.	a = 13.8846(4) Å, α= 90°. b = 27.9766(8) Å, β= 109.6476(17)°. c = 15.4294(4) Å, γ = 90°.
Volume	2387.67(11) $Å^3$	5644.5(3) $Å^3$
Z	**2**	4
Density (calculated)	1.423 Mg/m^3	1.305 Mg/m^3
Absorption coefficient	0.846 mm^{-1}	0.754 mm^{-1}
F(000)	1068	2336
Crystal size	0.218 × 0.069 × 0.03 mm^3	0.18 × 0.13 × 0.1 mm^3
Theta range for data collection	3.191 to 70.026°	3.159 to 70.082°

Index ranges	-14≤h≤14, -15≤k≤17, -18≤l≤18	-16≤h≤16, -33≤k≤34, -18≤l≤18
Reflections collected	43330	66990
Independent reflections	8932 [R(int) = 0.0671]	10587 [R(int) = 0.0744]
Completeness to theta= 67.679°	99.7%	99.6%
Absorption correction	Semi-empirical from equivalents	Semi-empirical from equivalents
Max. and min. transmission	0.7533 and 0.6653	0.7533 and 0.6362
Refinement method	Full-matrix least-squares on F^2	Full-matrix least-squares on F^2
Data/ restraints/ parameters	8932 / 89 / 767	10587 / 1229 / 1084
Goodness-of-fit on F^2	1.054	1.064
Final R indices [I>2σ(I)]	R1 = 0.0644, wR2 = 0.1726	R1 = 0.0800, wR2 = 0.2158
R indices (all data)	R1 = 0.0885, wR2 = 0.1882	R1 = 0.1008, wR2 = 0.2309
Largest diff. peak and hole	0.280 and -0.340 e.$Å^{-3}$	0.701 and -0.406 e.$Å^{-3}$

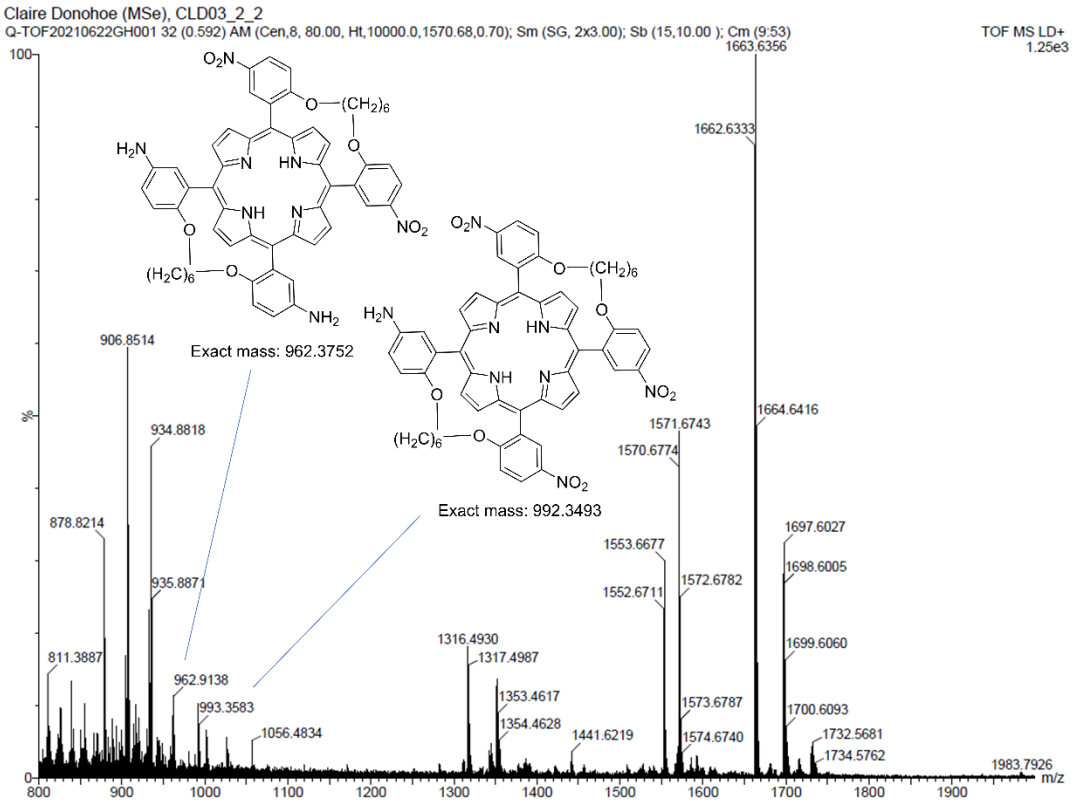

Figure S 22. MALDI mass spectrometry data for partially reduced strapped-porphyrin **4**.

4. Conclusion and Future Perspectives

The orientation of polar substituents in meso-tetraarylporphyrins, relative to the macrocycle plane, was determined as significant for cell membrane permeation and consequently, PDT efficacy. This was identified in Chapter 2, with the α_4 configuration of a pre-clinical PS for PDT, redaporfin. This configuration orientates the polar sulfonamide groups of redaporfin on the same side of the bacteriochlorin macrocycle. The heightened uptake of this atropisomer, relative to others present in the redaporfin drug mixture, was determined to be the result of a predominantly passive, enhanced interaction with the cell membrane. Orientation of polar sulfonamide groups to one side of a heteroaromatic plane appeared to promote an amphipathic character which enhanced uptake. The configuration was deemed as a promising cell-penetrating motif for the preparation of novel drugs. For proof of concept, Chapter 3 described the use of restrictive strapped moieties in PS design to enforce a configuration which enhances cell uptake.

Identification of motifs that may improve the efficiency of cell delivery is important for the development of novel therapies.[283] Cell uptake is a key process, particularly when interaction with an intracellular target is required for therapeutic efficacy.[284] The cell membrane is a thin bilayer (~ 5 nm) that comprises phospholipids, cholesterol and membrane anchoring proteins. It governs strict regulation of matter exchanged between cells and the external environement.[233,285] This positions the passage of cell membranes by therapeutics as a core process of medicinal chemistry. Accordingly, the design of a novel molecular structure for biological application should consider the potential for cell internalization.[233,283] A shift from small molecules (< 1 kDa) dominating the drug pipeline to also include larger structures such as macromolecules (> 1 kDa), proteins and nanoparticles has occurred in recent years.[285] These structures are generally less efficient at crossing the cell membrane,[283,285] thereby, reinforcing the need for efficient motifs to enhance permeation. Clinical tetrapyrrole PS may vary in size dramatically from ≤ 700 Da (temoporfin, verteporfin) to include macromolecules with molecular weight close to 1000 Da (padeliporfin, redaporfin) or greater (porfimer sodium).[4]

Consideration of how molecules gain access to the cell cytosol exposes important elements to incorporate into novel drug design. Permeation driven solely by a concentration or an electric potential gradient is described as passive diffusion, while permeation across the cell membrane via transmembrane proteins (known as carriers and channels) is described as facilitated diffusion.[285] When energy is required from cells to permit uptake, the processes are termed active transport and are considerably more complex than passive

internalization. These mechanisms are generally associated with hydrophilic and/ or larger molecules, which are unable to diffuse across the plasma membrane or via a transport protein.[284] Endocytosis is characterized by engulfment of the material to be internalized by the cell membrane in an energy-dependent manner. It includes different subtypes such as clathrin-mediated endocytosis, caveolae-mediated endocytosis, phagocytosis and macropinocytosis which are distinguished by the composition of the vesicle coat during particle entry and their fate within cells (Figure 37).[285-286] Activated cell surface receptors in a clathrin enriched membrane region may lead to membrane deformation towards a clathrin coated pit upon particle internalization. This ultimately forms a vesicle for clathrin-mediated endocytosis.[284] Caveolins, integral membrane proteins, can also induce an endocytic process.[285] There are several endocytic pathways which do not rely on clathrin or caveolin protein coats. Instead, highly ordered lipid microdomains, termed 'lipid rafts', regulate uptake.[287]

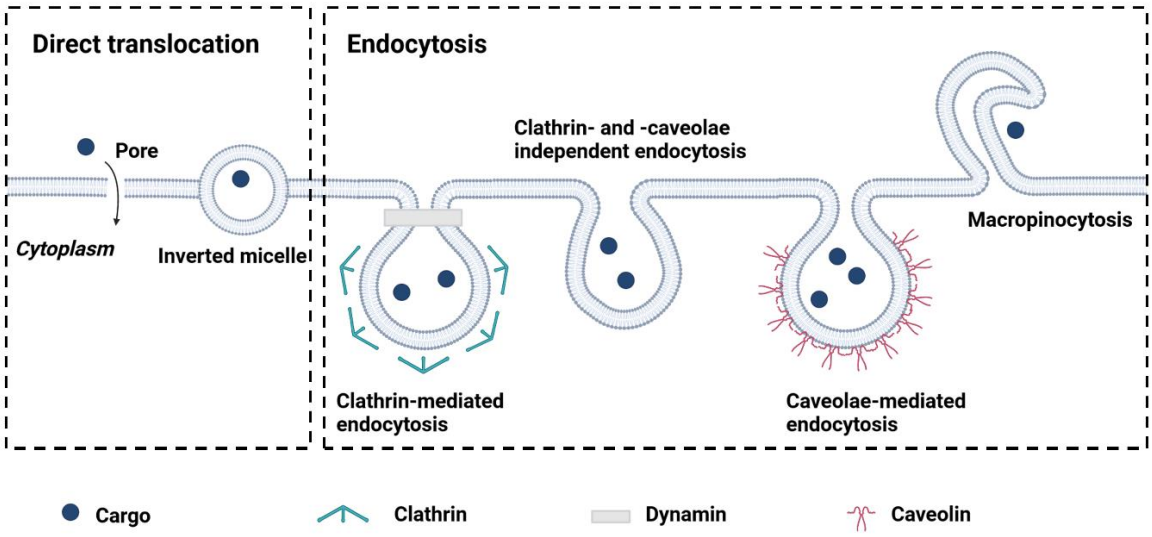

Figure 37. Energy dependent pathways of entry into the cell. Adapted from Gagat et al.[288-289]

Phagocytosis is a process linked to specialized cell types such as macrophages and has a key role in defense against infectious agents. Particles are tagged for macrophage recognition by a process called opsonization which initiates particle ingestion followed by enzymatic digestion.[284] Macropinocytosis is associated with the ingestion of fluids and suspended small particles.[290] In all subtypes of endocytosis, following membrane ruffling, particles are enclosed in endosomes where they can mature and fuse with lysosomes or alternatively be returned to the cell surface through recycling endosomes. Upon lysosome fusion, rapid acidification occurs in the presence of degradative enzymes.[291] With the

exception of drugs targeting lysosomal storage disorders, release from the endo-lysosomal compartments is required for drugs that experience endocytic uptake.[292]

The uptake of redaporfin atropisomers was determined to be due to a predominantly passive mechanism of internalization. This was established by the minimal impact of ATP on atropisomers uptake. Passive uptake processes are typically associated with small hydrophobic molecules.[285] However, there are exceptions such as cyclosporin or redaporfin which are large molecules (MW > 1000 Da).[248] In addition to lipophilicity and size, the charge of molecules also influences whether passive diffusion is favored. Neutral molecules are more likely to passively diffuse.[233] Strategies to promote passive diffusion of small molecules generally focus on increasing molecule lipophilicity to enhance affinity for the phospholipid membrane interior. This can be achieved using a prodrug method by masking polar groups with esterification.[285] While a certain degree of lipophilicity is necessary to ensure passage,[233] increasing lipophilicity may cause molecules to experience a strong interaction with the interior of the bilayer, preventing movement to the cytosol.[293] Additionally, higher lipophilicity can cause challenges during drug formulation for intravenous administration and may increase toxicity.[294] In such cases, employment of delivery systems, such as nanoparticles which alter solubility, may be necessary.[295]

Passive permeation of molecules can also be promoted through physical delivery strategies. Electroporation temporarily creates hydrophilic pores in the cell plasma membrane by application of rapid high-voltage electric field impulses. These pores enable passive permeation through a variety of cell types.[290,296] Clinical application of electroporation for gene delivery is currently under development with multiple clinical trials.[297] Microinjection directs non-permeable molecules into cells mechanically, using a microscope-guided glass microcapillary, employed clinically to assist *in vitro* fertilization techniques. For high throughput, beyond *in vitro* use, application is limited and technically demanding.[290] Both of these physical delivery strategies have specialized applications and are invasive. Therefore, development of permeation motifs which do not disturb the cell membrane integrity are desirable.

Cell penetrating peptides (CPPs) are short cationic peptides (< 30 residues) which can efficiently cross the cell membranes.[298] These peptides take advantage of arginine or lysine residues to promote hydrogen bonding interaction with the cell membranes prior to undergoing internalization.[299-300] Upon conjugation to therapeutics, CPPs may ferry

molecules across the cell membrane. Mechanisms of CPP uptake may vary between endocytosis or exploitation of protein translocation pathways.[301-302] In the case of endocytosis, CPP efficacy is determined by the efficiency of endosomal escape.[285] Activatable CPPs, triggered by tumor specific properties, including upregulated proteases, hypoxia and acidic pH, have expanded the potential of CPPs for anti-cancer treatment.[303-304] However, with multiple ongoing trials, clinical approval of CPPs has yet to be gained.[305] Other permeation motifs also interact advantageously with the anionic phospholipid bilayer exterior to promote internalization. For example, direct conjugation of guanidinium groups has demonstrated potential to participate in membrane hydrogen bonding and promote cell uptake.[190,201,306] Additionally, strained disulfide moieties have been investigated as part of therapeutic design to cross the membrane by covalent attachment, facilitated by the exchange with cell surface exterior thiols.[307]

For PDT, the use of ligand conjugation, either directly to a molecule or nanocarrier, is an active targeting strategy, employed to improve selectivity towards diseased tissue while sparing healthy cells. Active targeting may enhance drug tumor accumulation but also increase intracellular delivery through exploitation of the ligand endocytosis pathway.[43] Folic acid,[308] transferrin,[309] antibodies[45] and peptides[310] are among the ligands which have been demonstrated to promote efficient internalization. Water-insoluble PSs require delivery vehicles, often nanocarriers, for i.v. administration. These nanocarriers can alter PS uptake to both improve[212] or inhibit internalization.[311] Therefore, it is critical to consider physicochemical properties when choosing an appropriate nanocarrier. The nanocarrier size, shape and charge influences the success of cell membrane passage.[312] Alteration of the commercial, polyethylene glycol based Foscan formulation to liposomal formulations were observed to improve temoporfin cell uptake.[313] Liposomal,[314] nanoparticle[315] and polymeric micelles[316] have been observed to impact PS cell internalization and are frequently employed to participate in ligand targeting strategies.

Although promising strategies, the use of active targeting PS for PDT have limited clinical application to date.[45] This is likely due in part to the increased complexity associated with their pharmaceutical development which restricts clinical translation.[43] Additionally, the stability of carrier complexes to endosomal degradation can be a major limiting factor of these strategies for cytosolic delivery.[317] Photochemical internalization (PCI) is an approach to overcome this which delivers macromolecules from endocytic vesicles and lysosomes by using photodamage to trigger release. Activation of PSs with affinity for

endocytic vesicles may facilitate macromolecule cytosolic delivery. Ongoing trials, however, are limited to PCI activation of drugs which do not have high specificity for lysosomes, therefore, PCI is yet to realize its full clinical potential.[318] Passive diffusion of macromolecules, such as cyclosporin, may be possible in the absence of endocytosis, circumventing associated degradation issues, but requires identification of cell-penetrating motifs.[248]

The efficiency of tetrapyrrole PS uptake, as described in Chapter 1, is often simply considered to be a product of lipophilicity, described by $LogP_{OW}$.[75,77] However, correlation between uptake and lipophilicity has not been observed for all PSs.[78,85] Rather, a balance between the hydrophobic and hydrophilic character of a PS, amphiphilicity, has been proposed to improve PS cell uptake and efficacy.[82, 234,319] Limited studies have illustrated the importance of factors beyond lipophilicity, including charge and charge distribution, which benefit the amphiphilic character of a PS.[77,80] Through evaluation of the uptake of redaporfin atropisomers, described in Chapter 2, it became apparent that tetrapyrrole atropisomer conformation, specifically the distribution of polar substituents, can significantly alter passive permeation. Standard indicators of lipophilicity, including $LogP_{OW}$ values, did not correlate with cellular uptake of redaporfin atropisomers. Elution order of the atropisomers by chromatography did correlate with cell uptake, however, the order defied conventional expectations by presenting the same elution regardless of the polarity of the stationary phase used. The atropisomerism of redaporfin controls the orientation of polar sulfonamide substituents relative to the macrocycle plane in a manner which alters amphipathicity. For the α_4 atropisomer, this alteration is favorable in terms of cell uptake.

The passive uptake of molecules is not typically observed to be isomer specific.[233] The redaporfin α_4 atropisomer presents a conformation which supports enhanced hydrogen bonding interactions with the phospholipid bilayer exterior and diffusion. The use of the α_4 atropisomer may not only improve cellular-PDT efficacy relative to the other atropisomers but is potentially a more promising PS than the pre-clinical atropisomer mixture for cellular-PDT. This hypothesis should be explored in the future with other tumor models beyond CT26. The lack of significant skin photosensitivity observed *in vivo*, 7 days post administration with α_4, further illustrates the clinical potential of isolated α_4 as a PS.

Tetrapyrrole shape and distribution of polar substituents have been highlighted using the redaporfin atropisomers as important parameters for consideration in the design of novel PSs. These findings were successfully incorporated into the design of novel strapped porphyrins with enhanced cell internalization, as described in Chapter 3. Solubility issues and low yields limit the potential of the strapped porphyrins targeted as PSs for PDT. Nevertheless, as a proof-of-concept study, valuable insights could be gained from the strapped porphyrin preparation described in this thesis (Scheme 3B). Firstly, it was demonstrated that the *cis*-αα isomer, with polar substituent distribution which closely resembles the α_4 configuration, had enhanced cell-internalization and high thermal stability. Therefore, enforcing the α_4 molecular configuration may benefit other PSs beyond redaporfin. This work also indicates that preparation of future double strapped porphyrins PSs should incorporate condensation methods which favor *cis*-αα formation via the Lindsey condensation approach.

Exchange of meso-nitroaryl functional groups in strapped porphyrin **5** to more polar substituents carboxyl groups in strapped porphyrins **6** benefited DMSO solubility; however, greater aqueous solubility would be required to consider formulation for *in vivo* application. Potentially, functionalization of meso-aryl groups with multiple polar substituents (e.g., -F, -OH) could improve solubility when a hydrophobic strap is employed. Strapped porphyrins **4** displayed increased solubility relative to porphyrins **5**, indicating that a more flexible linker benefitted solubility. Only limited examples of strapped porphyrins designed for PDT application are available. Single-strapped porphyrins, with glycosyl functional groups appended to the macrocycle as straps, illustrated more phototoxicity *in vitro* when linked at the 5,15- rather than 5,10-positions.[273] Introduction of strapped moieties featuring glycosyl groups may improve solubility, but strap lengths would be long and, therefore, limit stability. Alternative polar straps (e.g., polyether) might be incorporated to the *cis*-αα strapped porphyrin to enhance aqueous solubility (Scheme 5). However, to improve cellular internalization, exchanging the polar substituents of meso-phenyl groups to hydrophobic and low molecular weight groups (e.g., -Me/ short alkyl chains) may be necessary to maintain the amphipathicity associated with the redaporfin α_4 configuration. This would ensure distribution of hydrophobic and hydrophilic moieties in a manner which could benefit membrane permeabilization, while also ensuring solubility is considered. An example of the potential synthetic route for a double strapped porphyrin with enhanced solubility is presented in Scheme 5.

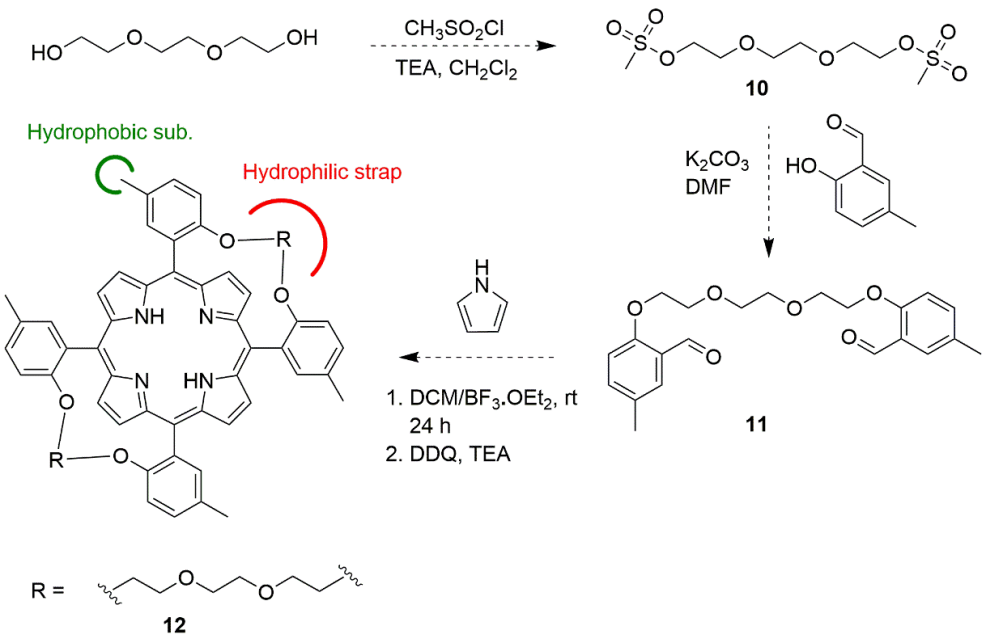

Scheme 5. Potential strapped porphyrins with altered solubility.

Overall, this work presents an investigation of the potential therapeutic implications of atropisomerism which are not typically considered. The predominant observation when examining atropisomer biological activity tends to be altered targeted selectivity.[111,117] Redaporfin atropisomers presented varied, unspecific and passive interactions with the cell membrane which altered cell-uptake and, ultimately, efficacy. The orientation of redaporfin sulfonamide groups on one side of the heteroaromatic plane appeared to favorably promote amphipathicity. The application of this α_4 configuration may assist the rational design of macromolecules to enable efficient passive diffusion. This motif was incorporated as a design element for novel strapped porphyrin PSs. The enhanced uptake highlighted the benefit of exploiting surface interactions with the cell membrane to achieve internalization. Beyond this, it also illustrated the advantages that consideration of atropisomerism can potentially provide for therapies, endorsing its investigation for drug development.

LIST OF FIGURES

Supplementary Figures

Schemes

LIST OF TABLES

REFERENCES

1. Dąbrowski, J. M.; Arnaut, L. G. Photodynamic therapy (PDT) of cancer: from local to systemic treatment. *Photochem. Photobiol. Sci.* **2015,** *14*, 1765-1780.
2. Callaghan, S.; Senge, M. O. The good, the bad, and the ugly – controlling singlet oxygen through design of photosensitizers and delivery systems for photodynamic therapy. *Photochem. Photobiol. Sci.* **2018,** *17*, 1490-1514.
3. Schaberle, F. A.; Gomes-da-Silva, L. C. A network representation of photodynamic therapy aiming the integration of knowledge and boosting clinical acceptance. *Photodiagn. Photodyn. Ther.* **2022,** *37*, 102715.
4. Abrahamse, H.; Hamblin, M. R. New photosensitizers for photodynamic therapy. *Biochem. J.* **2016,** *473*, 347-364.
5. Dolmans, D. E. J. G. J.; Fukumura, D.; Jain, R. K. Photodynamic therapy for cancer. *Nat. Rev. Cancer* **2003,** *3*, 380-387.
6. Brown, S. B.; Brown, E. A.; Walker, I. The present and future role of photodynamic therapy in cancer treatment. *Lancet. Oncol.* **2004,** *5*, 497-508.
7. Schmidt-Erfurth, U.; Hasan, T. Mechanisms of action of photodynamic therapy with verteporfin for the treatment of age-related macular degeneration. *Surv. Ophthalmol.* **2000,** *45*, 195-214.
8. Kalka, K.; Merk, H.; Mukhtar, H. Photodynamic therapy in dermatology. *J. Am. Acad. Dermatol.* **2000,** *42*, 389-413.
9. Dai, T.; Huang, Y.-Y.; Hamblin, M. R. Photodynamic therapy for localized infections—State of the art. *Photodiagn. Photodyn. Ther.* **2009,** *6*, 170-188.
10. Abdel-kader, M. H. Chapter 1 The Journey of PDT Throughout History: PDT from Pharos to Present. In *Photodynamic Medicine: From Bench to Clinic*, 1st Ed.;The Royal Society of Chemistry, 2016; pp 1-21.
11. Melissari, Z.; Williams, R. M.; Senge, M. O. Chapter 9 Porphyrinoids for Photodynamic Therapy. In *Applications of Porphyrinoids as Functional Materials*, 1st Ed.; The Royal Society of Chemistry, 2021; pp 252-291.
12. Raab, O. Uber die wirkung fluoreszierender stoffe auf infusorien, *Zeitung Biol.* **1900,** *39*, 524-526.
13. Moan, J.; Peng, Q. An outline of the history of PDT. In *Photodynamic Therapy*, Vol. 2; Patrice, T., Ed.;The Royal Society of Chemistry, 2003; pp 1-18.
14. Finsen, N. R. *Phototherapy*. 1st Ed.; Edward Arnold, 1901.
15. Spikes, J. D. The origin and meaning of the term "photodynamic" (as used in "photodynamic therapy", for example). *J. Photochem. Photobiol., B* **1991,** *9*, 369-371.
16. Meyer-Betz, F. Untersuchungcn iiber die biologische (photodynamische) Wirkung des Hiimatoporphyriris und anderer Derirate des Blut-und Gallenfarbstoffs. *Dtsch. Arch. Klin. Med*. **1913**, *112*, 476-503.
17. Lipson, R. L.; Baldes, E. J.; Olsen, A. M. Hematoporphyrin derivative: a new aid for endoscopic detection of malignant disease. *J. Thorac. Cardiovasc. Surg*. **1961,** *42*, 623-629.
18. Dougherty, T. J.; Grindey, G. B.; Fiel, R.; Weishaupt, K. R.; Boyle, D. G. Photoradiation therapy. II. Cure of animal tumors with hematoporphyrin and light. *J. Natl. Cancer Inst.* **1975,** *55*, 115-121.
19. Kelly, J. F.; Snell, M. E.; Berenbaum, M. C. Photodynamic destruction of human bladder carcinoma. *Br. J.Cancer* **1975,** *31*, 237-244.
20. Kelly, J. F.; Snell, M. E. Hematoporphyrin derivative: a possible aid in the diagnosis and therapy of carcinoma of the bladder. *J. Urol.* **1976,** *115*, 150-151.

21. Weishaupt, K. R.; Gomer, C. J.; Dougherty, T. J. Identification of singlet oxygen as the cytotoxic agent in photoinactivation of a murine tumor. *Cancer Res.* **1976,** *36*, 2326-2329.
22. Dougherty, T. J.; Kaufman, J. E.; Goldfarb, A.; Weishaupt, K. R.; Boyle, D.; Mittleman, A. Photoradiation therapy for the treatment of malignant tumors. *Cancer Res.* **1978,** *38*, 2628-2635.
23. Balchum, O. J.; Doiron, D. R.; Huth, G. C. Photoradiation therapy of endobronchial lung cancers employing the photodynamic action of hematoporphyrin derivative. *Lasers Surg. Med.* **1984,** *4*, 13-30.
24. McCaughan, J. S., Jr.; Hicks, W.; Laufman, L.; May, E.; Roach, R. Palliation of esophageal malignancy with photoradiation therapy. *Cancer* **1984,** *54*, 2905-2910.
25. Hayata, Y.; Kato, H.; Okitsu, H.; Kawaguchi, M.; Konaka, C. Photodynamic therapy with hematoporphyrin derivative in cancer of the upper gastrointestinal tract. *Semin. Surg. Oncol.* **1985,** *1*, 1-11.
26. Benson, R. C.; Farrow, G. M.; Kinsey, J. H.; Cortese, D. A.; Zincke, H.; Utz, D. C. Detection and localization of In situ carcinoma of the bladder with hematoporphyrin derivative. *Mayo Clin. Proc.* **1982,** *57*, 548-555.
27. Hamblin, M. R. Photodynamic Therapy for Cancer: What's Past is Prologue. *Photochem. Photobiol*. **2020,** *96*, 506-516.
28. Castano, A. P.; Demidova, T. N.; Hamblin, M. R. Mechanisms in photodynamic therapy: part one-photosensitizers, photochemistry and cellular localization. *Photodiagn. Photodyn. Ther.* **2004,** *1*, 279-293.
29. Dąbrowski, J. M.; Pucelik, B.; Regiel-Futyra, A.; Brindell, M.; Mazuryk, O.; Kyzioł, A.; Stochel, G.; Macyk, W.; Arnaut, L. G. Engineering of relevant photodynamic processes through structural modifications of metallotetrapyrrolic photosensitizers. *Coord. Chem. Rev.* **2016,** *325*, 67-101.
30. Moan, J.; Berg, K. The photodegradation of porphyrins in cells can be used to estimate the lifetime of singlet oxygen. *Photochem. Photobiol.* **1991,** *53*, 549-553.
31. Kessel, D. Subcellular Targeting as a Determinant of the Efficacy of Photodynamic Therapy. *Photochem. Photobiol.* **2017,** *93*, 609-612.
32. da Silva, E. F. F.; Pedersen, B. W.; Breitenbach, T.; Toftegaard, R.; Kuimova, M. K.; Arnaut, L. G.; Ogilby, P. R. Irradiation- and Sensitizer-Dependent Changes in the Lifetime of Intracellular Singlet Oxygen Produced in a Photosensitized Process. *J. Phys. Chem. B* **2012,** *116*, 445-461.
33. Abels, C. Targeting of the vascular system of solid tumours by photodynamic therapy (PDT). *Photochem. Photobiol. Sci.* **2004,** *3*, 765-771.
34. Donohoe, C.; Senge, M. O.; Arnaut, L. G.; Gomes-da-Silva, L. C. Cell death in photodynamic therapy: From oxidative stress to anti-tumor immunity. *Biochim. Biophys. Acta, Rev. Cancer* **2019,** *1872*, 188308.
35. Mroz, P.; Yaroslavsky, A.; Kharkwal, G. B.; Hamblin, M. R. Cell Death Pathways in Photodynamic Therapy of Cancer. *Cancers* **2011,** *3*, 2516-2539.
36. Dellinger, M. Apoptosis or Necrosis Following Photofrin® Photosensitization: Influence of the Incubation Protocol. *Photochem. Photobiol.* **1996,** *64*, 182-187.
37. Galluzzi, L.; Vitale, I.; Aaronson, S. A.; Abrams, J. M.; Adam, D.; Agostinis, P.; Alnemri, E. S.; Altucci, L.; Amelio, I.; Andrews, D. W.; Annicchiarico-Petruzzelli, M.; Antonov, A. V.; Arama, E.; Baehrecke, E. H.; Barlev, N. A.; Bazan, N. G.; Bernassola, F.; Bertrand, M. J. M.; Bianchi, K.; Blagosklonny, M. V.; Blomgren, K.; Borner, C.; Boya, P.; Brenner, C.; Campanella, M.; Candi, E.; Carmona-Gutierrez, D.; Cecconi, F.; Chan, F. K. M.; Chandel, N. S.; Cheng, E. H.; Chipuk, J. E.; Cidlowski, J. A.; Ciechanover, A.; Cohen, G. M.; Conrad, M.; Cubillos-Ruiz, J. R.; Czabotar, P. E.; D'Angiolella, V.; Dawson, T. M.;

Dawson, V. L.; De Laurenzi, V.; De Maria, R.; Debatin, K.-M.; DeBerardinis, R. J.; Deshmukh, M.; Di Daniele, N.; Di Virgilio, F.; Dixit, V. M.; Dixon, S. J.; Duckett, C. S.; Dynlacht, B. D.; El-Deiry, W. S.; Elrod, J. W.; Fimia, G. M.; Fulda, S.; García-Sáez, A. J.; Garg, A. D.; Garrido, C.; Gavathiotis, E.; Golstein, P.; Gottlieb, E.; Green, D. R.; Greene, L. A.; Gronemeyer, H.; Gross, A.; Hajnoczky, G.; Hardwick, J. M.; Harris, I. S.; Hengartner, M. O.; Hetz, C.; Ichijo, H.; Jäättelä, M.; Joseph, B.; Jost, P. J.; Juin, P. P.; Kaiser, W. J.; Karin, M.; Kaufmann, T.; Kepp, O.; Kimchi, A.; Kitsis, R. N.; Klionsky, D. J.; Knight, R. A.; Kumar, S.; Lee, S. W.; Lemasters, J. J.; Levine, B.; Linkermann, A.; Lipton, S. A.; Lockshin, R. A.; López-Otín, C.; Lowe, S. W.; Luedde, T.; Lugli, E.; MacFarlane, M.; Madeo, F.; Malewicz, M.; Malorni, W.; Manic, G.; Marine, J.-C.; Martin, S. J.; Martinou, J.-C.; Medema, J. P.; Mehlen, P.; Meier, P.; Melino, S.; Miao, E. A.; Molkentin, J. D.; Moll, U. M.; Muñoz-Pinedo, C.; Nagata, S.; Nuñez, G.; Oberst, A.; Oren, M.; Overholtzer, M.; Pagano, M.; Panaretakis, T.; Pasparakis, M.; Penninger, J. M.; Pereira, D. M.; Pervaiz, S.; Peter, M. E.; Piacentini, M.; Pinton, P.; Prehn, J. H. M.; Puthalakath, H.; Rabinovich, G. A.; Rehm, M.; Rizzuto, R.; Rodrigues, C. M. P.; Rubinsztein, D. C.; Rudel, T.; Ryan, K. M.; Sayan, E.; Scorrano, L.; Shao, F.; Shi, Y.; Silke, J.; Simon, H.-U.; Sistigu, A.; Stockwell, B. R.; Strasser, A.; Szabadkai, G.; Tait, S. W. G.; Tang, D.; Tavernarakis, N.; Thorburn, A.; Tsujimoto, Y.; Turk, B.; Vanden Berghe, T.; Vandenabeele, P.; Vander Heiden, M. G.; Villunger, A.; Virgin, H. W.; Vousden, K. H.; Vucic, D.; Wagner, E. F.; Walczak, H.; Wallach, D.; Wang, Y.; Wells, J. A.; Wood, W.; Yuan, J.; Zakeri, Z.; Zhivotovsky, B.; Zitvogel, L.; Melino, G.; Kroemer, G. Molecular mechanisms of cell death: recommendations of the Nomenclature Committee on Cell Death 2018. *Cell Death Differ.* **2018,** *25*, 486-541.

38. Kroemer, G.; Galluzzi, L.; Kepp, O.; Zitvogel, L. Immunogenic Cell Death in Cancer Therapy. *Annu. Rev. Immunol.* **2013,** *31*, 51-72.

39. Castano, A. P.; Mroz, P.; Hamblin, M. R. Photodynamic therapy and anti-tumour immunity. *Nat. Rev. Cancer* **2006,** *6*, 535-545.

40. Rocha, L. B.; Gomes-da-Silva, L. C.; Dąbrowski, J. M.; Arnaut, L. G. Elimination of primary tumours and control of metastasis with rationally designed bacteriochlorin photodynamic therapy regimens. *Eur. J. Cancer* **2015,** *51*, 1822-1830.

41. Preise, D.; Oren, R.; Glinert, I.; Kalchenko, V.; Jung, S.; Scherz, A.; Salomon, Y. Systemic antitumor protection by vascular-targeted photodynamic therapy involves cellular and humoral immunity. *Cancer Immunol. Immunother.* **2009,** *58*, 71-84.

42. Spring, B. Q.; Rizvi, I.; Xu, N.; Hasan, T. The role of photodynamic therapy in overcoming cancer drug resistance. *Photochem. Photobiol. Sci.* **2015,** *14*, 1476-1491.

43. Gierlich, P.; Mata, A. I.; Donohoe, C.; Brito, R. M. M.; Senge, M. O.; Gomes-da-Silva, L. C. Ligand-Targeted Delivery of Photosensitizers for Cancer Treatment. *Molecules* **2020**, *25*, 5317-5371.

44. Polo, L.; Valduga, G.; Jori, G.; Reddi, E. Low-density lipoprotein receptors in the uptake of tumour photosensitizers by human and rat transformed fibroblasts. *Int. J. Biochem. Cell Biol.* **2002,** *34*, 10-23.

45. Gomes-da-Silva, L. C.; Kepp, O.; Kroemer, G. Regulatory approval of photoimmunotherapy: photodynamic therapy that induces immunogenic cell death. *Oncoimmunology* **2020,** *9*, 1841393.

46. DeVita, V. T., Jr.; Chu, E. A history of cancer chemotherapy. *Cancer Res.* **2008,** *68*, 8643-8653.

47. Hadjipanayis, C. G.; Stummer, W. 5-ALA and FDA approval for glioma surgery. *J. Neuro-Oncol.* **2019,** *141*, 479-486.

48. van Doeveren, T. E. M.; Karakullukçu, M. B.; van Veen, R. L. P.; Lopez-Yurda, M.; Schreuder, W. H.; Tan, I. B. Adjuvant photodynamic therapy in head and neck cancer after tumor-positive resection margins. *Laryngoscope.* **2018,** *128*, 657-663.
49. DeVita, V. T., Jr.; Eggermont, A. M.; Hellman, S.; Kerr, D. J. Clinical cancer research: the past, present and the future. *Nat. Rev. Clin. Oncol.* **2014,** *11*, 663-669.
50. Hua, J.; Wu, P.; Gan, L.; Zhang, Z.; He, J.; Zhong, L.; Zhao, Y.; Huang, Y. Current Strategies for Tumor Photodynamic Therapy Combined With Immunotherapy. *Front. Oncol.* **2021,** *11*, 738323.
51. Muchowicz, A.; Wachowska, M.; Stachura, J.; Tonecka, K.; Gabrysiak, M.; Wołosz, D.; Pilch, Z.; Kilarski, W. W.; Boon, L.; Klaus, T. J.; Golab, J. Inhibition of lymphangiogenesis impairs antitumour effects of photodynamic therapy and checkpoint inhibitors in mice. *Eur. J. Cancer* **2017,** *83*, 19-27.
52. Corradi, R. B.; LaRosa, S.; Jebiwott, S.; Murray, K. S.; Rosenzweig, B.; Somma, A. J.; Gomez, R. S.; Scherz, A.; Kim, K.; Coleman, J. A. Effectiveness of the combination of vascular targeted photodynamic therapy and anti-cytotoxic T-lymphocyte-associated antigen 4 in a preclinical mouse model of urothelial carcinoma. *Int. J. Urol.* **2019,** *26*, 414-422.
53. Lobo, C. S.; Gomes-da-Silva, L. C.; Arnaut, L. G. Potentiation of Systemic Anti-Tumor Immunity with Photodynamic Therapy Using Porphyrin Derivatives. In *Handbook of Porphyrin Science*, Vol. 46; World Scientific, 2021; pp 279-344.
54. Mallidi, S.; Anbil, S.; Bulin, A.-L.; Obaid, G.; Ichikawa, M.; Hasan, T. Beyond the Barriers of Light Penetration: Strategies, Perspectives and Possibilities for Photodynamic Therapy. *Theranostics* **2016,** *6*, 2458-2487.
55. Szaciłowski, K.; Macyk, W.; Drzewiecka-Matuszek, A.; Brindell, M.; Stochel, G. Bioinorganic Photochemistry: Frontiers and Mechanisms. *Chem. Rev.* **2005,** *105*, 2647-2694.
56. Bashkatov, A. N.; Genina, E. A.; Kochubey, V. I.; Tuchin, V. V. Optical properties of human skin, subcutaneous and mucous tissues in the wavelength range from 400 to 2000 nm. *J. Phys. D: Appl. Phys.* **2005,** *38*, 2543-2555.
57. Schweitzer, C.; Schmidt, R. Physical Mechanisms of Generation and Deactivation of Singlet Oxygen. *Chem. Rev.***2003,** *103*, 1685-1758.
58. van Straten, D.; Mashayekhi, V.; de Bruijn, H. S.; Oliveira, S.; Robinson, D. J. Oncologic Photodynamic Therapy: Basic Principles, Current Clinical Status and Future Directions. *Cancers* **2017,** *9*, 19.
59. Ibarra, A. M. C.; Cecatto, R. B.; Motta, L. J.; Dos Santos Franco, A. L.; de Fátima Teixeira da Silva, D.; Nunes, F. D.; Hamblin, M. R.; Rodrigues, M. Photodynamic therapy for squamous cell carcinoma of the head and neck: narrative review focusing on photosensitizers. *Lasers Med. Sci.* **2022,** *37*, 1441-1470.
60. Holcombe, J. A.; Farnsworth, P. B. Atomic Emission and Fluorescence Theory. In *Encyclopedia of Spectroscopy and Spectrometry*, 3rd Ed.; Lindon, J. C.; Tranter, G. E.; Koppenaal, D. W., Eds.; Academic Press, 2017; pp 52-57.
61. Henderson, B. W.; Busch, T. M.; Snyder, J. W. Fluence rate as a modulator of PDT mechanisms. *Lasers. Surg. Med.* **2006**, *38*, 489-493.
62. Noweski, A.; Roosen, A.; Lebdai, S.; Barret, E.; Emberton, M.; Benzaghou, F.; Apfelbeck, M.; Gaillac, B.; Gratzke, C.; Stief, C.; Azzouzi, A. R. Medium-term Follow-up of Vascular-targeted Photodynamic Therapy of Localized Prostate Cancer Using TOOKAD Soluble WST-11 (Phase II Trials). *Eur. Urol. Focus* **2019,** *5*, 1022-1028.
63. Hanada, Y.; Pereira, S. P.; Pogue, B.; Maytin, E. V.; Hasan, T.; Linn, B.; Mangels-Dick, T.; Wang, K. K. EUS-guided verteporfin photodynamic therapy for pancreatic cancer. *Gastrointest. Endosc.* **2021,** *94*, 179-186.

64. Lin, X.; Song, J.; Chen, X.; Yang, H. Ultrasound-Activated Sensitizers and Applications. *Angew. Chem., Int. Ed.* **2020,** *59*, 14212-14233.
65. Lee See, K.; Forbes, I. J.; Betts, W. H. Oxygen dependency of photocytotoxicity with haematoporphyrin derivative. *Photochem. Photobiol.* **1984,** *39*, 631-634.
66. Wang, H. W.; Putt, M. E.; Emanuele, M. J.; Shin, D. B.; Glatstein, E.; Yodh, A. G.; Busch, T. M. Treatment-induced changes in tumor oxygenation predict photodynamic therapy outcome. *Cancer Res.* **2004,** *64*, 7553-7561.
67. Harris, A. L. Hypoxia--a key regulatory factor in tumour growth. *Nat. Rev. Cancer* **2002,** *2*, 38-47.
68. Shen, Z.; Ma, Q.; Zhou, X.; Zhang, G.; Hao, G.; Sun, Y.; Cao, J. Strategies to improve photodynamic therapy efficacy by relieving the tumor hypoxia environment. *NPG Asia Mater.* **2021,** *13*, 39.
69. Uchoa, A. F.; de Oliveira, K. T.; Baptista, M. S.; Bortoluzzi, A. J.; Iamamoto, Y.; Serra, O. A. Chlorin Photosensitizers Sterically Designed To Prevent Self-Aggregation. *J. Org. Chem.* **2011,** *76*, 8824-8832.
70. O'Connor, A. E.; Gallagher, W. M.; Byrne, A. T. Porphyrin and nonporphyrin photosensitizers in oncology: preclinical and clinical advances in photodynamic therapy. *Photochem. Photobiol.* **2009,** *85*, 1053-1074.
71. Battersby, A. R. Tetrapyrroles: the pigments of life. *Nat. Prod. Rep.* **2000,** *17*, 507-526.
72. Arai, T.; Tsukuni, A.; Kawazu, K.; Aoi, H.; Hamada, T.; Nishino, N. Synthesis of a membrane-spanning lipophilic porphyrin with links to two alamethicin fragments on each face. *J. Chem. Soc., Perkin Trans. 2* **2000,** *7*, 1381-1390.
73. Senge, M. O.; Sergeeva, N. N.; Hale, K. J. Classic highlights in porphyrin and porphyrinoid total synthesis and biosynthesis. *Chem. Soc. Rev.* **2021,** *50*, 4730-4789.
74. Arnaut, L. G. Chapter 5 - Design of porphyrin-based photosensitizers for photodynamic therapy. In *Advances in Inorganic Chemistry*, Vol. 63; Eldik, R. v.; Stochel, G., Eds.; Academic Press, 2011; pp 187-233.
75. Castano, A. P.; Demidova, T. N.; Hamblin, M. R. Mechanisms in photodynamic therapy: Part three-Photosensitizer pharmacokinetics, biodistribution, tumor localization and modes of tumor destruction. *Photodiagn. Photodyn. Ther.* **2005,** *2*, 91-106.
76. Reddi, E.; Zhou, C.; Biolo, R.; Menegaldo, E.; Jori, G. Liposome- or LDL-administered Zn (II)-phthalocyanine as a photodynamic agent for tumours. I. Pharmacokinetic properties and phototherapeutic efficiency. *Br. J. Cancer* **1990,** *61*, 407-411.
77. Ezzeddine, R.; Al-Banaw, A.; Tovmasyan, A.; Craik, J. D.; Batinic-Haberle, I.; Benov, L. T. Effect of molecular characteristics on cellular uptake, subcellular localization, and phototoxicity of Zn(II) N-alkylpyridylporphyrins. *J. Biol. Chem.* **2013,** *288*, 36579-36588.
78. Zheng, G.; Potter, W. R.; Camacho, S. H.; Missert, J. R.; Wang, G.; Bellnier, D. A.; Henderson, B. W.; Rodgers, M. A.; Dougherty, T. J.; Pandey, R. K. Synthesis, photophysical properties, tumor uptake, and preliminary *in vivo* photosensitizing efficacy of a homologous series of 3-(1'-alkyloxy)ethyl-3-devinylpurpurin-18-N-alkylimides with variable lipophilicity. *J. Med. Chem.* **2001,** *44*, 1540-1559.
79. Tasso, T. T.; Tsubone, T. M.; Baptista, M. S.; Mattiazzi, L. M.; Acunha, T. V.; Iglesias, B. A. Isomeric effect on the properties of tetraplatinated porphyrins showing optimized phototoxicity for photodynamic therapy. *Dalton Trans.* **2017,** *46* , 11037-11045.
80. Engelmann, F. M.; Mayer, I.; Gabrielli, D. S.; Toma, H. E.; Kowaltowski, A. J.; Araki, K.; Baptista, M. S. Interaction of cationic meso-porphyrins with liposomes, mitochondria and erythrocytes. *J. Bioenerg. Biomembr.* **2007,** *39*, 175-85.

81. Jensen, T. J.; Vicente, M. G. H.; Luguya, R.; Norton, J.; Fronczek, F. R.; Smith, K. M. Effect of overall charge and charge distribution on cellular uptake, distribution and phototoxicity of cationic porphyrins in HEp2 cells. *J. Photochem. Photobiol., B* **2010,** *100*, 100-111.
82. Osterloh, J.; Vicente, M. G. H. Mechanisms of porphyrinoid localization in tumors. *J. Porphyrins Phthalocyanines* **2002,** *6*, 305-324.
83. Kessel, D.; Luguya, R.; Vicente, M. G. Localization and photodynamic efficacy of two cationic porphyrins varying in charge distributions. *Photochem. Photobiol.* **2003,** *78*, 431-435.
84. Engelmann, F. M.; Rocha, S. V. O.; Toma, H. E.; Araki, K.; Baptista, M. S. Determination of n-octanol/water partition and membrane binding of cationic porphyrins. *Int. J. Pharm.* **2007,** *329*, 12-18.
85. Ben-Dror, S.; Bronshtein, I.; Wiehe, A.; Röder, B.; Senge, M. O.; Ehrenberg, B. On the correlation between hydrophobicity, liposome binding and cellular uptake of porphyrin sensitizers. *Photochem. Photobiol* **2006,** *82*, 695-701.
86. Moriwaki, S. I.; Misawa, J.; Yoshinari, Y.; Yamada, I.; Takigawa, M.; Tokura, Y. Analysis of photosensitivity in Japanese cancer-bearing patients receiving photodynamic therapy with porfimer sodium (Photofrin). *Photodermatol., Photoimmunol. Photomed.* **2001,** *17*, 241-243.
87. Collier, N. J.; Rhodes, L. E. Photodynamic Therapy for Basal Cell Carcinoma: The Clinical Context for Future Research Priorities. *Molecules* **2020,** *25*, 5398 - 5425.
88. Scott, L. J.; Goa, K. L. Verteporfin. *Drugs Aging.* **2000,** *16*, 139-146.
89. Wang, S.; Bromley, E.; Xu, L.; Chen, J. C.; Keltner, L. Talaporfin sodium. *Expert Opin. Pharmacother.* **2010,** *11*, 133-140.
90. Senge, M. O.; Brandt, J. C. Temoporfin (Foscan®, 5,10,15,20-tetra(m-hydroxyphenyl)chlorin)-a second-generation photosensitizer. *Photochem. Photobiol.* **2011,** *87*, 1240-1296.
91. Usuda, J.; Kato, H.; Okunaka, T.; Furukawa, K.; Tsutsui, H.; Yamada, K.; Suga, Y.; Honda, H.; Nagatsuka, Y.; Ohira, T.; Tsuboi, M.; Hirano, T. Photodynamic therapy (PDT) for lung cancers. *J. Thorac. Oncol.* **2006,** *1*, 489-93.
92. Mazor, O.; Brandis, A.; Plaks, V.; Neumark, E.; Rosenbach-Belkin, V.; Salomon, Y.; Scherz, A. WST11, a novel water-soluble bacteriochlorophyll derivative; cellular uptake, pharmacokinetics, biodistribution and vascular-targeted photodynamic activity using melanoma tumors as a model. *Photochem. Photobiol.* **2005,** *81*, 342-351.
93. Taneja, S. S.; Bennett, J.; Coleman, J.; Grubb, R.; Andriole, G.; Reiter, R. E.; Marks, L.; Azzouzi, A.-R.; Emberton, M. Final Results of a Phase I/II Multicenter Trial of WST11 Vascular Targeted Photodynamic Therapy for Hemi-Ablation of the Prostate in Men with Unilateral Low Risk Prostate Cancer Performed in the United States. *J. Urol.* **2016,** *196*, 1096-1104.
94. Santos, L. L.; Oliveira, J.; Monteiro, E.; Santos, J.; Sarmento, C. Treatment of Head and Neck Cancer with Photodynamic Therapy with Redaporfin: A Clinical Case Report. *Case Rep. Oncol.* **2018,** *11*, 769-776.
95. ClinicalTrials.gov. https://clinicaltrials.gov/ct2/show/NCT02070432 (accessed 01-05-2022).
96. Pucelik, B.; Sułek, A.; Dąbrowski, J. M. Bacteriochlorins and their metal complexes as NIR-absorbing photosensitizers: properties, mechanisms, and applications. *Coord. Chem. Rev.* **2020,** *416*, 213340.
97. Arnaut, L. G.; Pereira, M. M.; Dąbrowski, J. M.; Silva, E. F. F.; Schaberle, F. A.; Abreu, A. R.; Rocha, L. B.; Barsan, M. M.; Urbańska, K.; Stochel, G.; Brett, C. M. A.

Photodynamic Therapy Efficacy Enhanced by Dynamics: The Role of Charge Transfer and Photostability in the Selection of Photosensitizers. *Chem. - Eur. J.* **2014,** *20*, 5346-5357.
98. Soares, H. T.; Campos, J. R.; Gomes-da-Silva, L. C.; Schaberle, F. A.; Dabrowski, J. M.; Arnaut, L. G. Pro-oxidant and Antioxidant Effects in Photodynamic Therapy: Cells Recognise that Not All Exogenous ROS Are Alike. *ChemBioChem* **2016,** *17*, 836-842.
99. Gomes-da-Silva, L. C.; Zhao, L.; Arnaut, L. G.; Kroemer, G.; Kepp, O. Redaporfin induces immunogenic cell death by selective destruction of the endoplasmic reticulum and the Golgi apparatus. *Oncotarget* **2018,** *9*, 31169-31170.
100. Gomes-da-Silva, L. C.; Zhao, L.; Bezu, L.; Zhou, H.; Sauvat, A.; Liu, P.; Durand, S.; Leduc, M.; Souquere, S.; Loos, F.; Mondragón, L.; Sveinbjørnsson, B.; Rekdal, Ø.; Boncompain, G.; Perez, F.; Arnaut, L. G.; Kepp, O.; Kroemer, G. Photodynamic therapy with redaporfin targets the endoplasmic reticulum and Golgi apparatus. *EMBO J.* **2018,** *37*, e98354.
101. Saavedra, R.; Rocha, L. B.; Dąbrowski, J. M.; Arnaut, L. G. Modulation of biodistribution, pharmacokinetics, and photosensitivity with the delivery vehicle of a bacteriochlorin photosensitizer for photodynamic therapy. *ChemMedChem* **2014,** *9*, 390-398.
102. Karwicka, M.; Pucelik, B.; Gonet, M.; Elas, M.; Dąbrowski, J. M. Effects of Photodynamic Therapy with Redaporfin on Tumor Oxygenation and Blood Flow in a Lung Cancer Mouse Model. *Sci. Rep.* **2019,** *9*, 12655.
103. Lobo, A. C. S.; Gomes-da-Silva, L. C.; Rodrigues-Santos, P.; Cabrita, A.; Santos-Rosa, M.; Arnaut, L. G. Immune Responses after Vascular Photodynamic Therapy with Redaporfin. *J .Clin. Med.* **2019,** *9*, 104.
104. Rocha, L. B.; Soares, H. T.; Mendes, M. I. P.; Cabrita, A.; Schaberle, F. A.; Arnaut, L. G. Necrosis Depth and Photodynamic Threshold Dose with Redaporfin-PDT. *Photochem. Photobiol.* **2020,** *96*, 692-698.
105. Fereira Goncalves, N. P.; Cerca Martins dos Santos, T. P.; Pereira Nascimento Costa, G.; Pereira Monteiro, C. J.; Shaberle, F.; Correia Alfar, S.; Reis de Abreu, A. C.; Pereira, M. M.; Arnaut, L. G. Atropisomers of Halogenated Tetraphenylbacteriochlorins and Chlorins and their use in Photodynamic Therapy. WO2016151458A1, September 29, 2016.
106. Clayden, J.; Moran, W. J.; Edwards, P. J.; LaPlante, S. R. The Challenge of Atropisomerism in Drug Discovery. *Angew. Chem., Int. Ed.* **2009,** *48*, 6398-6401.
107. Christie, G. H.; Kenner, J. LXXI.—The molecular configurations of polynuclear aromatic compounds. Part I. The resolution of γ-6 : 6′-dinitro- and 4 : 6 : 4′ : 6′-tetranitro-diphenic acids into optically active components. *J. Chem. Soc., Trans.* **1922,** *121*, 614-620.
108. Kuhn, R., Molekulare asymmetrie. In *Stereochemie*, Freudenberg, K., Ed.; Franz Deutike,1933; pp 803-824.
109. Ernest, E. L.; Wilen, S. H.; Mander, L. N. *Stereochemistry of Organic Compounds*, Wiley Interscience, 1994; pp 1190.
110. Mislow, K., Die absolute Konfiguration der atropisomeren Diaryl-Verbindungen. *Angewandte Chemie* **1958,** *70*, 683-689.
111. LaPlante, S. R.; Fader, L. D.; Fandrick, K. R.; Fandrick, D. R.; Hucke, O.; Kemper, R.; Miller, S. P. F.; Edwards, P. J., Assessing Atropisomer Axial Chirality in Drug Discovery and Development. *J. Med. Chem.* **2011,** *54*, 7005-7022.
112. Oki, M. *Recent Advances in Atropisomerism,* Vol. 14.; Wiley, 1983.
113. de Ceuninck van Capelle, L. A.; Macdonald, J. M.; Hyland, C. J. T. Stereogenic and conformational properties of medium-ring benzo-fused N-heterocycle atropisomers. *Org. Biomol. Chem.* **2021,** *19*, 7098-7115.

114. Ramig, K. Stereodynamic Properties of Medium-Ring Benzo-Fused Nitrogenous Heterocycles: Benzodiazepines, Benzazepines, Benzazocines, and Benzazonines. *ChemInform* **2014,** *45*, 10783-10795.
115. LaPlante, S. R.; Edwards, P. J.; Fader, L. D.; Jakalian, A.; Hucke, O. Revealing Atropisomer Axial Chirality in Drug Discovery. *ChemMedChem* **2011,** *6*, 505-513.
116. Glunz, P. W. Recent encounters with atropisomerism in drug discovery. *Bioorg. Med. Chem. Lett.* **2018,** *28*, 53-60.
117. Toenjes, S. T.; Gustafson, J. L. Atropisomerism in medicinal chemistry: challenges and opportunities. *Future Med. Chem.* **2018,** *10* , 409-422.
118. LaPlante, S. R.; Forgione, P.; Boucher, C.; Coulombe, R.; Gillard, J.; Hucke, O.; Jakalian, A.; Joly, M.-A.; Kukolj, G.; Lemke, C.; McCollum, R.; Titolo, S.; Beaulieu, P. L.; Stammers, T. Enantiomeric Atropisomers Inhibit HCV Polymerase and/or HIV Matrix: Characterizing Hindered Bond Rotations and Target Selectivity. *J.Med. Chem.* **2014,** *57*, 1944-1951.
119. Elleraas, J.; Ewanicki, J.; Johnson, T. W.; Sach, N. W.; Collins, M. R.; Richardson, P. F. Conformational Studies and Atropisomerism Kinetics of the ALK Clinical Candidate Lorlatinib (PF-06463922) and Desmethyl Congeners. *Angew. Chem., Int. Ed.* **2016,** *55*, 3590-3595.
120. Glunz, P. W.; Mueller, L.; Cheney, D. L.; Ladziata, V.; Zou, Y.; Wurtz, N. R.; Wei, A.; Wong, P. C.; Wexler, R. R.; Priestley, E. S. Atropisomer Control in Macrocyclic Factor VIIa Inhibitors. *J. Med. Chem.* **2016,** *59*, 4007-4018.
121. Toenjes, S. T.; Basilaia, M.; Gustafson, J. L. Leveraging conformational control about a potential atropisomeric axis as a strategy in medical chemistry. *Future Med. Chem.* **2021,** *13*, 443-446.
122. Fabro, S.; Smith, R. L.; Williams, R. T. Toxicity and Teratogenicity of Optical Isomers of Thalidomide. *Nature* **1967,** *215*, 296-296.
123. Cotzias, G. C.; Van Woert, M. H.; Schiffer, L. M. Aromatic Amino Acids and Modification of Parkinsonism. *N. Engl. J. Med.* **1967,** *276*, 374-379.
124. Thomas, J. M.; Schug, S. A. Recent advances in the pharmacokinetics of local anaesthetics. Long-acting amide enantiomers and continuous infusions. *Clin. Pharmacokinet.* **1999,** *36*, 67-83.
125. Rickhaus, M.; Jundt, L.; Mayor, M. Determining Inversion Barriers in Atropisomers - A Tutorial for Organic Chemists. *Chimia* **2016,** *70*, 192-202.
126. Oguadinma, P.; Bilodeau, F.; LaPlante, S. R. NMR strategies to support medicinal chemistry workflows for primary structure determination. *Bioorganic & medicinal chemistry letters* **2017,** *27*, 242-247.
127. Porter, J.; Payne, A.; Whitcombe, I.; de Candole, B.; Ford, D.; Garlish, R.; Hold, A.; Hutchinson, B.; Trevitt, G.; Turner, J.; Edwards, C.; Watkins, C.; Davis, J.; Stubberfield, C. Atropisomeric small molecule Bcl-2 ligands: determination of bioactive conformation. *Bioorg. Med. Chem. Lett.* **2009,** *19*, 1767-1772.
128. Dai, J.; Wang, C.; Traeger, S. C.; Discenza, L.; Obermeier, M. T.; Tymiak, A. A.; Zhang, Y. The role of chromatographic and chiroptical spectroscopic techniques and methodologies in support of drug discovery for atropisomeric drug inhibitors of Bruton's tyrosine kinase. *J. Chromatogr. A* **2017,** *1487*, 116-128.
129. Wesolowski, S. S.; Pivonka, D. E. A rapid alternative to X-ray crystallography for chiral determination: case studies of vibrational circular dichroism (VCD) to advance drug discovery projects. *Bioorg. Med. Chem. Lett.* **2013,** *23*, 4019-4025.
130. Davoren, J. E.; Nason, D.; Coe, J.; Dlugolenski, K.; Helal, C.; Harris, A. R.; LaChapelle, E.; Liang, S.; Liu, Y.; O'Connor, R.; Orozco, C. C.; Rai, B. K.; Salafia, M.;

Samas, B.; Xu, W.; Kozak, R.; Gray, D. Discovery and Lead Optimization of Atropisomer D1 Agonists with Reduced Desensitization. *J. Med.Chem.* **2018,** *61*, 11384-11397.
131. Pivonka, D. E.; Wesolowski, S. S. Vibrational circular dichroism (VCD) chiral assignment of atropisomers: application to γ-aminobutyric acid (GABA) modulators designed as potential anxiolytic drugs. *Appl. Spectrosc.* **2013,** *67*, 365-371.
132. Zhou, Y. S.; Tay, L. K.; Hughes, D.; Donahue, S. Simulation of the Impact of Atropisomer Interconversion on Plasma Exposure of Atropisomers of an Endothelin Receptor Antagonist. *J. Clin. Pharmacol.* **2004,** *44*, 680-688.
133. Kanase, Y.; Kitada, T.; Tabata, H.; Makino, K.; Oshitari, T.; Ohashi, H.; Yoshinaga, T.; Natsugari, H.; Takahashi, H. 4-Substituted carbamazepine derivatives: Conformational analysis and sodium channel-blocking properties. *Bioorg. Med. Chem.* **2018,** *26*, 2508-2513.
134. Bu, X.; Skrdla, P. J.; Dormer, P. G.; Bereznitski, Y. Separation of triphenyl atropisomers of a pharmaceutical compound on a novel mixed mode stationary phase: a case study involving dynamic chromatography, dynamic NMR and molecular modeling. *J. Chromatogr. A* **2010,** *1217*, 7255-7264.
135. Ciogli, A.; Vivek Kumar, S.; Mancinelli, M.; Mazzanti, A.; Perumal, S.; Severi, C.; Villani, C. Atropisomerism in 3-arylthiazolidine-2-thiones. A combined dynamic NMR and dynamic HPLC study. *Org. Biomol. Chem.* **2016,** *14*, 11137-11147.
136. Casarini, D.; Lunazzi, L.; Mazzanti, A. Recent Advances in Stereodynamics and Conformational Analysis by Dynamic NMR and Theoretical Calculations. *Eur. J. Org. Chem.* **2010,** *11*, 2035-2056.
137. Ramig, K.; Greer, E. M.; Szalda, D. J.; Karimi, S.; Ko, A.; Boulos, L.; Gu, J.; Dvorkin, N.; Bhramdat, H.; Subramaniam, G. NMR Spectroscopic and Computational Study of Conformational Isomerism in Substituted 2-Aryl-3H-1-benzazepines: Toward Isolable Atropisomeric Benzazepine Enantiomers. *J. Org. Chem.* **2013,** *78*, 8028-8036.
138. Xing, L.; Devadas, B.; Devraj, R. V.; Selness, S. R.; Shieh, H.; Walker, J. K.; Mao, M.; Messing, D.; Samas, B.; Yang, J. Z.; Anderson, G. D.; Webb, E. G.; Monahan, J. B. Discovery and characterization of atropisomer PH-797804, a p38 MAP kinase inhibitor, as a clinical drug candidate. *ChemMedChem* **2012,** *7*, 273-280.
139. Carlier, P. R.; Sun, Y.-S.; Hsu, D. C.; Chen, Q.-H. Axial-Selective H/D Exchange of Glycine-Derived 1H-Benzo[*e*][1,4]diazepin-2(*3H*)-ones: Kinetic and Computational Studies of Enantiomerization. *J. Org. Chem.* **2010,** *75*, 6588-6594.
140. Yan, T. Q.; Riley, F.; Philippe, L.; Davoren, J.; Cox, L.; Orozco, C.; Rai, B.; Hardink, M. Chromatographic resolution of atropisomers for toxicity and biotransformation studies in pharmaceutical research. *J. Chromatogr. A* **2015,** *1398*, 108-120.
141. Wang, J.; Zeng, W.; Li, S.; Shen, L.; Gu, Z.; Zhang, Y.; Li, J.; Chen, S.; Jia, X. Discovery and Assessment of Atropisomers of (±)-Lesinurad. *ACS Med. Chem. Lett.* **2017,** *8*, 299-303.
142. Yoshida, K.; Itoyama, R.; Yamahira, M.; Tanaka, J.; Loaëc, N.; Lozach, O.; Durieu, E.; Fukuda, T.; Ishibashi, F.; Meijer, L.; Iwao, M. Synthesis, Resolution, and Biological Evaluation of Atropisomeric (aR)- and (aS)-16-Methyllamellarins N: Unique Effects of the Axial Chirality on the Selectivity of Protein Kinases Inhibition. *J. Med. Chem.* **2013,** *56*, 7289-7301.
143. Watterson, S. H.; De Lucca, G. V.; Shi, Q.; Langevine, C. M.; Liu, Q.; Batt, D. G.; Beaudoin Bertrand, M.; Gong, H.; Dai, J.; Yip, S.; Li, P.; Sun, D.; Wu, D.-R.; Wang, C.; Zhang, Y.; Traeger, S. C.; Pattoli, M. A.; Skala, S.; Cheng, L.; Obermeier, M. T.; Vickery, R.; Discenza, L. N.; D'Arienzo, C. J.; Zhang, Y.; Heimrich, E.; Gillooly, K. M.; Taylor, T. L.; Pulicicchio, C.; McIntyre, K. W.; Galella, M. A.; Tebben, A. J.; Muckelbauer, J. K.;

Chang, C.; Rampulla, R.; Mathur, A.; Salter-Cid, L.; Barrish, J. C.; Carter, P. H.; Fura, A.; Burke, J. R.; Tino, J. A. Discovery of 6-Fluoro-5-(R)-(3-(S)-(8-fluoro-1-methyl-2,4-dioxo-1,2-dihydroquinazolin-3(4H)-yl)-2-methylphenyl)-2-(S)-(2-hydroxypropan-2-yl)-2,3,4,9-tetrahydro-1H-carbazole-8-carboxamide (BMS-986142): A Reversible Inhibitor of Bruton's Tyrosine Kinase (BTK) Conformationally Constrained by Two Locked Atropisomers. *J. Med. Chem.* **2016,** *59*, 9173-9200.
144. Srivastava, A. S.; Ko, S.; Watterson, S. H.; Pattoli, M. A.; Skala, S.; Cheng, L.; Obermeier, M. T.; Vickery, R.; Discenza, L. N.; D'Arienzo, C. J.; Gillooly, K. M.; Taylor, T. L.; Pulicicchio, C.; McIntyre, K. W.; Yip, S.; Li, P.; Sun, D.; Wu, D.-R.; Dai, J.; Wang, C.; Zhang, Y.; Wang, B.; Pawluczyk, J.; Kempson, J.; Zhao, R.; Hou, X.; Rampulla, R.; Mathur, A.; Galella, M. A.; Salter-Cid, L.; Barrish, J. C.; Carter, P. H.; Fura, A.; Burke, J. R.; Tino, J. A. Driving Potency with Rotationally Stable Atropisomers: Discovery of Pyridopyrimidinedione-Carbazole Inhibitors of BTK. *ACS Med. Chem. Lett.* **2020,** *11*, 2195-2203.
145. Tichenor, M. S.; Wiener, J. J. M.; Rao, N. L.; Pooley Deckhut, C.; Barbay, J. K.; Kreutter, K. D.; Bacani, G. M.; Wei, J.; Chang, L.; Murrey, H. E.; Wang, W.; Ahn, K.; Huber, M.; Rex, E.; Coe, K. J.; Wu, J.; Seierstad, M.; Bembenek, S. D.; Leonard, K. A.; Lebsack, A. D.; Venable, J. D.; Edwards, J. P. Discovery of a Potent and Selective Covalent Inhibitor of Bruton's Tyrosine Kinase with Oral Anti-Inflammatory Activity. *ACS Med, Chem. Lett.* **2021,** *12*, 782-790.
146. Smith, D. E.; Marquez, I.; Lokensgard, M. E.; Rheingold, A. L.; Hecht, D. A.; Gustafson, J. L. Exploiting Atropisomerism to Increase the Target Selectivity of Kinase Inhibitors. *Angew. Chem., Int. Ed.* **2015,** *54*, 11754-11759.
147. Graceffa, R. F.; Boezio, A. A.; Able, J.; Altmann, S.; Berry, L. M.; Boezio, C.; Butler, J. R.; Chu-Moyer, M.; Cooke, M.; DiMauro, E. F.; Dineen, T. A.; Feric Bojic, E.; Foti, R. S.; Fremeau, R. T.; Guzman-Perez, A.; Gao, H.; Gunaydin, H.; Huang, H.; Huang, L.; Ilch, C.; Jarosh, M.; Kornecook, T.; Kreiman, C. R.; La, D. S.; Ligutti, J.; Milgram, B. C.; Lin, M.-H. J.; Marx, I. E.; Nguyen, H. N.; Peterson, E. A.; Rescourio, G.; Roberts, J.; Schenkel, L.; Shimanovich, R.; Sparling, B. A.; Stellwagen, J.; Taborn, K.; Vaida, K. R.; Wang, J.; Yeoman, J.; Yu, V.; Zhu, D.; Moyer, B. D.; Weiss, M. M. Sulfonamides as Selective NaV1.7 Inhibitors: Optimizing Potency, Pharmacokinetics, and Metabolic Properties to Obtain Atropisomeric Quinolinone (AM-0466) that Affords Robust *in Vivo* Activity. *J. Med. Chem.* **2017,** *60*, 5990-6017.
148. Szeleczky, Z.; Szakács, Z.; Bozó, É.; Baska, F.; Vukics, K.; Lévai, S.; Temesvári, K.; Vass, E.; Béni, Z.; Krámos, B.; Magdó, I.; Szántay, C.; Kóti, J.; Domány-Kovács, K.; Greiner, I.; Bata, I. Synthesis and Characterization of New V1A Antagonist Compounds: The Separation of Four Atropisomeric Stereoisomers. *J. Med. Chem.* **2021,** *64*, 10445-10468.
149. Lanman, B. A.; Allen, J. R.; Allen, J. G.; Amegadzie, A. K.; Ashton, K. S.; Booker, S. K.; Chen, J. J.; Chen, N.; Frohn, M. J.; Goodman, G.; Kopecky, D. J.; Liu, L.; Lopez, P.; Low, J. D.; Ma, V.; Minatti, A. E.; Nguyen, T. T.; Nishimura, N.; Pickrell, A. J.; Reed, A. B.; Shin, Y.; Siegmund, A. C.; Tamayo, N. A.; Tegley, C. M.; Walton, M. C.; Wang, H.-L.; Wurz, R. P.; Xue, M.; Yang, K. C.; Achanta, P.; Bartberger, M. D.; Canon, J.; Hollis, L. S.; McCarter, J. D.; Mohr, C.; Rex, K.; Saiki, A. Y.; San Miguel, T.; Volak, L. P.; Wang, K. H.; Whittington, D. A.; Zech, S. G.; Lipford, J. R.; Cee, V. J. Discovery of a Covalent Inhibitor of KRASG12C (AMG 510) for the Treatment of Solid Tumors. *J. Med. Chem.* **2020,** *63*, 52-65.
150. Szlavik, Z.; Csekei, M.; Paczal, A.; Szabo, Z. B.; Sipos, S.; Radics, G.; Proszenyak, A.; Balint, B.; Murray, J.; Davidson, J.; Chen, I.; Dokurno, P.; Surgenor, A. E.; Daniels, Z. M.; Hubbard, R. E.; Le Toumelin-Braizat, G.; Claperon, A.; Lysiak-Auvity, G.; Girard, A.-

M.; Bruno, A.; Chanrion, M.; Colland, F.; Maragno, A.-L.; Demarles, D.; Geneste, O.; Kotschy, A. Discovery of S64315, a Potent and Selective Mcl-1 Inhibitor. *J. Med. Chem.* **2020,** *63*, 13762-13795.
151. Chandrasekhar, J.; Dick, R.; Van Veldhuizen, J.; Koditek, D.; Lepist, E. I.; McGrath, M. E.; Patel, L.; Phillips, G.; Sedillo, K.; Somoza, J. R.; Therrien, J.; Till, N. A.; Treiberg, J.; Villaseñor, A. G.; Zherebina, Y.; Perreault, S. Atropisomerism by Design: Discovery of a Selective and Stable Phosphoinositide 3-Kinase (PI3K) β Inhibitor. *J. Med. Chem.* **2018,** *61*, 6858-6868.
152. Nalbandian, C.; Hecht, D.; Gustafson, J. L. The Preorganization of Atropisomers to Increase Target Selectivity. *Synlett* **2016,** *27*, 977-983.
153. Saal, C.; Becker, A.; Krier, M.; Fuchß, T. Atropisomerism - A Neglected Way to Escape Out of Solubility Flatlands. *J. Pharm. Sci.* **2022,** *111*, 206-213.
154. Eveleigh, P.; Hulme, E. C.; Schudt, C.; Birdsall, N. J. The existence of stable enantiomers of telenzepine and their stereoselective interaction with muscarinic receptor subtypes. *Mol. Pharmacol.* **1989,** *35*, 477-83.
155. Yang, C.; Zhou, D.; Shen, Z.; Wilson, D. M.; Renner, M.; Miner, J. N.; Girardet, J. L.; Lee, C. A. Characterization of Stereoselective Metabolism, Inhibitory Effect on Uric Acid Uptake Transporters, and Pharmacokinetics of Lesinurad Atropisomers. *Drug Metab Dispos.* **2019,** *47*, 104-113.
156. ClinicalTrials.gov. https://clinicaltrials.gov/ct2/show/NCT03600883 (accessed 01/05/2022).
157. ClinicalTrials.gov. https://clinicaltrials.gov/ct2/show/NCT04629443 (accessed 01/05/2022).
158. Waaler, J.; Leenders, R. G. G.; Sowa, S. T.; Alam Brinch, S.; Lycke, M.; Nieczypor, P.; Aertssen, S.; Murthy, S.; Galera-Prat, A.; Damen, E.; Wegert, A.; Nazaré, M.; Lehtiö, L.; Krauss, S. Preclinical Lead Optimization of a 1,2,4-Triazole Based Tankyrase Inhibitor. *J. Med. Chem.* **2020,** *63*, 6834-6846.
159. Yamaguchi-Sasaki, T.; Kawaguchi, T.; Okada, A.; Tokura, S.; Tanaka-Yamamoto, N.; Takeuchi, T.; Ogata, Y.; Takahashi, R.; Kurimoto-Tsuruta, R.; Tamaoki, T.; Sugaya, Y.; Abe-Kumasaka, T.; Arikawa, K.; Yoshida, I.; Sugiyama, H.; Kanuma, K.; Yoshinaga, M. Discovery of a potent dual inhibitor of wild-type and mutant respiratory syncytial virus fusion proteins through the modulation of atropisomer interconversion properties. *Bioorg. Med. Chem.* **2020,** *28*, 115818.
160. Albert, J. S.; Ohnmacht, C.; Bernstein, P. R.; Rumsey, W. L.; Aharony, D.; Masek, B. B.; Dembofsky, B. T.; Koether, G. M.; Potts, W.; Evenden, J. L. Design and optimization of cyclized NK1 antagonists with controlled atropisomeric properties. *Tetrahedron* **2004,** *60*, 4337-4347.
161. Perreault, S.; Arjmand, F.; Chandrasekhar, J.; Hao, J.; Keegan, K. S.; Koditek, D.; Lepist, E.-I.; Matson, C. K.; McGrath, M. E.; Patel, L.; Sedillo, K.; Therrien, J.; Till, N. A.; Tomkinson, A.; Treiberg, J.; Zherebina, Y.; Phillips, G. Discovery of an Atropisomeric PI3Kβ Selective Inhibitor through Optimization of the Hinge Binding Motif. *ACS Med. Chem. Lett.* **2020,** *11*, 1236-1243.
162. Norvaiša, K.; O'Brien, J. E.; Gibbons, D. J.; Senge, M. O. Elucidating Atropisomerism in Nonplanar Porphyrins with Tunable Supramolecular Complexes. *Chem. - Eur. J.* **2021,** *27*, 331-339.
163. Crossley, M. J.; Field, L. D.; Forster, A. J.; Harding, M. M.; Sternhell, S. Steric effects on atropisomerism in tetraarylporphyrins. *J. Am. Chem. Soc.* **1987,** *109*, 341-348.
164. Kottas, G. S.; Clarke, L. I.; Horinek, D.; Michl, J. Artificial Molecular Rotors. *Chem. Rev.* **2005,** *105*, 1281-1376.

165. Zhou, Z.; Zhang, X.; Liu, Q.; Yan, Z.; Lv, C.; Long, G. Geometry and Temperature Dependence of meso-Aryl Rotation in Strained Metalloporphyrins: Adjustable Turnstile Molecules. *Inorg. Chem.* **2013,** *52*, 10258-10263.
166. Gottwald, L. K.; Ullman, E. F. Biphenyl-type atropisomerism as a probe for conformational rigidity of α,β,γ,δ-tetraarylporphines. *Tetrahedron Lett.* **1969,** *10*, 3071-3074.
167. Kingsbury, C. J.; Senge, M. O. The shape of porphyrins. *Coord. Chem. Rev.* **2021,** *431*, 213760.
168. Collman, J. P.; Gagne, R. R.; Reed, C.; Halbert, T. R.; Lang, G.; Robinson, W. T. Picket fence porphyrins. Synthetic models for oxygen binding hemoproteins. *J. Am. Chem. Soc.* **1975,** *97*, 1427-1439.
169. Tomé, A. C.; Silva, A. M. S.; Alkorta, I.; Elguero, J. Atropisomerism and conformational aspects of meso-tetraarylporphyrins and related compounds. *J. Porphyrins Phthalocyanines* **2011,** *15*, 1-28.
170. Alkorta, I.; Elguero, J.; Silva, A. M. S.; Tomé, A. C. A theoretical study of the conformation of meso-tetraphenylporphyrin ($TPPH_2$), its anions, cations and metal complexes (Mg^{2+}, Ca^{2+} and Zn^{2+}). *J. Porphyrins Phthalocyanines* **2010,** *14*, 630-638.
171. Urbani, M.; Torres, T. Tautomerism and atropisomerism in free-base (meso)-strapped porphyrins: static and dynamic aspects. *Chemistry.* **2014,** *20*, 16337-16349.
172. Medforth, C. J.; Haddad, R. E.; Muzzi, C. M.; Dooley, N. R.; Jaquinod, L.; Shyr, D. C.; Nurco, D. J.; Olmstead, M. M.; Smith, K. M.; Ma, J.-G.; Shelnutt, J. A. Unusual Aryl−Porphyrin Rotational Barriers in Peripherally Crowded Porphyrins. *Inorg. Chem.* **2003,** *42*, 2227-2241.
173. Okuno, Y.; Kamikado, T.; Yokoyama, S.; Mashiko, S. Theoretical study of aryl-ring rotation in arylporphyrins. *J. Mol. Struct.: THEOCHEM* **2002,** *594*, 55-60.
174. Senge, M. O. Highly Substituted Porphyrins. In *The Porphyrin Handbook*, Vol. 1; 1st ed.; Kadish, K. M.; Smith, K. M.; Guilard, R., Eds.; Academic Press, 2000; pp 239-249.
175. Simonis, U.; Walker, F. A.; Lee, P. L.; Hanquet, B. J.; Meyerhoff, D. J.; Scheidt, W. R. Synthesis, spectroscopic, and structural studies of extremely short chain basket handle porphyrins and their zinc(II) complexes. *J. Am. Chem. Soc.* **1987,** *109*, 2659-2668.
176. Wijesekera, T. P.; Paine, J. B.; Dolphin, D.; Einstein, F. W. B.; Jones, T. Enforced deformation of porphyrins by short-strap bridging. *J. Am. Chem. Soc.* **1983,** *105*, 6747-6749.
177. Reddy, D.; Chandrashekar, T. K. Short-chain basket handle porphyrins: synthesis and characterisation. *J. Chem. Soc., Dalton Trans.*,**1992,** 619-625.
178. Almog, J.; Baldwin, J. E.; Crossley, M. J.; Debernardis, J. F.; Dyer, R. L.; Huff, J. R.; Peters, M. K. Synthesis of "capped porphyrins". *Tetrahedron* **1981,** *37*, 3589-3601.
179. Baldwin, J. E.; Crossley, M. J.; Klose, T.; O Rear, E. A.; Peters, M. Syntheses and oxygenation of iron(II) strapped porphyrin complexes. *Tetrahedron* **1982,** *38*, 27-39.
180. Collman, J. P.; Decréau, R. A.; Costanzo, S. Appending a Tris-imidazole Ligand with a Tyr244 Mimic on the Distal Face of Bromoacetamidoporphyrin. *Org. Lett.* **2004,** *6*, 1033-1036.
181. Norvaiša, K.; Flanagan, K. J.; Gibbons, D.; Senge, M. O. Conformational Re-engineering of Porphyrins as Receptors with Switchable N−H···X-Type Binding Modes. *Angew. Chem., Int. Ed.* **2019,** *58*, 16553-16557.
182. Groves, J. T.; Myers, R. S. Catalytic asymmetric epoxidations with chiral iron porphyrins. *J. Am. Chem. Soc.* **1983,** *105*, 5791-5796.
183. Hatano, K. Chiral Porphryin Atropisomers. *Chem. Pharm. Bull.* **1985,** *33*, 4116-4119.

184. Martin, D. J.; Mercado, B. Q.; Mayer, J. M. All Four Atropisomers of Iron Tetra(o-N,N,N-trimethylanilinium)porphyrin in Both the Ferric and Ferrous States. *Inorg. Chem.* **2021,** *60*, 5240-5251.
185. Hagan, W. J., Jr.; Barber, D. C.; Whitten, D. G.; Kelly, M.; Albrecht, F.; Gibson, S. L.; Hilf, R. Picket-fence porphyrins as potential phototherapeutic agents. *Cancer Res.* **1988,** *48*, 1148-1152.
186. Barber, D. C.; VanDerMeid, K. R.; Gibson, S. L.; Hilf, R.; Whitten, D. G. Photosensitizing activities of picket fence porphyrins *in vitro* and *in vivo*. *Cancer res.* **1991,** *51*, 1836-1845.
187. Feng, X.; Shi, Y.; Xie, L.; Zhang, K.; Wang, X.; Liu, Q.; Wang, P. Synthesis, Characterization, and Biological Evaluation of a Porphyrin-Based Photosensitizer and Its Isomer for Effective Photodynamic Therapy against Breast Cancer. *J. Med. Chem.* **2018,** *61*, 7189-7201.
188. Arnaut, L. Transitions between electronic states. In Chemical Kinetics, 2nd Ed.; Arnaut, L., Ed.; Elsevier, 2021; pp. 463-521.
189. Sakamoto, K.; Michibata, J.; Hirai, Y.; Ide, A.; Ikitoh, A.; Takatani-Nakase, T.; Futaki, S. Potentiating the Membrane Interaction of an Attenuated Cationic Amphiphilic Lytic Peptide for Intracellular Protein Delivery by Anchoring with Pyrene Moiety. *Bioconj. Chem.* **2021,** *32*, 950-957.
190. McKinlay, C. J.; Waymouth, R. M.; Wender, P. A. Cell-Penetrating, Guanidinium-Rich Oligophosphoesters: Effective and Versatile Molecular Transporters for Drug and Probe Delivery. *J. Am. Chem. Soc.* **2016,** *138*, 3510-3517.
191. Pei, D.; Buyanova, M. Overcoming Endosomal Entrapment in Drug Delivery. *Bioconj. Chem.* **2019,** *30*, 273-283.
192. Guha, S.; Ghimire, J.; Wu, E.; Wimley, W. C. Mechanistic Landscape of Membrane-Permeabilizing Peptides. *Chem. Rev.* **2019,** *119*, 6040-6085.
193. Allen, J.; Najjar, K.; Erazo-Oliveras, A.; Kondow-McConaghy, H. M.; Brock, D. J.; Graham, K.; Hager, E. C.; Marschall, A. L. J.; Dübel, S.; Juliano, R. L.; Pellois, J.-P. Cytosolic Delivery of Macromolecules in Live Human Cells Using the Combined Endosomal Escape Activities of a Small Molecule and Cell Penetrating Peptides. *ACS Chem. Biol.* **2019,** *14*, 2641-2651.
194. López-Andarias, J.; Saarbach, J.; Moreau, D.; Cheng, Y.; Derivery, E.; Laurent, Q.; González-Gaitán, M.; Winssinger, N.; Sakai, N.; Matile, S. Cell-Penetrating Streptavidin: A General Tool for Bifunctional Delivery with Spatiotemporal Control, Mediated by Transport Systems Such as Adaptive Benzopolysulfane Networks. *J. Am. Chem. Soc.* **2020,** *142*, 4784-4792.
195. Pulcu, G. S.; Galenkamp, N. S.; Qing, Y.; Gasparini, G.; Mikhailova, E.; Matile, S.; Bayley, H. Single-Molecule Kinetics of Growth and Degradation of Cell-Penetrating Poly(disulfide)s. *J. Am. Chem. Soc.* **2019,** *141*, 12444-12447.
196. Kelly, C. N.; Townsend, C. E.; Jain, A. N.; Naylor, M. R.; Pye, C. R.; Schwochert, J.; Lokey, R. S. Geometrically Diverse Lariat Peptide Scaffolds Reveal an Untapped Chemical Space of High Membrane Permeability. *J. Am. Chem. Soc.* **2021,** *143*, 705-714.
197. Appiah Kubi, G.; Qian, Z.; Amiar, S.; Sahni, A.; Stahelin, R. V.; Pei, D. Non-Peptidic Cell-Penetrating Motifs for Mitochondrion-Specific Cargo Delivery. *Angew. Chem. Int. Ed.* **2018,** *57*, 17183-17188.
198. Vinogradov, A. A.; Yin, Y.; Suga, H. Macrocyclic Peptides as Drug Candidates: Recent Progress and Remaining Challenges. *J. Am. Chem. Soc.* **2019,** *141*, 4167-4181.

199. Barlow, N.; Chalmers, D. K.; Williams-Noonan, B. J.; Thompson, P. E.; Norton, R. S. Improving Membrane Permeation in the Beyond Rule-of-Five Space by Using Prodrugs to Mask Hydrogen Bond Donors. *ACS Chem. Biol.* **2020,** *15*, 2070-2078.
200. Gao, Y.-H.; Lovreković, V.; Kussayeva, A.; Chen, D.-Y.; Margetić, D.; Chen, Z.-L. The photodynamic activities of dimethyl 131-[2-(guanidinyl)ethylamino] chlorin e6 photosensitizers in A549 tumor. *Eur. J. Med. Chem.* **2019,** *177*, 144-152.
201. Sibrian-Vazquez, M.; Nesterova, I. V.; Jensen, T. J.; Vicente, M. G. H. Mitochondria Targeting by Guanidine− and Biguanidine−Porphyrin Photosensitizers. *Bioconj. Chem.* **2008,** *19*, 705-713.
202. Smyth, J. E.; Butler, N. M.; Keller, P. A. A twist of nature – the significance of atropisomers in biological systems. *Nat. Prod. Rep.* **2015,** *32*, 1562-1583.
203. Bonnett, R. Photosensitizers of the porphyrin and phthalocyanine series for photodynamic therapy. *Chem. Soc. Rev.* **1995,** *24*, 19-33.
204. Frochot, C.; Mordon, S. Update of the situation of clinical photodynamic therapy in Europe in the 2003–2018 period. *J. Porphyrins Phthalocyanines* **2019,** *23*, 347-357.
205. Lindsey, J. S.; Schreiman, I. C.; Hsu, H. C.; Kearney, P. C.; Marguerettaz, A. M. Rothemund and Adler-Longo reactions revisited: synthesis of tetraphenylporphyrins under equilibrium conditions. *J. Org. Chem.* **1987,** *52*, 827-836.
206. Gonsalves, A. M. d. A. R.; Varejão, J. M. T. B.; Pereira, M. M. Some new aspects related to the synthesis of meso-substituted porphyrins. *J. Heterocycl. Chem.* **1991,** *28*, 635-640.
207. Singh, S.; Aggarwal, A.; Bhupathiraju, N. V. S. D. K.; Arianna, G.; Tiwari, K.; Drain, C. M. Glycosylated Porphyrins, Phthalocyanines, and Other Porphyrinoids for Diagnostics and Therapeutics. *Chem. Rev.* **2015,** *115* (18), 10261-10306.
208. Ressurreição, A. S. M.; Pineiro, M.; Arnaut, L. G.; Gonsalves, A. M. d. A. R. Atropisomers of 5,10,15,20-tetrakis(2,6-dichloro-3-sulfamoyl-phenyl)porphyrins. *J. Porphyrins Phthalocyanines* **2007,** *11*, 50-57.
209. Zhu, L.; Himmel, L.; Merkes, J. M.; Kiessling, F.; Rueping, M.; Banala, S. Atropisomers of meso Tetra(N-Mesyl Pyrrol-2-yl) Porphyrins: Synthesis, Isolation and Characterization of All-Pyrrolic Porphyrins. *Chem. Eur. J.* **2020,** *26*, 4232-4235.
210. Richter, A. M.; Jain, A. K.; Canaan, A. J.; Waterfield, E.; Sternberg, E. D.; Levy, J. G. Photosensitizing efficiency of two regioisomers of the benzoporphyrin derivative monoacid ring a (BPD-MA). *Biochem. Pharmacol.* **1992,** *43*, 2349-2358.
211. Pereira, M. M.; Abreu, A. R.; Goncalves, N. P. F.; Calvete, M. J. F.; Simões, A. V. C.; Monteiro, C. J. P.; Arnaut, L. G.; Eusébio, M. E.; Canotilho, J. An insight into solvent-free diimide porphyrin reduction: a versatile approach for meso-aryl hydroporphyrin synthesis. *Green Chem.* **2012,** *14*, 1666-1672.
212. Pucelik, B.; Arnaut, L. G.; Stochel, G.; Dąbrowski, J. M. Design of Pluronic-Based Formulation for Enhanced Redaporfin-Photodynamic Therapy against Pigmented Melanoma. *ACS Appl. Mater. Interfaces* **2016,** *8*, 22039-22055.
213. Krzykawska-Serda, M.; Dąbrowski, J. M.; Arnaut, L. G.; Szczygieł, M.; Urbańska, K.; Stochel, G.; Elas, M. The role of strong hypoxia in tumors after treatment in the outcome of bacteriochlorin-based photodynamic therapy. *Free Radical Biol. Med.* **2014,** *73*, 239-251.
214. Bruker *APEX-3 v2016.9-0*, Bruker AXS Inc: Madison, 2016.
215. Bruker *XREP Version 2014/2*, Bruker AXS Inc.: Madison, 2014.
216. Hubschle, C. B.; Sheldrick, G. M.; Dittrich, B. ShelXle: a Qt graphical user interface for SHELXL. *J. Appl. Crystallogr.* **2011,** *44*, 1281-1284.
217. Sheldrick, G. SHELXT - Integrated space-group and crystal-structure determination. *Acta Crystallogr., Sect. A: Found. Crystallogr.* **2015,** *71*, 3-8.

218. Sheldrick, G. Crystal structure refinement with SHELXL. *Acta Crystallogr., Sect. C: Struct. Chem.* **2015,** *71*, 3-8.
219. *CrystalMaker® Software, Oxford www.crystalmaker.com.*
220. Arnaut, L. Reaction order and rate constants. In *Chemical Kinetics,* 2nd ed.; Arnaut, L., Ed.; Elsevier, 2021; pp 93-138.
221. Rurack, K.; Spieles, M. Fluorescence Quantum Yields of a Series of Red and Near-Infrared Dyes Emitting at 600−1000 nm. *Anal. Chem.* **2011,** *83*, 1232-1242.
222. Silva, E. F.; Serpa, C.; Dabrowski, J. M.; Monteiro, C. J.; Formosinho, S. J.; Stochel, G.; Urbanska, K.; Simões, S.; Pereira, M. M.; Arnaut, L. G. Mechanisms of singlet-oxygen and superoxide-ion generation by porphyrins and bacteriochlorins and their implications in photodynamic therapy. *Chem. Eur. J.* **2010,** *16*, 9273-9286.
223. Schmidt, R.; Tanielian, C.; Dunsbach, R.; Wolff, C. Phenalenone, a universal reference compound for the determination of quantum yields of singlet oxygen $O_2(^1\Delta_g)$ sensitization. *J. Photochem. Photobiol., A* **1994,** *79*, 11-17.
224. Schaberle, F. A. Assessment of the actual light dose in photodynamic therapy. *Photodiagn. Photodyn. Ther.* **2018,** *23*, 75-77.
225. Czekanska, E. M. Assessment of cell proliferation with resazurin-based fluorescent dye. In *Methods in Molecular Biology*, Vol. 740; Stoddart, M., Ed.; Humana Press, 2011; pp. 27-32.
226. Mantel, N. Evaluation of survival data and two new rank order statistics arising in its consideration. *Cancer Chemother. Rep.* **1966,** *50*, 163-170.
227. Norvaiša, K.; Maguire, S.; Donohoe, C.; O'Brien, J. E.; Twamley, B.; Gomes-da-Silva, L. C.; Senge, M. O. Steric Repulsion Induced Conformational Switch in Supramolecular Structures. *Chem. Eur. J.* **2022,** *28*, e202103879.
228. Welerowicz, T.; Buszewski, B. The effect of stationary phase on lipophilicity determination of β-blockers using reverse-phase chromatographic systems. *Biomed. Chromatogr.* **2005,** *19*, 725-736.
229. Spek, A. PLATON SQUEEZE: a tool for the calculation of the disordered solvent contribution to the calculated structure factors. *Acta Crystallogr., Sect. C: Struct. Chem.* **2015,** *71*, 9-18.
230. Houborg, K.; Harris, P.; Petersen, J.; Rowland, P.; Poulsen, J. C.; Schneider, P.; Vind, J.; Larsen, S. Impact of the physical and chemical environment on the molecular structure of Coprinus cinereus peroxidase. *Acta Crystallogr., Sect. D: Biol. Crystallogr.* **2003,** *59*, 989-996.
231. Reddy, R. V. R.; Basumatary, B.; Murugavel, M.; Keshav, K.; Sekhar, A. R.; Sankar, J. Sterically hindered 5,15-tetraphenylbenzene-porphyrins: syntheses, structures, atropisomerism and photophysical properties. *J. Chem. Sci.* **2018,** *130*, 81-92.
232. Ayaz, F.; Colak, S. G.; Ocakoglu, K. Investigating the Immunostimulatory and Immunomodulatory Effects of *cis* and *trans* Isomers of Ruthenium Polypyridyl Complexes on the Mammalian Macrophage-Like Cells. *ChemistrySelect* **2020,** *5*, 11648-11653.
233. Sugano, K.; Kansy, M.; Artursson, P.; Avdeef, A.; Bendels, S.; Di, L.; Ecker, G. F.; Faller, B.; Fischer, H.; Gerebtzoff, G.; Lennernaes, H.; Senner, F. Coexistence of passive and carrier-mediated processes in drug transport. *Nat. Rev. Drug Discovery* **2010,** *9*, 597-614.
234. Pucelik, B.; Arnaut, L. G.; Dąbrowski, J. M. Lipophilicity of Bacteriochlorin-Based Photosensitizers as a Determinant for PDT Optimization through the Modulation of the Inflammatory Mediators. *J. Clin. Med.* **2019,** *9*, 8-34.
235. Ricchelli, F. Photophysical properties of porphyrins in biological membranes. *J. Photochem. Photobiol., B* **1995,** *29*, 109-118.

236. Kelbauskas, L.; Dietel, W. Internalization of Aggregated Photosensitizers by Tumor Cells: Subcellular Time-resolved Fluorescence Spectroscopy on Derivatives of Pyropheophorbide-a Ethers and Chlorin e6 under Femtosecond One- and Two-photon Excitation. *Photochem. Photobiol.* **2002,** *76*, 686-694.
237. Tomoda, H.; Kishimoto, Y.; Lee, Y. C. Temperature effect on endocytosis and exocytosis by rabbit alveolar macrophages. *J. Biol. Chem.* **1989,** *264*, 15445-15450.
238. Mix, K. A.; Lomax, J. E.; Raines, R. T. Cytosolic Delivery of Proteins by Bioreversible Esterification. *J. Am. Chem. Soc.* **2017,** *139*, 14396-14398.
239. Gunn, M. D.; Sen, A.; Chang, A.; Willerson, J. T.; Buja, L. M.; Chien, K. R. Mechanisms of accumulation of arachidonic acid in cultured myocardial cells during ATP depletion. *Am. J. Physiol. - Heart Circ. Physiol.* **1985,** *249*, H1188-H1194.
240. Trimble, W. S.; Grinstein, S. Barriers to the free diffusion of proteins and lipids in the plasma membrane. *J. Cell. Biol.* **2015,** *208*, 259-271.
241. Ricchelli, F.; Jori, G.; Gobbo, S.; Tronchin, M. Liposomes as models to study the distribution of porphyrins in cell membranes. *Biochim. Biophys. Acta, Biomembr*. **1991**, *1065*, 42-48.
242. Korbelik, M.; Hung, J.; Lam, S.; Palcic, B. The effects of low density lipoproteins on uptake of Photofrin II. P*hotochem. Photobiol*. **1990,** *51*, 191-196.
243. Michael-Titus, A. T.; Whelpton, R.; Yaqub, Z. Binding of temoporfin to the lipoprotein fractions of human serum. *Br. J. Clin. Pharmacol.* **1995,** *40*, 594-597.
244. Barber, D. C.; Whitten, D. G. Metalation of surfactant porphyrins at anionic interfaces in micelles and reversed micelles: dramatic effects of chain length and atropisomer structure on reactivity. *J. Am. Chem. Soc.* **1987,** *109*, 6842-6844.
245. Barber, D. C.; Woodhouse, T. E.; Whitten, D. G. Diverse reactivities of picket fence porphyrin atropisomers in organized media: a probe of molecular location and orientation. *J. Phys. Chem.* **1992,** *96*, 5106-5114.
246. Collins-Gold, L. C.; Barber, D. C.; Hagan, W. J.; Gibson, S. L.; Hilf, R.; Whitten, D. G. Synthetic porphyrins at interfaces; photosensitization and related reactions of atropisomers of o-substituted tetraphenylporphine derivatives in films, reversed micelles and membranes. *Photochem. Photobiol.* **1988,** *48*, 165-175.
247. Dougherty, P. G.; Sahni, A.; Pei, D. Understanding Cell Penetration of Cyclic Peptides. *Chem. Rev.* **2019,** *119*, 10241-10287.
248. Wang, C. K.; Swedberg, J. E.; Harvey, P. J.; Kaas, Q.; Craik, D. J. Conformational Flexibility Is a Determinant of Permeability for Cyclosporin. *J. Phys. Chem. B* **2018**, *122*, 2261-2276.
249. Lindsey, J. Increased yield of a desired isomer by equilibriums displacement on binding to silica gel, applied to meso-tetrakis(*o*-aminophenyl)porphyrin. *J. Org.Chem.* **1980,** *45*, 5215-5215.
250. Collman, J. P.; Bröring, M.; Fu, L.; Rapta, M.; Schwenninger, R.; Straumanis, A. Novel Protecting Strategy for the Synthesis of Porphyrins with Different Distal and Proximal Superstructures. *J.Org.Chem.* **1998,** *63*, 8082-8083.
251. Collman, J. P.; Decréau, R. A. 5,10,15-Tris(o-aminophenyl) Corrole (TAPC) as a Versatile Synthon for the Preparation of Corrole-Based Hemoprotein Analogs. *Org. Lett.* **2005,** *7*, 975-978
252. Ishizuka, T.; Tanaka, S.; Uchida, S.; Wei, L.; Kojima, T. Selective Convergence to Atropisomers of a Porphyrin Derivative Having Bulky Substituents at the Periphery. *J. Org. Chem.* **2020,** *85*, 12856-12869.
253. Žuvela, P.; Skoczylas, M.; Jay Liu, J.; Bączek, T.; Kaliszan, R.; Wong, M. W.; Buszewski, B. Column Characterization and Selection Systems in Reversed-Phase High-Performance Liquid Chromatography. *Chem. Rev.* **2019,** *119*, 3674-3729.

254. Ogoshi, H.; Sugimoto, H.; Yoshida, Z.-i. Cyclophane porphyrin - II access control in axial ligation to iron complex of cyclophane porphyrin. *Tetrahedron Lett.* **1976,** *17*, 4481-4484.
255. Battersby, A. R.; Buckley, D. G.; Hartley, S. G.; Turnbull, M. D. Synthetic sudies related to myoglobin: syntheses of bridged porphyrin systems. *J. Chem. Soc., Chem. Commun.,* **1976,** 879-881.
256. Baldwin, J. E.; Klose, T.; Peters, M. Syntheses of 'strapped' porphyrins and the oxygenation of their iron(II) complexes. *J. Chem. Soc., Chem. Commun.,* **1976,** 881-883.
257. Wagner, R.; Johnson, T.; Lindsey, J. Investigation of the one-flask synthesis of porphyrins bearing meso-linked straps of variable length, rigidity, and redox activity. *Tetrahedron* **1997,** *53*, 6755-6790.
258. Wytko, J. A.; Graf, E.; Weiss, J. A highly rigid capped porphyrin. *J. Org. Chem.* **1992,** *57*, 1015-1018.
259. Rose, E.; Ren, Q.-Z.; Andrioletti, B. A Unique Binaphthyl Strapped Iron–Porphyrin Catalyst for the Enantioselective Epoxidation of Terminal Olefins. *Chem. - Eur. J.* **2004,** *10*, 224-30.
260. Tang, M.; Liang, Y.; Lu, X.; Miao, X.; Jiang, L.; Liu, J.; Bian, L.; Wang, S.; Wu, L.; Liu, Z. Molecular-strain engineering of double-walled tetrahedra. *Chem* **2021,** *7*, 2160-2174.
261. Callaghan, S.; Flanagan, K. J.; O'Brien, J. E.; Senge, M. O. Short-Chained Anthracene Strapped Porphyrins and their Endoperoxides. *Eur. J. Org. Chem.* **2020,** *2020*, 2735-2744.
262. Adler, A. D.; Longo, F. R.; Finarelli, J. D.; Goldmacher, J.; Assour, J.; Korsakoff, L. A simplified synthesis for meso-tetraphenylporphine. *J. Org. Chem.* **1967,** *32*, 476-476.
263. Momenteau, M.; Mispelter, J.; Loock, B.; Bisagni, E. Both-faces hindered porphyrins. Part 1. Synthesis and characterization of basket-handle porphyrins and their iron complexes. *J. Chem. Soc., Perkin Trans. 1,* **1983,** 189-196.
264. Weiser, J.; Staab, H. A. Synthesis of a Porphyrin Sandwiched between Two Parallel p-Benzoquinone Units. *Angew. Chem., Int. Ed. Engl.* **1984,** *23*, 623-625.
265. Lindsey, J. The Synthesis of meso-Substituted Porphyrins. In *Metalloporphyrins Catalyzed Oxidations*, Vol. 17; Montanari, F., Casella, L. Eds.; Springer, 1994; pp 48-86.
266. Momenteau, M.; Mispelter, J.; Loock, B.; Lhoste, J.-M. Both-faces hindered porphyrins. Part 2. Synthesis and characterization of internally five-co-ordinated iron(II) basket-handle porphyrins derived from 5,10,15,20-tetrakis(o-hydroxyphenyl)porphyrin. *J. Chem. Soc., Perkin Trans. 1,* **1985,** 61-70.
267. Gehrold, A. C.; Bruhn, T.; Schneider, H.; Radius, U.; Bringmann, G. Monomeric Chiral and Achiral Basket-Handle Porphyrins: Synthesis, Structural Features, and Arrested Tautomerism. *J. Org. Chem.* **2015,** *80*, 12359-12378.
268. Gehrold, A. C.; Bruhn, T.; Bringmann, G. Axial, Helical, and Planar Chirality in Directly Linked Basket-Handle Porphyrin Arrays. *J. Org. Chem.* **2016,** *81*, 1075-1088.
269. Liu, Q.; Zhou, X.; Liu, H.; Zhang, X.; Zhou, Z. Fractional Transfer of a Free Unpaired Electron to Overcome Energy Barriers in the Formation of Fe^{4+} from Fe^{3+} during Core Contraction of Macrocycles: Implication for Heme Distortion. *Org. Biomol. Chem.* **2015,** *13*, 2939-2946.
270. Liu, Q.; Zhang, J.; Tang, M.; Yang, Y.; Zhang, J.; Zhou, Z. Geometric deconstruction of core and electron activation of a π-system in a series of deformed porphyrins: mimics of heme. *Org. Biomol. Chem.* **2018,** *16*, 7725-7736.
271. Ravikanth, M.; Reddy, D.; Chandrashekar, T. K. Fluorescence properties of distorted short-chain basket handle porphyrins. *J. Photochem. Photobiol., A* **1993,** *72*, 61-67.

272. Röder, B.; Büchner, M.; Rückmann, I.; Senge, M. O. Correlation of photophysical parameters with macrocycle distortion in porphyrins with graded degree of saddle distortion. *Photochem. Photobiol. Sci.* **2010,** *9*, 1152-1158.
273. Davoust, E.; Granet, R.; Krausz, P.; Carré, V.; Guilloton, M. Synthesis of glycosyl strapped porphyrins. *Tetrahedron Lett.* **1999,** *40*, 2513-2516.
274. Martínez-Crespo, L.; Sun-Wang, J. L.; Sierra, A. F.; Aragay, G.; Errasti-Murugarren, E.; Bartoccioni, P.; Palacín, M.; Ballester, P. Facilitated Diffusion of Proline across Membranes of Liposomes and Living Cells by a Calix[4]pyrrole Cavitand. *Chem* **2020,** *6*, 3054-3070.
275. Dolomanov, O. V.; Bourhis, L. J.; Gildea, R. J.; Howard, J. A. K.; Puschmann, H. OLEX2: a complete structure solution, refinement and analysis program. *J. Appl. Crystallogr.* **2009,** *42*, 339-341.
276. Bruker *APEX3 v2017.3-0*, Bruker AXS Inc: Madison, WI, USA, 2017.
277. Bruker *SAINT v8.38A*, Bruker AXS Inc: Madison, WI, USA, 2018.
278. Krause, L.; Herbst-Irmer, R.; Sheldrick, G. M.; Stalke, D. Comparison of silver and molybdenum microfocus X-ray sources for single-crystal structure determination. *J. Appl. Crystallogr.* **2015,** *48*, 3-10.
279. Osuka, A.; Kobayashi, F.; Maruyama, K. Synthesis of Strapped, Dimeric, and Trimeric Porphyrins Based on Intramolecular Macrocyclization Reactions. *Bull. Chem. Soc. Jpn.* **1991,** *64*, 1213-1225.
280. Charisiadis, A.; Bagaki, A.; Fresta, E.; Weber, K. T.; Charalambidis, G.; Stangel, C.; Hatzidimitriou, A. G.; Angaridis, P. A.; Coutsolelos, A. G.; Costa, R. D. Peripheral Substitution of Tetraphenyl Porphyrins: Fine-Tuning Self-Assembly for Enhanced Electroluminescence. *ChemPlusChem* **2018,** *83*, 254-265.
281. Zhang, Y.; Starynowicz, P.; Christoffers, J. Fluorescent Bis(oligophenylylamino)terephthalates. *Eur. J. Org. Chem.* **2008,** *2008*, 3488-3495.
282. Mathai, S.; Smith, T. A.; Ghiggino, K. P. Singlet oxygen quantum yields of potential porphyrin-based photosensitisers for photodynamic therapy. *Photochem. Photobiol. Sci.* **2007,** *6*, 995-1002.
283. Zhang, R.; Qin, X.; Kong, F.; Chen, P.; Pan, G. Improving cellular uptake of therapeutic entities through interaction with components of cell membrane. *Drug Deliv.* **2019,** *26*, 328-342.
284. Hillaireau, H.; Couvreur, P. Nanocarriers' entry into the cell: relevance to drug delivery. *Cell. Mol. Life Sci.* **2009,** *66*, 2873-2896.
285. Mosquera, J.; García, I.; Liz-Marzán, L. M. Cellular Uptake of Nanoparticles versus Small Molecules: A Matter of Size. *Acc. Chem. Res.* **2018,** *51*, 2305-2313.
286. Khalil, I. A.; Kogure, K.; Akita, H.; Harashima, H. Uptake Pathways and Subsequent Intracellular Trafficking in Nonviral Gene Delivery. *Pharmacol. Rev.* **2006,** *58*, 32-45.
287. Mayor, S.; Pagano, R. E. Pathways of clathrin-independent endocytosis. *Nat. Rev. Mol. Cell Biol.* **2007,** *8*, 603-612.
288. Gagat, M.; Zielińska, W.; Grzanka, A. Cell-penetrating peptides and their utility in genome function modifications (Review). *Int. J. Mol. Med.* **2017,** *40*, 1615-1623.
289. Biorender. https://biorender.com/ (accessed 25/05/22).
290. Chou, L. Y.; Ming, K.; Chan, W. C. Strategies for the intracellular delivery of nanoparticles. *Chem. Soc. Rev.* **2011,** *40*, 233-245.
291. Iversen, T.-G.; Skotland, T.; Sandvig, K. Endocytosis and intracellular transport of nanoparticles: Present knowledge and need for future studies. *Nano Today* **2011,** *6*, 176-185.

292. Bareford, L. M.; Swaan, P. W. Endocytic mechanisms for targeted drug delivery. *Adv. Drug Delivery Rev.* **2007,** *59*, 748-758.
293. Walrant, A.; Vogel, A.; Correia, I.; Lequin, O.; Olausson, B. E. S.; Desbat, B.; Sagan, S.; Alves, I. D. Membrane interactions of two arginine-rich peptides with different cell internalization capacities. *Biochim. Biophys. Acta, Biomembr.* **2012,** *1818*, 1755-1763.
294. Price, D. A.; Blagg, J.; Jones, L.; Greene, N.; Wager, T. Physicochemical drug properties associated with *in vivo* toxicological outcomes: a review. *Expert Opin. Drug Metab. Toxicol.* **2009,** *5*, 921-931.
295. Zhang, Y.; Wang, B.; Zhao, R.; Zhang, Q.; Kong, X. Multifunctional nanoparticles as photosensitizer delivery carriers for enhanced photodynamic cancer therapy. *Mater. Sci. Eng., C.* **2020,** *115*, 111099.
296. Stephens, D. J.; Pepperkok, R. The many ways to cross the plasma membrane. *Proc Natl. Acad. Sci.U. S. A.* **2001,** *98*, 4295-4298.
297. Lambricht, L.; Lopes, A.; Kos, S.; Sersa, G.; Préat, V.; Vandermeulen, G. Clinical potential of electroporation for gene therapy and DNA vaccine delivery. *Expert Opin. Drug Delivery* **2016,** *13*, 295-310.
298. Vivès, E.; Brodin, P.; Lebleu, B. A truncated HIV-1 Tat protein basic domain rapidly translocates through the plasma membrane and accumulates in the cell nucleus. *J. Biol.Chem.* **1997,** *272*, 16010-16017.
299. Su, Y.; Waring, A. J.; Ruchala, P.; Hong, M. Membrane-bound dynamic structure of an arginine-rich cell-penetrating peptide, the protein transduction domain of HIV TAT, from solid-state NMR. *Biochemistry* **2010,** *49*, 6009-6020.
300. Su, Y.; Doherty, T.; Waring, A. J.; Ruchala, P.; Hong, M. Roles of arginine and lysine residues in the translocation of a cell-penetrating peptide from (13)C, (31)P, and (19)F solid-state NMR. *Biochemistry* **2009,** *48*, 4587-4595.
301. Bechara, C.; Sagan, S. Cell-penetrating peptides: 20 years later, where do we stand? *FEBS Lett.* **2013,** *587*, 1693-1702.
302. Vazdar, M.; Heyda, J.; Mason, P. E.; Tesei, G.; Allolio, C.; Lund, M.; Jungwirth, P. Arginine "Magic": Guanidinium Like-Charge Ion Pairing from Aqueous Salts to Cell Penetrating Peptides. *Acc. Chem. Res.* **2018,** *51*, 1455-1464.
303. Guidotti, G.; Brambilla, L.; Rossi, D. Cell-Penetrating Peptides: From Basic Research to Clinics. *Trends Pharmacol. Sci.* **2017,** *38*, 406-424.
304. Olson, E. S.; Aguilera, T. A.; Jiang, T.; Ellies, L. G.; Nguyen, Q. T.; Wong, E. H.; Gross, L. A.; Tsien, R. Y. *In vivo* characterization of activatable cell penetrating peptides for targeting protease activity in cancer. *Integr. Biol.* **2009,** *1*, 382-393.
305. Matijass, M.; Neundorf, I. Cell-penetrating peptides as part of therapeutics used in cancer research. *Med. Drug Discovery* **2021,** *10*, 100092.
306. Luedtke, N. W.; Carmichael, P.; Tor, Y. Cellular Uptake of Aminoglycosides, Guanidinoglycosides, and Poly-arginine. *J. Am. Chem. Soc.* **2003,** *125*, 12374-12375.
307. Abegg, D.; Gasparini, G.; Hoch, D. G.; Shuster, A.; Bartolami, E.; Matile, S.; Adibekian, A. Strained Cyclic Disulfides Enable Cellular Uptake by Reacting with the Transferrin Receptor. *J. Am. Chem. Soc.* **2017,** *139*, 231-238.
308. Zhao, L.; Kim, T. H.; Kim, H. W.; Ahn, J. C.; Kim, S. Y. Enhanced cellular uptake and phototoxicity of Verteporfin-conjugated gold nanoparticles as theranostic nanocarriers for targeted photodynamic therapy and imaging of cancers. *Mater. Sci. Eng., C* **2016,** *67*, 611-622.
309. Kaspler, P.; Lazic, S.; Forward, S.; Arenas, Y.; Mandel, A.; Lilge, L. A ruthenium(ii) based photosensitizer and transferrin complexes enhance photo-physical properties, cell uptake, and photodynamic therapy safety and efficacy. *Photochem. Photobiol. Sci.* **2016,** *15*, 481-95.

310. Yu, L.; Wang, Q.; Wong, R. C. H.; Zhao, S.; Ng, D. K. P.; Lo, P.-C., Synthesis and biological evaluation of phthalocyanine-peptide conjugate for EGFR-targeted photodynamic therapy and bioimaging. *Dyes Pigm.* **2019,** *163*, 197-203.
311. Singh, R.; Tønnesen, H. H.; Kristensen, S.; Berg, K. The influence of Pluronics® on dark cytotoxicity, photocytotoxicity, localization and uptake of curcumin in cancer cells: studies of curcumin and curcuminoids XLIX. *Photochem. Photobiol. Sci.* **2013,** *12*, 559-575.
312. Lin, L.; Xiong, L.; Wen, Y.; Lei, S.; Deng, X.; Liu, Z.; Chen, W.; Miao, X. Active Targeting of Nano-Photosensitizer Delivery Systems for Photodynamic Therapy of Cancer Stem Cells. *J. Biomed. Nanotechnol.* **2015,** *11*, 531-54.
313. Gaio, E.; Scheglmann, D.; Reddi, E.; Moret, F. Uptake and photo-toxicity of Foscan®, Foslip® and Fospeg® in multicellular tumor spheroids. *J. Photochem. Photobiol., B* **2016,** *161*, 244-52.
314. Dai, Y.; Wang, B.; Sun, Z.; Cheng, J.; Zhao, H.; Wu, K.; Sun, P.; Shen, Q.; Li, M.; Fan, Q. Multifunctional Theranostic Liposomes Loaded with a Hypoxia-Activated Prodrug for Cascade-Activated Tumor Selective Combination Therapy. *ACS Appl. Mater. Interfaces* **2019,** *11*, 39410-39423.
315. Wang, Y.; Xie, Y.; Li, J.; Peng, Z. H.; Sheinin, Y.; Zhou, J.; Oupický, D. Tumor-Penetrating Nanoparticles for Enhanced Anticancer Activity of Combined Photodynamic and Hypoxia-Activated Therapy. *ACS nano* **2017,** *11*, 2227-2238.
316. Pucelik, B.; Gürol, I.; Ahsen, V.; Dumoulin, F.; Dąbrowski, J. M. Fluorination of phthalocyanine substituents: Improved photoproperties and enhanced photodynamic efficacy after optimal micellar formulations. *Eur. J. Med. Chem.* **2016,** *124*, 284-298.
317. Morris, M. C.; Deshayes, S.; Heitz, F.; Divita, G. Cell-penetrating peptides: from molecular mechanisms to therapeutics. *Biol. Cell* **2008,** *100*, 201-17.
318. Jerjes, W.; Theodossiou, T. A.; Hirschberg, H.; Høgset, A.; Weyergang, A.; Selbo, P. K.; Hamdoon, Z.; Hopper, C.; Berg, K. Photochemical Internalization for Intracellular Drug Delivery. From Basic Mechanisms to Clinical Research. *J. Clin. Med.* **2020,** *9*, 528.
319. Wiehe, A.; Simonenko, E. J.; Senge, M. O.; RÖder, B. Hydrophilicity vs hydrophobicity—varying the amphiphilic structure of porphyrins related to the photosensitizer m-THPC. *J. Porphyrins Phthalocyanines* **2001,** *5*, 758-761.